ATLAS NOTE

ATL-COM-PHYS-2016-929

25th August 2016

Draft version 0.5

Measurement of the tau lepton reconstruction and identification performance in the ATLAS experiment using pp collisions at $\sqrt{s} = 13$ TeV

Not reviewed, for internal circulation only

Mitani, Takashi[b], Pickering, Mark Andrew[a], Zhang, Lei[r], Chan, Wing Sheung[f], Drechsler, Eric[i], Ohman, Henrik[u], Ikai, Takashi[b], Janus, Michel[i], Megy, Theo Jean[r], Mori, Tatsuya[h], Xia, Ligang[d], Buat, Quentin[w], Davey, Will[m], Deviveiros, Pier-Olivier[t], Zanzi, Daniele[l], Ali, Babar[c], Andreazza, Attilio[x], Ayoub, Mohamad Kassem[k], Bouhova-Thacker, Evelina Vassileva[s], Burghgrave, Blake[v], Duschinger, Dirk[g], Fox, Harald[s], Griffiths, Justin[q], Hauswald, Lorenz[g], Jabbar, Samina[y], Kaczmarska, Anna[o], Le, Brian[l], Martin dit Latour, Bertrand[p], Nellist, Clara[k], Parker, Adam Jackson[s], Rompotis, Nikolaos[n], Ruthmann, Nils[t], Shan, Lianyou[e], Soloshenko, Alexei[j], Thomsen, Lotte Ansgaard[z], Yuen, Stephanie P.[m], Wagner, Peter[m], Winter, Benedict Tobias[m], Wolter, Marcin Wladyslaw[o], Zinonos, Zinonas[i]

[a]*Department of Physics, Oxford University*

[b]*Waseda University, Waseda Research Institute for Science and engineering (WISE)*

[c]*Czech Technical University in Prague, Inst. of Exp. and Applied Physics, Fac. of Nuclear Sciences and Physical Engineering, Fac. of Mechanical Engineering, Fac. of Transportation Sciences*

[d]*Tsinghua University*

[e]*Institute of High Energy Physics, Chinese Academy of Sciences*

[f]*The Chinese University of Hong Kong*

[g]*Institut fuer Kern- und Teilchenphysik, Technische Universitaet Dresden*

[h]*International Center for Elementary Particle Physics and Department of Physics, The University of Tokyo*

[i]*Georg-August-Universitat Goettingen, II. Physikalisches Institut*

[j]*Joint Institute for Nuclear Research*

[k]*LAL, Univ. Paris-Sud, IN2P3/CNRS, Universite Paris-Saclay*

[l]*ARC Centre of Excellence in Particle Physics at the Terascale, School of Physics, The University of Melbourne*

[m]*University of Bonn*

[n]*Department of Physics, University of Washington, Seattle*

[o]*Institute of Nuclear Physics Polish Academy of Sciences, Krakow*

[p]*University of Bergen*

[q]*The University of Texas at Arlington*

[r]*Albert-Ludwigs-Universitaet Freiburg, Fakultaet fuer Mathematik und Physik*

[s]*Lancaster University, Department of Physics*

[t]*European Laboratory for Particle Physics, CERN*

[u]*Uppsala University, Department of Physics and Astronomy*

[v]*Northern Illinois University*

[w]*Simon Fraser University*

[x]*INFN Milano and Universita' di Milano, Dipartimento di Fisica*

[y]*University of Alberta*

[z]*Yale University*

Abstract

This document details measurements of the performance of the reconstruction and identification of hadronic tau lepton decays using the ATLAS detector. The performance of these algorithms is measured with Z boson or top quark decays to tau leptons and uses the full 2015 dataset of pp collisions collected at the LHC, corresponding to an integrated luminosity of 3.2 fb^{-1} and a center-of-mass energy $\sqrt{s}$ = 13 TeV. The measurements include the performance of the offline and online identification algorithms, the energy calibration and the electron discrimination algorithm for reconstructed tau candidates. The offline tau identification efficiency is measured with a precision of between 5.0% and 6.0%, depending on the number of associated tracks. For hadronic tau lepton decays selected by offline algorithms, the tau trigger identification efficiency is measured with a precision of between 2% and 10%, depending on the transverse energy, for tau candidates with a transverse energy below 100 GeV. The tau energy scale is measured with a precision of between 1.4% and 2.6%, depending on the number of associated tracks. The probability of misidentifying an electron as a tau lepton is measured to be $< 2\%$ for tau candidates with 20 GeV $< p_{\mathrm{T}} <$ 50 GeV.

Contents

0 Notes **7**

1 Introduction **8**

2 ATLAS detector **9**

3 Data and simulation samples **9**

4 Object selection **10**

5 Updates to the tau energy calibration and electron discrimination algorithm **11**
- 5.1 MVA-based tau energy calibration 11
- 5.2 Electron discrimination algorithm 14

6 $Z \to \tau_{\mu}\tau_{\text{had}}$ tag-and-probe analyses **14**
- 6.1 Common event selection 14
- 6.2 Offline tau identification efficiency measurement 15
  - 6.2.1 Signal and Background estimation 16
  - 6.2.2 Results 17
- 6.3 Trigger efficiency measurement 31
  - 6.3.1 Signal and Background estimation 31
  - 6.3.2 Results 32
- 6.4 Offline $\tau_{\text{had-vis}}$ energy calibration 34
  - 6.4.1 Signal and Background estimation 34
  - 6.4.2 Results 35

7 $t\bar{t}$ tag-and-probe analyses **36**
- 7.1 Offline tau identification efficiency measurement 36
- 7.2 Trigger efficiency measurement 36
  - 7.2.1 Event selection 36
  - 7.2.2 Signal and background processes 36
  - 7.2.3 Results 37

8 $Z \to ee$ tag-and-probe analysis **38**
- 8.1 Event selection 38
- 8.2 Signal and background processes 39
- 8.3 Results 39

9 Summary and conclusions **40**

Appendix **44**

A Offline tau identification efficiency measurement **44**
- A.1 Event selection 44
- A.2 Efficiency extraction 45
- A.3 Results 47

B Online tau identification efficiency measurement **54**
B.1 Object & Event Selection 54
B.2 Backgrounds Estimation 55
B.2.1 Multi-jets Estimation 56
B.2.2 W+jets Estimation 57
B.2.3 Summary of Backgrounds Estimation 59
B.3 Method 60
B.4 Systematic Uncertainties 60
B.5 Results 61
B.5.1 Kinematics before applying τ trigger 61
B.5.2 Kinematics after applying τ trigger 61
B.5.3 Efficiencies and Scale factors 64

C Electron misidentification probability measurement **70**
C.1 Eveto tuning 70
C.2 Event selection 71
C.3 QCD Control Region 72
C.4 W Control Region 74
C.5 Kinematics of fake taus 76
C.6 Efficiency Measurement and Scalefactors 80
C.6.1 Rejection of loose electrons 81
C.6.2 Rejection of medium electrons 82
C.6.3 Rejection of tight electrons 83

D In-situ tau energy scale calibration **84**
D.1 Introduction of the in-situ method 84
D.2 Background estimation 84
D.3 Event selection 85
D.4 TES estimation 87
D.5 systematic uncertainties 87

E Offline $t\bar{t}$ tau identification efficiency measurement **93**
E.1 Brief Review Of This Study 93
E.1.1 Object Definition 93
E.1.2 Pre-Selection For The Signal Region 94
E.1.3 Tag And Probe Selection 94
E.1.4 Plots At The Signal Region ('No Tau ID' vs 'Tight ID') 95
E.2 Background Estimation 95
E.2.1 Track Multiplicity For Template Fit 95
E.2.2 Configuration Of Template Fit 103
E.2.3 Total Channel 104
E.2.4 Pass Channel 104
E.2.5 Building Templates For Fake-Jets In A Data-Driven Way 106
E.2.6 Measurement Of Fake-Jet Efficiency 106
E.3 Result 107
E.4 Events Where Probe Is B-Jet 108
E.5 Contribution Of Multi-Jet Events 108

E.6 Geometrical Uncertainty On Tau Template 109
E.7 Systematic Uncertainty On Fake-Jet Efficiency 109
E.7.1 Variation of Photon Isolation 109
E.7.2 Comparison of $\gamma + jet$ and $W + jet$ 111
E.8 All Triggers For The $\gamma + jet$ Sample 112

F Online $t\bar{t}$ tau identification efficiency measurement 119
F.1 Event Selection 119
F.2 Backgrounds and Templates 119
F.2.1 Signal events 119
F.2.2 Jet fakes modeled with data 119
F.2.3 Jet fakes modeled with simulated events 121
F.2.4 Lepton fakes 121
F.2.5 SS data normalization factors 121
F.3 Systematic Uncertainties 122
F.4 Method 125
F.5 Results 126
F.5.1 Control plots 126
F.5.2 Control plots with τ trigger 126
F.5.3 Efficiencies and scale factors 130
F.6 Combination of results from $Z \to \tau\tau$ and $t\bar{t}$ trigger tag-and-probe analyses 130

G High-p_{T} tau identification 135
G.1 Samples and event selection 135
G.2 Mis-identification rate of tau particles 136
G.3 High-p_{T} tau uncertainty inflation 141

H MVA-based $\tau_{\mathrm{had-vis}}$ energy calibration 148
H.1 MVA regression algorithms 148
H.2 Input variables and regression target 148
H.3 Raw values and ratios of variables 152
H.4 Interpolated transverse momentum 154
H.5 Settings of BDT training 154

0. Notes

The CONF document here describes several performance analyses performed on the 2015 dataset.

This is the first formal draft of the note, referred to as draft version 0.5. Previous editions revised by the working group can be found via the svn link in the section "drafts".

Major changes to do still:

- Move the offline ttbar information into the main CONF body.
- Restyling of MVA TES performance plots
- Add systematics tables for all results i.e. eveto and Ztautau online.
- Add eVeto update performance plot
- Decide on presentation of BDT variable plots - where to put
- Add TES-MVA in-situ results
- Online ttbar stack plots (before after trigger as for Ztautau)

1. Introduction

With a mass of 1.777 GeV and a proper decay length of 87 μm [1], tau leptons decay either leptonically ($\tau \to \ell \nu_\ell \nu_\tau$, $\ell = e, \mu$) or hadronically ($\tau \to$ hadrons ν_τ, labelled as τ_{had}) and do so typically before reaching active regions of the ATLAS detector. In this note, only hadronic tau lepton decays are considered. The hadronic tau lepton decays represent 65% of all possible decay modes. The hadronic decay products are one or three charged pions in 72% and 22% of all cases, respectively. In 78% of all hadronic decays, up to one associated neutral pion is also produced. The neutral and charged hadrons stemming from the tau lepton decay make up the visible part of the tau lepton, and in the following are referred to as $\tau_{\text{had-vis}}$.

The main background of hadronic tau lepton decays is from jets of energetic hadrons produced via the fragmentation of quarks and gluons. This background is present at the trigger (also referred to as *online* in the following) as well as during the event reconstruction (referred to as *offline*). Discriminating variables based on the narrow shower in the calorimeter, the distinct number of tracks and the displaced tau lepton decay vertex are used to distinguish $\tau_{\text{had-vis}}$ candidates from jets. Electrons also form an important background for $\tau_{\text{had-vis}}$ containing one charged hadron.

Final states with hadronically decaying tau leptons are an important part of the ATLAS physics program. This places strong requirements on both $\tau_{\text{had-vis}}$ reconstruction and identification algorithms, as well as the performance measurements of the algorithms. The algorithms involved in triggering, reconstructing and identifying tau leptons during proton-proton collisions with a center-of-mass energy $\sqrt{s} = 8$ TeV are described in Ref. [2], and the updates to these algorithms for the collection of 2015, $\sqrt{s} = 13$ TeV data are described in Ref. [3].

This note first describes further updates to these algorithms for 2016 data-taking, and then describes performance measurements of several analyses related to the triggering, reconstruction and identification of hadronic tau lepton decays using the 2015 data. The performance of online and offline tau identification, and the tau energy scale calibration is measured using a *tag-and-probe* method applied to events enriched in $Z \to \tau\tau$ processes, with one tau lepton decaying to a muon, τ_μ (*tag*), and the other decaying hadronically, τ_{had} (*probe*). The performance of the online and offline tau identification algorithms in simulation and in recorded data are measured and correction factors are derived. For the tau energy scale measurement, the reconstructed visible mass distribution of the muon and $\tau_{\text{had-vis}}$ system is determined in both data and simulation, and the energy calibration required to obtain agreement calculated.

In order to extend the range of the p_{T} spectrum of tau candidates, the performance of the offline tau identification algorithm is also measured using events enriched in $t\bar{t}$ processes. This measurement similarly uses the tag-and-probe method with a muon (tag) and a hadronic tau lepton decay (probe) present to investigate the online tau identification efficiency and correction factors between simulation and data. Finally, the performance of the electron rejection algorithm is measured. The tag-and-probe method is used in events enriched in $Z \to ee$ decays featuring at least one electron (tag) and a tau candidate (probe), and the efficiency of the electron rejection algorithm is measured.

This note is organised as follows. After a description of the ATLAS detector in section 2, the data and simulation samples used in the studies presented are described in section 3. The reconstruction and requirements on the objects used in this note are described in section 4. Updates to the 2015 tau energy calibration, and electron rejection method are described in section 5. The 2015 tau identification and energy scale performance measurements using the tag-and-probe method in $Z \to \tau_\mu \tau_{\text{had}}$ events are described in section 6. Similarly the tag-and-probe studies carried out using $t\bar{t}$ and $Z \to ee$ events are described in sections 7 and 8 respectively.

2. ATLAS detector

The ATLAS detector [4] consists of an inner tracking system surrounded by a superconducting solenoid, electromagnetic (EM) and hadronic (HAD) calorimeters, and a muon spectrometer (MS).

The inner detector is immersed in a 2 T axial magnetic field, and consists of silicon pixel and microstrip (SCT) detectors inside a transition radiation tracker (TRT), providing charged particle tracking in the region $|\eta| < 2.5$. [1] For the $\sqrt{s} = 13$ TeV run, a fourth layer of the pixel detector, the Insertable B-Layer (IBL) [5], has been inserted at an average radius of 33.2 mm, providing an additional position measurement with 8 μm resolution in the (x, y) plane and 40 μm along z.

The EM calorimeter uses lead and liquid argon (LAr) as absorber and active materials, respectively. In the central rapidity region, the EM calorimeter is divided in three layers, one of them segmented in thin η strips for optimal γ/π^0 separation, completed by a presampler layer for $|\eta| < 1.8$. Hadron calorimetry is based on different detector technologies, with scintillator tiles ($|\eta| < 1.7$) or LAr ($1.5 < |\eta| < 4.9$) as active media, and uses steel, copper, or tungsten as the absorber material. The calorimeters provide coverage within $|\eta| < 4.9$. The MS consists of superconducting air-core toroids, a system of trigger chambers covering the range $|\eta| < 2.4$, and high-precision tracking chambers allowing muon momentum measurements within $|\eta| < 2.7$.

The ATLAS trigger system consists of two levels which reduce the initial bunch crossing rate to a manageable rate for disk storage while keeping interesting physics events. The first level (L1) is hardware-based and uses a subset of the detector information to reduce the accepted event rate to 100 kHz [6]. This is followed by a software-based High Level Trigger (HLT) that further reduces the average recorded collision rate to around 1 kHz.

3. Data and simulation samples

The data used in this note were recorded by the ATLAS experiment during the 2015 LHC run with proton-proton collisions at a centre-of-mass energy of $\sqrt{s} = 13$ TeV. They correspond to an integrated luminosity of 3.2 fb^{-1}. To ensure good data quality, the inner-detector tracking systems, calorimeters and muon spectrometer are required to be fully operational.

Signal and background samples are produced using Monte Carlo (MC) simulation with various event generators. These generated event samples are then propagated through a detailed Geant4 simulation [7] of the ATLAS detector and subdetector-specific digitisation algorithms [8]. The simulated events are reconstructed with the same algorithms as the data. Background samples of W and Z/γ^* bosons produced in association with jets, $t\bar{t}$, single top and diboson processes are used. All W and Z/γ^* samples are generated with Powheg [9] and showered with Pythia8 [10]. The $t\bar{t}$ and single top samples are also generated with Powheg and showered with Pythia6 [11]. Diboson events are generated using the SHERPA generator [12].

[1] ATLAS uses a right-handed coordinate system with its origin at the nominal interaction point (IP) in the centre of the detector and the z-axis along the beam direction. The x-axis points from the IP to the centre of the LHC ring, and the y-axis points upward. Cylindrical coordinates (r, ϕ) are used in the transverse (x, y) plane, ϕ being the azimuthal angle around the beam direction. The pseudorapidity is defined in terms of the polar angle θ as $\eta = -\ln\tan(\theta/2)$. The distance ΔR in the $\eta - \phi$ space is defined as $\Delta R = \sqrt{(\Delta\eta)^2 + (\Delta\phi)^2}$.

The effect of multiple proton (pp) interactions, referred to as pile-up, is simulated by overlaying minimum-bias interactions on the generated events. The simulated events are reweighted such that the average number of pp interactions per bunch crossing has the same distribution in data and simulation.

4. Object selection

Muons are reconstructed by combining an inner detector track with a track from the MS [13]. They are required to have $p_{\mathrm{T}} > 22$ GeV and $|\eta| < 2.5$. Corrections on simulated reconstruction efficiencies, derived from the data, are applied to the simulated samples.

Electrons are reconstructed by matching clustered energy deposits in the electromagnetic calorimeter to tracks reconstructed in the inner detector, and are required to have $p_{\mathrm{T}} > 15$ GeV and $|\eta| < 2.47$ (excluding the region $1.37 < |\eta| < 1.52$) [14]. They must satisfy the *medium* likelihood-based identification criteria as described in Ref. [15]. Corrections to the reconstruction and identification efficiencies derived from the data are applied to the simulated samples.

For muons and electrons, the scalar sum of the transverse momenta of tracks within a cone of p_{T}-dependent size, $\Delta R <\min\,(10\ GeV/p_{\mathrm{T}}, 0.3)$, centred on the lepton candidate track and excluding the lepton track, is required to be less than a p_{T}-dependent fraction of the lepton transverse momentum. Additionally, the sum of the calorimeter energy deposits in a cone of size $\Delta R < 0.2$ around the lepton, excluding energy associated with the lepton candidate, must be less than a p_{T} dependent percentage of the lepton energy. Two working points of this varied cone definition are used in the note: the first one, called *loose*, has a 99% efficiency constant across the full p_{T} range, and the second one called gradient which 90(99)% efficiency at 25 (60) GeV. The loose isolation is used in the $t\bar{t}$ offline identification efficiency measurement, whilst gradient is used in the $t\bar{t}$ and $Z \to \tau_{\mu}\tau_{\mathrm{had}}$ trigger efficiency measurement, as well as $Z \to ee$ tag-and-probe analysis. Another isolation criteria uses a similar definition, except with a fixed cone size of $\Delta R < 0.4$ for tracks and with the threshold values fixed at 1% and 4% for the sum of track momenta, and the sum of the calorimeter energy deposits respectively. This isolation, referred to as *fixed-threshold* isolation, provides a stronger multi-jet rejection. Fixed-threshold isolation is used in the online tau identification and tau energy scale measurements.

Jets are constructed using the anti-k_t algorithm [16], with a distance parameter $R = 0.4$. Three-dimensional clusters of calorimeter cells called *TopoClusters* [17], calibrated using a local hadronic calibration (LC) [18], serve as inputs to the jet algorithm. Jets are required to be within $|\eta| < 4.5$. A dedicated b-tagging algorithm described in Ref. [19] is used to identify jets associated with the decay of a b-quark with a 77% efficiency.

Tau candidates are seeded by jets as described above. The triggering, reconstruction and identification of $\tau_{\mathrm{had-vis}}$ candidates is described in detail in Ref. [2]. The energy calibration and tau identification have been updated for the expected conditions in 13 TeV collisions in Ref. [3]. The tau identification uses Boosted Decision Tree (BDT) based methods [20, 21], whereby the BDT is used to combine a set of discriminating variables. Three working points, labelled *tight*, *medium* and *loose*, are provided, and correspond to different tau identification efficiency values, with the efficiency designed to be independent of p_{T}. To reduce the electron background, reconstructed $\tau_{\mathrm{had-vis}}$ candidates within a distance of $\Delta R < 0.4$ of a reconstructed electron are rejected if the electron passes a *very loose* working point of the electron likelihood discriminator. This electron veto is tuned to yield a 95% efficiency, and is dependent on the p_{T} and η of the tau candidate.

In this note, $\tau_{\mathrm{had-vis}}$ candidates are required to have $p_{\mathrm{T}} > 20$ GeV and $|\eta| < 2.5$ (excluding the transition region between the barrel and endcap calorimeters, corresponding to the region $1.37 < |\eta| < 1.52$). The application of the tau identification criteria to a tau candidate depends on the analysis considered, and is described in the respective sections. The $\tau_{\mathrm{had-vis}}$ candidates are required to have one or three associated tracks in the *core region* ($\Delta R < 0.2$) around the $\tau_{\mathrm{had-vis}}$ axis and an absolute electric charge of one, as this is the most common selection used in searches and measurements.

The geometric overlap of objects with $\Delta R < 0.2$ is resolved by selecting only one of the overlapping objects in the following order of priority: muons, electrons, $\tau_{\mathrm{had-vis}}$ candidates, and jets. The missing transverse momentum, with magnitude $E_{\mathrm{T}}^{\mathrm{miss}}$, is calculated from the vector sum of the transverse momenta of all reconstructed electrons, muons, $\tau_{\mathrm{had-vis}}$ and jets in the event, as well as a term for the remaining tracks [22].

5. Updates to the tau energy calibration and electron discrimination algorithm

After 2015 data-taking, several updates have been made to the tau energy calibration and the electron discrimination algorithm.

5.1. MVA-based tau energy calibration

The baseline calculation of $\tau_{\mathrm{had-vis}}$ energy [3] uses TopoClusters within $\Delta R < 0.2$ from the initial seed-jet axis. It includes a final tau-specific calibration derived from simulated samples, which accounts for out-of-cone energy, underlying event, the typical composition of hadrons in hadronic tau decays and contributions from multiple interactions occurring in the same and neighbouring bunch crossings (called pileup). The resolution is excellent at high-p_{T} but quickly degrades at low-p_{T}. A new method of reconstructing the individual charged and neutral hadrons in tau decays was recently developed by the ATLAS experiment [23], called “Tau Particle Flow" (TPF). The method significantly improves the tau energy resolution at low-p_{T} due to the superior measurement of the charged pion momentum from the tracking system.

In this note, a new calibration is introduced which combines the information from the baseline and TPF methods together with some additional calorimeter and tracking information via a multivariate-analysis (MVA) technique. This technique is referred to as a boosted regression tree (BRT) method, and is implemented using the TMVA package [24].

To optimise the BRT, tau candidates satisfying the medium tau identification requirement coming from simulated $Z/\gamma^{*} \to \tau\tau$ events are used. The two figures of merit used in optimising the BRT are defined as follows: the *resolution* is defined as the half-width of the symmetric 68% confidence interval of the ratio of the calibrated $\tau_{\mathrm{had-vis}}$ transverse momentum, $p_{\mathrm{T}}^{\mathrm{cali}}$, to the generated $\tau_{\mathrm{had-vis}}$ transverse momentum, $p_{\mathrm{T}}^{\mathrm{true,vis}}$, whilst the *non-closure* is the offset of the most probable value of the ratio $p_{\mathrm{T}}^{\mathrm{cali}}/p_{\mathrm{T}}^{\mathrm{true,vis}}$ from unity. The transverse component of the sum of the momenta of the reconstructed charged hadron and neutral pion constituents is referred to as $p_{\mathrm{T}}^{\mathrm{TPF}}$, and the transverse momentum at LC scale is $p_{\mathrm{T}}^{\mathrm{LC}}$. As at low p_{T} the

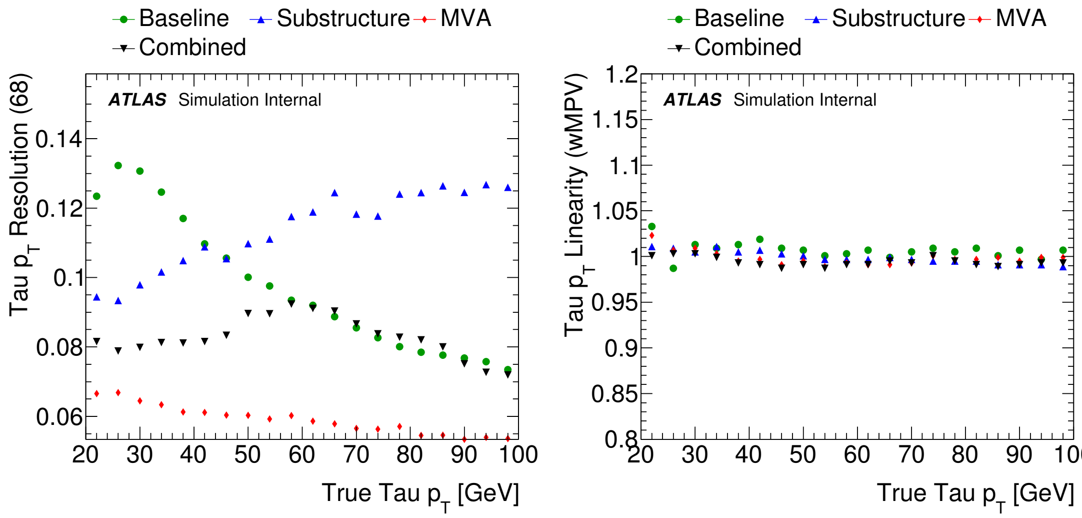

Figure 1: The resolution (a) and the linearity (b) of the MVA-based $\tau_{\text{had-vis}}$ energy calibration, compared to the Baseline and TPF reconstructions, and the resolution-weighted average of both (Combined). The resolution, shown as a function of the generated tau p_{T}, is defined as the half-width of the symmetric 68% confidence interval of the ratio of the calibrated p_{T} to the true visible p_{T}. The linearity is defined as the most probable value of the ratio of the calibrated p_{T} to the true visible p_{T}.

resolution of $p_{\text{T}}^{\text{TPF}}$ is better than p_{T}^{LC} and vice-versa at higher p_{T}, the interpolated transverse momentum, $p_{\text{T}}^{\text{interp}}$, is defined in the following equation:

$$p_{\text{T}}^{\text{interp}} = f_x \times p_{\text{T}}^{\text{LC}} + (1 - f_x) \times p_{\text{T}}^{\text{TPF}}, \tag{1}$$

where f_x is a weight between zero and one and is a function of p_{T}^{LC}:

$$f_x(p_{\text{T}}^{\text{LC}}) = \frac{1}{2}\left(1 + \tanh \frac{p_{\text{T}}^{\text{LC}} - x\ \text{GeV}}{20\ \text{GeV}}\right). \tag{2}$$

The symbol x defines the point where the transition from low p_{T} to high p_{T} occurs, and is chosen to be $x = 250$. The regression target is the ratio of the generated $\tau_{\text{had-vis}}$ transverse momentum to $p_{\text{T}}^{\text{interp}}$.

The final input variables used in the regression BRT are listed and described in Table 1. The transverse momenta p_{T}^{LC} and $p_{\text{T}}^{\text{TPF}}$ provide basic knowledge about the $\tau_{\text{had-vis}}$ energy. The regression BRT is less powerful when two variables are highly correlated and so to reduce the correlation, ratios of these variables $p_{\text{T}}^{\text{LC}}/p_{\text{T}}^{\text{interp}}$ and $p_{\text{T}}^{\text{TPF}}/p_{\text{T}}^{\text{interp}}$ are used instead of the raw values. Cluster variables such as λ_{centre}, $\left\langle \lambda^2 \right\rangle$, $\langle \rho \rangle$, $f_{\text{presampler}}$, and P_{EM}, used in the LC calibration, as described in Ref. [18], of the $\tau_{\text{had-vis}}$ energy are found to be powerful input variables in the MVA tau energy calibration. The variables μ and n_{PV} are included to provide information about multiple interactions occurring in the same and neighbouring bunch crossings, whilst γ_π and n_{π^0} are variables that provide information about the tau candidate's decay modes and improve the resolution at low p_{T}.

Figure 1 shows the performance of the MVA energy scale calibration. In the region $p_{\text{T}} < 100$ GeV, the MVA tau energy calibration improves on the baseline resolution by a factor of two, while at high p_{T} the performance is comparable.

Number of primary vertices, n_{PV} Number of primary vertices in the event
Average interactions per crossing, μ Average number of interactions per bunch crossing
Cluster shower depth, $\lambda_{\mathrm{centre}}$ Distance of the cluster shower centre from the calorimeter front face measured along the shower axis
Cluster second moment in λ, $\langle\lambda^2\rangle$ Distance of a cell from the shower centre along the shower axis
Cluster first moment in energy density, $\langle\rho\rangle$ Cluster first moment in energy density $\rho = E/V$
Cluster presampler fraction, $f_{\mathrm{presampler}}$ Fraction of cluster energy deposited in the barrel and endcap presamplers
Cluster EM-like probability, P_{EM} Classification probability of the cluster to be EM-like, as described in Ref. [18]
Number of associated tracks, n_{track} Number of tracks associated with the $\tau_{\mathrm{had-vis}}$
Number of reconstructed neutral pions, n_{π^0} Number of reconstructed neutral pions associated with the $\tau_{\mathrm{had-vis}}$
Relative difference of pion energies, γ_π Relative difference of the total charged pion energy E_{charged} and the total neutral pion energy E_{neutral}: $\gamma_\pi = (E_{\mathrm{charged}} - E_{\mathrm{neutral}})/(E_{\mathrm{charged}} + E_{\mathrm{neutral}})$
Calorimeter-based pseudorapidity, η_{calo} Calorimeter-based (Baseline) pseudorapidity
Interpolated transverse momentum, $p_{\mathrm{T}}^{\mathrm{interp}}$ Transverse momentum interpolated from calorimetric corrections to energy measurement and TPF reconstruction.
Ratio of $p_{\mathrm{T}}^{\mathrm{LC}}$ to $p_{\mathrm{T}}^{\mathrm{interp}}$, $p_{\mathrm{T}}^{\mathrm{LC}}/p_{\mathrm{T}}^{\mathrm{interp}}$ Ratio of the local hadron calibration transverse momentum to $p_{\mathrm{T}}^{\mathrm{interp}}$
Ratio of $p_{\mathrm{T}}^{\mathrm{TPF}}$ to $p_{\mathrm{T}}^{\mathrm{interp}}$, $p_{\mathrm{T}}^{\mathrm{TPF}}/p_{\mathrm{T}}^{\mathrm{interp}}$ Ratio of the TPF reconstruction transverse momentum, $p_{\mathrm{T}}^{\mathrm{TPF}}$, to $p_{\mathrm{T}}^{\mathrm{interp}}$

Table 1: List of input variables used for $\tau_{\mathrm{had-vis}}$ energy MVA regression. The cluster variables are the energy weighted averages over the jet seed constituents within the tau cone, as described in detail in Ref. [18].

5.2. Electron discrimination algorithm

The likelihood (LLH) electron veto (e-veto) algorithm operates by placing p_T- and η-dependent cuts on the likelihood score used to identify prompt electron candidates matched to the reconstructed tau candidates within $\Delta R < 0.4$. The updated e-veto uses a new LLH tune which is better modelled by the simulation [25]. The cuts on the LLH score have been updated accordingly to maintain a 95% efficiency for $\tau_{\mathrm{had-vis}}$ in simulated $Z \to \tau\tau$ events with 2015 data-taking and pile-up conditions. The tau candidates are required to have one reconstructed track, $p_T > 20$ GeV and to be geometrically matched to a generated $\tau_{\mathrm{had-vis}}$. The tuning of the cuts was performed in bins of η and p_T to give 95% efficiency for the generated $\tau_{\mathrm{had-vis}}$ described above. The residual mismodelling of simulation is absorbed in the scale factors reported in section 8.

6. $Z \to \tau_\mu \tau_{\mathrm{had}}$ tag-and-probe analyses

To perform physics analyses involving hadronic tau lepton decays, it is important to evaluate the performance of the tau identification algorithms and the tau energy scale with data. For the $\tau_{\mathrm{had-vis}}$ signal, this is done on a sample enriched in $Z \to \tau_\mu \tau_{\mathrm{had}}$ events where one tau lepton decays to a muon and the other decays hadronically, with associated neutrinos. The chosen tag-and-probe approach consists of selecting events triggered by the presence of a muon (tag) and containing a hadronically decaying tau lepton candidate (probe) in the final state and studying the performance of the identification and energy reconstruction algorithms.

6.1. Common event selection

To select $Z \to \tau_\mu \tau_{\mathrm{had}}$ events, a single-muon trigger with an online requirement of $p_{\mathrm{T}} > 20$ GeV is used. The offline reconstructed muon candidate must have $p_{\mathrm{T}} > 22$ GeV and geometrically match the online muon. Events are required to have no additional electrons or muons and at least one $\tau_{\mathrm{had-vis}}$ candidate. If there are multiple $\tau_{\mathrm{had-vis}}$ candidates, only the leading p_{T} one is considered. In addition, a very loose requirement on the tau identification BDT output is made which suppresses jets while being more than 99% efficient for the simulated $Z \to \tau\tau$ events. The muon and $\tau_{\mathrm{had-vis}}$ candidates are required to have opposite-sign electric charges (OS). To suppress the top quark backgrounds, events with b-tagged jets are rejected. The associated b-tagging systematic uncertainty is found to be negligible.

A series of selection requirements is used to suppress W+jets (mainly $W \to \mu\nu_\mu$) events. The transverse mass of the muon and $E_{\mathrm{T}}^{\mathrm{miss}}$ system, $m_{\mathrm{T}} = \sqrt{2p_{\mathrm{T}}^{\mu} \cdot E_{\mathrm{T}}^{\mathrm{miss}}(1 - \cos\Delta\phi(\mu, E_{\mathrm{T}}^{\mathrm{miss}}))}$, is required to be less than 50 GeV, where p_{T}^{μ} is the transverse momentum of the muon, and $\cos\Delta\phi(\mu, E_{\mathrm{T}}^{\mathrm{miss}})$ is the cosine of the $\Delta\phi$ separation between the muon and the missing transverse momentum. The sum of the $\cos\Delta\phi$ between the muon and $E_{\mathrm{T}}^{\mathrm{miss}}$ (neutrinos) and between the $\tau_{\mathrm{had-vis}}$ and $E_{\mathrm{T}}^{\mathrm{miss}}$, $\Sigma\cos\Delta\phi = \cos\Delta\phi(\mu, E_{\mathrm{T}}^{\mathrm{miss}}) + \cos\Delta\phi(\tau_{\mathrm{had-vis}}, E_{\mathrm{T}}^{\mathrm{miss}})$, is required to be greater than -0.5.

In addition to the above common selection, the medium offline tau identification requirement is applied in the energy scale measurements, and the impact of the offline identification working point choice has been estimated as the systematic uncertainty. Several offline working points, i.e. loose, medium and tight, are applied in the online tau identification efficiency to derive the corresponding trigger efficiencies. A requirement on the invariant mass of the muon and tau candidate $m_{\mathrm{vis}}(\mu, \tau_{\mathrm{had-vis}})$, 45 GeV $< m_{\text{vis}}(\mu, \tau_{\text{had-vis}}) <$ 80 GeV, is applied in both online and offline tau identification efficiency measurements, but not in the energy scale measurement since the $m_{\text{vis}}(\mu, \tau_{\text{had-vis}})$ distribution is used to constrain the tau energy scale. To reduce the large contamination from misidentified jets in the offline tau identification efficiency measurement, in which the medium tau identification requirement is not applied, the lower threshold on $\Sigma \cos \Delta\phi$ is tightened to -0.1. The detailed event selections and the signal purity, i.e fraction of the generated tau leptons estimated from simulation after the selection requirements listed above, are summarised in table 2.

Analyses	Offline Identification	Online Identification	TES
m_{T}	$<$ 50 GeV	$<$ 50 GeV	$<$ 50 GeV
$\Sigma \cos \Delta\phi$	> -0.1	> -0.5	> -0.5
m_{vis}	(45-80 GeV)	(45-80 GeV)	–
Tau Identification	–	various	medium
Purity	20%	65%	65%

Table 2: Summary of the $Z \to \tau_\mu \tau_{\text{had}}$ event selections and purities in the online and offline tau identification analyses, and the tau energy scale measurement.

After the final selection, besides a small fraction of muons misidentified as hadronic tau lepton decays (which are modelled via simulation), the main background for the probe $\tau_{\text{had-vis}}$ candidates are jets misidentified as hadronic τ decays from W+jets and multi-jet events. The charge sign of misidentified jets has a weaker correlation with that of the muon than in the case of $Z \to \tau_\mu \tau_{\text{had}}$ signal events, particularly in the case of multi-jet events. Therefore, the events with same sign (SS) charge are used to model the jet to τ fake background.

To improve the modelling of the jet background, two control regions of events enriched in specific background processes are used. A W+jets control region, as shown in figure 2, is selected by requiring $E_{\text{T}}^{\text{miss}}>$ 30 GeV and $m_{\text{T}} >$ 60 GeV, and a multi-jet control region, as shown in figure 3, is selected by inverting the muon isolation requirement. The identification is applied in the control regions for the TES and the online identification measurements, while the offline identification measurement has the control regions both with and without the tau identification requirement, in order to extract the yield with and without the tau identification.

6.2. Offline tau identification efficiency measurement

The large contamination from jet backgrounds before applying the tau identification poses the greatest challenge for the offline tau identification efficiency measurement. To estimate the background contamination in data, a template fit is performed using a variable with high separation between signal and background and that is well modelled by the simulation. The variable used is the track multiplicity, defined as the sum of the number of core ($\Delta R < 0.2$) and outer ($0.2 < \Delta R < 0.6$) tracks associated to the $\tau_{\text{had-vis}}$ candidate. Outer tracks are only considered if they fulfil the track separation requirement, $D^{\text{outer}} = \min([\, p_{\text{T}}^{\text{core}}/p_{\text{T}}^{\text{outer}}\,] \cdot \Delta R(\text{core, outer})) < 4$, where $p_{\text{T}}^{\text{core}}$ refers to any track in the core region, and $\Delta R(\text{core, outer})$ refers to the distance between the candidate outer track and any track in the core region. More details can be found in Sec. 4.1 in Ref. [2]. The expected distributions of this variable for both signal and background events are then fitted to extract the $\tau_{\text{had-vis}}$ signal.

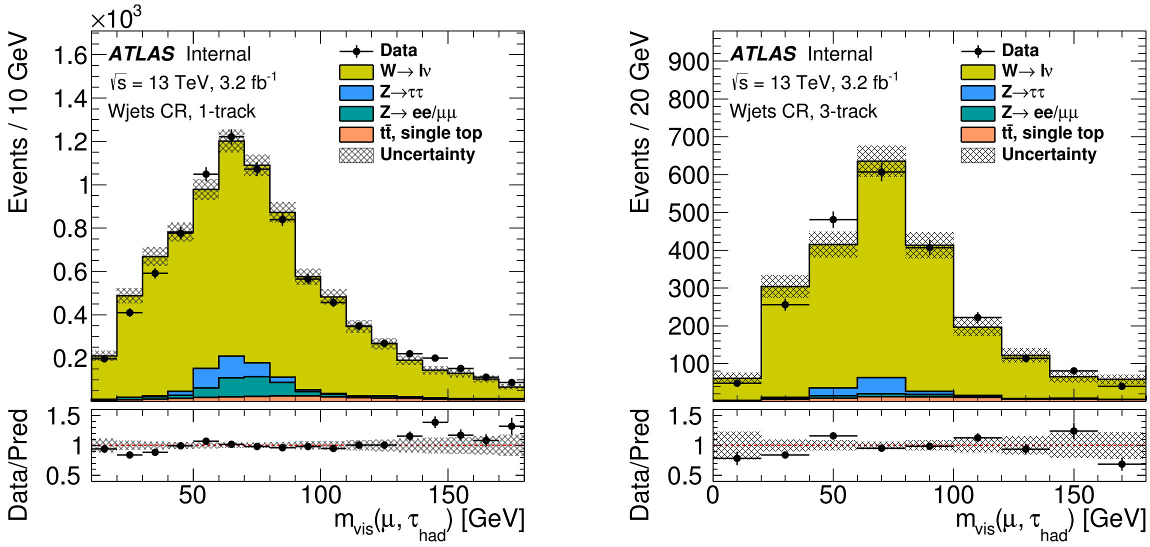

(a) 1-track (b) 3-track

Figure 2: The distribution of m_{vis}: the invariant mass of the $\tau_{\text{had-vis}}$ and muon system. Here, the tau candidate is required to pass medium identification. The error band only contains statistical uncertainty.

6.2.1. Signal and Background estimation

The signal track multiplicity distribution is modelled using simulated $Z \to \tau_\mu \tau_{\text{had}}$ events. Only reconstructed $\tau_{\text{had-vis}}$ matched to a generated hadronic tau lepton decay are considered.

A single template is used to model the background from quark- and gluon-initiated jets that are misidentified as hadronic tau lepton decays. The background is mainly composed of multi-jet and W+jets events with a minor contribution from Z+jets events. The template is constructed starting from the same sign control region, enriched in events with jets misidentified as tau candidates. The contributions from W+jets and Z+jets in the SS control region are subtracted to yield the multi-jet contribution. The template is then scaled by the ratio of OS/SS multi-jet events, measured in the multi-jet control region. A non-negligible contribution of $Z \to \tau\tau$ events is found in the OS multi-jet control region, and is challenging to model accurately via simulation. The mismodelling impacts the ratio of OS/SS multi-jet events, and as such, events with 45 GeV $< m_{\text{vis}}(\ell, \tau_{\text{had-vis}}) <$ 80 GeV in the multi-jet control region are rejected. Finally, the OS contributions from W+jets are added to complete the template. The shape of the W+jets contribution is estimated from the W+jets control region and normalised to the signal region using transferring factors derived using simulated W+jets events. The same procedure is performed to build the templates both before and after the identification requirement applied.

An additional background shape is used to take into account the contamination due to misidentified muons and electrons. This small background contribution (stemming mainly from $Z \to \mu\mu$ events) is modelled by taking the shape predicted by simulation using candidates in events of $Z \to \tau\tau$, $t\bar{t}$, diboson, $Z \to ee/\mu\mu$ where the reconstructed tau candidate probe is matched to a generated muon. For the fit, the contribution of these backgrounds is fixed to the value predicted by the simulation, which is typically less than 1% of the total signal yield.

To measure the yield of $\tau_{\text{had-vis}}$ signal and background before requiring identification, the signal plus

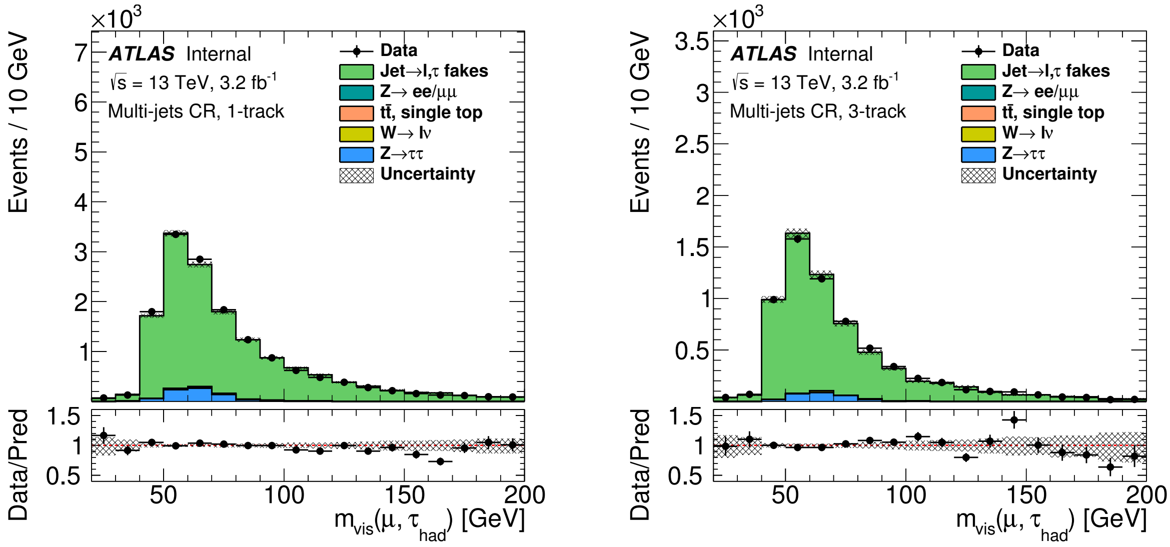

(a) 1-track (b) 3-track

Figure 3: The distribution of m_{vis}: the invariant mass of the $\tau_{\text{had-vis}}$ and muon system. Here, the tau candidate is required to pass medium identification. The error band only contains statistical uncertainty.

background model is fitted to the data, with the normalisation of both the $\tau_{\text{had-vis}}$ and jet template allowed to float. The track multiplicity included in the fit is up to 15. The signal templates are obtained by requiring exactly one or three tracks reconstructed in the core region of the $\tau_{\text{had-vis}}$ candidate. To improve the fit stability, the ratio of the one track to three track normalisation is fixed to the value predicted by the simulation. After the fit, the yield of each component can be obtained.

To extract the efficiency, the yield of real tau leptons passing different identification levels is determined from the data subtracted by the backgrounds where the normalisation is corrected by normalisation factors from the pre-identification fit.

6.2.2. Results

Figure 4 shows the track multiplicity distributions before and after applying the medium tau identification requirement. The peaks in the one- and three-track bins are due to contributions from the signal and become considerably more prominent after identification requirements are applied, due to the large amount of background rejection provided by the identification algorithm. To account for the small differences between data and the background model, correction factors (also referred to as scale factors), defined as the ratio of the efficiency in data to the efficiency in simulation for $\tau_{\text{had-vis}}$ signal to pass a certain level of identification, are derived. The results are shown in figure 5 and found to be compatible with unity.

The sources of uncertainty on the scale factors are summarised in table 3. The uncertainty on the signal template is estimated by comparing simulated signal generated with different configurations, such as variations on the amount of detector material, and the hadronic interaction model, e.g. QGSP and FTFP models [7, 26–28]. The uncertainty on the jet template accounts for differences between the W+jets shape in the signal and control regions and is derived from comparisons to simulated W+jets events, as well as the differences between the multi-jet shape in the opposite sign and same sign region derived by varying

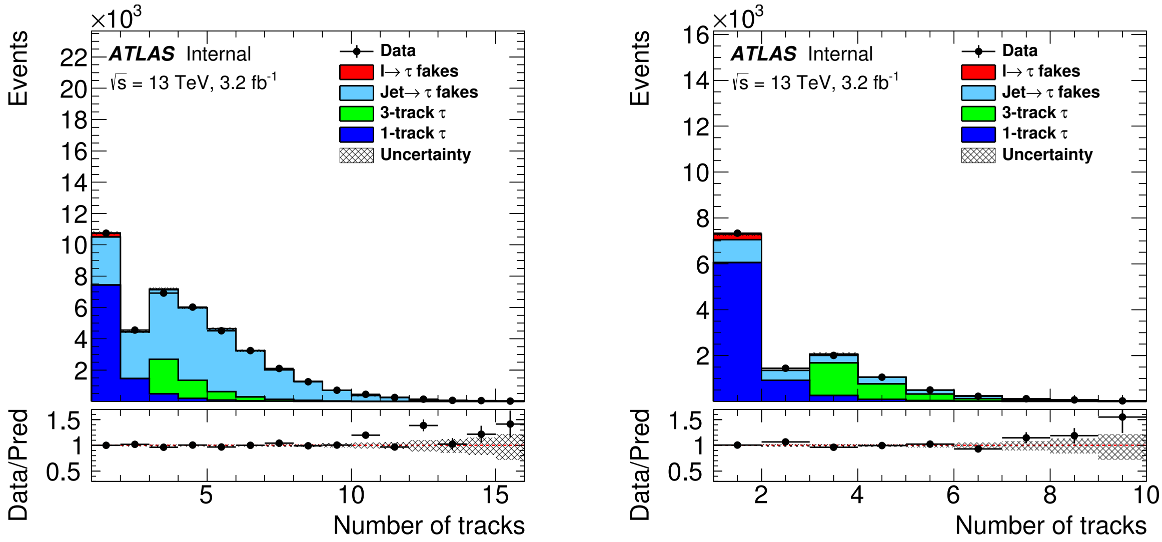

(a) Before ID

(b) Passed medium ID

Figure 4: Track multiplicity: the sum of the number of core tracks and the outer tracks in $0.2 < \Delta R < 0.6$ that fulfil the requirement $D^{\text{outer}} < 4$, as defined in the text and Ref. [2]. The true tau and jet → tau fake component are fit to data while the lepton → tau component is fixed to the simulation prediction. The uncertainty band includes only the statistical uncertainty.

the multi-jet control region selections. The uncertainty on the template due to the uncertainty on the lepton faking tau is estimated conservatively by varying the normalisation up and down by 50%.

Source	Uncertainty [%] 1-track	Uncertainty [%] 3-track
Jet template	1.5	1.5
Tau template	4.4	4.3
Lepton template	1.7	1.7
Statistics	1.7	2.8
Total	4.9	4.9

Table 3: Dominant uncertainties on the tau identification efficiency scale factors estimated with the Z boson tag-and-probe method, and the total uncertainty, which combines systematic and statistical uncertainties. These uncertainties apply to $\tau_{\text{had-vis}}$ candidates passing the medium tau identification algorithm with $p_{\text{T}} > 20$ GeV.

Figure 6 shows the jet BDT score distribution, while figures 7 to 25 show the input variables of the jet discriminant BDT. In both sets of plots, the estimations of the signal and background are as described previously in this section. The definition of the input variables can be found in Sec. 5.1 in Ref. [3].

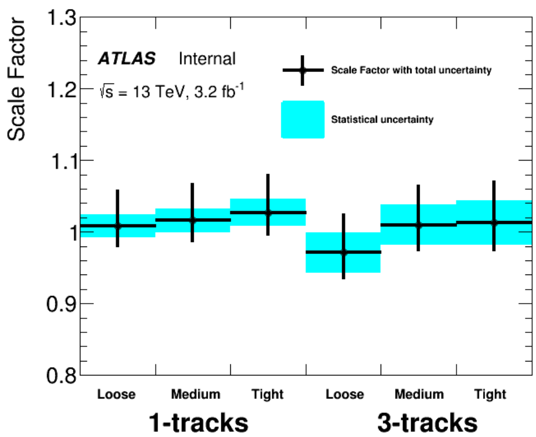

Figure 5: The scale factors needed to bring the offline tau identification efficiency in simulation to the level observed in data for one track and three track $\tau_{\mathrm{had-vis}}$ candidates with $p_{\mathrm{T}} > 20$ GeV. The combined systematic and statistical uncertainties are shown.

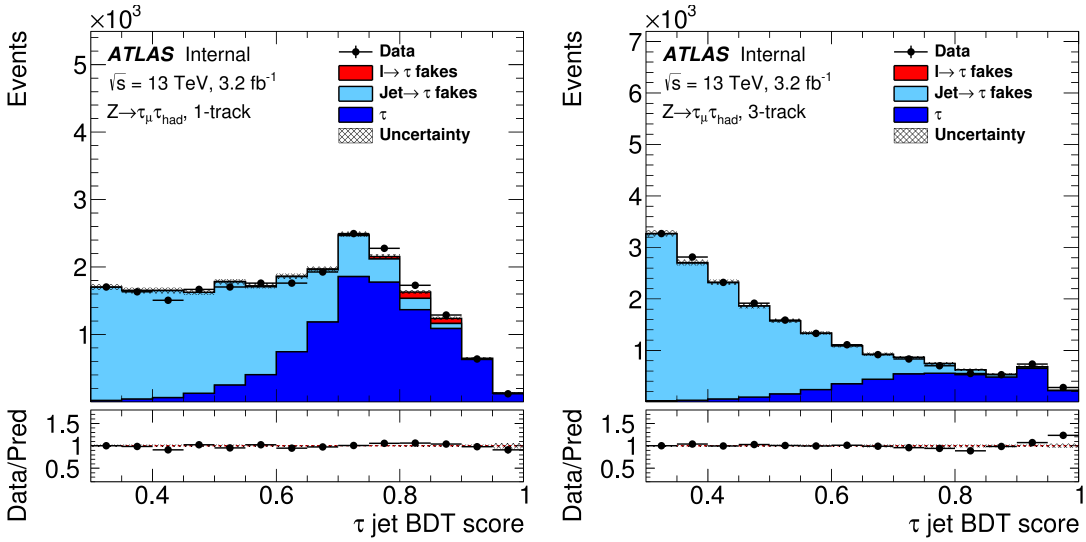

Figure 6: The jet discriminant BDT output distribution for one track (a) and three track(b) $\tau_{\mathrm{had-vis}}$ candidates. As mentioned in the text, a very loose cut, BDT>0.3, is applied in the $\tau_{\mathrm{had-vis}}$ selection, which leads less than 1% inefficiency. The background estimation is the same as the main analysis as shown in figure 4 and the normalisation factors of the templates from the fit have been applied. The uncertainty band includes only the statistical uncertainty.

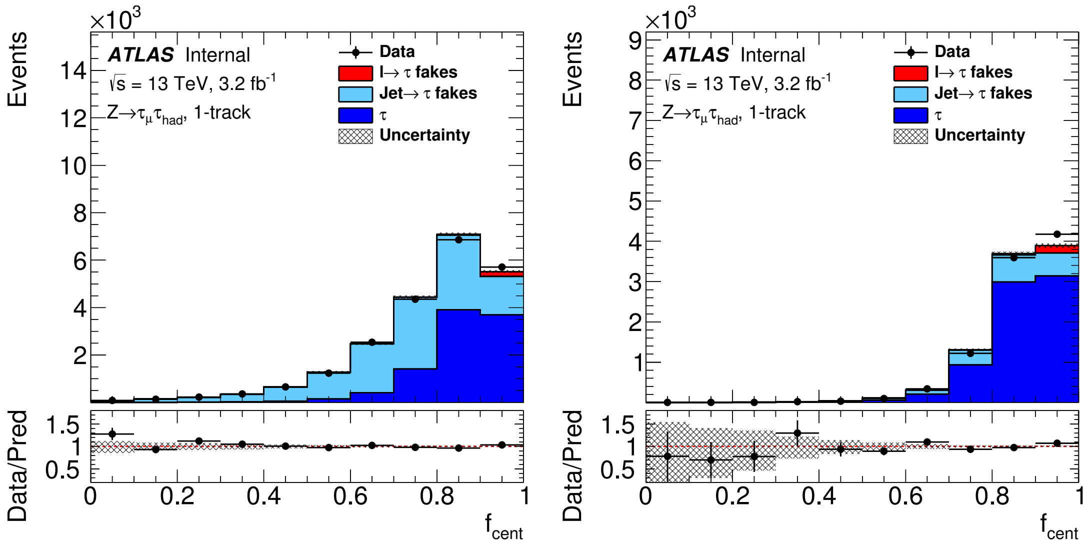

Figure 7: The jet discriminant BDT inputs: **Central energy fraction f_{cent}** for $\tau_{\mathrm{had-vis}}$ candidates before (a) and after (b) medium identification requirement. The background estimation is the same as the main analysis as shown in figure 4 and the normalisation factors of the templates from the fit have been applied. The uncertainty band includes only the statistical uncertainty.

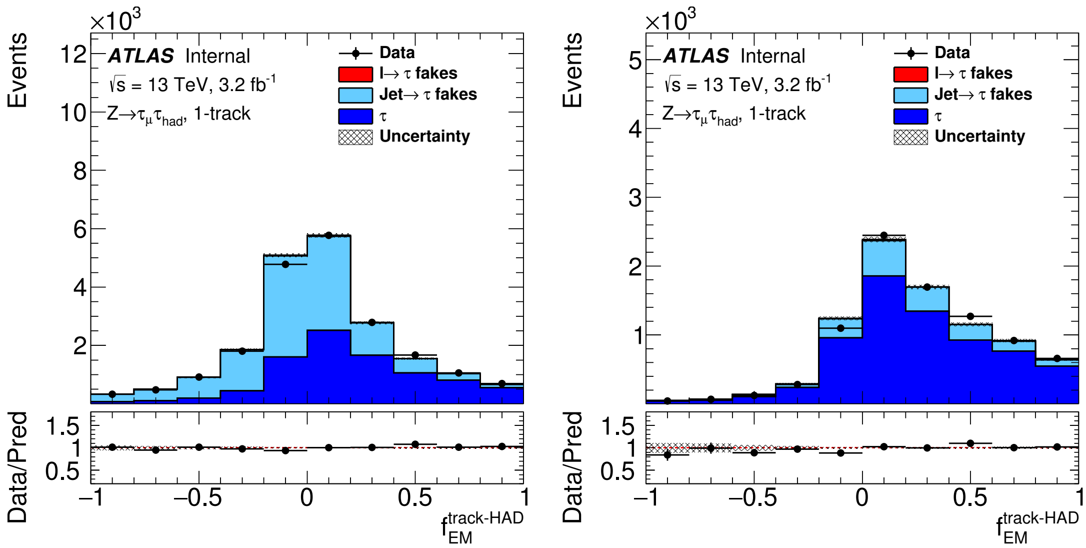

Figure 8: The jet discriminant BDT inputs: **Fraction of EM energy from charged pions $f_{\mathrm{EM}}^{\mathrm{track-HAD}}$** for $\tau_{\mathrm{had-vis}}$ candidates before (a) and after (b) medium identification requirement. The background estimation is the same as the main analysis as shown in figure 4 and the normalisation factors of the templates from the fit have been applied. The uncertainty band includes only the statistical uncertainty.

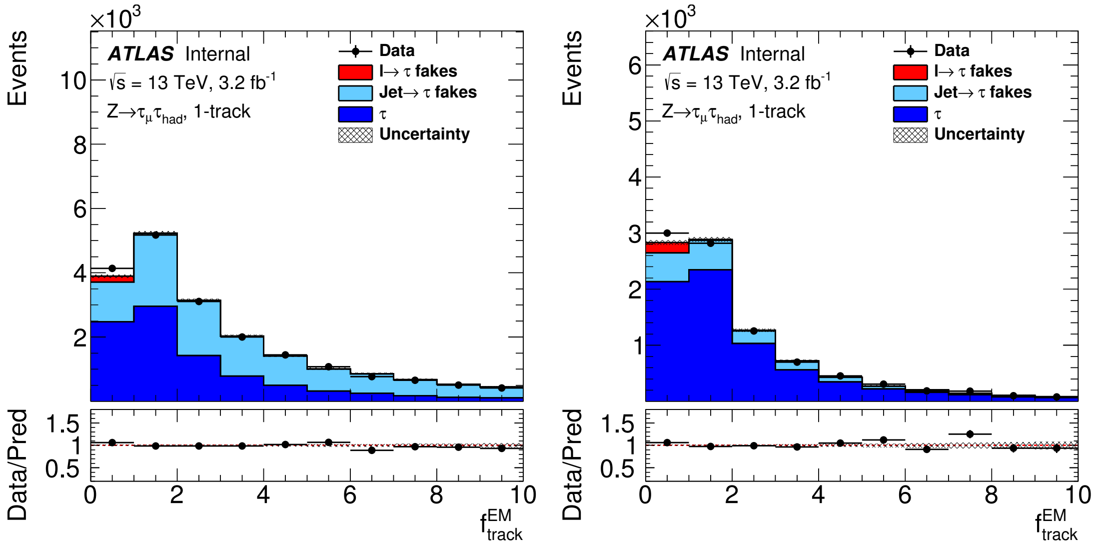

Figure 9: The jet discriminant BDT inputs: **Ratio of EM energy to track momentum f^{EM}_{track}** for $\tau_{had-vis}$ candidates before (a) and after (b) medium identification requirement. The background estimation is the same as the main analysis as shown in figure 4 and the normalisation factors of the templates from the fit have been applied. The uncertainty band includes only the statistical uncertainty.

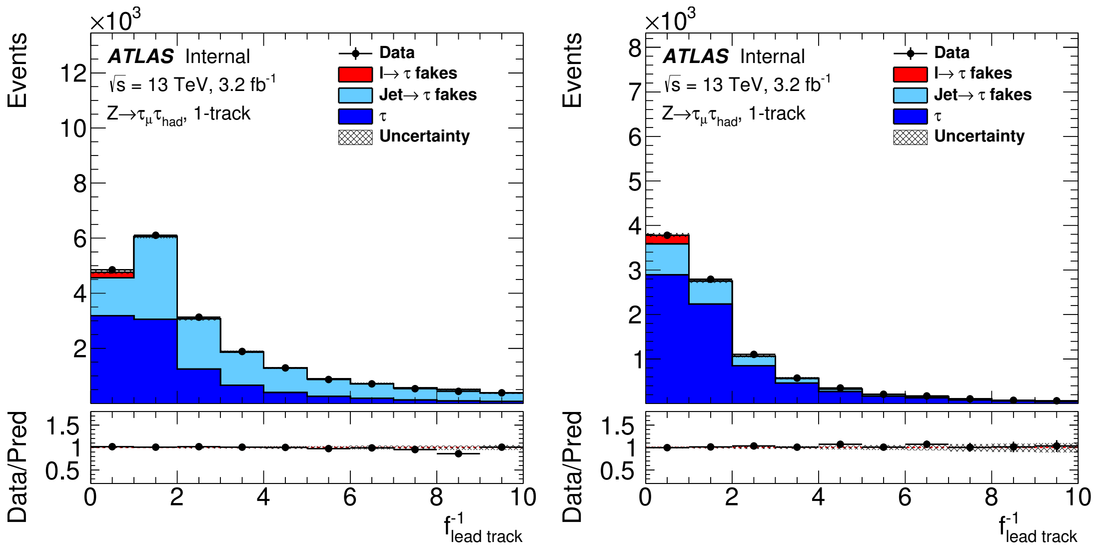

Figure 10: The jet discriminant BDT inputs: **Leading track momentum fraction $f^{-1}_{lead\ track}$** for $\tau_{had-vis}$ candidates before (a) and after (b) medium identification requirement. The background estimation is the same as the main analysis as shown in figure 4 and the normalisation factors of the templates from the fit have been applied. The uncertainty band includes only the statistical uncertainty.

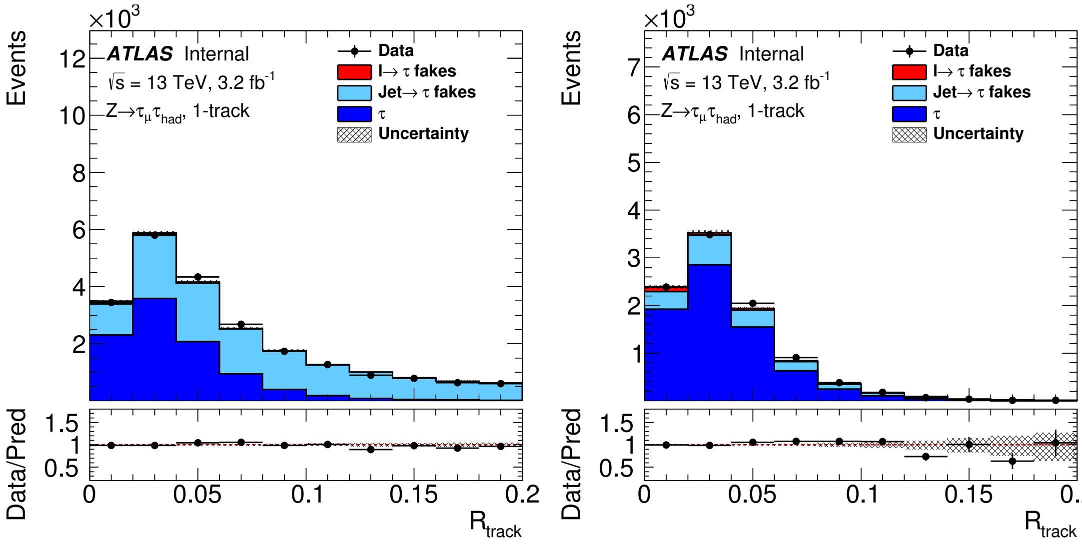

Figure 11: The jet discriminant BDT inputs: **Track radius $\mathbf{R_{track}}$** for $\tau_{\mathrm{had-vis}}$ candidates before (a) and after (b) medium identification requirement. The background estimation is the same as the main analysis as shown in figure 4 and the normalisation factors of the templates from the fit have been applied. The uncertainty band includes only the statistical uncertainty.

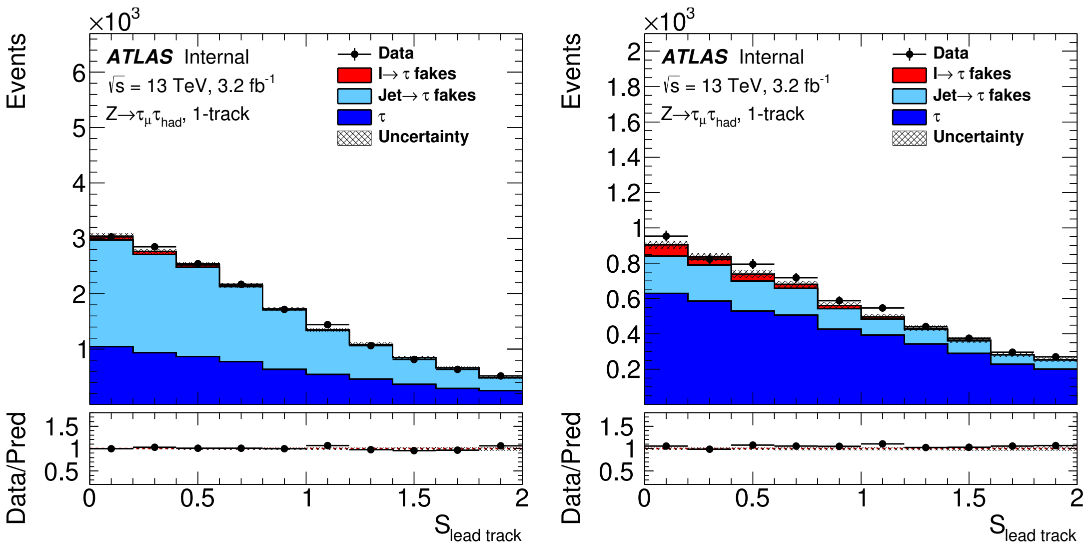

Figure 12: The jet discriminant BDT inputs: **Leading track IP significance $\mathbf{S_{lead\ track}}$** for $\tau_{\mathrm{had-vis}}$ candidates before (a) and after (b) medium identification requirement. The background estimation is the same as the main analysis as shown in figure 4 and the normalisation factors of the templates from the fit have been applied. The uncertainty band includes only the statistical uncertainty.

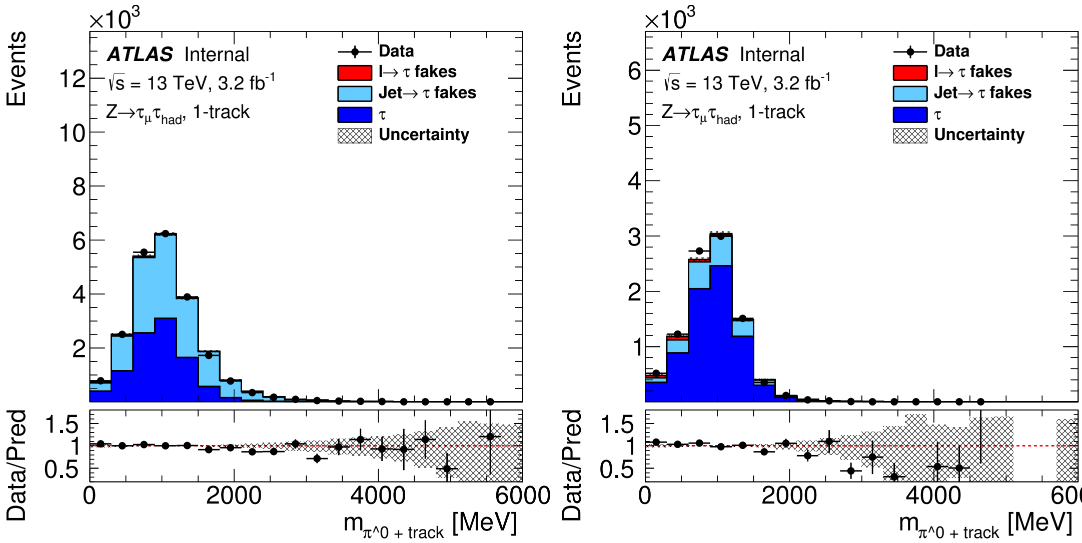

Figure 13: The jet discriminant BDT inputs: **Track-plus-EM-system mass $\mathbf{m_{\pi^0+track}}$** for $\tau_{\mathrm{had-vis}}$ candidates before (a) and after (b) medium identification requirement. The background estimation is the same as the main analysis as shown in figure 4 and the normalisation factors of the templates from the fit have been applied. The uncertainty band includes only the statistical uncertainty.

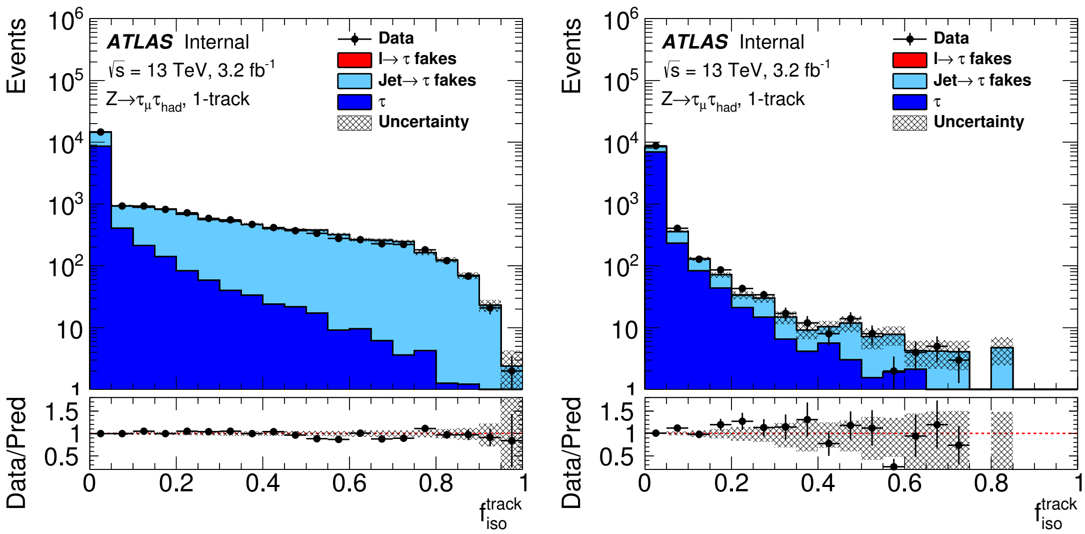

Figure 14: The jet discriminant BDT inputs: **Fraction of tracks p_{T} in the isolation region $\mathbf{f_{iso}^{track}}$** for $\tau_{\mathrm{had-vis}}$ candidates before (a) and after (b) medium identification requirement. The background estimation is the same as the main analysis as shown in figure 4 and the normalisation factors of the templates from the fit have been applied. The uncertainty band includes only the statistical uncertainty.

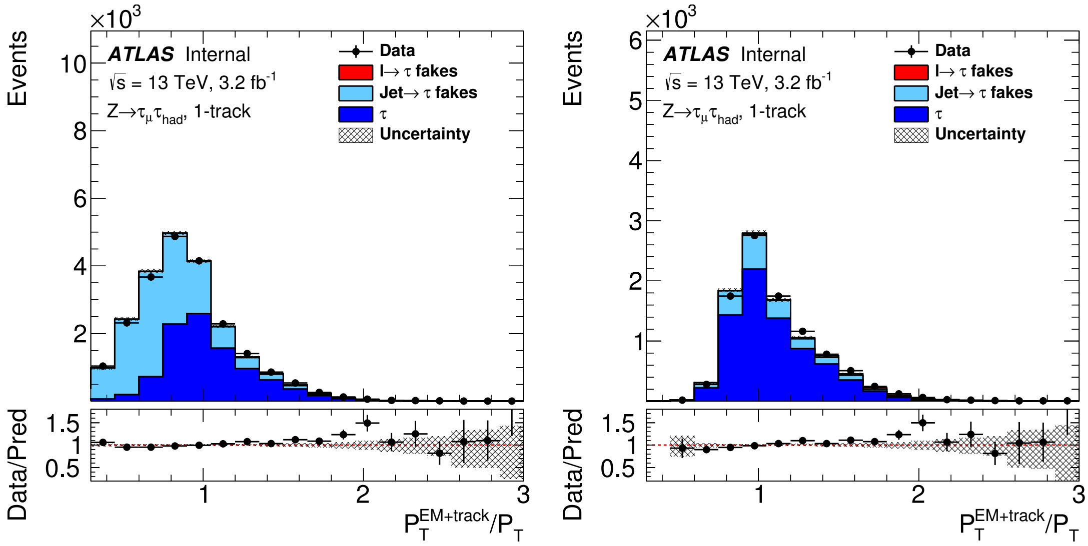

Figure 15: The jet discriminant BDT inputs: **Ratio of track-plus-EM-system to p_T $P_T^{EM+track}/P_T$** for $\tau_{\text{had-vis}}$ candidates before (a) and after (b) medium identification requirement. The background estimation is the same as the main analysis as shown in figure 4 and the normalisation factors of the templates from the fit have been applied. The uncertainty band includes only the statistical uncertainty.

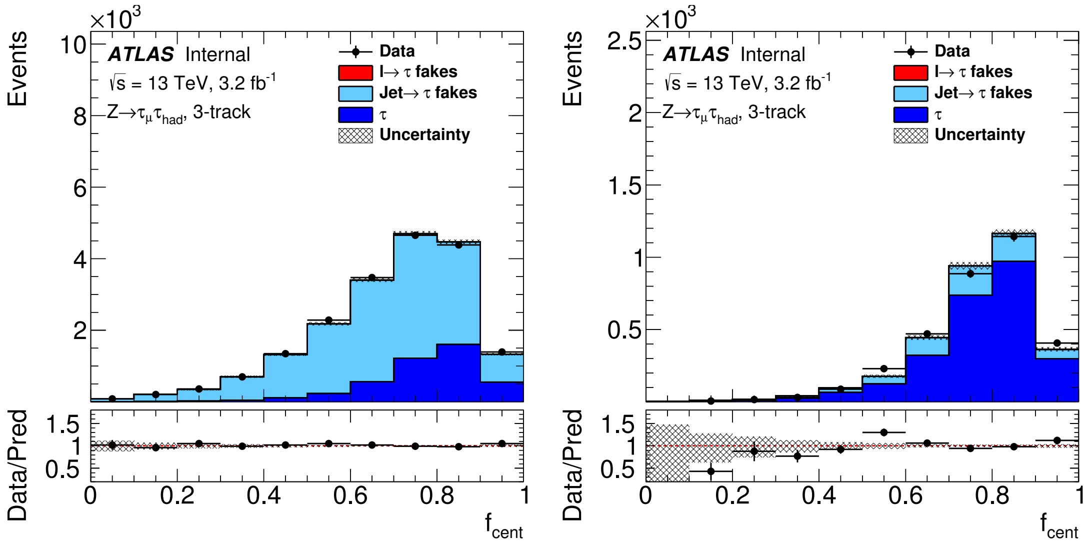

Figure 16: The jet discriminant BDT inputs: **Central energy fraction $f_{\mathbf{cent}}$** for $\tau_{\mathrm{had-vis}}$ candidates before (a) and after (b) medium identification requirement. The background estimation is the same as the main analysis as shown in figure 4 and the normalisation factors of the templates from the fit have been applied. The uncertainty band includes only the statistical uncertainty.

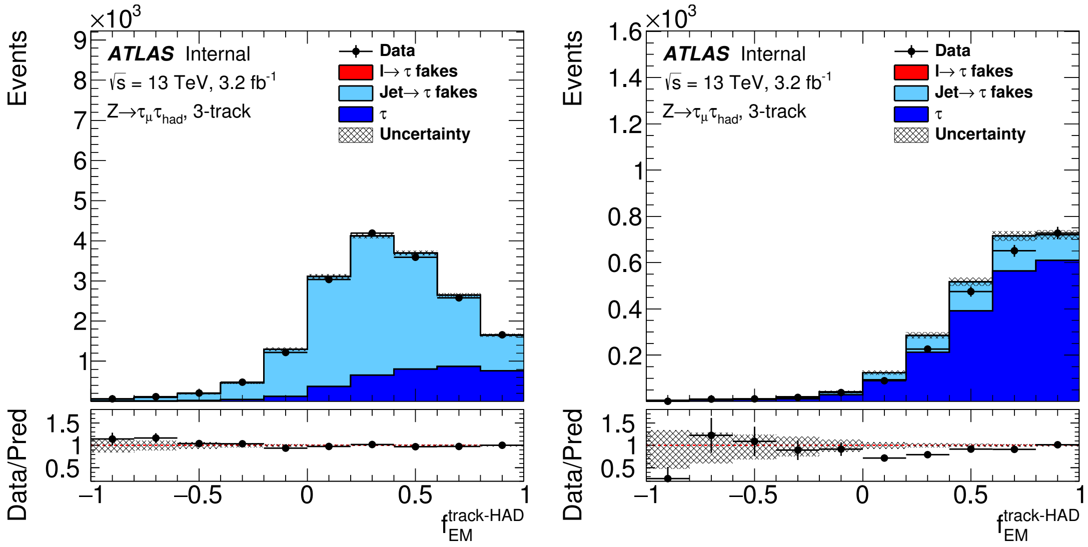

Figure 17: The jet discriminant BDT inputs: **Fraction of EM energy from charged pions $\mathbf{f_{EM}^{track-HAD}}$** for $\tau_{\mathrm{had-vis}}$ candidates before (a) and after (b) medium identification requirement. The background estimation is the same as the main analysis as shown in figure 4 and the normalisation factors of the templates from the fit have been applied. The uncertainty band includes only the statistical uncertainty.

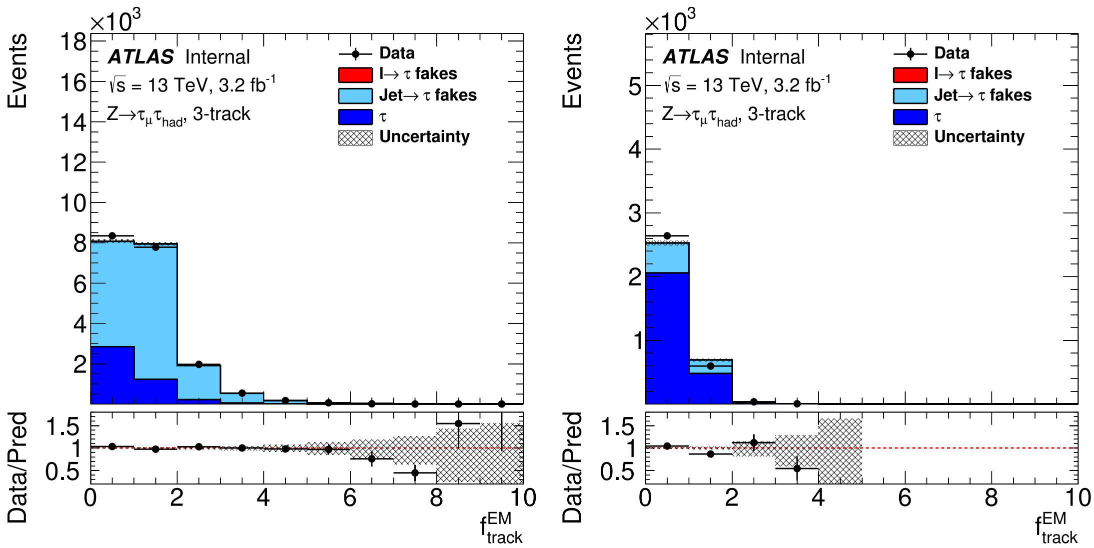

Figure 18: The jet discriminant BDT inputs: **Ratio of EM energy to track momentum $\mathbf{f_{track}^{EM}}$** for $\tau_{\mathrm{had-vis}}$ candidates before (a) and after (b) medium identification requirement. The background estimation is the same as the main analysis as shown in figure 4 and the normalisation factors of the templates from the fit have been applied. The uncertainty band includes only the statistical uncertainty.

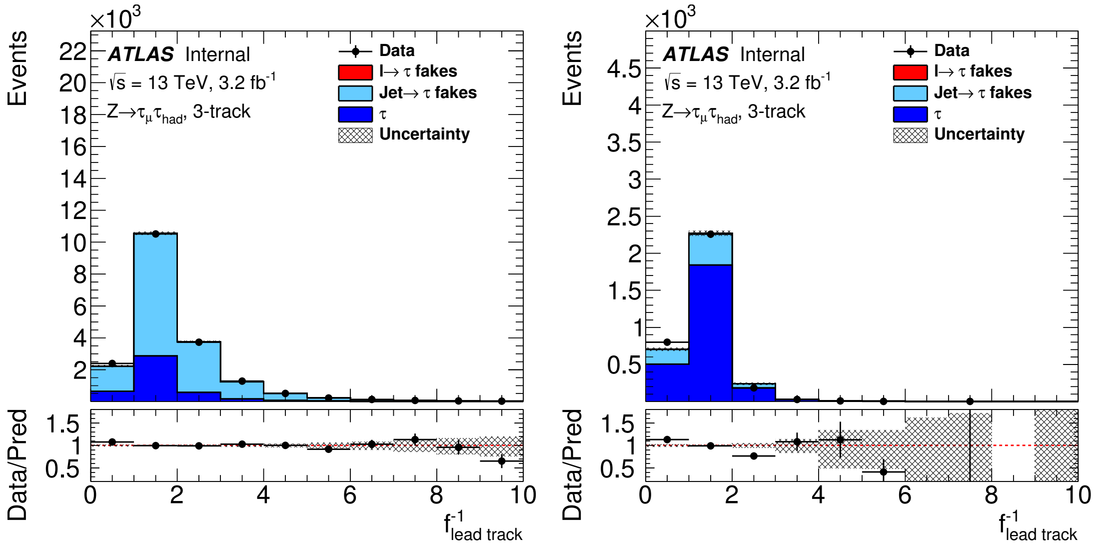

Figure 19: The jet discriminant BDT inputs: **Leading track momentum fraction $f^{-1}_{\text{lead track}}$** for $\tau_{\text{had-vis}}$ candidates before (a) and after (b) medium identification requirement. The background estimation is the same as the main analysis as shown in figure 4 and the normalisation factors of the templates from the fit have been applied. The uncertainty band includes only the statistical uncertainty.

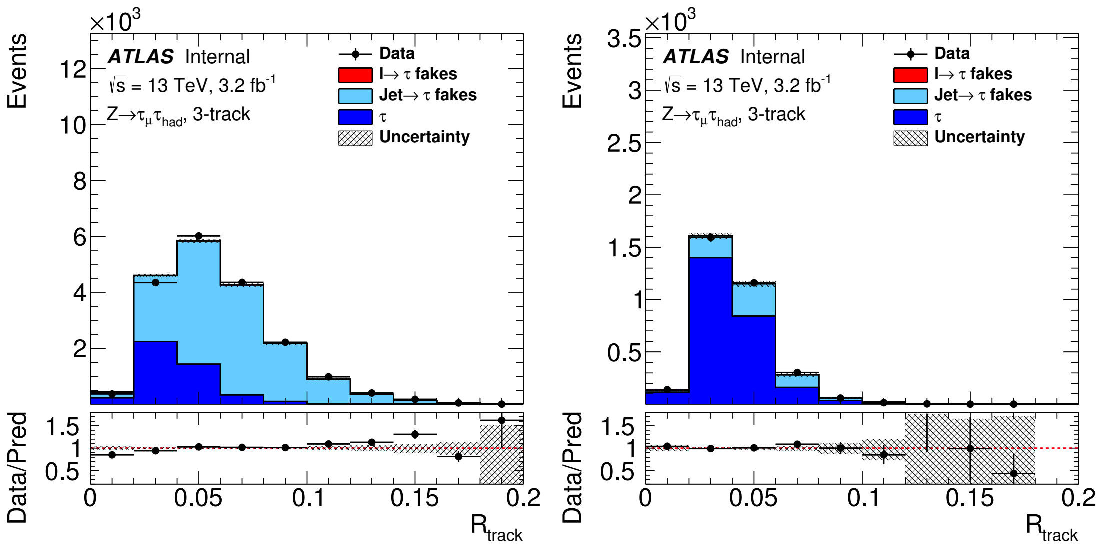

Figure 20: The jet discriminant BDT inputs: **Track radius R_{track}** for $\tau_{\text{had-vis}}$ candidates before (a) and after (b) medium identification requirement. The background estimation is the same as the main analysis as shown in figure 4 and the normalisation factors of the templates from the fit have been applied. The uncertainty band includes only the statistical uncertainty.

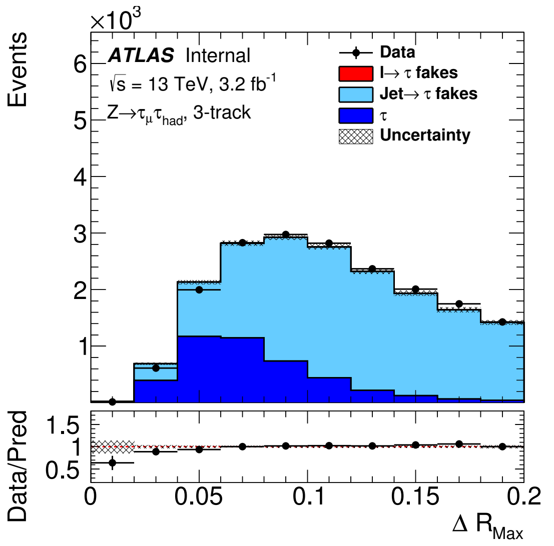

Figure 21: The jet discriminant BDT inputs: **Leading track IP significance $S_{\text{lead track}}$** for $\tau_{\text{had-vis}}$ candidates before (a) and after (b) medium identification requirement. The background estimation is the same as the main analysis as shown in figure 4 and the normalisation factors of the templates from the fit have been applied. The uncertainty band includes only the statistical uncertainty.

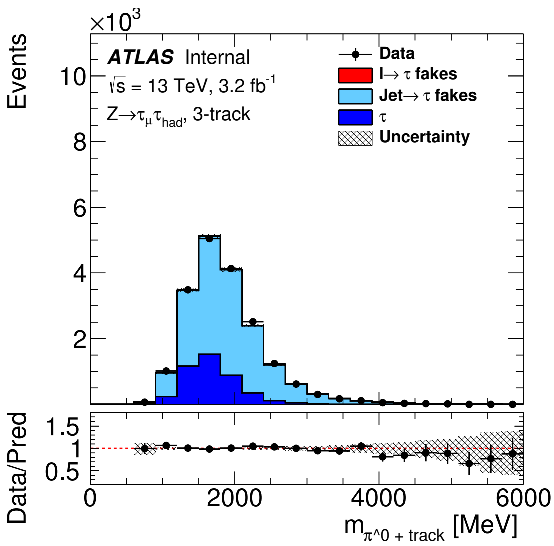

Figure 22: The jet discriminant BDT inputs: **Track-plus-EM-system mass $m_{\pi^0+\text{track}}$** for $\tau_{\text{had-vis}}$ candidates before (a) and after (b) medium identification requirement. The background estimation is the same as the main analysis as shown in figure 4 and the normalisation factors of the templates from the fit have been applied. The uncertainty band includes only the statistical uncertainty.

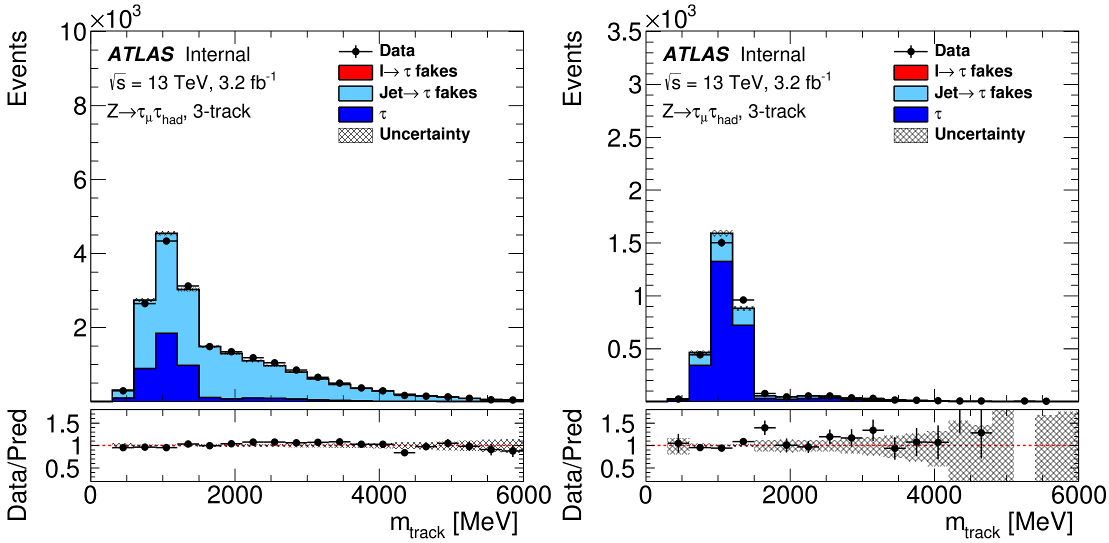

Figure 23: The jet discriminant BDT inputs: **Track mass $\mathbf{m_{track}}$** for $\tau_{\mathrm{had-vis}}$ candidates before (a) and after (b) medium identification requirement. The background estimation is the same as the main analysis as shown in figure 4 and the normalisation factors of the templates from the fit have been applied. The uncertainty band includes only the statistical uncertainty.

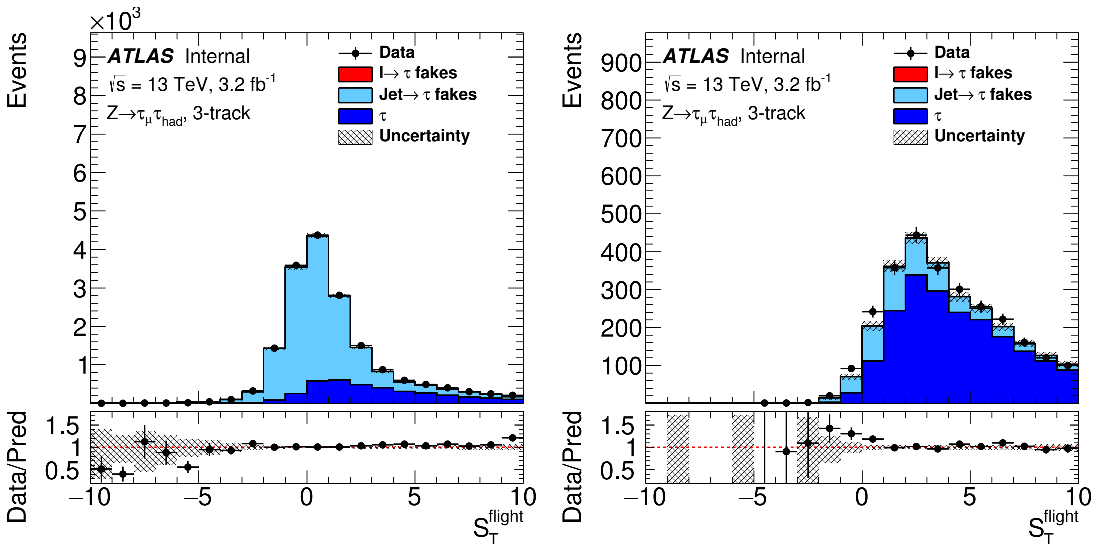

Figure 24: The jet discriminant BDT inputs: **Transverse flight path significance $\mathbf{S_T^{flight}}$** for $\tau_{\mathrm{had-vis}}$ candidates before (a) and after (b) medium identification requirement. The background estimation is the same as the main analysis as shown in figure 4 and the normalisation factors of the templates from the fit have been applied. The uncertainty band includes only the statistical uncertainty.

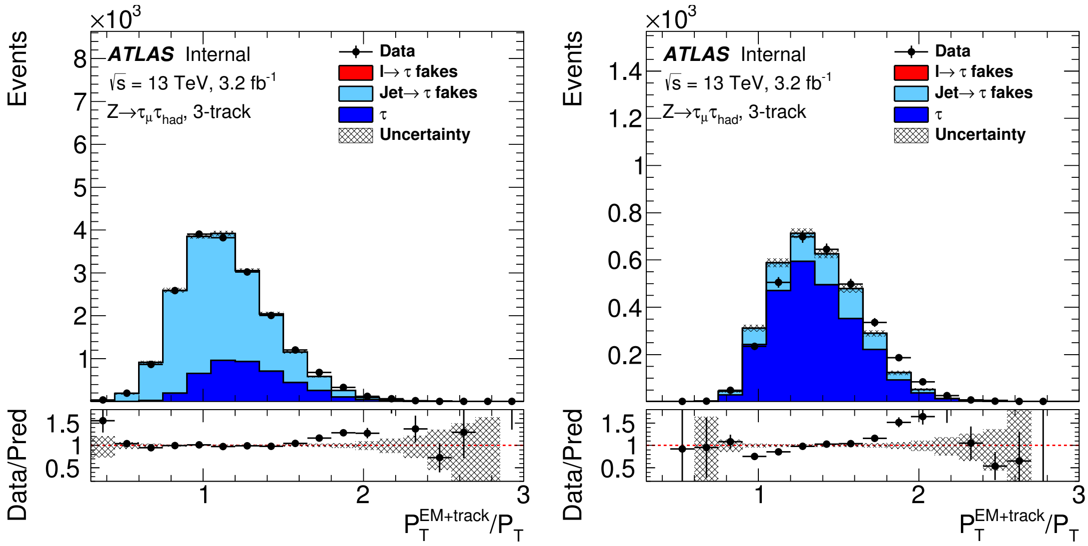

Figure 25: The jet discriminant BDT inputs: **Ratio of track-plus-EM-system to p_T $P_T^{EM+track}/P_T$** for $\tau_{had-vis}$ candidates before (a) and after (b) medium identification requirement. The background estimation is the same as the main analysis as shown in figure 4 and the normalisation factors of the templates from the fit have been applied. The uncertainty band includes only the statistical uncertainty.

6.3. Trigger efficiency measurement

The performance of the tau trigger is important in meeting the event rate constraints in data taking. In this section, a comparison is made of the efficiency of the online tau identification measured in data and simulation using the tag-and-probe method. The selection of $Z \to \tau_\mu \tau_{had}$ events used in the measurement of the online tau identification efficiency is described in section 6.1.

6.3.1. Signal and Background estimation

The dominant background contributions come from the misidentification of jets as $\tau_{had-vis}$ candidates in multi-jet and W+jets events. These backgrounds are estimated via data-driven methods, using control regions enriched in multi-jet and W+jets. The shape of the multi-jet background is taken from the same sign control region, and normalisation factors (r_{QCD}) are derived in the multi-jet control region. The normalisation factors are defined as the ratio of OS to SS charge events and are parametrised by the number of charged tracks (N_{track}) associated with the $\tau_{had-vis}$ candidate, as well as its p_T.

The shape of the W+jets background is modelled with simulated events, with normalisation factors derived from the W+jets control region. Additionally, the requirements on the invariant mass of the muon and tau candidate, and the sum of the distance in the azimuthal plane between the muon and E_T^{miss} and between the $\tau_{had-vis}$ and E_T^{miss}, are dropped. The normalisation factors are defined as the ratio of data to simulated W+jets events in the control region and are again parametrised by the number of charged tracks (N_{track}) associated with the $\tau_{had-vis}$ candidate, as well as its p_T. All other backgrounds are estimated via simulation. Figure 26 shows the signal region offline tau p_T distributions before and after the application of the tau trigger.

6.3.2. Results

The online tau identification efficiency is measured with respect to tau candidates reconstructed and identified offline as a function of both the reconstructed transverse momentum of the tau candidate, and the number of primary vertices in the event. At L1, the tau trigger has requirements of $p_{\mathrm{T}} > 12$ GeV and calorimetric isolation, whereby energy deposited in a ring surrounding the L1 tau object is required to be lower than a threshold dependent on the L1 tau energy. At HLT, the trigger has requirements of $p_{\mathrm{T}} > 25$ GeV, the number of associated charged tracks restricted to three or less, and a medium working point selection on the online BDT score. Figure 27 shows the online tau identification efficiency measured in data (with estimated backgrounds subtracted) for the different levels of the trigger.

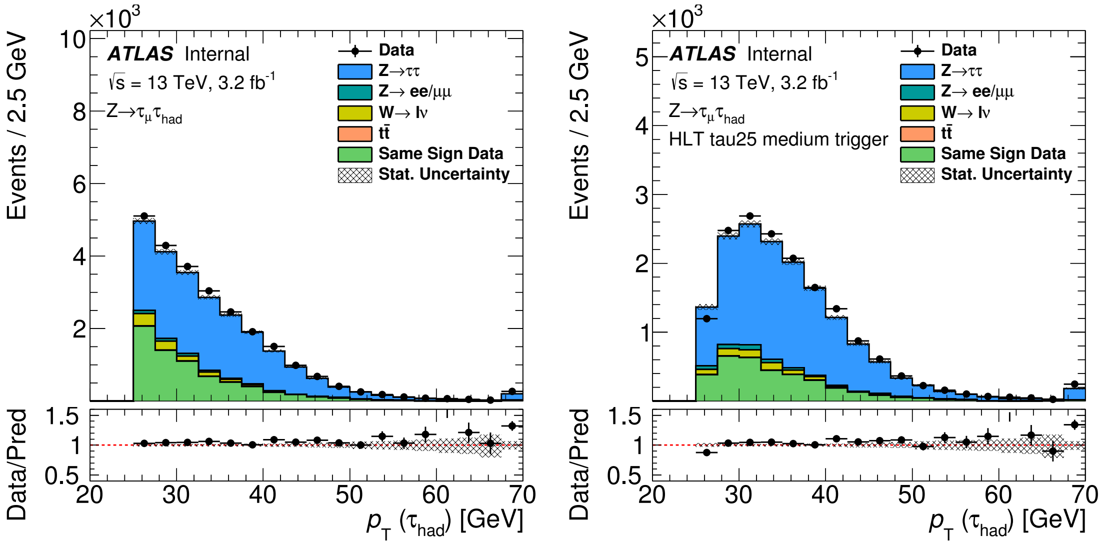

(a) (b)

Figure 26: The p_{T} and distribution of the tau candidate passing the offline medium tau identification a) before, and b) after the application of the tau trigger. The tau trigger has an online p_{T} requirement of 25 GeV, and a medium online identification. The events are from a selection designed to be enriched in the process $Z \to \tau_{\mu}\tau_{\mathrm{had}}$.

The measured online tau identification efficiency is compared to simulated $Z \to \tau\tau$ events in figure 28 and is shown to be well modelled outside the turn-on region. As in the offline tau identification efficiency measurement, scale factors are derived to account for the differences between data and simulation and are found to be consistent with unity for tau candidates with a reconstructed transverse momentum above 30 GeV.

The dominant systematic uncertainties considered for the efficiency measurement are shown in table 4, and are associated with the background subtraction. The largest systematic uncertainty results from the uncertainty on the estimation of the multi-jet background. The systematic uncertainties are larger in the low-p_{T} region due to the larger background contribution.

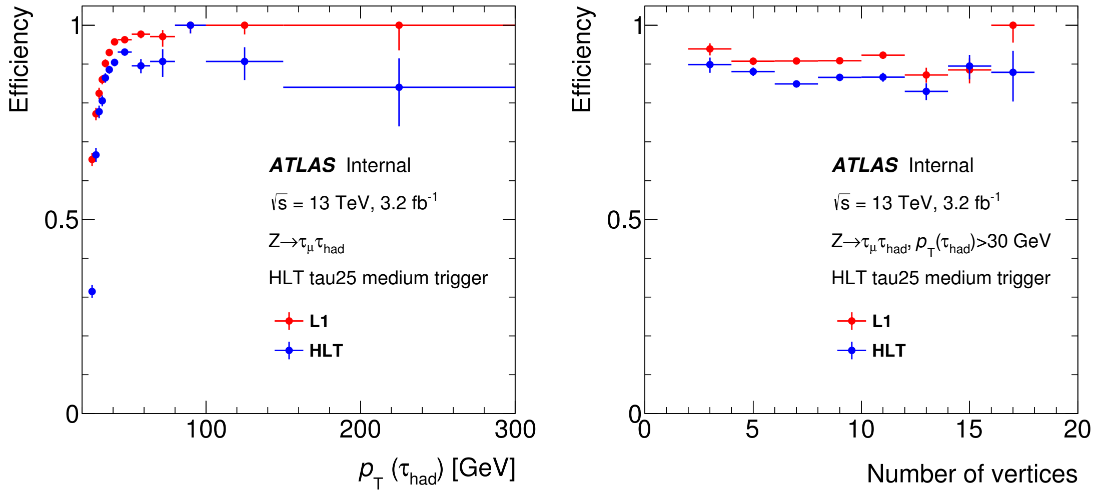

(a) (b)

Figure 27: The Level 1 (red) and High Level Trigger (blue) online tau identification efficiency for $\tau_{\mathrm{had-vis}}$ candidates identified by the offline medium tau identification, as a function of (a) the offline $\tau_{\mathrm{had-vis}}$ transverse energy and (b) the number of primary vertices. The error bars correspond to the statistical uncertainty in data.

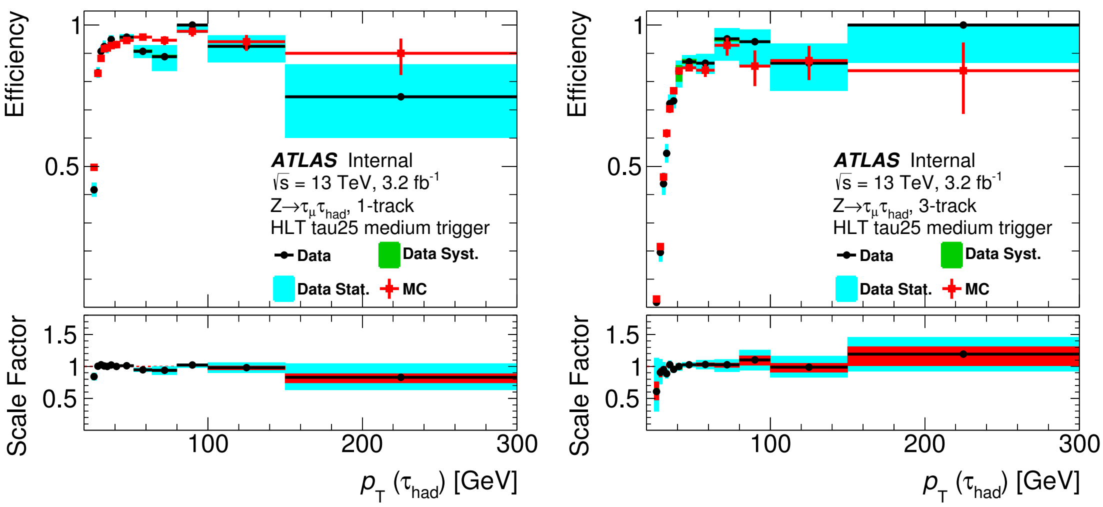

(a) (b)

Figure 28: The online tau identification efficiency measured in data and simulation, for offline $\tau_{\mathrm{had-vis}}$ candidates passing the medium tau identification, as a function of the offline $\tau_{\mathrm{had-vis}}$ transverse energy. The expected background contribution has been subtracted from the data. The uncertainty band on the ratio reflects the statistical uncertainties associated with data and simulation as well as the sources of systematic uncertainty. The Scale Factor is defined as the ratio of data to MC.

	1-track		3-track	
	Without trigger	**With trigger**	**Without trigger**	**With trigger**
XXX	$x.xx\%$	$x.xx\%$	$x.xx\%$	$x.xx\%$
XXX	$x.xx\%$	$x.xx\%$	$x.xx\%$	$x.xx\%$
XXX	$x.xx\%$	$x.xx\%$	$x.xx\%$	$x.xx\%$
XXX	$x.xx\%$	$x.xx\%$	$x.xx\%$	$x.xx\%$
XXX	$x.xx\%$	$x.xx\%$	$x.xx\%$	$x.xx\%$
XXX	$x.xx\%$	$x.xx\%$	$x.xx\%$	$x.xx\%$
XXX	$x.xx\%$	$x.xx\%$	$x.xx\%$	$x.xx\%$
XXX	$x.xx\%$	$x.xx\%$	$x.xx\%$	$x.xx\%$

Table 4: Overall effect of individual systematic uncertainties on all backgrounds measured in selections with and without the application of the τ trigger with a p_{T} threshold of 25 GeV. The systematic uncertainties are shown for 1-track and 3-track τ candidates separately. If the systematic uncertainty consists of both upward and downward variations, the variation resulting in the highest effect is shown. Systematic uncertainties (or pairs thereof) whose overall effect is 0.05% or less are not shown. (After collecting information, these will be updated)

6.4. Offline $\tau_{\mathrm{had-vis}}$ energy calibration

The tau energy scale (TES), a tau-specific energy correction derived from simulation, is applied after the local hadronic calibration to the tau candidate energy. A full description is detailed in Ref. [2]. This section describes the in-situ measurement of the tau energy scale based on collision data. The method is based on the fact that the distribution of the reconstructed visible mass, m_{vis} in $Z \to \tau_\mu \tau_{\mathrm{had}}$ events can be used to measure a TES shift between data and simulation.

6.4.1. Signal and Background estimation

The signal and background estimations are as described in section 6.1, with the difference being the selection criteria, as shown in table 2. The m_{vis} variable is defined as the invariant mass of the $\tau_{\mathrm{had-vis}}$ and muon system. The tau energy is parametrised as $E_{\mathrm{T}} \to (1+\alpha)E_{\mathrm{T}}$ by introducing a TES shift α, while the muon momentum scale is measured independently with high precision. In Run-1, α was determined by comparing the m_{vis} fitted peak value between data and simulation [2]. One drawback of this peak-fit method is that the peak value is easily affected by the statistical fluctuations. In Run-2, a new method has been developed by comparing the full m_{vis} shape and α is determined by finding the value at which the simulation and data maximally agree. The new method is more robust against statistical fluctuations and the tau energy resolution. Technically, α is determined by minimising the $\chi^2(\alpha, f)$ defined as Eq. 3:

$$\chi^2(\alpha, f) = \sum_i \frac{(N_i^{\mathrm{data}} - f N_i^{\mathrm{sig}}(\alpha) - N_i^{\mathrm{bkg}})^2}{(\sqrt{N_i^{\mathrm{data}}})^2 + f^2(\Delta N_i^{\mathrm{sig}}(\alpha))^2 + (\Delta N_i^{\mathrm{bkg}})^2} \,. \tag{3}$$

Here $N_i^{\mathrm{data/sig/bkg}}$ is the number of events in the i-th bin of the visible mass distribution in the data, signal or background; $\Delta N_i^{\mathrm{sig/bkg}}$ is the corresponding uncertainty in the number of events; N_i^{bkg} ($\Delta N_i^{\mathrm{bkg}}$) is corresponds to the sum of the contributions from all backgrounds; the parameter f is introduced to reduce the impact of overall normalisation discrepancies between data and simulation. The signal yield in each bin depends upon the in-situ TES parameter α.

6.4.2. Results

The measured TES shift is $\alpha = -0.7\% \pm 0.8\%$ (stat) $\pm$ 1.2% (syst) and $\alpha = -3.6\% \pm 1.2\%$ (stat) $\pm$ 2.3% (syst) for $\tau_{\mathrm{had-vis}}$ with one and three associated tracks, respectively. The corrections are negative and applied to the momentum of $\tau_{\mathrm{had-vis}}$ in simulation in order to yield agreement (on average) with data. The uncertainties only account for differences between data and simulation. The resulting m_{vis} distribution for data and simulation is shown in figure 29 after applying the TES correction.

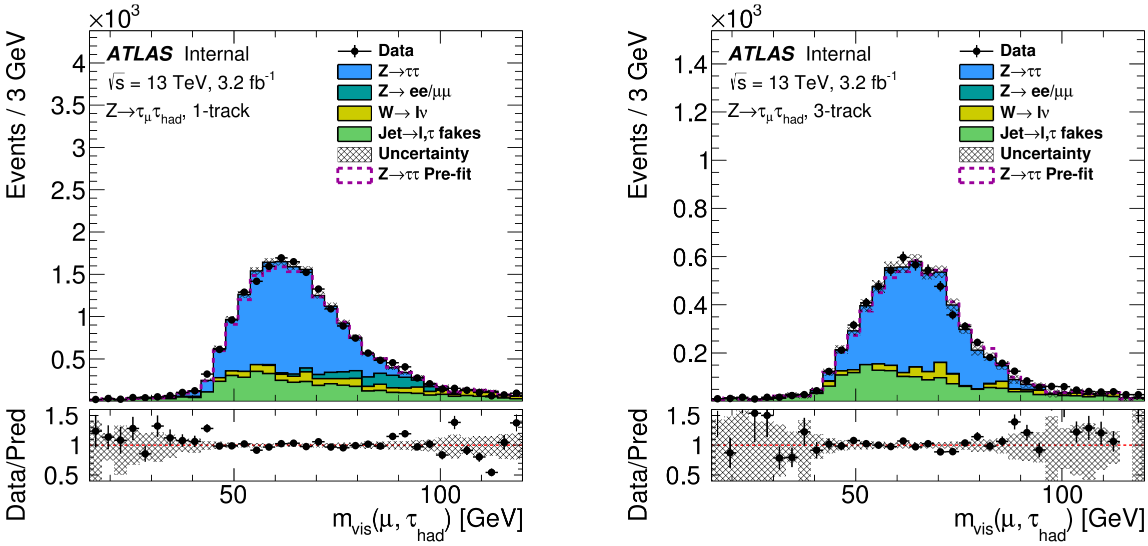

(a) 1-track (b) 3-track

Figure 29: The distribution of m_{vis}: the invariant mass of the $\tau_{\mathrm{had-vis}}$ and muon system

The dominant systematic uncertainties of the in-situ measurement are due to the uncertainty related to the tau identification, the potential bias of the fit obtained by varying the fit range, and the normalisation of the jet background. The main systematic uncertainties are summarised in table 5. The impact of the uncertainty related to the tau energy resolution is significantly reduced with respect to the previous method [2].

Source	Uncertainty [%]	
	1-track	3-track
Fit bias	0.8	0.6
Tau energy resolution	0.3	0.6
Tau identification	0.5	2.6
Muon	0.2	0.6
Jet background	0.7	1.2
Total	1.2	3.0

Table 5: Dominant systematic uncertainties on the tau energy scale estimated using the in-situ method. In general, the values depend on the number of associated tracks. All other systematic uncertainties are smaller than 0.1%.

7. $t\bar{t}$ tag-and-probe analyses

The higher mass of the top quark in comparison to the Z boson results in decays to tau leptons with a harder p_{T} spectrum, as shown in Fig. 30. This enables online and offline tau identification performance measurements in a p_{T} region that is difficult to access and provides a useful cross check to the $Z \to \tau\tau$ analyses discussed in section 6. In this section, two tag-and-probe analyses are described with differing final states.

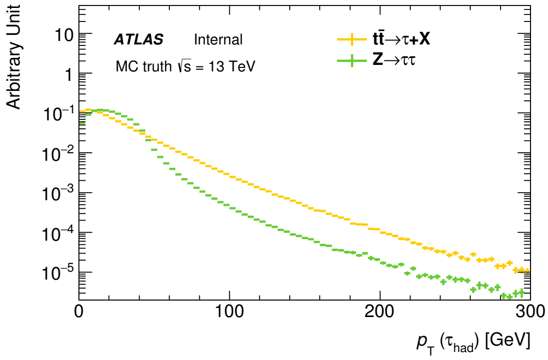

Figure 30: The p_{T} distribution of tau candidates matched to generated taus from $t\bar{t}$ and $Z \to \tau\tau$ events.

7.1. Offline tau identification efficiency measurement

this is currently a placeholder

7.2. Trigger efficiency measurement

7.2.1. Event selection

In the online tau identification efficiency measurement, the process $t\bar{t} \to [b\mu\nu_\mu][b\tau\nu_\tau]$ is considered in which the muon constitutes the 'tag' object, and the hadronically decaying $\tau_{\mathrm{had-vis}}$ is probed. The selection and triggering of the muon candidate is the same as described in section 6. Likewise, events with additional electrons or muons are vetoed and at least one opposite sign charge $\tau_{\mathrm{had-vis}}$ is required, with the leading p_{T} candidate considered. Non-$t\bar{t}$ processes are suppressed by requiring at least two jets with $p_{\mathrm{T}} > 20$ GeV in the event, and with at least one b-tagged.

7.2.2. Signal and background processes

All simulated events originating from $t\bar{t}$, single top, and W/Z+jets processes where the probe is geometrically matched to a generated, hadronically decaying $\tau_{\mathrm{had-vis}}$ particle are considered as signal events. The main backgrounds are events where a quark- or gluon-initiated jet is reconstructed and misidentified as the probe object. These backgrounds principally result from multi-jet processes as well as $t\bar{t}$, single top, and W/Z+jets processes. The combined shape of these backgrounds is taken from events in which the muon and the $\tau_{\text{had-vis}}$ have the same sign charge. Normalisation factors (r_{QCD}) for the backgrounds are derived in a control region enriched in multi-jet events, defined by inverting the isolation requirement on the muon and dropping the b-tag requirement. The normalisation factors are defined as the ratio of OS to SS charge events and are parametrised by the number of tracks associated with the $\tau_{\text{had-vis}}$ candidate, as well as its p_{T}. The r_{QCD} value is computed separately for events before and after the application of the tau trigger.

Events containing $t\bar{t}$, single top, and W/Z+jets processes, where a jet is misidentified as the probe, are modelled by simulated events with the OS requirement. The small background of events in which the lepton is misidentified as the probe is also modelled by simulated events with the subset of events with the same sign requirement subtracted.

7.2.3. Results

The online tau identification efficiency is measured with respect to tau candidates reconstructed and identified offline in the same manner as described in section 6.3, and as a function of the reconstructed transverse momentum of the tau candidate. For the tau trigger with a p_{T} threshold of 25 GeV and for events with tau candidates reconstructed with the offline medium identification requirement, the efficiencies and corresponding scale factors in simulated signal and data events (with the estimated backgrounds subtracted) are shown in figure 31. The scale factors are consistent with 1 above 39 GeV for 1-track $\tau_{\text{had-vis}}$ candidates, and above 43 GeV for 3-track $\tau_{\text{had-vis}}$ candidates.

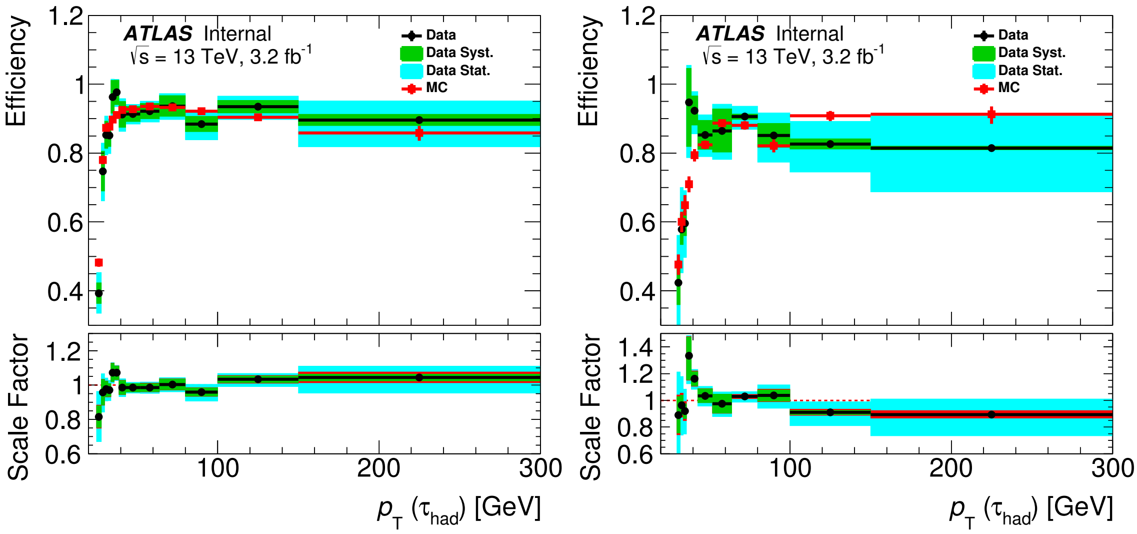

(a) 1-track

(b) 3-track

Figure 31: Efficiencies for signal and background subtracted data and corresponding scale factors for the tau trigger with online $p_{\text{T}} > 25$ GeV as a function of the transverse momentum of offline $\tau_{\text{had-vis}}$ candidates with a medium identification requirement. The efficiency is measured using the tag-and-probe with events primarily resulting from $t\bar{t}$ decays. The Scale Factor is defined as the ratio of data to MC.

Sources of systematic uncertainty include the reconstruction and identification efficiencies and the energy scale of the muon, the reconstruction efficiency of the b-jets, and the estimation of the r_{QCD} normalisation factor. With the exception of r_{QCD}, which is calculated separately depending on the application of the tau trigger, all are considered with and without the tau trigger applied. The systematic uncertainties enter through the subtraction of estimated backgrounds from data. The main sources of systematic uncertainty are displayed in table 6. The largest source of uncertainty, the multi-jet normalisation factor, contains a statistical component related to the number of events in the SS control region, and a systematic component derived by varying the choice of selection criteria used to define the control region.

Source	Uncertainty [%]	
	1-track	3-track
multi-jet normalisation	7.7	13.7
b-tagging	< 1	< 1%
muon	< 1	< 1%

Table 6: Dominant uncertainties on the estimated backgrounds for the $t\bar{t}$ tag-and-probe efficiency measurement.

8. $Z \to ee$ tag-and-probe analysis

The probability of misidentifying the electron as a candidate tau is measured in events dominated by $Z \to ee$ processes. As in the previous sections, a tag-and-probe approach is used. Events are selected by triggering on the presence of an electron (tag) and must contain a candidate tau lepton decaying hadronically with a single track (probe).

8.1. Event selection

The event selection is chosen to produce a sample of events enriched in $Z \to ee$ processes. The tag object in the event is a reconstructed electron with $p_{\mathrm{T}} > 25$ GeV, and *tight* likelihood identification requirements. Several triggers are available, with online medium electron likelihood identification and varying online p_{T} requirements. These select events containing electrons with varying levels of efficiency, and therefore the trigger used to select events is dependent on the p_{T} of the reconstructed electron in order to maximise acceptance. Events in which the reconstructed electron has offline $p_{\mathrm{T}} > 135$ GeV, 65 GeV $< p_{\mathrm{T}} <$ 135 GeV or 25 $< p_{\mathrm{T}} <$ 65 GeV, are selected and geometrically matched to a trigger object with a respective online requirement of $p_{\mathrm{T}} > 120$ GeV, $p_{\mathrm{T}} > 60$ GeV or $p_{\mathrm{T}} > 24$ GeV. The probe $\tau_{\mathrm{had-vis}}$ candidate must have a single track, $p_{\mathrm{T}} > 20$ GeV, and a veto is placed on events containing muons or b-tagged jets.

To ensure the selected events contain a high purity of $Z \to ee$ decays, an additional selection is placed on the signal region, requiring the electron $p_{\mathrm{T}} > 30$ GeV, the invariant mass of the electron and tau system to be within 80 GeV $< m_{\mathrm{vis}}(e, \tau_{\mathrm{had-vis}}) <$ 100 GeV, and the transverse mass of the electron and $E_{\mathrm{T}}^{\mathrm{miss}}$ system, $m_{\mathrm{T}}(e, E_{\mathrm{T}}^{\mathrm{miss}})$, to be less than 40 GeV.

8.2. Signal and background processes

The data sample enriched in $Z \to ee$ processes is compared to an estimation of signal events and background processes. The $Z \to ee$ signal process is estimated via simulation and the probe tau from both signal and background processes must be within a cone of size $\Delta R < 0.2$ of a generated electron for simulated events. The contribution to the signal region from $Z \to \tau\tau$ and top-quark processes are also estimated from simulation.

W+jets processes are estimated via simulated events, with a scale factor extracted from a W+jets dominated control region. The control region is defined by requiring exactly one electron in the event, $m_{\text{vis}}(e, \tau_{\text{had-vis}}) < 80$ GeV, $m_{\text{T}}(e, E_{\text{T}}^{\text{miss}}) > 70$ GeV, and $E_T^{miss} > 30$ GeV.

The shape of the multi-jet background is taken from events in which the electron and the tau lepton have the same charge and scaled with a normalisation factor derived in a control region enriched in multi-jet events. The multi-jet control region is defined by inverting the isolation requirement on the electron, such that the ratio of transverse energy in a cone of $\Delta R < 0.2$ around the electron to the electron p_{T}, and the ratio of transverse momentum in a cone of $\Delta R < 0.4$ around the electron to the electron p_{T}, are greater than 12% and 8% respectively. Same sign events from the simulated $Z \to \tau\tau$, W+jets and top backgrounds are subtracted from the same sign background.

The p_{T} and η distributions of the tau candidate are shown in figure 32 after the full event selection and with the background estimation described above.

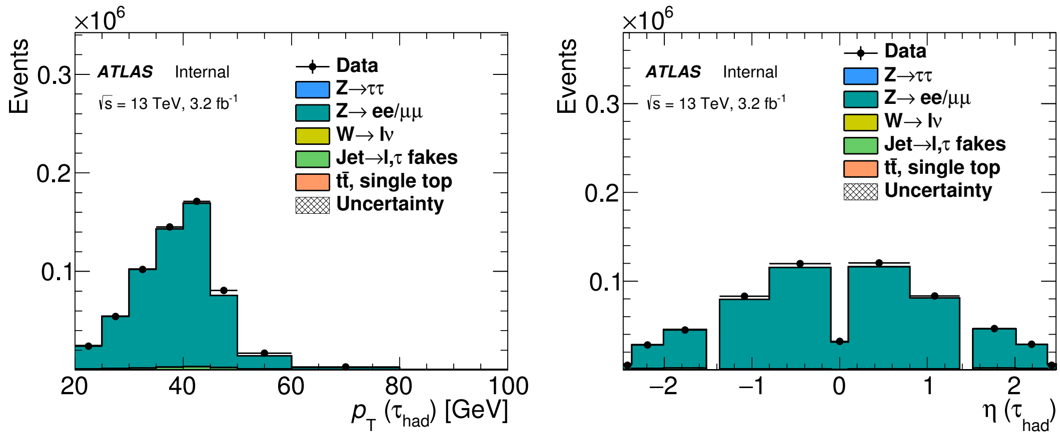

(a) tau candidate p_{T}

(b) tau candidate η

Figure 32: The p_{T} and η distributions of the tau candidate after the full event selection.

8.3. Results

The electron misidentification probability is defined as the probability of an electron passing both the tau identification and the electron discrimination algorithm. It is measured by taking the ratio of signal region events passing the medium tau identification and the *very loose* electron discrimination requirements to all signal region events, and is calculated for both data and the simulated $Z \to ee$ signal process. For the efficiency in data, the estimated contribution to the signal region coming from non-$Z \rightarrow ee$ events is first subtracted. The efficiencies in data and simulation, and the ratio or correction factors are shown in figure 33. The misidentification probability ranges between 0.5% and 2.5% across the η spectrum of the tau candidate and is below 1% for tau candidates with $p_{\mathrm{T}} < 50$ GeV.

Sources of systematic uncertainty include uncertainties associated with the reconstruction, identification and energy scale of the electron and $\tau_{\mathrm{had-vis}}$, and the electron trigger. The estimation of the multi-jet and W+jets normalisation factors contribute as additional sources of uncertainty.

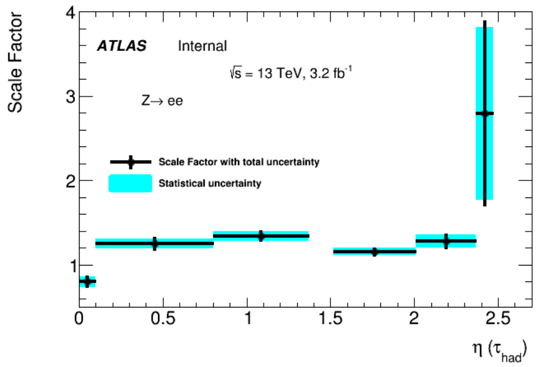

Figure 33: Electron misidentification probability and corresponding scale factors for the requirement that $\tau_{\mathrm{had-vis}}$ candidates with overlapping electrons pass a medium tau identification criteria and the electron discrimination algorithm. The measurements are carried out on data enriched in $Z \rightarrow ee$ events and with estimated backgrounds subtracted, as well as simulated $Z \rightarrow ee$ events, and the ratio is displayed as a scale factor.

9. Summary and conclusions

The performance of the online and offline tau identification, and the energy calibration is measured using $Z \rightarrow \tau\tau$ tag-and-probe measurements. The uncertainties on the offline tau identification efficiency measurement are approximately (5–6)%, depending on the working point, inclusive in η and for a visible transverse momentum greater than 20 GeV. The online tau identification efficiency is measured with a precision of (3–10)% depending on the transverse energy of the tau candidate, by using the hadronic tau lepton decays from Z bosons, selected by offline algorithms. The transverse energy range of the online tau identification efficiency measurement is extended via measurements on tau lepton decays from $t\bar{t}$ processes, and the results are found to be consistent with unity above 45 GeV. The probability of misidentifying electrons as tau candidates is measured to be < 2% for tau candidates with 20 GeV $< p_{\mathrm{T}} <$ 50 GeV. The reconstructed tau energy scale is measured with a precision of approximately (2–3)%.

References

[1] K Nakamura et al., *Review of Particle Physics*, **37** (2010) 075021, and 2011 partial update for the 2012 edition, URL: http://stacks.iop.org/0954-3899/37/i=7A/a=075021.

[2] ATLAS Collaboration, *Identification and energy calibration of hadronically decaying tau leptons with the ATLAS experiment in pp collisions at* $\sqrt{s}$ = 8 TeV, Eur. Phys. J. **C75** (2015) 303, arXiv: 1412.7086 [hep-ex].

[3] ATLAS Collaboration, *Reconstruction, Energy Calibration, and Identification of Hadronically Decaying Tau Leptons in the ATLAS Experiment for Run-2 of the LHC* (), https://cds.cern.ch/record/2064383, URL: https://cds.cern.ch/record/2064383.

[4] ATLAS, *The ATLAS Experiment at the CERN Large Hadron Collider*, JINST **3** (2008) S08003.

[5] ATLAS Collaboration, *ATLAS Insertable B-Layer Technical Design Report*, CERN-LHCC-2010-013, ATLAS-TDR-19, 2010, URL: http://cdsweb.cern.ch/record/1291633.

[6] 'Technical Design Report for the Phase-I Upgrade of the ATLAS TDAQ System', tech. rep. CERN-LHCC-2013-018. ATLAS-TDR-023, Final version presented to December 2013 LHCC.: CERN, 2013, URL: https://cds.cern.ch/record/1602235.

[7] GEANT4 Collaboration, S. Agostinelli et al., *Geant4 – a simulation toolkit*, Nucl. Instr. and Meth. **A 506** (2003) 250 .

[8] ATLAS Collaboration, *The ATLAS Simulation Infrastructure*, Eur. Phys. J. C **70** (2010) 823, arXiv: 1005.4568 [hep-ex].

[9] S. Alioli et al., *A general framework for implementing NLO calculations in shower Monte Carlo programs: the POWHEG BOX*, JHEP **06** (2010) 043, arXiv: 1002.2581 [hep-ph].

[10] T. Sjöstrand, S. Mrenna and P. Skands, *A brief introduction to PYTHIA 8.1*, Comput. Phys. Commun. **178** (2008) 852, arXiv: 0710.3820 [hep-ph].

[11] T. Sjöstrand, S. Mrenna and P. Skands, *PYTHIA 6.4 physics and manual*, JHEP **05**, 026 (2006) 26, arXiv: hep-ph/0603175.

[12] T. Gleisberg et al., *Event generation with SHERPA 1.1*, JHEP **02** (2009) 007, arXiv: 0811.4622 [hep-ph].

[13] ATLAS Collaboration, *Measurement of the muon reconstruction performance of the ATLAS detector using 2011 and 2012 LHC proton–proton collision data*, Eur. Phys. J. C **74** (2014) 3130, arXiv: 1407.3935 [hep-ex].

[14] ATLAS Collaboration, *Electron and photon energy calibration with the ATLAS detector using LHC Run 1 data*, Eur. Phys. J. C **74** (2014) 3071, arXiv: 1407.5063 [hep-ex].

[15] *Electron efficiency measurements with the ATLAS detector using the 2012 LHC proton-proton collision data* (2014), URL: https://cds.cern.ch/record/1706245.

[16] M. Cacciari, G. P. Salam and G. Soyez, *The anti-k_t jet clustering algorithm*, JHEP **04** (2008) 063, arXiv: 0802.1189 [hep-ph].

[17] W Lampl et al., 'Calorimeter clustering algorithms: description and performance', tech. rep. ATL-LARG-PUB-2008-002, 2008.

[18] T Barillari et al., 'Local Hadronic Calibration', tech. rep. ATL-LARG-PUB-2009-001-2. ATL-COM-LARG-2008-006. ATL-LARG-PUB-2009-001, CERN, 2008, URL: https://cds.cern.ch/record/1112035.

[19] *Expected performance of the ATLAS b-tagging algorithms in Run-2* (2015), URL: https://cds.cern.ch/record/2037697.

[20] L. Breiman et al., *Classification and Regression Trees*, New York: Chapman & Hall, 1984.

[21] Y. Freund and R. E. Schapire, *A decision-theoretic generalization of on-line learning and an application to boosting*, J. Comput. Syst. Sci. **55** (1997).

[22] ATLAS Collaboration, *Performance of missing transverse momentum reconstruction in proton–proton collisions at $\sqrt{s}$ = 7 TeV with ATLAS*, Eur. Phys. J. C **72** (2012) 1844, arXiv: 1108.5602 [hep-ex].

[23] ATLAS Collaboration, *Reconstruction of hadronic decay products of tau leptons with the ATLAS experiment*, Eur. Phys. J. **C 76** (2015) 296, arXiv: 1512.05955 [hep-ex], URL: http://arxiv.org/abs/1512.05955.

[24] A. Hocker et al., *TMVA - Toolkit for Multivariate Data Analysis*, PoS **ACAT** (2007) 040, arXiv: physics/0703039 [PHYSICS].

[25] ATLAS Collaboration, *Electron efficiency measurements with the ATLAS detector using the 2015 LHC proton-proton collision data*, ATLAS-CONF-2016-024, 2016, URL: https://cds.cern.ch/record/2157687.

[26] J. W. G. Folger, *eConf C0303241 MOMT007 (2003)* (), arXiv: 0306007 [nucl-th].

[27] H. Bertini, Phys. Rev. **188** (1969) 1711–1730.

[28] B. N.-A. B. Andersson G. Gustafson, Nucl. Phys. B **281** ().

[29] M. Czakon, P. Fiedler and A. Mitov, *Total Top-Quark Pair-Production Cross Section at Hadron Colliders Through $O(\alpha_S^4)$*, Phys. Rev. Lett. **110** (2013) 252004, arXiv: 1303.6254 [hep-ph].

[30] J. Glatzer, 'Inclusive top pair production at 7, 8 and 13 TeV in ATLAS', tech. rep. ATL-PHYS-PROC-2015-172, CERN, 2015, URL: https://cds.cern.ch/record/2111202.

[31] L. Lyons, D. Gibaut and P. Clifford, *How to Combine Correlated Estimates of a Single Physical Quantity*, Nucl. Instrum. Meth. **A270** (1988) 110.

[32] A. Valassi, *Combining correlated measurements of several different physical quantities*, Nucl. Instrum. Meth. **A500** (2003) 391.

[33] E Petit et al., 'Combination of Photon identification measurements with 2012 data', tech. rep. ATL-COM-PHYS-2014-773, CERN, 2014, URL: https://cds.cern.ch/record/1735251.

[34] R. Nisius, ‘BLUE: a software package to combine correlated estimates of physics observables within ROOT using the Best Linear Unbiased Estimate method - Program manual, Version 2.1.0’, URL: http://blue.hepforge.org.

[35] R. Nisius, *On the combination of correlated estimates of a physics observable*, The European Physical Journal C **74** (2014) 1, ISSN: 1434-6052, URL: http://dx.doi.org/10.1140/epjc/s10052-014-3004-2.

Appendix

A. Offline tau identification efficiency measurement

The goal of this study is to derive the identification efficiency of hadronically decaying tau leptons from the data recorded by the ATLAS detector, and compare it to the efficiency expected from Monte Carlo. This is performed by using Z→ $\tau\tau$ events, selected following a *tag-and-probe* approach: events triggered by the presence of a muon (tag) and containing a hadronically decaying tau candidate (probe) are selected. The Z→ $\tau_\mu\tau_{had}$ signal will be subject to several backgrounds, those considered in this study being W+jet, Z→ll, top and multijet.
In order to get the efficiency, one must determine and compare the number of reconstructed τ_{had} before and after application of the identification algorithm.

A.1. Event selection

A pre-selection (FIG. 34) is first applied, requiring one single trigger matched muon with a p_T over 22 GeV and at least one τ_{had} candidate with a p_T over 20 GeV. If several, the candidate with the highest p_T is chosen. Some distributions after this pre-selection are shown in FIG. 35.

Pre-selection	HLT_mu20_iloose_L1MU15 muTrig_Match_HLT_mu20_iloose_L1MU15 N_{pvx} ≥1 Exactly 1 muon, electron veto
Tau requirements	Only leading tau candidate p_T ≥20 GeV $\lvert\eta\rvert$ ≤1.37 and 1.52≤ $\lvert\eta\rvert$ ≤2.47 N_{tracks} = 1 or 3, $\lvert q\rvert$=1 tau jet BDT score≥0.30
Muon requirements	p_T ≥22 GeV medium Id ptcone40/pt≤0.01 etcone20/pt≤0.04

Figure 34: Pre-Selection

A signal region, enriched in Z→ $\tau\tau$ events, is then defined by applying cuts on the transverse mass ($M_T = \sqrt{2p_T(\mu).E_T^{miss}.(1 - cos\Delta\Phi(\mu, E_T^{miss}))}$), SumCosDPhi (=$cos\Delta\Phi(\mu, E_T^{miss}) + cos\Delta\Phi(\tau_{had}, E_T^{miss})$) and the visible mass from the muon and the tau (FIG. 36).
Two control regions, respectively enriched in W+jet and multijet events, are also defined in order to perform the background estimation.

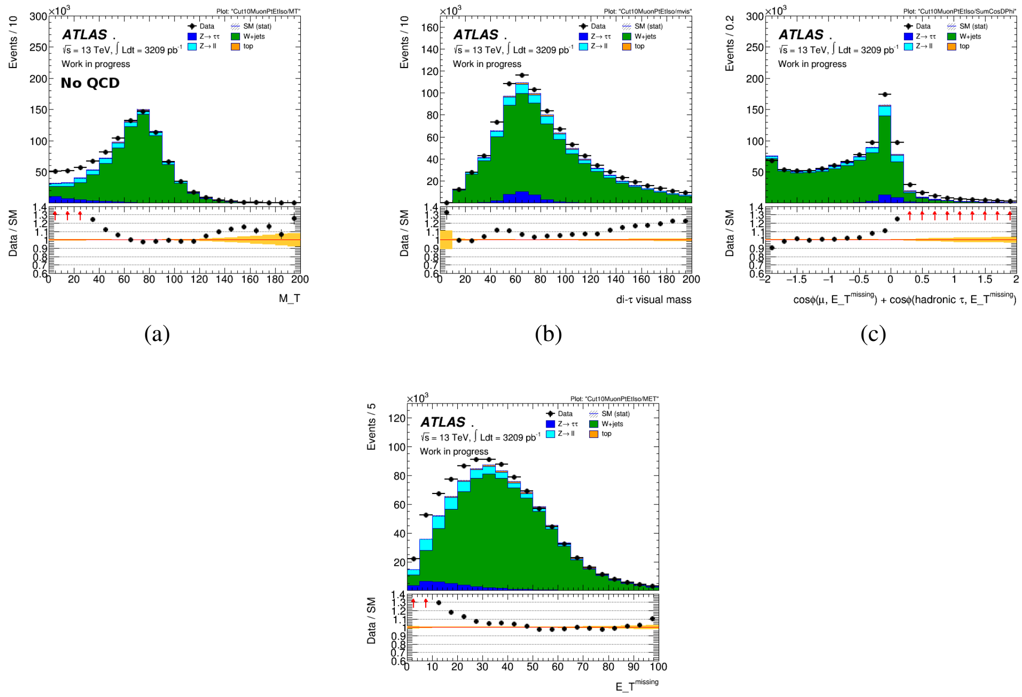

(a) (b) (c)

(d)

Figure 35: Distribution after pre-selection of the transverse mass (a), the visible mass of the muon and the tau (b), SumCosDPhi (c) and the transverse missing energy (d).

A.2. Efficiency extraction

The identification efficiency is derived by performing a fit in the OS signal region. The variable used for this fit is the track multiplicity of the τ_{had} candidate, defined as the sum of the number of core tracks ($0 \leq \Delta R \leq 0.2$) and of the number of outer tracks ($0.2 \leq \Delta R \leq 0.6$) satisfying the criterion $min(\frac{p_T^{core}}{p_T^{outer}} \times \Delta R(core, outer)) \leq 4$. This criterion, on top of suppressing tracks from pileup and underlying events, will enable to separate the true tau leptons from the jet fakes by requiring the outer tracks to have a p_T close to the core tracks and to be close to them. The track multiplicity will therefore tend to be higher for jet fakes than for true tau leptons.

Three templates are built in order to perform the fit:

- Tau template: the signal template, built from Monte Carlo Z→ $\tau\tau$ and top ($t\bar{t}$) events with truth matched taus. It is split between 1 and 3 prong;
- Lepton template: first background template, built from Monte Carlo Z→ll, Z→ $\tau\tau$ and top events with lepton fake taus;
- Jet template: second background template, accounting for jet fakes (W+jet and Multijet). This template is data driven and needs a specific construction.

Signal region	$M_{\rm T}$ ≤50 GeV SumCosDPhi≥-0.1 42≤visible mass (μ, τ)≤82 GeV μ p_T ≤40 GeV, $\Delta\Phi(\mu,\tau)$ ≥2.4
W+jet control region	$M_{\rm T}$ ≥60 GeV $E_{\rm T}^{\rm miss}$ ≥30 GeV SumCosDPhi ≤0
Multijet control region	Same as signal region except: ptcone40/pt≥0.01 etcone20/pt≥0.04 15≤visible mass≤50 GeV and visible mass≥90 GeV

Figure 36: Definition of the signal region and the control regions

Jet template construction The jet template accounts for the jet fakes in the OS signal region, it is therefore built as sum of the contributions from W+jet and Multijet, which need both to be estimated. The W+jet contribution in the OS signal region is obtained by taking the data distribution in the OS W+jet control region, and by applying it a (OS W) transfer factor defined as the ratio between W+Jet Monte Carlo's in the OS signal region and the OS W+jet control region (FIG. 37).

The multijet contribution must first be estimated in the SS signal region, before applying it a multijet transfer factor, defined as the ratio between data in the OS multijet control region and the SS multijet control region (FIG. 39). This estimation of multijet in the SS signal region is obtained by taking the data distribution in the SS signal region, and subtracting an estimation of W+jet in this same region (defined the same way as W+jet in the OS signal region, FIG. 38).
The three transfer factor used are applied as flat normalisation factors, their shapes being taken into account in the systematics. The different templates are presented in FIG. 40.

Pre-Id fit The choice was made to perform the fit in the pre-Id region, rather than making simultaneous fits in the passed and failed Id regions. Indeed, a fit in the failed Id region is too dependent on the jet template modelling and would lead to uncontrollable systematics. In addition, the pre-Id fit also enables to increase the tau statistics and therefore the fit power.
For this fit, the tau templates (1 and 3 prong) are floated with a common parameter, the jet template is also floated and the lepton template is constrained to the Monte Carlo prediction.
This pre-Id fit (FIG. 41(a)) enables to extract two essential elements for the computation of the efficiency: the yield of tau before Id and the jet normalization factor (i.e. the floated parameter for the jet template).

Efficiency To get the efficiency, the yield of tau in the passed Id region is also needed. To get this, templates in the passed Id region are built (splitting between 1 and 3 prong for all of them, FIG. 43). The jet templates are built following the same procedure as for the pre-Id jet template, the different transfer factors used are shown in FIG. 42.
The jet normalization factor extracted from the fit is then applied on the jet templates in passed Id, and the

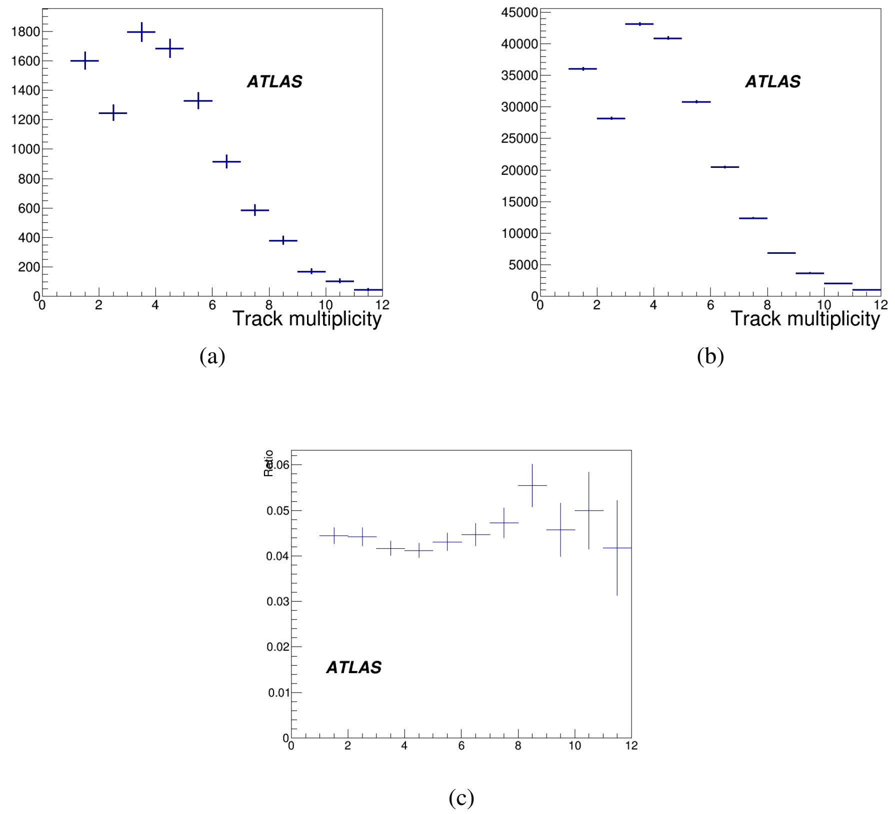

Figure 37: W+jet distribution in the OS signal region (a), W+jet distribution in the OS W+jet control region (b) and OS W transfer factor (c).

yield of tau in passed Id is obtained by subtracting the lepton and the jet templates to data. The efficiency is then computed as the ratio between the yield of tau in passed Id and before Id.

A.3. Results

Here are given the results obtained with the full 2015 dataset, i.e. an integrated luminosity of 3.2 fb^{-1}, and MC15b samples. The results are split between 1 and 3 prong, and between three identification requirements: tight (FIG. 44), medium (FIG. 45) and loose (FIG. 46).

The systematics considered come from the definition of the templates:

- The transfer factors used to build the jet template are a source of systematics. For the W transfer factors (OS and SS), the uncertainties on the normalisation factors applied are considered, as well as the shapes of the transfer factors as a function of the track multiplicity. For this latter, the OS and SS transfer factors are respectively fitted to a 3rd and 2nd order polynomial, and the resulting function is used instead of the flat normalisation factor. The shape of the multijet transfer factor is also taken into account, and in addition the reliability of the multijet control region is estimated by splitting into three sub-regions and deriving a transfer factor for each.

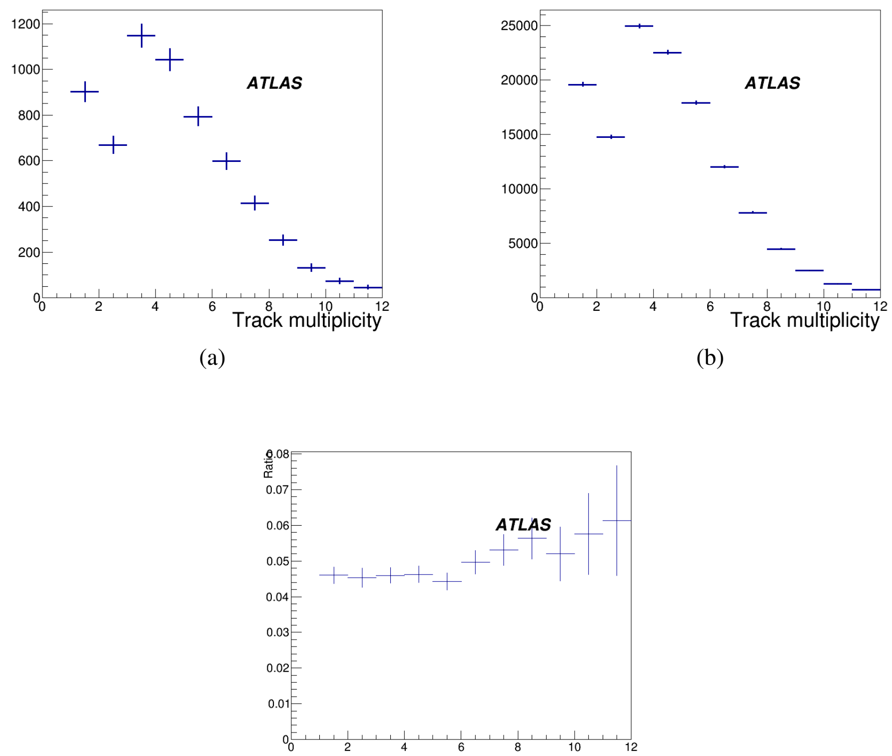

(a) (b) (c)

Figure 38: W+jet distribution in the SS signal region (a), W+jet distribution in the SS W+jet control region (b) and SS W transfer factor (c).

- The systematics on the tau template are estimated by using different Z→ $\tau\tau$ Monte Carlo samples, with alternative detector geometries (Alternative GEO (+5%), Alternative IBL GEO) or different physics lists in Geant 4 (QGSP_BIC, FTFP_BERT_BIC).
- For the lepton template, an arbitrary uncertainty on the modelling of 50 % is propagated.

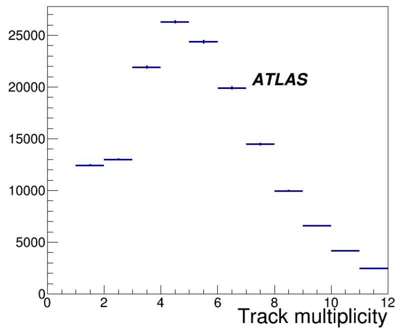

(a)

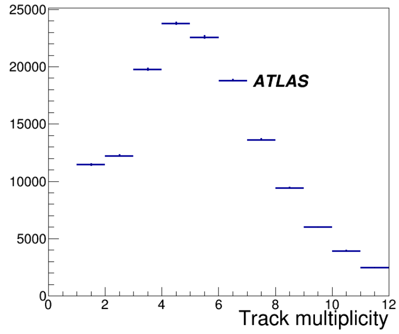

(b)

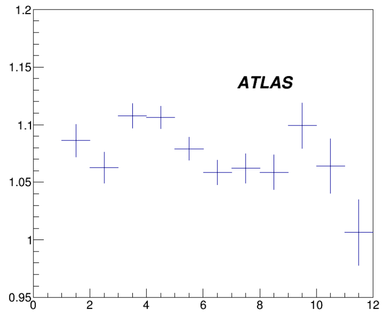

(c)

Figure 39: Data distribution in the OS multijet control region (a), in the SS multijet control region (b) and multijet transfer factor (c).

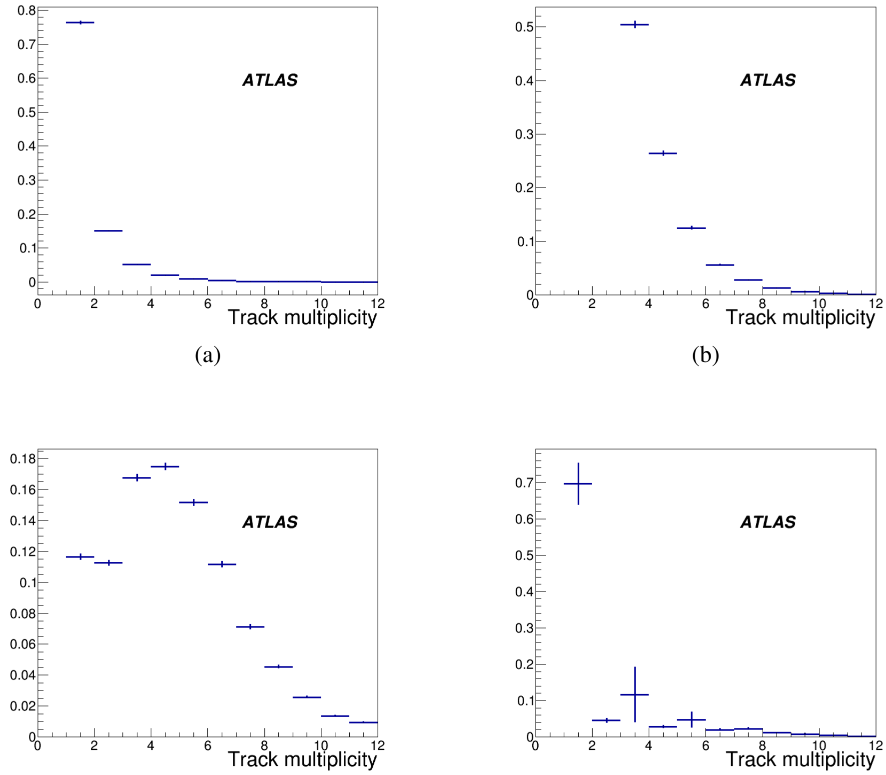

(a) (b) (c) (d)

Figure 40: Tau template, split between 1 (a) and 3 prong (b), jet template (c) and lepton template (d).

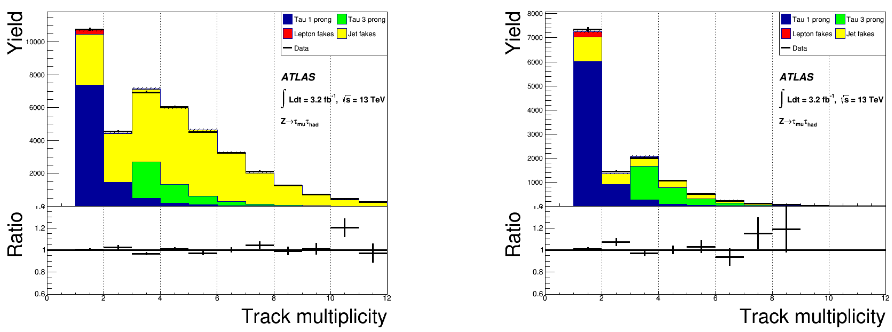

(a) (b)

Figure 41: Track multiplicity before Id (a) and for passed Id (b).

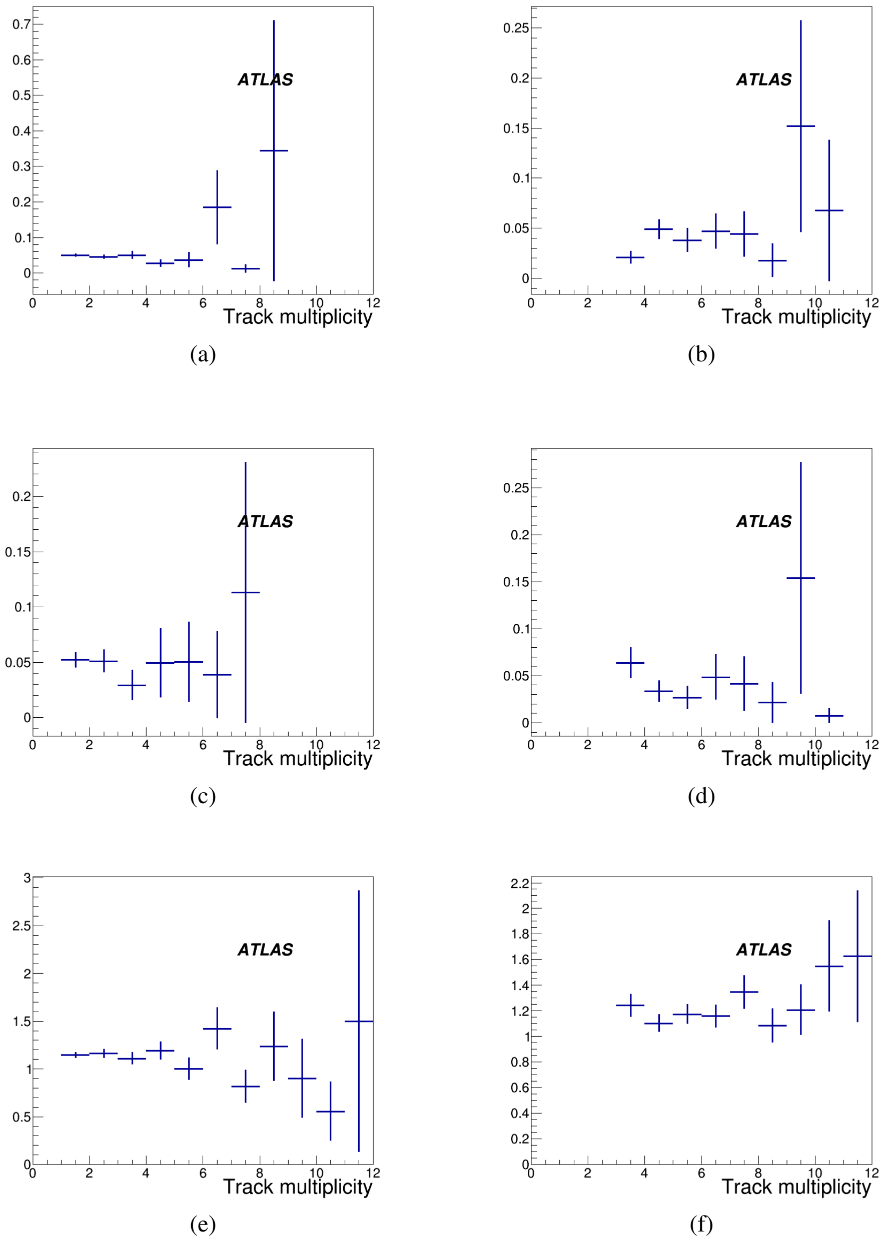

Figure 42: Passed identification: OS W transfer factor 1 (a) and 3 prong (b), SS W transfer factor 1 (c) and 3 prong (d) and multijet transfer factor 1 (e) and 3 prong (f).

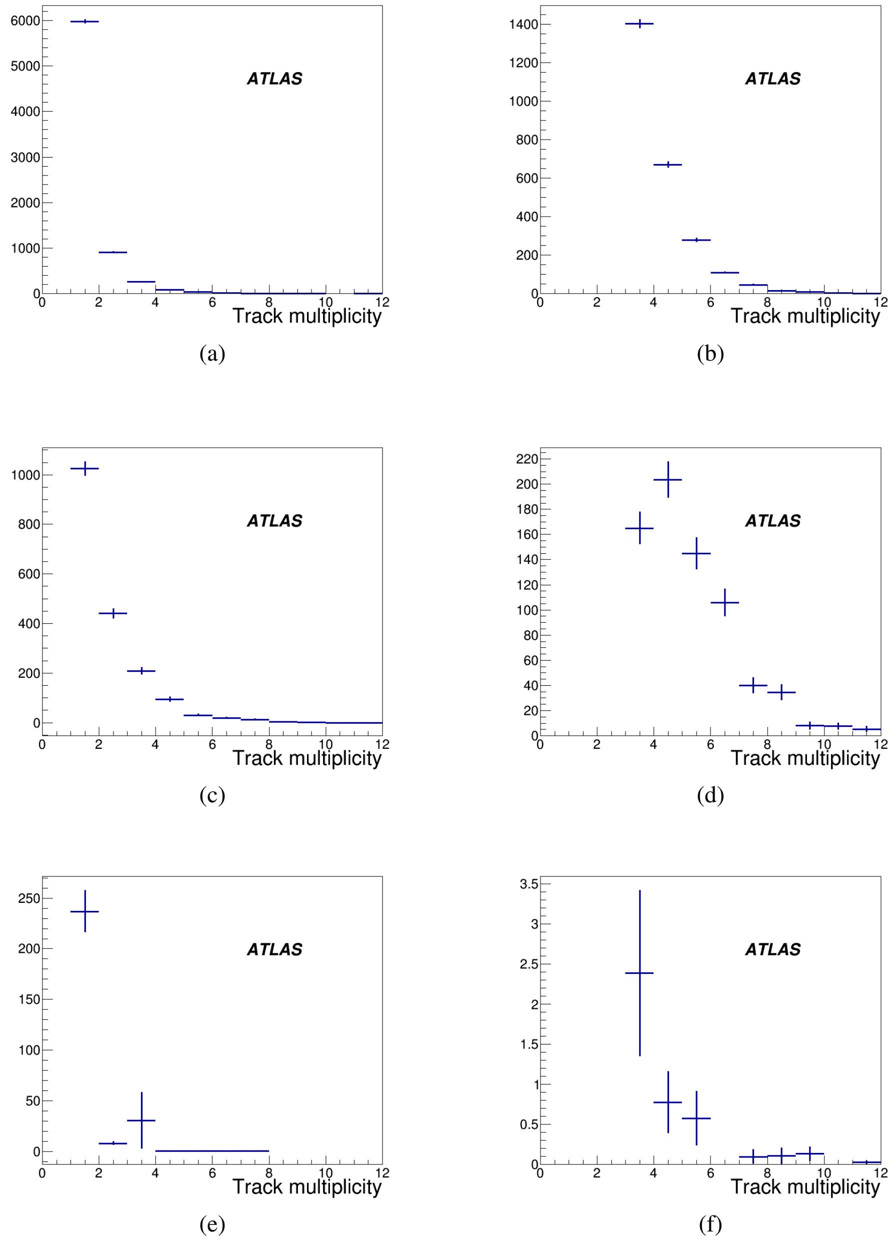

Figure 43: Passed identification: tau template 1 (a) and 3 prong (b), jet template 1 (c) and 3 prong (d) and lepton template 1 (e) and 3 prong (f).

	1 prong	3 prong
Data efficiency	0.606±0.010	0.430±0.011
MC efficiency	0.590	0.424
SF	$1.027 \pm 0.019(\text{stat.})^{+0.051}_{-0.024}(\text{sys.})$	$1.013 \pm 0.031(\text{stat.})^{+0.050}_{-0.024}(\text{sys.})$

Figure 44: Tau identification efficiency from data and Monte Carlo for the tight identification requirement. The scale factor is the ratio between measured and expected efficiencies.

	1 prong	3 prong
Data efficiency	0.771 ± 0.012	0.592 ± 0.015
MC efficiency	0.760	0.586
SF	$1.016 \pm 0.017(\text{stat.})^{+0.049}_{-0.024}(\text{sys.})$	$1.010 \pm 0.028(\text{stat.})^{+0.049}_{-0.023}(\text{sys.})$

Figure 45: Tau identification efficiency from data and Monte Carlo for the medium identification requirement. The scale factor is the ratio between measured and expected efficiencies.

	1 prong	3 prong
Data efficiency	0.860 ± 0.013	0.723 ± 0.019
MC efficiency	0.852	0.745
SF	$1.008 \pm 0.016(\text{stat.})^{+0.048}_{-0.023}(\text{sys.})$	$0.971 \pm 0.028(\text{stat.})^{+0.046}_{-0.023}(\text{sys.})$

Figure 46: Tau identification efficiency from data and Monte Carlo for the loose identification requirement. The scale factor is the ratio between measured and expected efficiencies.

B. Online tau identification efficiency measurement

A tau trigger in the ATLAS experiment has been designed and implemented to select events which contains hadronically decaying tau leptons (τ_{had}) in the final state.

The ATLAS trigger system is consist of two level triggers to efficiently collect interesting events keeping trigger rate. The first level is hardware-based trigger named Level 1 (L1) while the second one is software based trigger named High Level Trigger (HLT). At L1, the tau reconstruction is performed based on the energy deposit in the electromagnetic (EM) and hadronic (HAD) calorimeters. These energy deposits are read out in calorimetric towers with a granularity of $\delta\eta \times \delta\phi = 0.1 \times 0.1$. Taus are identified if the uncalibrated sum of the energy depoists in 2×1 EM towers and 2×2 HAD towers behind the EM towers exceed a given threshold. An additonal isolation requirement can be applied by setting an upper threshold for the energy deposited in 4×4 ring surrounding the 2×2 towers in the EM calorimeter. Isolation thresholds has been implemented with respect to its core energy from 2015 Run. Isolation requirments can effectively reject QCD jets whicle keeping a high-efficiency for selecting τ_{had}. The position of the L1 energy deposit is defined as a region of interest (RoI). At HLT, three sequential selections are made around RoIs. Firstly, a cut on the transverse energy of the tau candidate is made using topological clusters of calorimeter cells, with a dedicated tau energy calibration applied. Secondly, a two-step fast tracking is used to select tau candidates with a low track multiplicity. A leading track is found within a narrow ΔR of the tau direction, follwied by a second fast-tracking step using a larger ΔR but with the tracks requireed to emanate from the same position along the beamline as the leading track. Finallly, the full HLT precision tracking is run and a collection of variables, built from calorimeter and track quantities, are fed into a BDT for the final tau identification. BDT tau identification has been harmonised with the offline tau identification as much as possible.

The efficiency of the tau trigger was measured on real data using a Z$\rightarrow \tau_{\mu}\tau_{\text{had}}$ tag-and-probe method. The presense of an isolated muon coming from a τ_{μ} decay is required to tag the Z$\rightarrow \tau_{\mu}\tau_{\text{had}}$ event while the τ_{had} is used as an unbiased probe of tau trigger performance. In order to measure the efficiency, tau p_{T} spectrum is measured before and after passing single tau trigger.

B.1. Object & Event Selection

In this analysis, hadronic taus in Z$\rightarrow \tau_{\mu}\tau_{\text{had}}$ events are considered. The selected events are accepted by the lowest unprescaled single muon trigger are tagged by an offline reconstructed muon passing gradient isolation requirement with transverse momentum above 22 GeV. The presense of an offline reconstructed tau with transverse momentum above 25 GeV, one or three tracks, passing the offline tau identification working point (loose, medium and tight); tau identification working point depends on which measurement are performed. The electric charge of tau is required to be opposite to the one of muon. The event selection used to enhance the Z$\rightarrow \tau_{\mu}\tau_{\text{had}}$ events. To reject $Z(\rightarrow \mu\mu)$+jets and di-leptonic ttbar events, it is required that there is exactly only one reconstructed muon and no other reconstructed light lepton; i.e. electron and muon. To reject QCD multi-jets and W$\rightarrow \mu\nu$+jets events, the invariant mass of the muon and the offline tau candidate is required to be between 45 and 80 GeV, the transverse mass of the muon and $E_{\text{T}}^{\text{miss}}$ ($m_{\text{T}} = \sqrt{2p_T^{\mu}E_{\text{T}}^{\text{miss}}(1-\cos\Delta\phi(\mu, E_{\text{T}}^{\text{miss}}))}$) has to be less than 50 GeV and the distance in the azimuthal plane between the muon and $E_{\text{T}}^{\text{miss}}$ and between the offline tau candidate and $E_{\text{T}}^{\text{miss}}$ ($\Sigma\cos\Delta\phi = \cos\Delta\phi(\mu, E_{\text{T}}^{\text{miss}}) + \cos\Delta\phi(\tau, E_{\text{T}}^{\text{miss}})$) has to be greater than -0.5. Finally, no b-tagged jet with 77% working point is required to suppless a littie bit contribution from ttbar events.

The full list of selection requirements are summarized in Table 7.

Table 7: Event selection requirements for $Z \rightarrow \tau_{\mu}\tau_{had}$ events

	Requirement
Trigger	`HLT_mu20_iloose_L1MU15`
μ	Medium quality Trigger matched Gradient or inverted Gradient isolation $p_{\mathrm{T}} > 22$ GeV $\lvert\eta\rvert < 2.5$
e	Loose likelihood ID $p_{\mathrm{T}} > 15$ GeV $\lvert\eta\rvert < 2.5$
τ	Loose, Medium, or Tight BDT ID $\lvert q\rvert = 1$ $N_{\mathrm{track}} = 1$ or $N_{\mathrm{track}} = 3$ $p_{\mathrm{T}} > 25$ GeV $\lvert\eta\rvert < 1.37$ or $1.52 < \lvert\eta\rvert < 2.47$ no overlapping electron
jet	$p_{\mathrm{T}} > 20$ GeV $\lvert\eta\rvert < 4.5$ JVT > 0.64 for $\lvert\eta\rvert < 2.5$ & $p_{\mathrm{T}} < 50$ GeV 77% identification efficiency for b-jets
preselection	one primary vertex with at least 4 tracks one reconstructed μ no other reconstructed leptons one or more reconstructed τ the μ and the τ have opposite sign charge no b-tagged jet
signal region	Gradient isolation on the μ $\mathrm{m_T} < 50$ GeV $cos(\Delta\phi(\mu, \mathrm{E_T^{miss}})) + \cos(\Delta\phi(\tau, \mathrm{E_T^{miss}})) > -0.5$ $45 < M_{\mu,\tau}[\text{ GeV}] < 80$
QCD control region	inverted Gradient isolation on the μ $\mathrm{m_T} < 50$ GeV $cos(\Delta\phi(\mu, \mathrm{E_T^{miss}})) + \cos(\Delta\phi(\tau, \mathrm{E_T^{miss}})) > -0.5$
W+Jet control region	Gradient isolation on the μ $\mathrm{E_T^{miss}} > 30$ GeV $\mathrm{m_T} > 60$ GeV

B.2. Backgrounds Estimation

After applying event selection in B.1, the dominant sources of background events are $W \rightarrow \mu\nu$ + jets and QCD multi-jets events. Since it is difficult to estimate jet to τ_{had} fake only with MC simulation, these backgrounds are estimated using data in the dedicated control regions.

B.2.1. Multi-jets Estimation

QCD multi-jets events are modeled from real data events where the offline tau candidate and the muon have the same sign electric charge (SS data). The shape of the background events is taken from the same requirements as signal region but using the SS data. Considering the difference of the amonut of multi-jets contribution between opposite sign (OS) and SS data, the normalization factor (r_{QCD}) is derived from the dedicated control region (QCD control region in Table 7), where QCD multi-jets events are dominant by requiring that muon candidate does not pass gradient isolation requirments. Unlike signal region, Z mass window cut is dropped in QCD multi-jet control region not to enhance Z→ $\tau_{\mu}\tau_{\mathrm{had}}$ fraction.

The r_{QCD}factors are parameterized by the followings.

- offline τ identification requirement: loose, medium, tight;
- τ N_{track} requirement: 1 or 3;
- τ: $p_{\mathrm{T}} \leq 40$ GeV or $p_{\mathrm{T}} > 40$ GeV;

The r_{QCD}factors are computed as the ratio of opposite-sign and same-sign events in the QCD control region with the selected parameterization after subtracting all MC contributions.

$$r_{\mathrm{QCD}}(N_{\mathrm{track}}, \mathrm{ID}, p_{\mathrm{T}}) = \frac{N_{\mathrm{OS}}^{\mathrm{QCD\ CR\ Data}}(N_{\mathrm{track}}, \mathrm{ID}, p_{\mathrm{T}}) - N_{\mathrm{OS}}^{\mathrm{QCD\ CR\ MC}}(N_{\mathrm{track}}, \mathrm{ID}, p_{\mathrm{T}})}{N_{\mathrm{SS}}^{\mathrm{QCD\ CR\ Data}}(N_{\mathrm{track}}, \mathrm{ID}, p_{\mathrm{T}}) - N_{\mathrm{OS}}^{\mathrm{QCD\ CR\ MC}}(N_{\mathrm{track}}, \mathrm{ID}, p_{\mathrm{T}})}.$$

These factors are applied to same sign events in the signal region to estimate SS data background.

$$\mathrm{SS\ data}(N_{\mathrm{track}}, \mathrm{ID}, p_{\mathrm{T}}) = \sum_{N_{\mathrm{track}}, \mathrm{ID}, p_{\mathrm{T}}} r_{\mathrm{QCD}}(N_{\mathrm{track}}, \mathrm{ID}, p_{\mathrm{T}}) \times \mathrm{SS}^{\mathrm{SR}}(N_{\mathrm{track}}, \mathrm{ID}, p_{\mathrm{T}})$$

Both statistical and systematic components are considerd for the r_{QCD}uncertainties. The statistical components is computed assuming that number of OS and SS events in the QCD control region are distributed according to the normal distribution. To derive the systematic component, cuts on two isolation variables are used: the distribution of momentum of tracks inside a cone of $\Delta R < 0.3$ (`ptvarcone30`), and the distribution of energy of calorimeter deposits inside a cone of $\Delta R < 0.2$ (`topoetcone20`) of the μ direction, relative to the offline μ p_{T}. The cuts are placed and varied individually (between 0.1 and 0.4), and the envelope of the change of the r_{QCD}factor under each variation makes one component of the systematic uncertainty. The total systematic uncertainty on the r_{QCD}factor is computed by adding the two components in quadrature.

The r_{QCD}factors for 1-track, 3-track, and 1- or 3-track τ candidates are shown in Table 8. The τ p_{T} distributions of opposite-sign and same-sign events in the QCD control region with a *medium* offline τ identification requirement are shown in Figure 47.

	loose	medium	tight
1-track τ candidate			
p_T inclusive	1.15 ± 0.01 ± 0.03	1.19 ± 0.02 ± 0.03	1.21 ± 0.02 ± 0.08
$p_T \leq 40$ GeV	1.11 ± 0.02 ± 0.03	1.15 ± 0.02 ± 0.05	1.17 ± 0.03 ± 0.07
$p_T > 40$ GeV	1.20 ± 0.02 ± 0.05	1.25 ± 0.03 ± 0.06	1.27 ± 0.04 ± 0.11
3-track τ candidate			
p_T inclusive	1.25 ± 0.02 ± 0.05	1.28 ± 0.03 ± 0.08	1.39 ± 0.05 ± 0.14
$p_T \leq 40$ GeV	1.19 ± 0.02 ± 0.05	1.21 ± 0.03 ± 0.10	1.29 ± 0.06 ± 0.16
$p_T > 40$ GeV	1.36 ± 0.03 ± 0.09	1.42 ± 0.06 ± 0.16	1.62 ± 0.11 ± 0.25
1 or 3-track τ candidate			
p_T inclusive	1.18 ± 0.01 ± 0.03	1.21 ± 0.01 ± 0.03	1.24 ± 0.02 ± 0.08
$p_T \leq 40$ GeV	1.14 ± 0.01 ± 0.03	1.17 ± 0.02 ± 0.04	1.19 ± 0.03 ± 0.08
$p_T > 40$ GeV	1.25 ± 0.02 ± 0.05	1.28 ± 0.02 ± 0.06	1.32 ± 0.04 ± 0.10

Table 8: $r_{\mathrm{QCD}}$with statistical and systematic uncertainties for events with 1-track, 3-track and 1- or 3-track τ candidates, for selections with a p_T threshold of 25 GeV, and for different ranges in τ p_T.

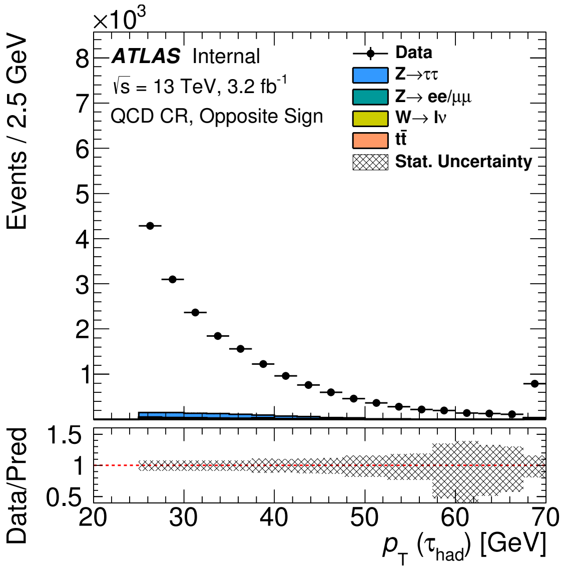

(a)

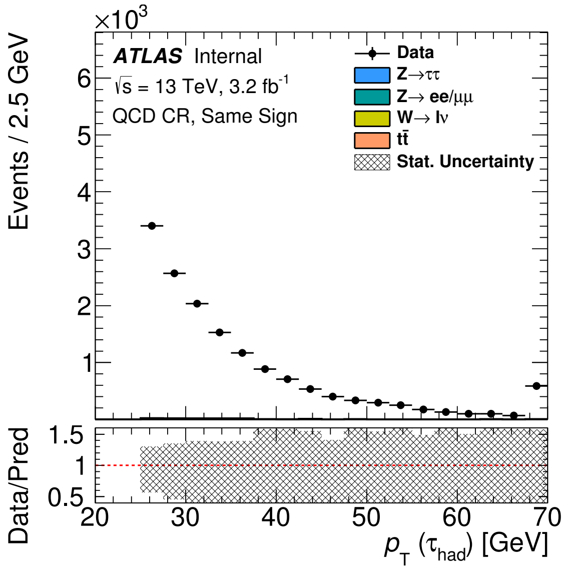

(b)

Figure 47: Distributions of τ p_T in data and simulated events (MC) in the QCD control region, with opposite-sign and same-sign events in the left and right plots respectively.

B.2.2. W+jets Estimation

The shape of the W+jets background events are modeled with MC simulation. Normalization factor (k_W) is derived from real data in the dedicated control region (W+Jet control region in Table ??). The transverse mass of the muon and E_T^{miss} ($m_T = \sqrt{2p_T^{\mu}E_T^{\mathrm{miss}}(1 - \cos\Delta\phi(\mu, E_T^{\mathrm{miss}}))}$) has to be more than 60 GeV to enhance the the purity of the W+Jet events. And E_T^{miss} has to be more than 30 GeV to reject the QCD multi-jet contributions. Taking into account the difference of the amount of the W+Jet contribution between OS and SS events, the normalization factors are extracted OS and SS data, respectively.

The k_{W}factors are also parameterized by the followings.

- offline τ identification requirement: loose, medium, tight;
- τ N_{track} requirement: 1 or 3;
- τ: $p_{\mathrm{T}} \leq 40$ GeV or $p_{\mathrm{T}} > 40$ GeV;

Both k_{W}factors in OS and SS events ($k_{\mathrm{W}}^{\mathrm{OS}}$and $k_{\mathrm{W}}^{\mathrm{SS}}$) are computed as the ratio of real data and W+Jet MC simulation events in the W+Jet control region with the selected parameterization, requiring opposite and same sign charge between tau and muon candidate, respectively. For these computation, all MC contributions except W+Jet are subtracted from real data.

$$k_{\mathrm{W}}^{\mathrm{OS}}(N_{\mathrm{track}}, \mathrm{ID}, p_{\mathrm{T}}) = \frac{N_{OS}^{\text{W+Jet CR Data}}(N_{\mathrm{track}}, \mathrm{ID}, p_{\mathrm{T}}) - N_{OS}^{\text{W+Jet CR MC(all)}}(N_{\mathrm{track}}, \mathrm{ID}, p_{\mathrm{T}})}{N_{OS}^{\text{W+Jet CR MC(W+Jet)}}(N_{\mathrm{track}}, \mathrm{ID}, p_{\mathrm{T}})}.$$

$$k_{\mathrm{W}}^{\mathrm{SS}}(N_{\mathrm{track}}, \mathrm{ID}, p_{\mathrm{T}}) = \frac{N_{SS}^{\text{W+Jet CR Data}}(N_{\mathrm{track}}, \mathrm{ID}, p_{\mathrm{T}}) - N_{SS}^{\text{W+Jet CR MC(all)}}(N_{\mathrm{track}}, \mathrm{ID}, p_{\mathrm{T}})}{N_{SS}^{\text{W+Jet CR MC(W+Jet)}}(N_{\mathrm{track}}, \mathrm{ID}, p_{\mathrm{T}})}.$$

Both statistical and systematic components are also considerd for the k_{W}uncertainties. The statistical components is computed taking into account both statistics of real data and W+Jet MC simulation events. To derive the systematic component, cuts on transverse mass of the muon and $E_{\mathrm{T}}^{\mathrm{miss}}$ is used. The cuts are placed and varied individually (between 60 GeV and 120 GeV), and the envelope of the change of the k_{W}factor under each variation makes the systematic uncertainty.

The $k_{\mathrm{W}}^{\mathrm{OS}}$and $k_{\mathrm{W}}^{\mathrm{SS}}$factors for 1-track, 3-track, and 1- or 3-track τ candidates are shown in Table 9 and Table 10, respectively. The transverse mass distributions of opposite-sign and same-sign events in the W+Jet control region with a *medium* offline τ identification requirement are shown in Figure 48.

	loose	**medium**	**tight**
1-track τ candidate			
p_{T} inclusive	$1.32 \pm 0.02 \pm 0.03$	$1.35 \pm 0.02 \pm 0.03$	$1.42 \pm 0.04 \pm 0.03$
$p_{\mathrm{T}} \leq 40$ GeV	$1.29 \pm 0.02 \pm 0.05$	$1.33 \pm 0.03 \pm 0.05$	$1.42 \pm 0.04 \pm 0.05$
$p_{\mathrm{T}} > 40$ GeV	$1.38 \pm 0.03 \pm 0.05$	$1.38 \pm 0.04 \pm 0.04$	$1.41 \pm 0.06 \pm 0.07$
3-track τ candidate			
p_{T} inclusive	$1.43 \pm 0.03 \pm 0.06$	$1.47 \pm 0.05 \pm 0.13$	$1.60 \pm 0.09 \pm 0.11$
$p_{\mathrm{T}} \leq 40$ GeV	$1.41 \pm 0.03 \pm 0.09$	$1.43 \pm 0.06 \pm 0.09$	$1.63 \pm 0.10 \pm 0.08$
$p_{\mathrm{T}} > 40$ GeV	$1.49 \pm 0.06 \pm 0.09$	$1.56 \pm 0.10 \pm 0.20$	$1.54 \pm 0.17 \pm 0.25$
1 or 3-track τ candidate			
p_{T} inclusive	$1.36 \pm 0.02 \pm 0.03$	$1.37 \pm 0.02 \pm 0.03$	$1.45 \pm 0.03 \pm 0.03$
$p_{\mathrm{T}} \leq 40$ GeV	$1.33 \pm 0.02 \pm 0.03$	$1.35 \pm 0.03 \pm 0.03$	$1.46 \pm 0.04 \pm 0.06$
$p_{\mathrm{T}} > 40$ GeV	$1.41 \pm 0.03 \pm 0.05$	$1.41 \pm 0.04 \pm 0.07$	$1.42 \pm 0.06 \pm 0.07$

Table 9: $k_{\mathrm{W}}^{\mathrm{OS}}$with statistical and systematic uncertainties for events with 1-track, 3-track and 1- or 3-track τ candidates, for selections with a p_{T} threshold of 25 GeV, and for different ranges in τ p_{T}.

	loose	**medium**	**tight**
1-track τ candidate			
p_T inclusive	1.65 ± 0.04 ± 0.10	1.68 ± 0.05 ± 0.15	1.63 ± 0.07 ± 0.19
$p_T \leq 40$ GeV	1.56 ± 0.04 ± 0.15	1.59 ± 0.06 ± 0.20	1.53 ± 0.08 ± 0.19
$p_T > 40$ GeV	1.93 ± 0.09 ± 0.09	1.95 ± 0.12 ± 0.14	1.93 ± 0.17 ± 0.33
3-track τ candidate			
p_T inclusive	1.48 ± 0.05 ± 0.05	1.63 ± 0.09 ± 0.22	2.10 ± 0.20 ± 0.38
$p_T \leq 40$ GeV	1.40 ± 0.05 ± 0.05	1.57 ± 0.09 ± 0.19	2.02 ± 0.22 ± 0.58
$p_T > 40$ GeV	1.76 ± 0.12 ± 0.11	1.86 ± 0.21 ± 0.33	2.38 ± 0.47 ± 0.33
1 or 3-track τ candidate			
p_T inclusive	1.58 ± 0.03 ± 0.06	1.67 ± 0.05 ± 0.09	1.70 ± 0.07 ± 0.15
$p_T \leq 40$ GeV	1.50 ± 0.03 ± 0.09	1.59 ± 0.05 ± 0.13	1.61 ± 0.07 ± 0.12
$p_T > 40$ GeV	1.87 ± 0.07 ± 0.05	1.93 ± 0.11 ± 0.06	2.00 ± 0.16 ± 0.31

Table 10: k_W^{SS} with statistical and systematic uncertainties for events with 1-track, 3-track and 1- or 3-track τ candidates, for selections with a p_T threshold of 25 GeV, and for different ranges in τ p_T.

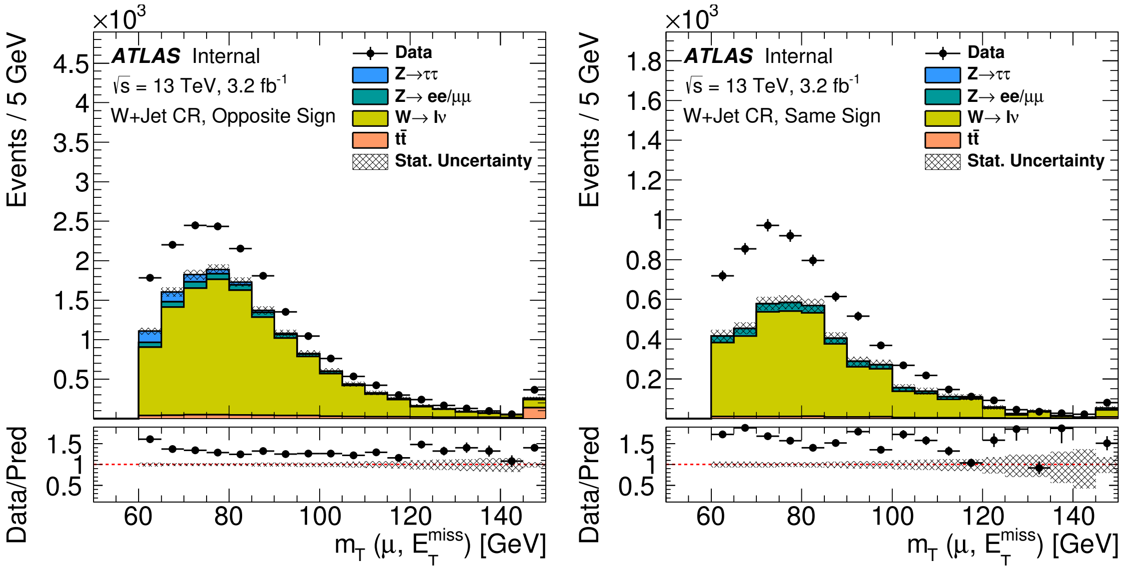

(a) (b)

Figure 48: Distributions of transverse mass in data and simulated events (MC) in the W+Jet control region, with opposite-sign and same-sign events in the left and right plots respectively.

B.2.3. Summary of Backgrounds Estimation

All the contributions in the signal regions are estimated by the following equations, using MC simulation samples and the same sign data with r_{QCD} and k_W factors.

$$\text{Data}_{\text{OS}}^{\text{SR}} = r_{\text{QCD}} \times \text{Data}_{\text{SS}}^{\text{SR}} + Z\tau_\mu\tau_{\text{had}}{}_{\text{OS-SS}}^{\text{SR}} + \text{W+Jet}_{\text{OS-SS}}^{\text{SR}} + \text{Z+Jet}_{\text{OS-SS}}^{\text{SR}} + \text{ttbar}_{\text{OS-SS}}^{\text{SR}}.$$

$$Z\tau_\mu\tau_{\rm had}{}^{\rm SR}_{\rm OS\text{-}SS} = Z\tau_\mu\tau_{\rm had}({\rm MC})^{\rm SR}_{\rm OS} - r_{\rm QCD} \times Z\tau_\mu\tau_{\rm had}({\rm MC})^{\rm SR}_{\rm SS}.$$

$$\text{Z+Jet}^{\rm SR}_{\rm OS\text{-}SS} = \text{Z+Jet(MC)}^{\rm SR}_{\rm OS} - r_{\rm QCD} \times \text{Z+Jet(MC)}^{\rm SR}_{\rm SS}.$$

$$\text{ttbar}^{\rm SR}_{\rm OS\text{-}SS} = \text{ttbar(MC)}^{\rm SR}_{\rm OS} - r_{\rm QCD} \times \text{ttbar(MC)}^{\rm SR}_{\rm SS}.$$

$$\text{W+Jet}^{\rm SR}_{\rm OS\text{-}SS} = k^{\rm OS}_{\rm W} \times \text{W+Jet(MC)}^{\rm SR}_{\rm OS} - k^{\rm SS}_{\rm W} \times r_{\rm QCD} \times \text{W+Jet(MC)}^{\rm SR}_{\rm SS}.$$

In SS data, there are not only QCD multi-jets events but also W+Jet, and a few contribution from Z→ $\tau_\mu\tau_{\rm had}$, Z+Jet and ttbar events. To avoid double counting, all the MC contribution applied same requirements as signal region but requied same sign charge between muon and tau candidates (denoted as $\text{MC}^{\rm SR}_{\rm SS}$) are subtracted from MC contribution in signal region (denoted as $\text{MC}^{\rm SR}_{\rm OS}$) taking into account $r_{\rm QCD}$and $k_{\rm W}$factors.

B.3. Method

The tau trigger efficiency is defined as the fraction of tau trigger candidates that pass the trigger decision with respect to the total number of offline tau candidates. The efficiency is computed as the following in data.

$$\epsilon = \frac{\text{N}^{\rm TRG}_{\rm Data} - \text{N}^{\rm TRG}_{\rm BKG}}{\text{N}_{\rm Data} - \text{N}_{\rm BKG}}$$

Here, $\text{N}_{\rm Data}$ and $\text{N}_{\rm BKG}$ mean number of data and all background events in signal region before requiring tau trigger, and $\text{N}^{\rm TRG}_{\rm Data}$ and $\text{N}^{\rm TRG}_{\rm BKG}$ are the ones after passing tau trigger. All backgrounds described in section B.2 are subtracted from real data for the tau trigger efficiency measurement. The efficiency is calculated in each offline reconstructed τ $p_{\rm T}$ bin. The statistical uncertainty on the efficiency is computed using a Bayesian prior condition in the division, where the efficiency is restricted to the [0,1]. The tau trigger efficiency is also studied in Z→ $\tau_\mu\tau_{\rm had}$ MC simulation sample. The ratio of the efficiency in MC simulation and data (scale factor) can be used to correct the simulated events where a offline reconstructed τ candidate is matched to the τ trigger object and to a true hadronically decaying τ.

B.4. Systematic Uncertainties

The systematic uncertainties considerd in this measurements are listed in the followings.

- μ: trigger; reconstruction, and offline identification efficiency; energy scale
- τ: reconstruction and offline identification efficiency; energy scale
- The soft term of the $E_{\rm T}^{\rm miss}$
- pile-up reweighting
- $r_{\rm QCD}$and $k_{\rm W}$factors

The systematic uncertainties related to offline muon and tau reconstruction, identification efficiencies and the energy scale are treated. For the muon, the uncertainty related to the single muon trigger is also treated. The normalization factors for SS data and W+Jet is also considered. These systematics have both statistical and systematic componetns, which are treated individually The uncertainties for the soft term of the $E_{\mathrm{T}}^{\mathrm{miss}}$, which is calculated from calorimeter cells and tracks not associated to high-p_{T} objects, is taken into account. The uncertainties for the scale factor of the pile-up from MC to data is also treated. The overall effect of a specific systematic uncertainty is measured by comparing the yields of background events from SS data and MC simulation events with and without applying the systematic variation. All systematic uncertainties are listed in Table 11.

	1-track		**3-track**	
	Without trigger	**With trigger**	**Without trigger**	**With trigger**
XXX	$x.xx\%$	$x.xx\%$	$x.xx\%$	$x.xx\%$
XXX	$x.xx\%$	$x.xx\%$	$x.xx\%$	$x.xx\%$
XXX	$x.xx\%$	$x.xx\%$	$x.xx\%$	$x.xx\%$
XXX	$x.xx\%$	$x.xx\%$	$x.xx\%$	$x.xx\%$
XXX	$x.xx\%$	$x.xx\%$	$x.xx\%$	$x.xx\%$
XXX	$x.xx\%$	$x.xx\%$	$x.xx\%$	$x.xx\%$
XXX	$x.xx\%$	$x.xx\%$	$x.xx\%$	$x.xx\%$
XXX	$x.xx\%$	$x.xx\%$	$x.xx\%$	$x.xx\%$

Table 11: Overall effect of individual systematic uncertainty on all backgrounds measured in selections without and with requiring a τ trigger with a p_{T} threshold of 25 GeV, and for 1-track and 3-track τ candidates separately. If the systematic uncertainty consists of both upward and downward variations, the variation resulting in the highest effect is shown. Systematic uncertainties (or pairs thereof) whose overall effect is 0.05% or less are not shown.(After collecting information, these will be updated)

B.5. Results

B.5.1. Kinematics before applying τ trigger

A comparison between data and Z→ $\tau_\mu \tau_{\mathrm{had}}$ plus all backgruonds are shown for distributions of kinematic variables and event variables in the signal region with a *medium* offline identification requirement on the hadronically decaying τ candidate, and with 1 or 3 tracks inclusively. Distributions of kinematic variables of the μ can be found in Figure 49, while those related to the hadronically decaying τ candidate can be found in Figure 50. Figure 51 shows distributions of the τ N_{track} and the output score of the offline τ identification boosted decision tree (BDT) algorithm. Distributions of N_{vtx} and N_{jets} can be found in Figure 52, and distributions of $E_{\mathrm{T}}^{\mathrm{miss}}$ and the invariant mass between the τ and the muon in Figure 53.

B.5.2. Kinematics after applying τ trigger

The comparison between data and Z→ $\tau_\mu \tau_{\mathrm{had}}$ plus all backgruonds are made for events in the signal region with a *medium* offline identification requirement on the hadronically decaying τ candidate, and also for events fulfilling the same selection with the additional requirement that the τ trigger with a p_{T} threshold of 25 GeV is fired. The τ p_{T} distributions with and without applying the τ trigger with a p_{T} threshold of

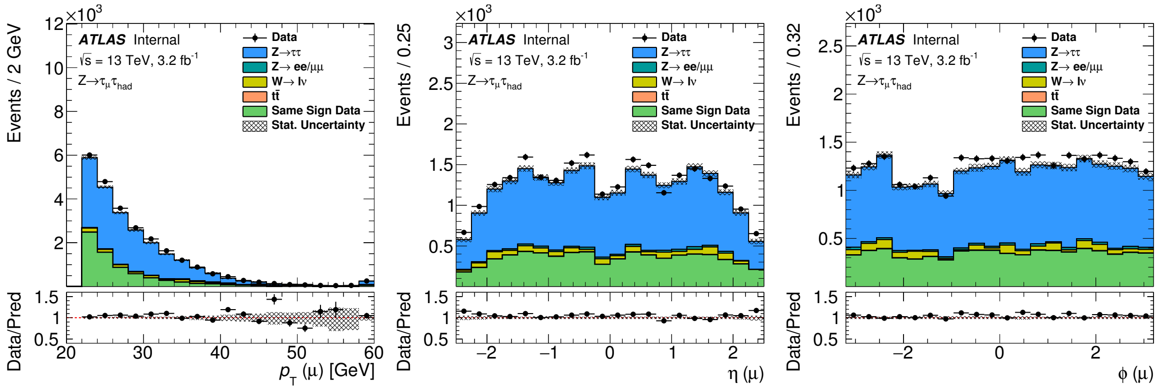

(a) (b) (c)

Figure 49: Kinematic distributions of the tag μ in the signal region with a *medium* offline identification requirement on the hadronically decaying τ candidate, and with 1 or 3 tracks inclusively.

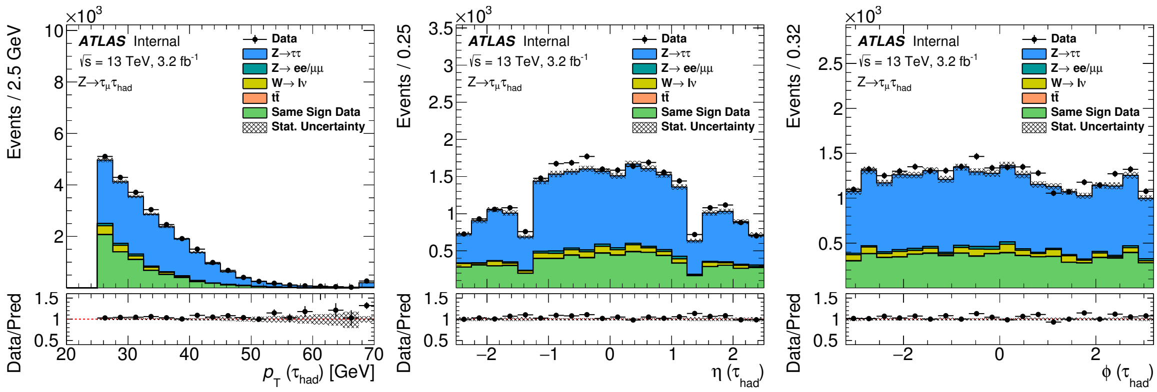

(a) (b) (c)

Figure 50: Kinematic distributions of the probe τ in the signal region with a *medium* offline identification requirement on the hadronically decaying τ candidate, and with 1 or 3 tracks inclusively.

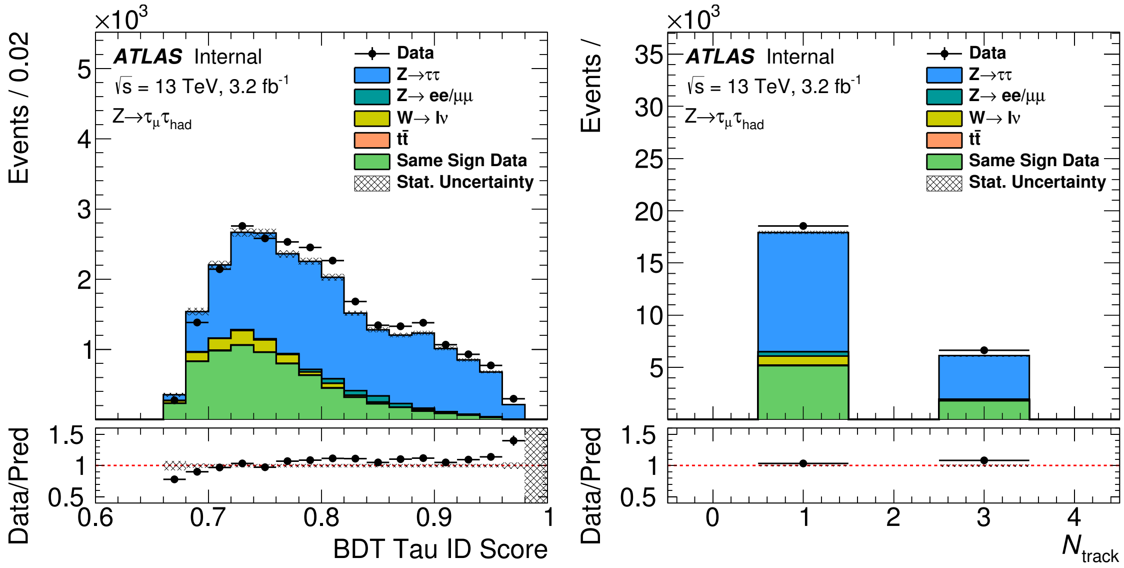

(a)

(b)

Figure 51: Distributions of the offline τ BDT score and N_{track} in the signal region with a *medium* offline identification requirement on the hadronically decaying τ candidate, and with 1 or 3 tracks inclusively.

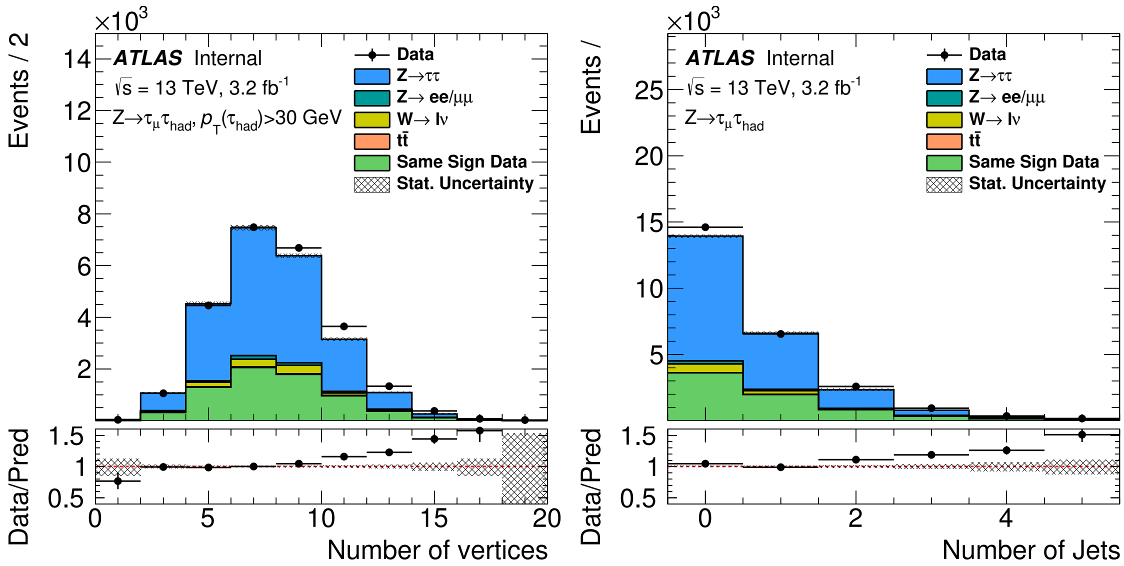

(a)

(b)

Figure 52: Distributions of the number of verticices and jets in the signal region with a *medium* offline identification requirement on the hadronically decaying τ candidate, and with 1 or 3 tracks inclusively.

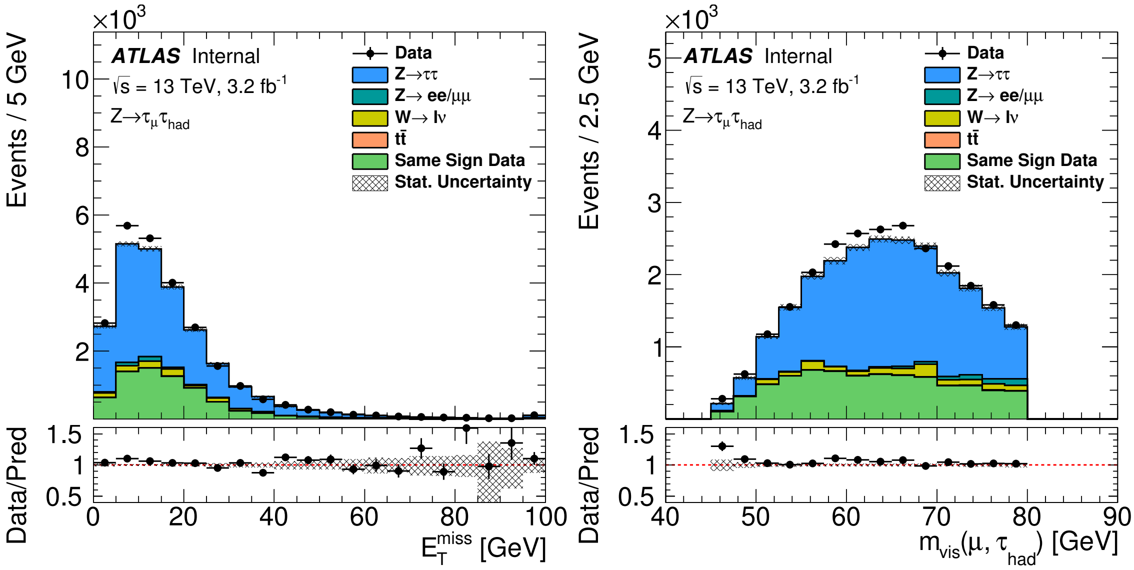

(a) (b)

Figure 53: Distributions of $E_{\mathrm{T}}^{\mathrm{miss}}$ and invariant mass between tau and muon candidate in the signal region with a *medium* offline identification requirement on the hadronically decaying τ candidate, and with 1 or 3 tracks inclusively.

25 GeV in barrel (τ $|\eta| < 1.37$) and endcap (τ $|\eta| > 1.52$) region are shown in Figure 54 and Figure 55, respectively.

B.5.3. Efficiencies and Scale factors

The efficiencies for signal and data-background, as well as the corresponding scale factors for the τ trigger with a p_{T} threshold of 25 GeV are shown in Figure 56, Figure 57, and Figure 58 for a *loose*, *medium*, and *tight* offline identification requirement on the hadronically decaying τ candidate, respectively.

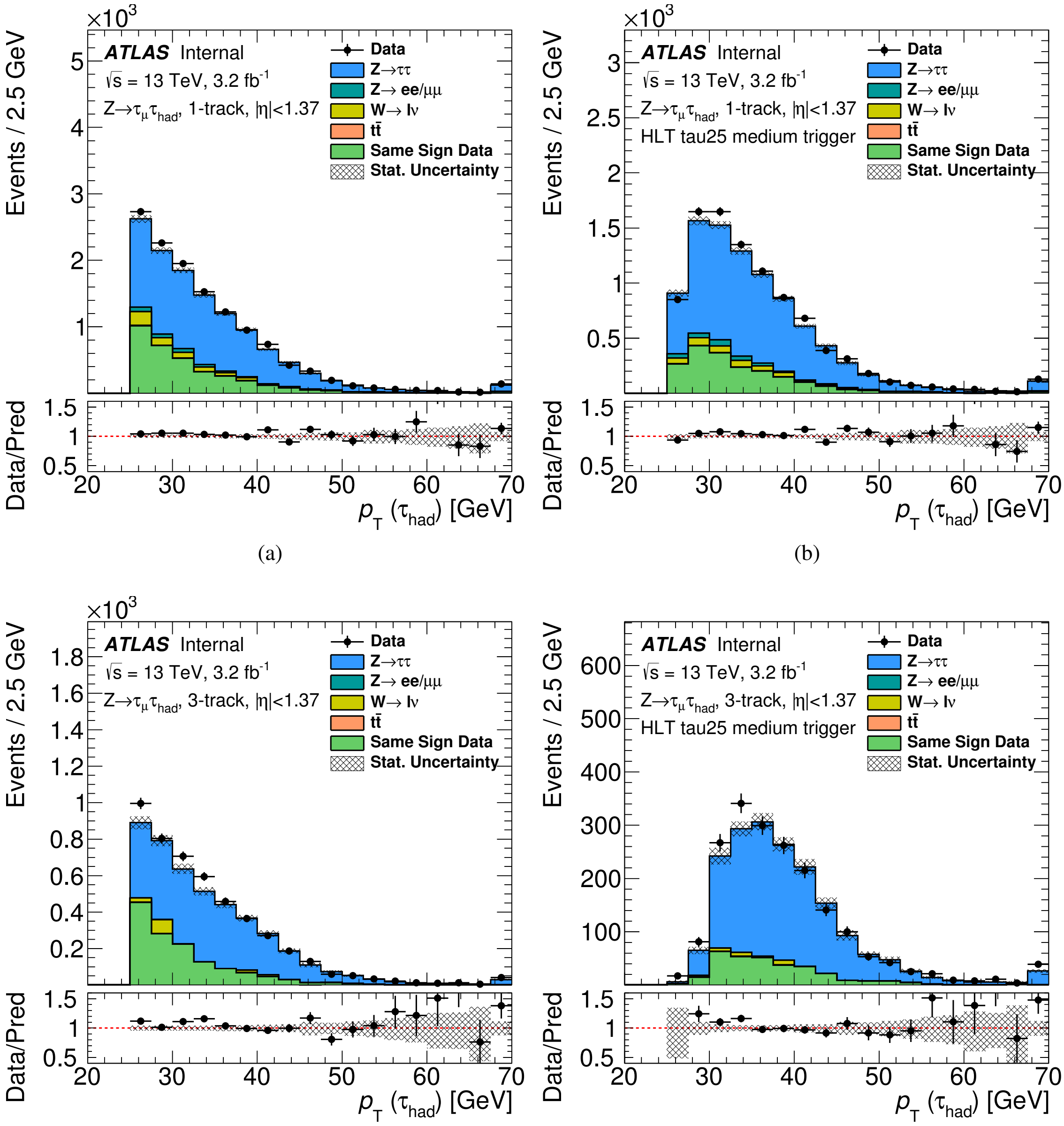

Figure 54: Distributions of τ p_{T} in the signal region with a *medium* offline identification requirement on the hadronically decaying τ candidate in barrel region (τ $|\eta| < 1.37$). The distributions on the top and bottom rows are for 1-track and 3-track τ candidates, while the left and right columns are with and without applying the τ trigger with a p_{T} threshold of 25 GeV, respectively. (Currently they are not separated w.r.t its η and prong. These will be updated.)

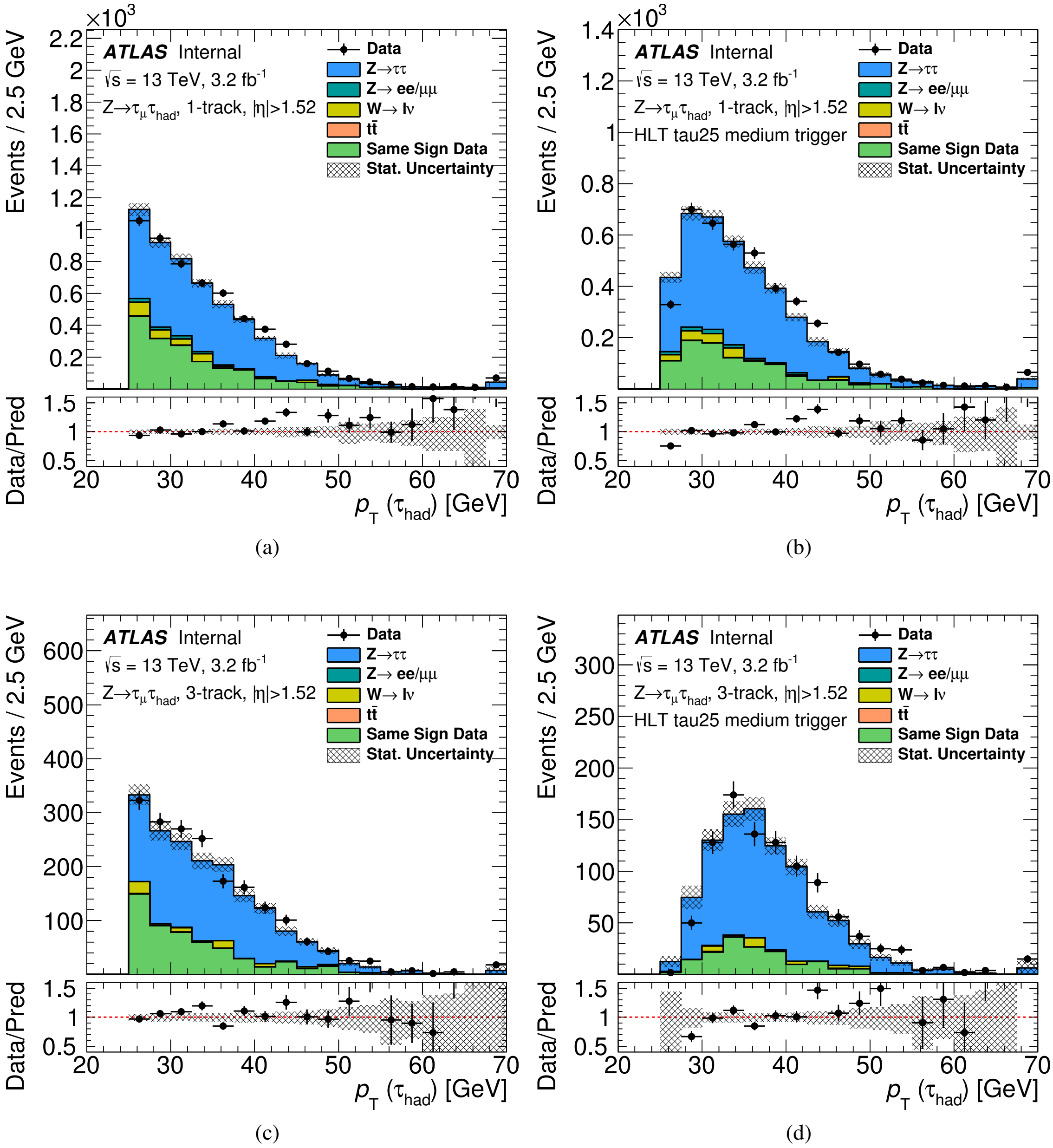

Figure 55: Distributions of τ p_{T} in the signal region with a *medium* offline identification requirement on the hadronically decaying τ candidate in endcap region (τ $|\eta| > 1.52$). The distributions on the top and bottom rows are for 1-track and 3-track τ candidates, while the left and right columns are with and without applying the τ trigger with a p_{T} threshold of 25 GeV, respectively. (Currently they are not separated w.r.t its η and prong. These will be updated.)

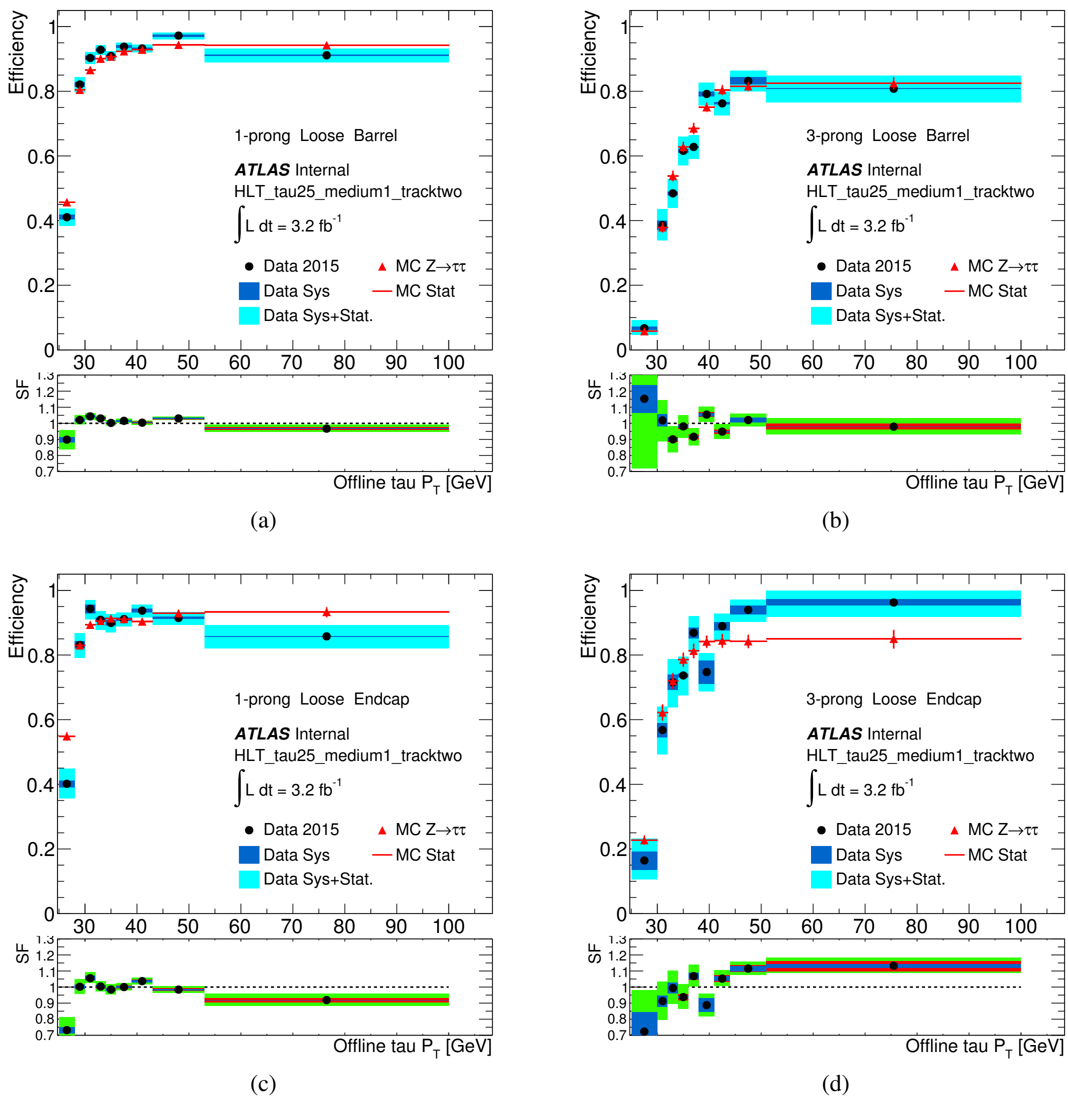

Figure 56: Efficiencies for signal and data-background and corresponding scale factors for the τ trigger with $p_{\mathrm{T}} > 25$ GeV, and for hadronically decaying τ candidates with a *loose* offline identification requirement.

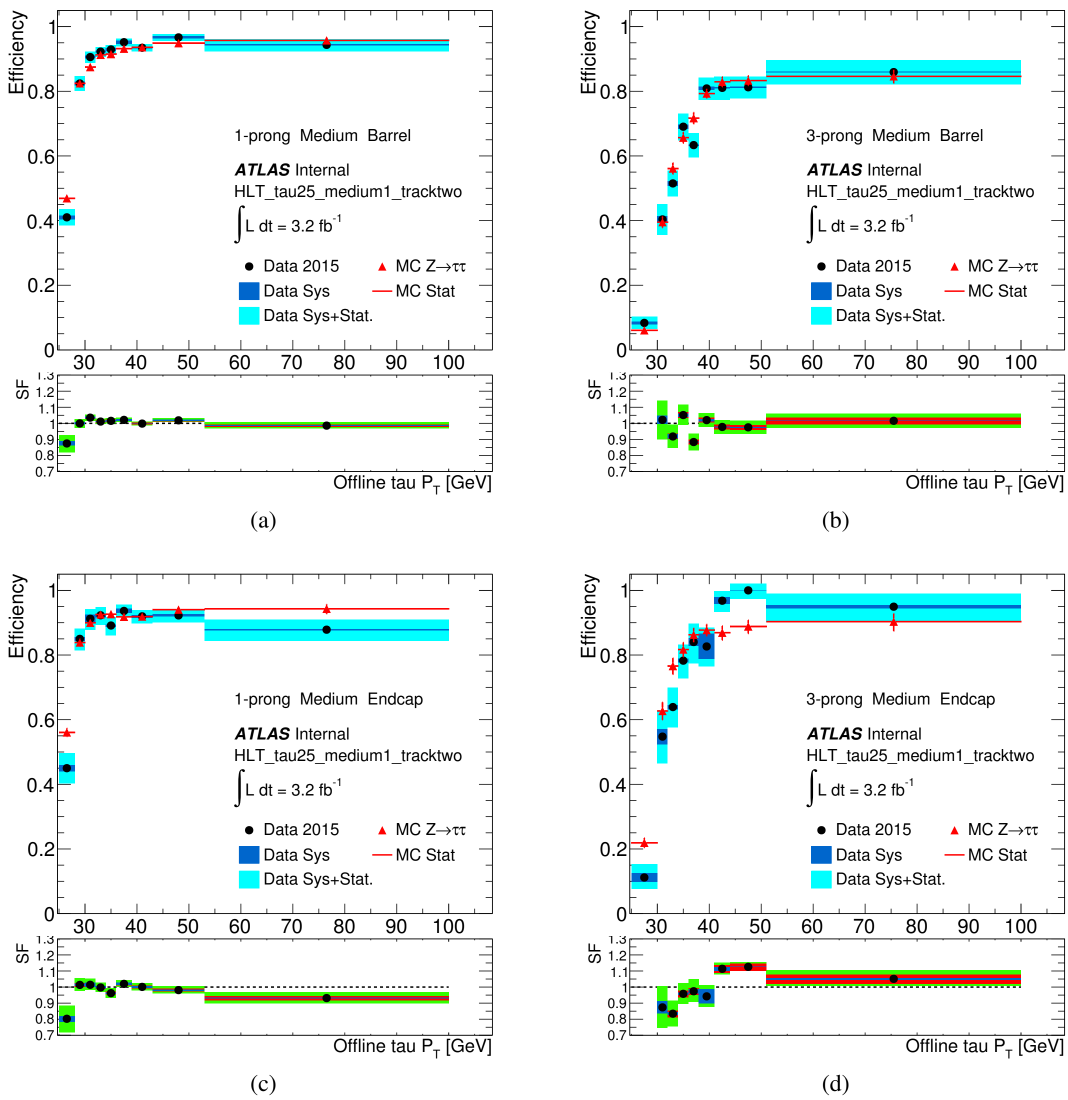

Figure 57: Efficiencies for signal and data-background and corresponding scale factors for the τ trigger with $p_T > 25$ GeV, and for hadronically decaying τ candidates with a *medium* offline identification requirement.

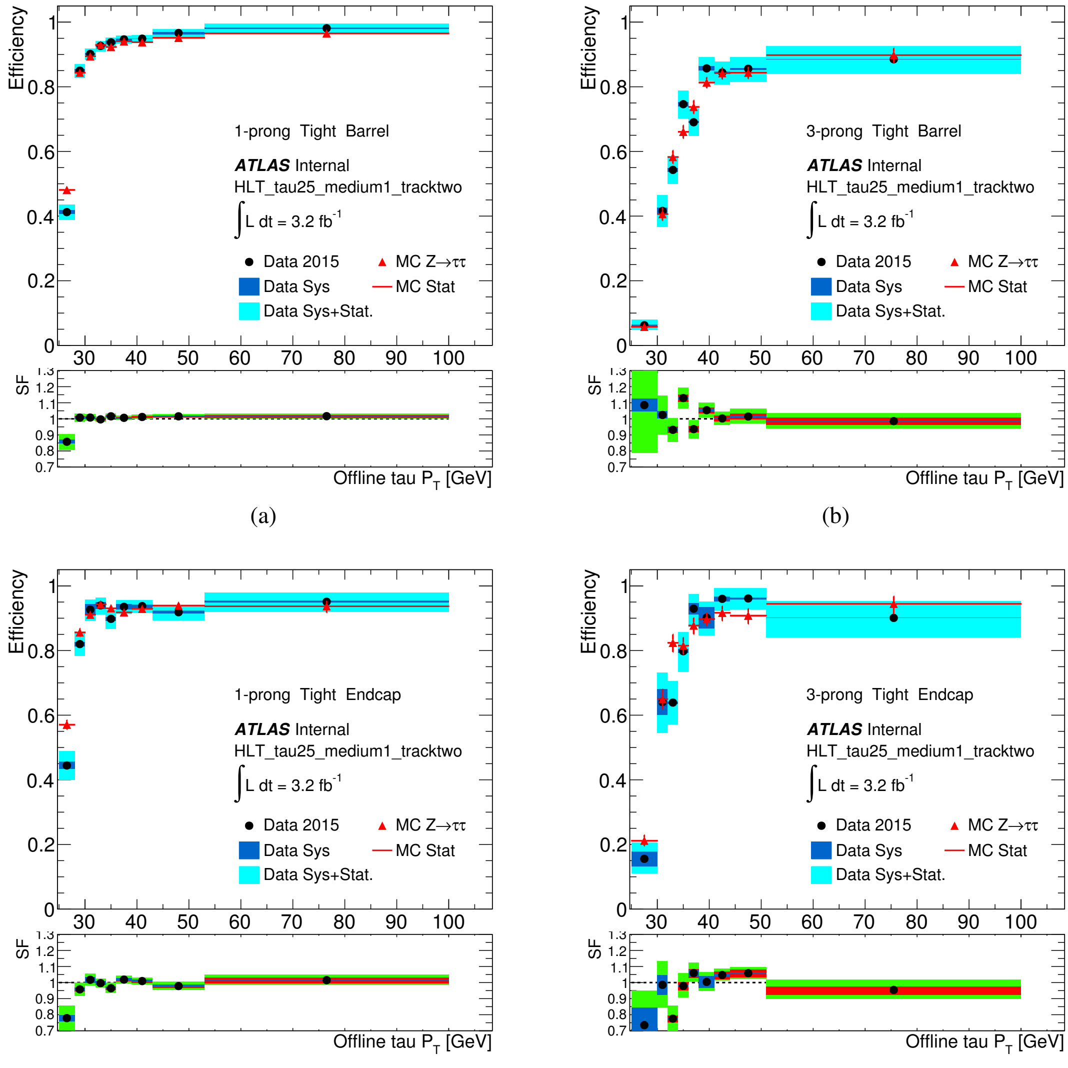

(a) (b) (c) (d)

Figure 58: Efficiencies for signal and data-background and corresponding scale factors for the τ trigger with $p_{\mathrm{T}} > 25$ GeV, and for hadronically decaying τ candidates with a *tight* offline identification requirement.

C. Electron misidentification probability measurement

Section in progress. Plots ready, text being written.

C.1. Eveto tuning

The likelihood (Llh) electron veto (eveto) algorithm operates by placing p_T- and η-dependent cuts on the likelihood score used to identify prompt electron candidates matched to the reconstructed tau candidates within $\Delta R < 0.2$. Since the optimization of the Llh eveto available at the start of 2015 data taking was orginially performed on early Run 2 validation samples from before data taking was even started, it was necessary to re-optimize the cut values used in the Llh veto algorithm on a Monte Carlo sample tuned to 2015 data-taking and pile-up conditions. The sample used for this purpose was:

```
mc15_13TeV.361108.PowhegPythia8EvtGen_AZNLOCTEQ6L1_Ztautau.merge.DAOD_TAUP1.e3601_s2726_r73
```

This sample is the same used for performing the eveto tag-and-probe efficiency scale factor measurement. Since this sample was processed with the `TAUP1` derivation setup, the following set of cuts was applied:

- The same set of triggers as used in the tag-and-probe analysis are applied.
- At least one electron with $p_T > 26$ GeV, $|\eta| < 2.6$ and passing the loose cut-based or likelihood identification is present in each event.
- No muons with $p_T > 10$ GeV, $|\eta| < 2.0$ and passing normal muon quality criteria are present in the events.
- At least one tau candidate with $p_T > 12$ GeV, $|\eta| < 2.6$ and absolute reconstruction charged equal to one is present in each event.

On top of this, the tau candidates where required to have one reconstructed track, $p_T > 20$ GeV and to be truth matched to real hadronic tau decays. The reoptimization of the eveto cut values used the new electron Llh tune performed by the egamma group in June 2015 which used MC15b samples and was validated against data for the normal electron identification working points. The tuning of the cuts was performed in bins of η and p_T, with the following bin edges in p_T:

```
{20, 25, 35, 45, 55, 75, 255}
```

and in η

```
{0.0, 0.6, 0.8, 1.15, 1.37, 1.52, 1.81, 2.01, 2.47}
```

to give 95% efficiency for the truth-matched tau candidates described above. The actual cut values are illustrated in Figure ??. The achieved background rejection was approximately a factor two better than the previous cut tune at same efficiency. Also the inclusion of the new tune of the electron likelihood, which was validated against data, reduced strongly the mismodelling between data and simulation. The residual mismodeling, which is expected due to the cut tune on the likelihood score being much looser than any working point used by the egamma group, is absorbed in the scale factors reported below.

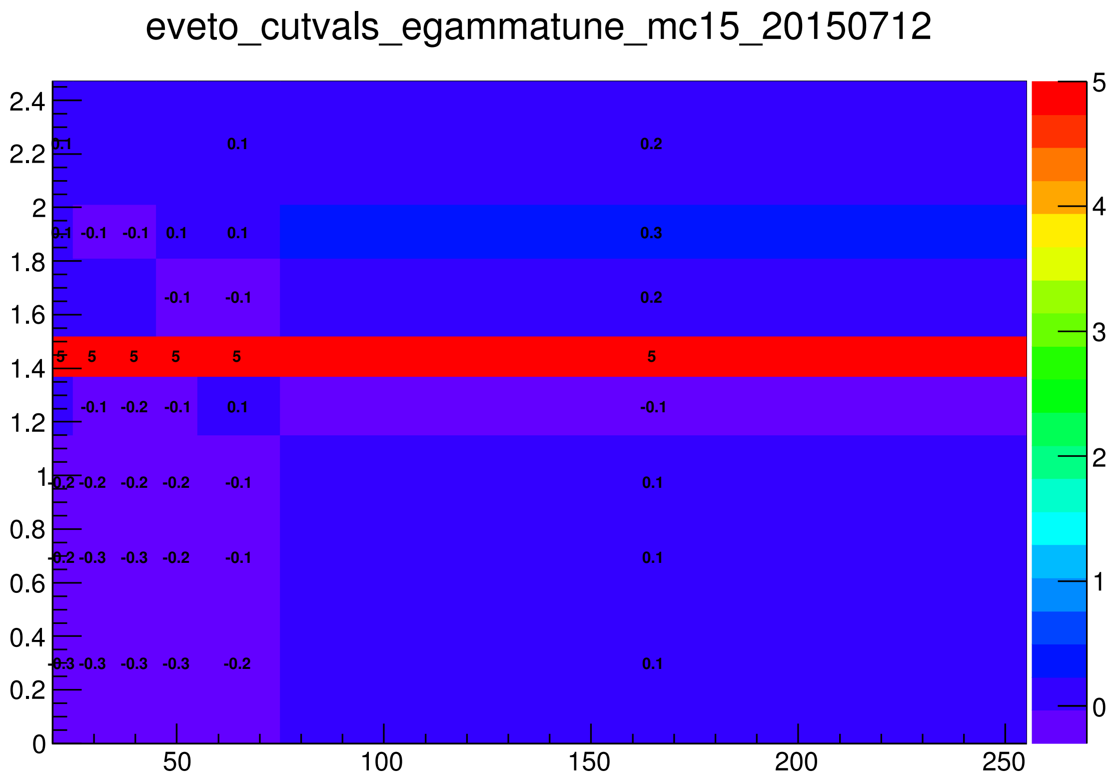

Figure 59: Re-optimized cut values for electron likehihood veto in the actual p_T- and η binning used for the eveto algorithm.

C.2. Event selection

- single electron triggers
- trigger logic:
- if offline $p_T(e) < 65GeV$:
- 24 GeV trigger on medium LH electrons
- if offline $65GeV < p_T(e) < 135GeV$:
- 60 GeV trigger on medium LH electrons
- if offline $p_T(e) > 135GeV$:
- 120 GeV trigger on medium LH electrons
- at least one τ and one e
- no μ, no b-jets
- exactly one primary vertex

- electron requirements:
- $p_T(e) > 25GeV$
- tight quality
- $|q(e)| = 1$
- gradient isolation
- $0 < |\eta(e)| < 2.47$, excluding crack region $\eta > 1.37$ and $\eta < 1.52$
- association of electron track to primary vertex
- tau requirements:
- 1-prong τ only
- $p_T(\tau) > 20GeV$
- $|q(\tau)| = 1$
- $0 < |\eta(\tau)| < 2.47$, excluding crack region $\eta > 1.37$ and $\eta < 1.52$
- medium JetBDT as indicated
- truth match within $\Delta R < 0.2$ to electron

C.3. QCD Control Region

- require anti isolation for electron:
- $E_T^{cone20}/p_T > 12\%$
- $p_T^{cone40}/p_T > 8\%$

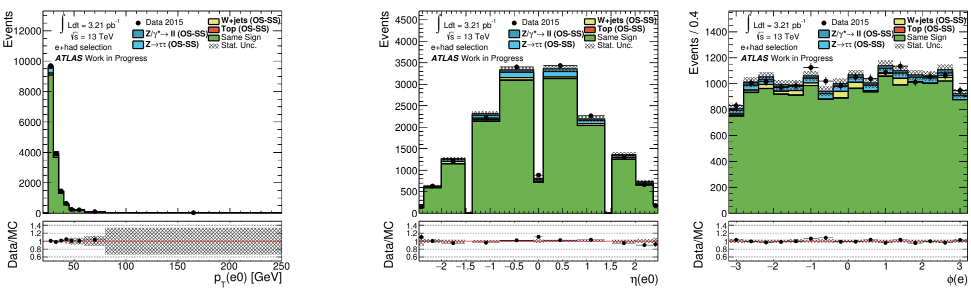

(a) (b) (c)

Figure 60

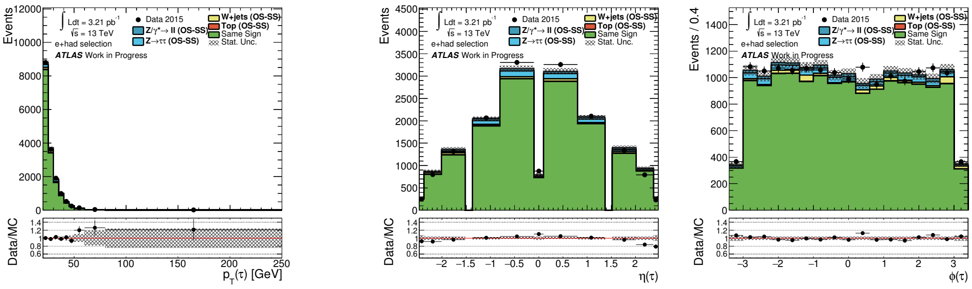

(a) (b) (c)

Figure 61

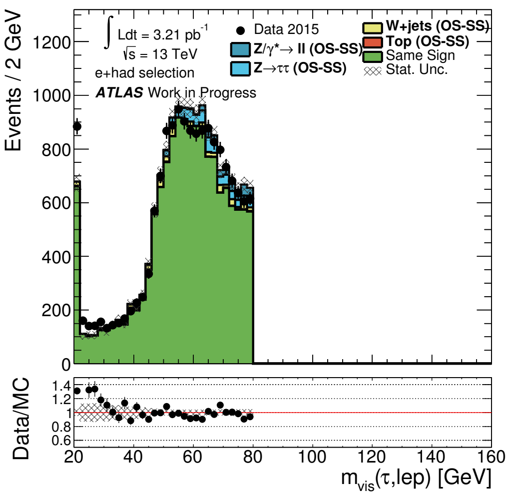

(a) SF p_t

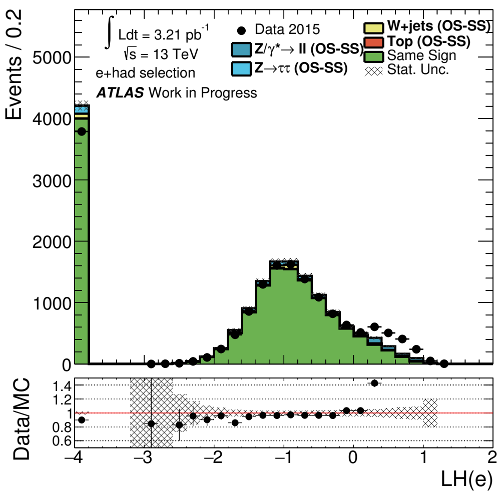

(b) SF η

C.4. W Control Region

- exactly one electron
- $/E_T > 30GeV$
- $m_T(e, /E_T) > 70GeV$
- $m_{vis}(\tau, e) < 80GeV$

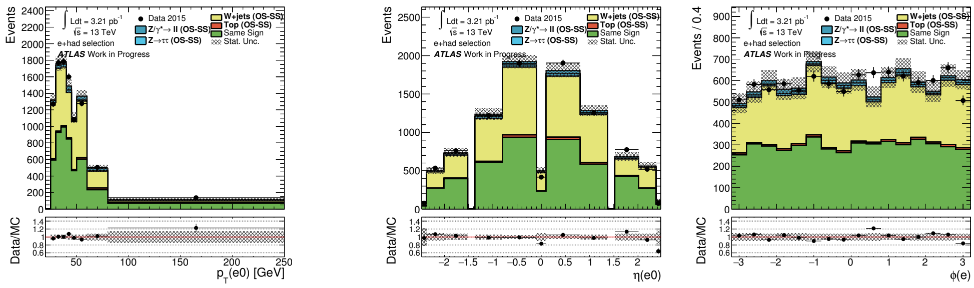

(a) (b) (c)

Figure 62

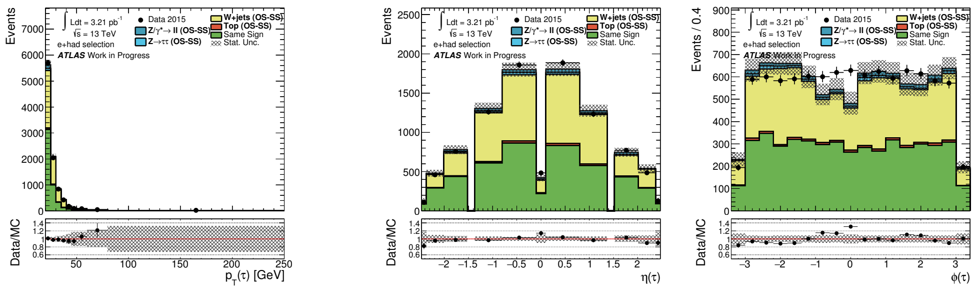

(a) (b) (c)

Figure 63

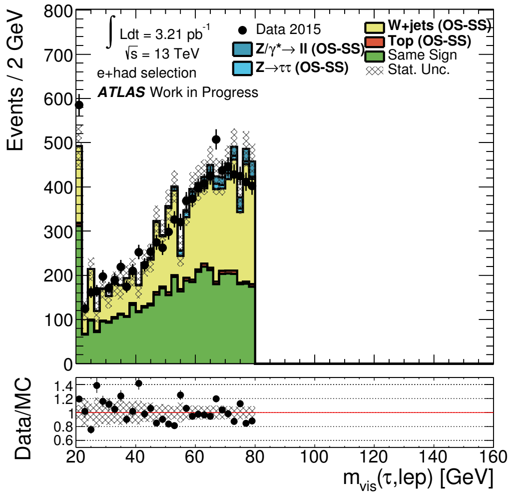

(a) SF p_t

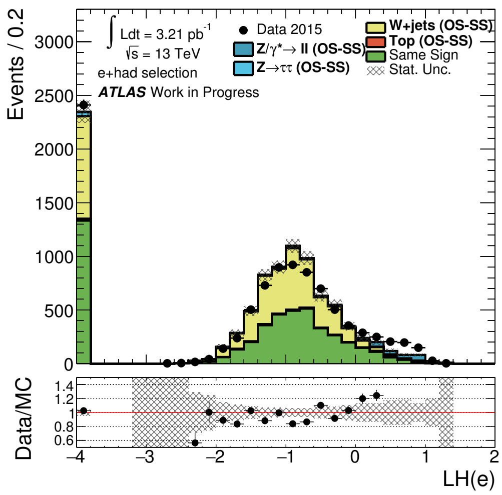

(b) SF η

C.5. Kinematics of fake taus

- $p_T(e) > 30GeV$
- $m_T(e, /E_T) < 40GeV$
- $80GeV < m_{vis}(\tau, e) < 100GeV$

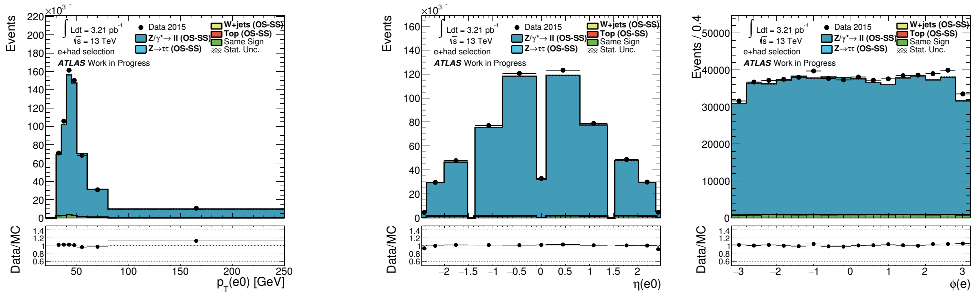

(a) (b) (c)

Figure 64

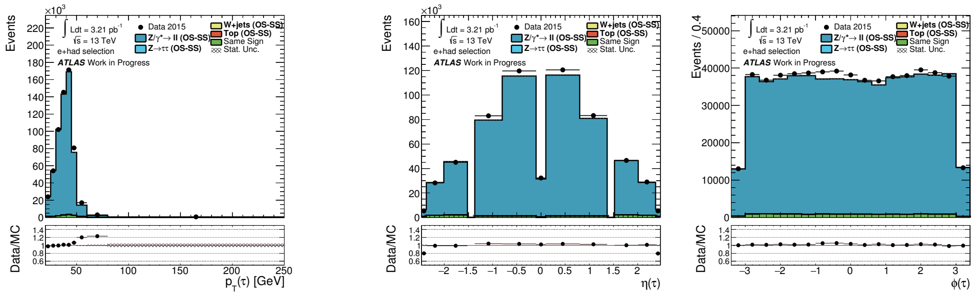

(a) (b) (c)

Figure 65

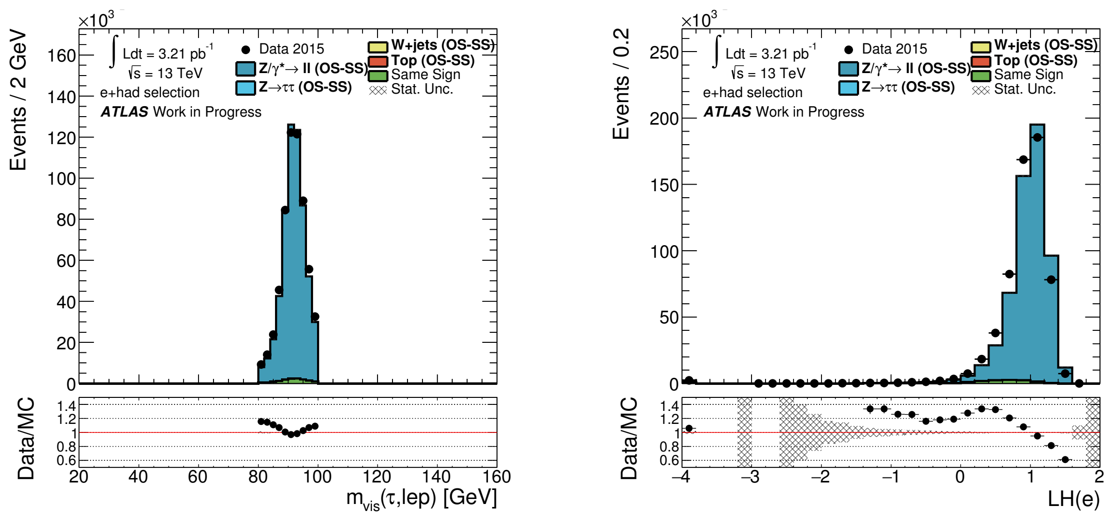

(a) SF p_t (b) SF η

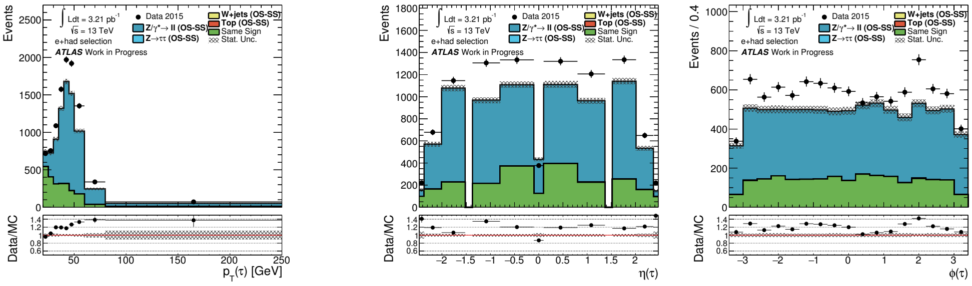

(a) (b) (c)

Figure 66

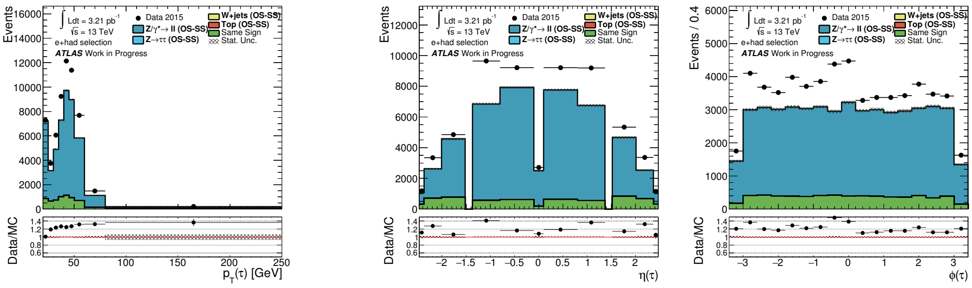

(a) (b) (c)

Figure 67

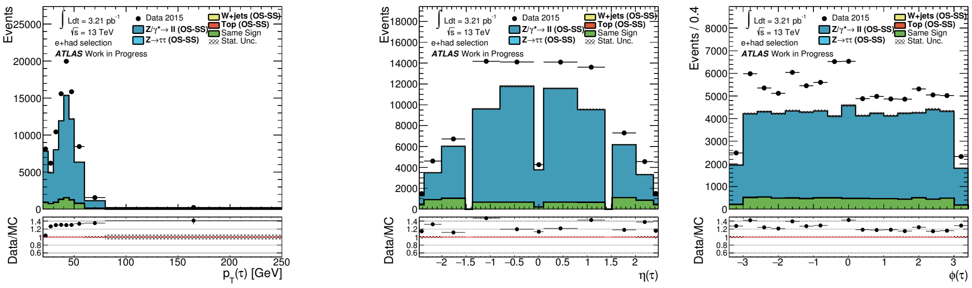

(a) (b) (c)

Figure 68

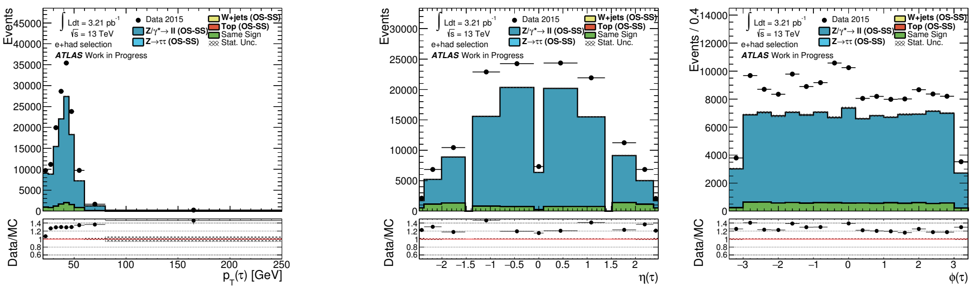

(a) (b) (c)

Figure 69

C.6. Efficiency Measurement and Scalefactors

- idea of fake rejection method: reject any τ candidate which overlaps within $\Delta R < 0.2$ with an electron
- different electron quality working points give different rejection
- use 3 standard working points loose LH, medium LH, tight LH and perform standard OLR: if and overlap is found, reject tau candidate (independent pt, eta)
- fourth working point - the electron veto - corresponds to OLR with very loose electrons
- OLR removal performed dependent on tau pt,eta and electron LH score
- cuts tuned to yield 95% signal efficiency

$$\varepsilon = \frac{\mathrm{N}^{\mathrm{reco}}(\tau) \parallel \text{Veto truthmatched MediumJetBDT}}{\mathrm{N}^{\mathrm{reco}}(\tau) \parallel \text{truthmatched NoJetBDT}}$$

Rejection of very loose electrons

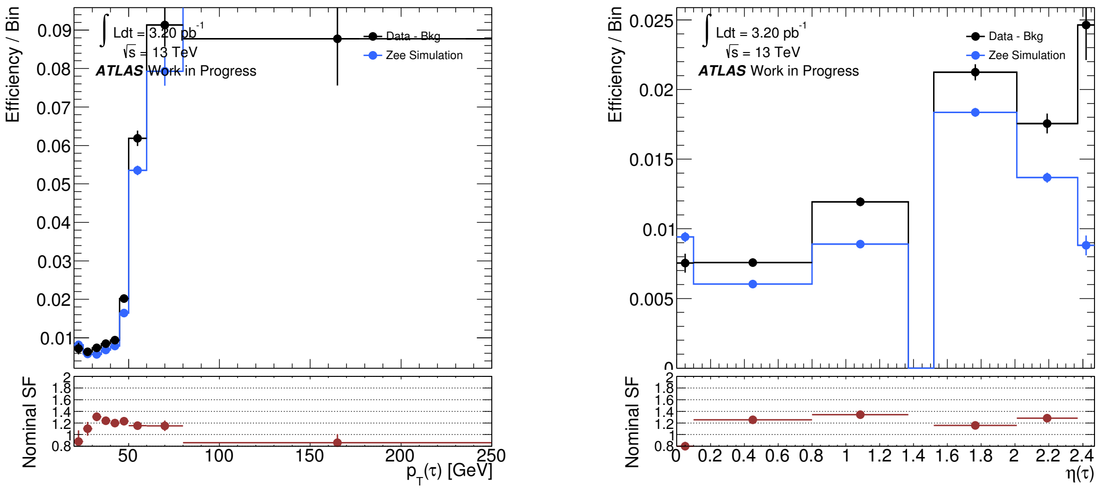

(a) SF p_t

(b) SF η

Corrections for rejection of very loose electrons

Combined:

bin-center	SF	stat	sym sys	stat [%]	sym sys [%]
0.05	0.800	0.079	0.034	9.844	4.298
0.45	1.255	0.045	0.041	3.623	3.294
1.08	1.342	0.043	0.021	3.188	1.563
1.45	1.000	0.000	0.000	0.000	0.000
1.76	1.157	0.037	0.014	3.226	1.242
2.19	1.284	0.062	0.024	4.847	1.870
2.42	2.796	0.365	0.141	13.071	5.057

Combined:

bin-center	SF	stat	sym sys	stat [%]	sym sys [%]
0.05	1.070	0.026	0.013	2.455	1.215
0.45	1.149	0.011	0.009	0.957	0.810
1.08	1.373	0.013	0.010	0.958	0.743
1.45	1.000	0.000	0.000	0.000	0.000
1.76	1.130	0.016	0.015	1.456	1.359
2.19	1.407	0.028	0.031	2.024	2.177
2.42	1.406	0.048	0.020	3.392	1.410

C.6.1. Rejection of loose electrons

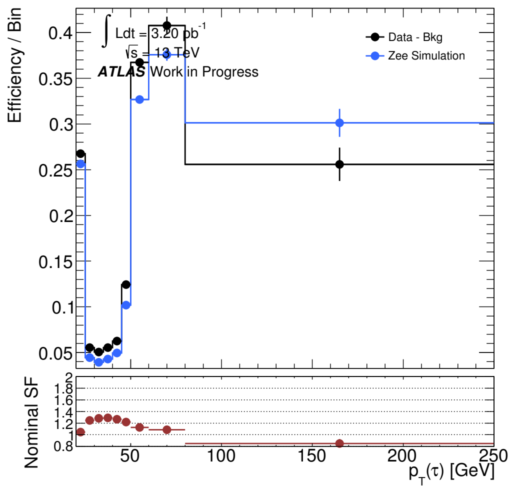

(a) SF p_t

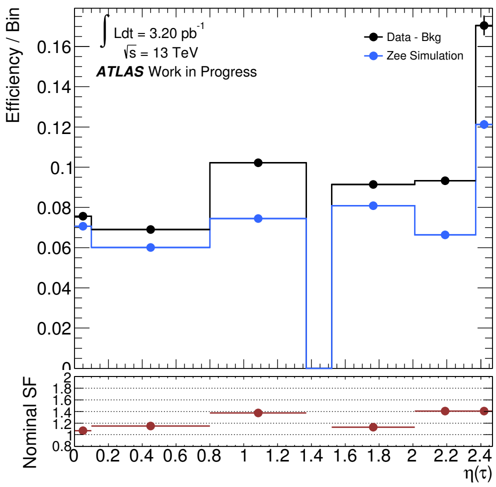

(b) SF η

Corrections for rejection of loose electrons

Combined:

bin-center	SF	stat	sym sys	stat [%]	sym sys [%]
0.05	1.119	0.021	0.010	1.866	0.924
0.45	1.178	0.009	0.007	0.741	0.573
1.08	1.434	0.011	0.010	0.763	0.668
1.45	1.000	0.000	0.000	0.000	0.000
1.76	1.186	0.014	0.016	1.218	1.334
2.19	1.468	0.025	0.030	1.686	2.074
2.42	1.531	0.046	0.024	3.009	1.569

C.6.2. Rejection of medium electrons

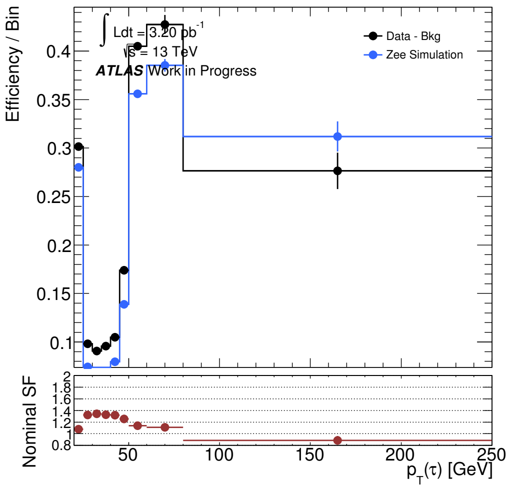

(a) SF p_t

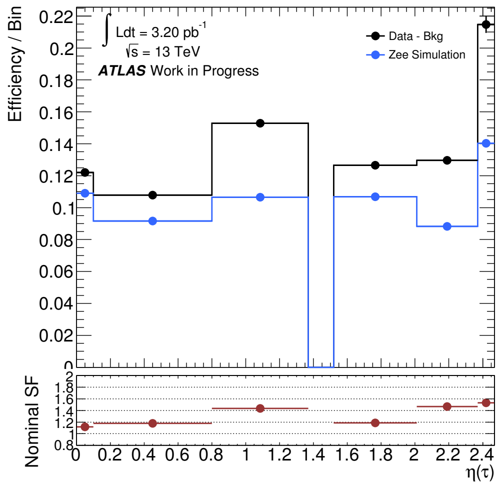

(b) SF η

Corrections for rejection of medium electrons

Combined:

bin-center	SF	stat	sym sys	stat [%]	sym sys [%]
0.05	1.134	0.015	0.006	1.327	0.553
0.45	1.166	0.006	0.005	0.527	0.414
1.08	1.415	0.008	0.007	0.558	0.478
1.45	1.000	0.000	0.000	0.000	0.000
1.76	1.246	0.011	0.013	0.910	1.069
2.19	1.429	0.018	0.023	1.253	1.596
2.42	1.645	0.038	0.025	2.309	1.513

C.6.3. Rejection of tight electrons

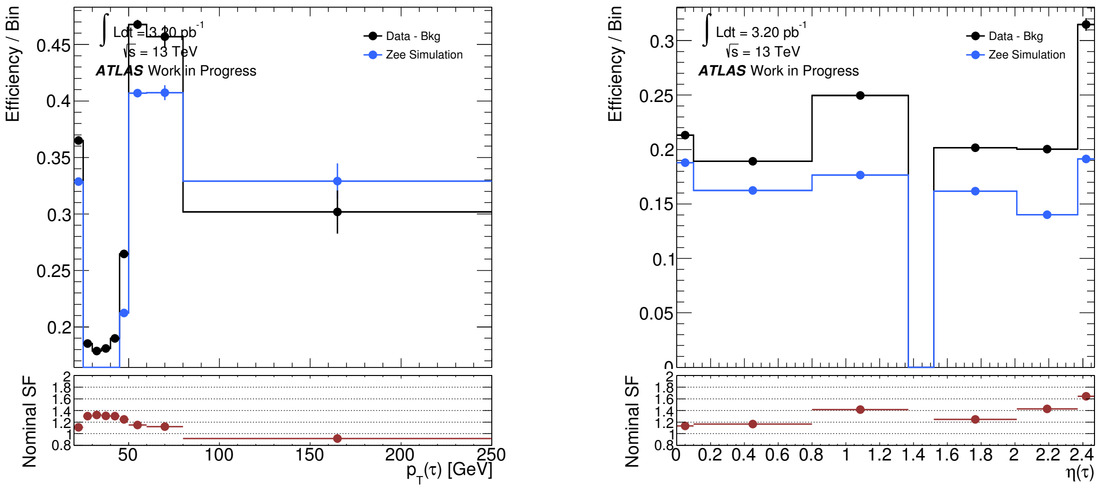

(a) SF p_t

(b) SF η

Corrections for rejection of tight electrons

D. In-situ tau energy scale calibration

D.1. Introduction of the in-situ method

The TES in-situ, embodied by the parameter α, is determined by comparing the visible mass distribution of $Z \to \tau\tau \to \mu\tau_{\rm had}$ in the data and that obtained from a Monte Carlo sample. The visible mass is calculated by the reconstructed momentum of the muon and the hadronic tau. As the muon momentum scale can be determined to a high precision, the visible mass thus depends upon $p_{\rm T}^{\tau_{\rm had}}$. The parameter α is defined in Eq. 4.

$$p_{\rm T}^{\tau_{\rm had}}(\alpha) = (1+\alpha)p_{\rm T}^{\tau_{\rm had}}({\rm MC})\,, \tag{4}$$

where $p_{\rm T}^{\tau_{\rm had}}({\rm MC})$ is the transverse momentum of the hadronical tau lepton in the MC simulation. The α is determined by the best fit of the MC to the data. It is to minimize the following $\chi^2(\alpha, f)$.

$$\chi^2(\alpha, f) = \sum_i \frac{(N_i^{\rm data} - fN_i^{\rm sig}(\alpha) - N_i^{\rm bkg})^2}{(\sqrt{N_i^{\rm data}})^2 + f^2(\Delta N_i^{\rm sig}(\alpha))^2 + (\Delta N_i^{\rm bkg})^2}\,. \tag{5}$$

Here $N_i^{\rm data/sig/bkg}$ is the number of events in the i-th bin of the visible mass distribution in the data/signal/background; $\Delta N_i^{\rm sig/bkg}$ is the corresponding uncertainty of the number of events; $N_i^{\rm bkg}$ ($\Delta N_i^{\rm bkg}$) is understood as the sum of the contributions from all backgrounds; the parameter f is introduced to consider the possible normalization uncertainty. The signal yield in each bin depends upon the TES in-situ α.

D.2. Background estimation

The main backgrounds are the multi-jet and W+jets backgrounds. In the former background, the muon and tau candidates are faked by the jets. It is estimated by the data in which the muon and tau candidates have the same charge sign (same-sign data for simplicity). For the latter background, the M_{vis} shape is determined by the MC simulatin while the normalization is determined by the data in a control region where the W+jets events are dominant.

We introduce the following notation system. A bra $\langle X|$ denotes the sample "X". A ket $|{\rm CR}\rangle$ denotes the control region or/and selection conditions "CR". The product $\langle X|{\rm CR}\rangle$ represents some quantity, such as the yield N or dN/dm_{vis}, of the sample X in the control region or/and satisfying the selection conditions "CR". The following operations are also defined.

$$\langle s|c_1\rangle|c_2\rangle \equiv \langle s|c_1, c_2\rangle \tag{6}$$

$$(\langle s_1| + \langle s_2|)|c\rangle \equiv \langle s_1|c\rangle + \langle s_2|c\rangle \tag{7}$$

The selected events in the signal region can be decomposed in the way shown in Eq. 8.

$$\begin{aligned}\langle {\rm data}|{\rm SR, OS}\rangle = \quad & R_{\rm QCD}\langle {\rm MJ}|{\rm SR, SS}\rangle + \langle Z\tau\tau|{\rm SR, OS}\rangle + \langle Zll + {\rm jets}|{\rm SR, OS}\rangle \\ & + k_W^{\rm OS}\langle W + {\rm jets}|{\rm SR, OS}\rangle + \langle {\rm top}|{\rm SR, OS}\rangle \end{aligned} \tag{8}$$

$$\begin{aligned}\langle {\rm MJ}|{\rm SR, SS}\rangle = \quad & \langle {\rm data}|{\rm SR, SS}\rangle - \langle Z\tau\tau|{\rm SR, SS}\rangle - \langle Zll + {\rm jets}|{\rm SR, SS}\rangle \\ & - k_W^{\rm SS}\langle W + {\rm jets}|{\rm SR, SS}\rangle - \langle {\rm top}|{\rm SR, SS}\rangle \end{aligned} \tag{9}$$

Here $|SR\rangle$ denotes the signal region; $|\mathrm{SS}\rangle$ ($|\mathrm{OS}\rangle$) denotes the requirement that the muon and tau candidates have the same (opposite) charge sign; $\langle Z\tau\tau|$, $\langle Zll+\mathrm{jets}|$, $\langle W+\mathrm{jets}|$ and $\langle \mathrm{top}|$ denotes the signal, $Zll+$jets, $W+$jets and top background, respectively.

In the right hand side of Eq. 8, the first term ($\langle \mathrm{MJ}|$)represents the multi-jet background which is estimated by the same-sign data subtracting all other components, indicated by Eq. 9. The normalization difference between the requirement $|\mathrm{OS}\rangle$ and $|\mathrm{SS}\rangle$ is considered by the factor R_{QCD}. R_{QCD} can be estimated in the control region where the multi-jet faking events are dominant ($|\mathrm{MJCR}\rangle$). It is calculated according to Eq. 10. The rest terms denotes the signal and the other backgrounds.

$$R_{\mathrm{QCD}} = \frac{(\langle \mathrm{data}| - \langle Z\tau\tau| - \langle Zll+\mathrm{jets}| - \langle W+\mathrm{jets}| - \langle \mathrm{top}|)|\mathrm{MJCR,OS}\rangle}{(\langle \mathrm{data}| - \langle Z\tau\tau| - \langle Zll+\mathrm{jets}| - \langle W+\mathrm{jets}| - \langle \mathrm{top}|)|\mathrm{MJCR,SS}\rangle} \quad (10)$$

For the $W+$jets background, the shape of the M_{vis} distribution is estimated by the MC simulation while the yield is estimated by the data in a control region where the $W+$jets background is dominant ($|\mathrm{WCR}\rangle$). Because the same-sign and opposite-sign events have obviously asymmetric behaviours, the normalization factors, k_W^{OS} and k_W^{SS}, are estimated individually, as indicated by Eq. 11.

$$\begin{aligned} k_W^{\mathrm{OS}} &= \frac{(\langle \mathrm{data}| - \langle Z\tau\tau| - \langle Zll+\mathrm{jets}| - \langle \mathrm{top}|)|\mathrm{WCR,OS}\rangle}{\langle W+\mathrm{jets}|\mathrm{WCR,OS}\rangle} \\ k_W^{\mathrm{SS}} &= \frac{(\langle \mathrm{data}| - \langle Z\tau\tau| - \langle Zll+\mathrm{jets}| - \langle \mathrm{top}|)|\mathrm{WCR,SS}\rangle}{\langle W+\mathrm{jets}|\mathrm{WCR,SS}\rangle} \end{aligned} \quad (11)$$

The selection conditions for the signal and control regions are elaborated in next section.

D.3. Event selection

To present the selection criteria, we introduce the following denotations for convenience. They are also summarized in Table 12.

1. $|\mathrm{Trigger}\rangle$ denotes the trigger condition "HLT_mu20_iloose_L1MU15" and the trigger object matching condition "muTrigMatch_0_HLT_mu20_iloose_L1MU15".

2. $|\mathrm{Base}\rangle$ denotes the basic selection conditions. One muon candidate (N_μ), at lease one tau candidate ($N_{\tau_{\mathrm{had}}} \geq 1$), no electron candidate ($N_e = 0$), no b-jet candidate ($N_{b-\mathrm{jet}} = 0$), at least one primary vertex ($N_{\mathrm{pvx}} \geq 1$), and the trigger conditions.

3. $|\mathrm{Tau}\rangle$ defines a tau candidate. $p_{\mathrm{T}} > 20$ GeV, $|\eta| < 1.37$ and $1.52 < |\eta| < 2.47$, a unit charge ($|Q| = 1$), and one or three charged tracks ($N_{\mathrm{trk}} = 1, 3$). It is required to pass the medium identification criteria.

4. $|\mathrm{Mu}\rangle$ defines a muon candidate. It is required to have $p_{\mathrm{T}} > 22$ GeV and to pass the medium identification criteria.

5. $|\mathrm{iso}\rangle$ defines the isolation conditions for the muon candidate, which suppress the multi-jet background. etcone20/$p_{\mathrm{T}} < 0.04$ and ptcone40/$p_{\mathrm{T}} < 0.01$. $|\overline{\mathrm{iso}}\rangle$ defines the opposite of the isolation conditions.

6. $|\mathrm{SS}\rangle$ ($|\mathrm{OS}\rangle$) denotes that the muon candidate and the tau candidate have the same (opposite) charge sign.

Table 12: Definition of various selection conditions

Denotation	Definition
$\|\text{Trigger}\rangle$	HLT_mu20_iloose_L1MU15, muTrigMatch_0_HLT_mu20_iloose_L1MU15
$\|\text{Base}\rangle$	$N_\mu = 1$, $N_{\tau_{\text{had}}} \geq 1$, $N_e = 0$, $N_{b\text{-jet}} = 0$, $N_{\text{pvx}} \geq 1$, $\|\text{Trigger}\rangle$
$\|\text{Tau}\rangle$	$p_{\text{T}} > 20$ GeV, $\|\eta\| < 1.37$ and $1.52 < \|\eta\| < 2.47$, $\|Q\| = 1$, $N_{\text{trk}} = 1, 3$, medium identification criteria
$\|\text{Muon}\rangle$	$p_{\text{T}} > 22$ GeV, medium identificaiton criteria
$\|\text{iso}\rangle$	etcone20/$p_{\text{T}} < 0.04$ and ptcone40/$p_{\text{T}} < 0.01$ for the muon candidate
$\|\overline{\text{iso}}\rangle$	etcone20/$p_{\text{T}} > 0.04$ or ptcone40/$p_{\text{T}} > 0.01$ for the muon candidate
$\|\text{Low } m_{\text{T}}\rangle$	$m_{\text{T}} < 50$ GeV
$\|\text{High } m_{\text{T}}\rangle$	$m_{\text{T}} > 60$ GeV
$\|D\phi\rangle$	$D\phi > -0.5$
$\|E_{\text{T}}^{\text{miss}}\rangle$	$E_{\text{T}}^{\text{miss}} > 30$ GeV
$\|\text{SS}\rangle$	$Q_\mu Q_{\tau_{\text{had}}} = +1$
$\|\text{OS}\rangle$	$Q_\mu Q_{\tau_{\text{had}}} = -1$

We now give the conditions for the signal selection and the various control regions.

- For the signal region $|\text{SR}\rangle$, we require at least one tau candidate satisfying the condition $|\text{Tau}\rangle$ and one isolated muon candidate satisfying the condition $|\text{Muon}\rangle$. The W + jets background is reduced by the two conditions below, denoted by $|\text{Low } m_{\text{T}}\rangle$ and $|D\phi\rangle$ respectively.

$$m_{\text{T}} \equiv \sqrt{2 p_{\text{T}}(\mu) E_{\text{T}}^{\text{miss}} (1 - \cos(\phi(\mu) - \phi(E_{\text{T}}^{\text{miss}})))} < 50 \text{ GeV}\,, \tag{12}$$

  and

$$D\phi \equiv \cos(\phi(\tau_{\text{had}}) - \phi(E_{\text{T}}^{\text{miss}})) + \cos(\phi(\mu) - \phi(E_{\text{T}}^{\text{miss}})) > -0.5\,. \tag{13}$$

  For the W + jets backgorund, the transverse mass m_{T} is large due to the decay $W \to \mu\nu_\mu$ and the large mass of the W boson; in the decays $W \to \mu\nu_\nu/\tau\nu_\tau$, the azimuthal angle difference between the visible μ/τ_{had} and the missing transverse energy tends to be close to π and $D\phi$ has a large negative value if the W boson is produced nearly still.

- The definition of the multi-jet control region $|\text{MJCR}\rangle$ is the same as the signal region except that the muon candiate is required to be not isolated (just reverse the isolation condition in $|\text{SR}\rangle$).

- The control region for the W+jets background is defined to have large transverse mass, $m_{\text{T}} > 60$ GeV (denoted by $|\text{High } m_{\text{T}}\rangle$), and large missing transverse energy, $E_{\text{T}}^{\text{miss}} > 30$ GeV (denoted by $|E_{\text{T}}^{\text{miss}}\rangle$).

The selection criteria above are summarized in Table 13.

Table 13: Selection criteria for the signal and control regions.

Denotation	Definition
Signal region, $\|\text{SR}\rangle$	$\|\text{Base}\rangle\|\text{Muon}\rangle\|\text{Tau}\rangle\|\text{iso}\rangle\|\text{Low } m_{\text{T}}\rangle\|D\phi\rangle$
Multi-jet control region, $\|\text{MJCR}\rangle$	$\|\text{Base}\rangle\|\text{Muon}\rangle\|\text{Tau}\rangle\|\overline{\text{iso}}\rangle\|\text{Low } m_{\text{T}}\rangle\|D\phi\rangle$
W backround control region, $\|\text{WCR}\rangle$	$\|\text{Base}\rangle\|\text{Muon}\rangle\|\text{Tau}\rangle\|\text{iso}\rangle\|\text{High } m_{\text{T}}\rangle\|E_{\text{T}}^{\text{miss}}\rangle$

D.4. TES estimation

The TES in-situ is estimated individually for the tau candidate with one and three charged tracks. In the first place, the factors R_{QCD}, k_W^{OS} and k_W^{SS} are determined and listed in Table 14. The TES in-situ is

Table 14: Summary of the factors and the TES in-situ for the τ_{had} with one or three charged tracks. The uncertainties are only statistical.

Factor	One-track τ_{had}	Three-track τ_{had}
R_{QCD}	1.20 ± 0.01	1.24 ± 0.01
k_W^{SS}	1.36 ± 0.02	1.35 ± 0.04
k_W^{OS}	1.17 ± 0.01	1.28 ± 0.03
f	1.06 ± 0.02	1.03 ± 0.03
α	$(-0.70 \pm 0.81)\%$	$(-3.60 \pm 1.16)\%$
α (Forward-η)	$(1.51 \pm 1.10)\%$	$(-2.80 \pm 1.86)\%$
α (Center-η)	$(-3.58 \pm 1.01)\%$	$(-2.63 \pm 2.04)\%$

determined by minimizing the $\chi^2(\alpha, f)$ defined in Eq. 5. Here are the procedures.

1. In practise, a sequence of signal MC samples with different hypotheses α are produced. For the signal MC sample with the hypothesis value α, $p_{\mathrm{T}}^{\tau_{\mathrm{had}}}$ in each event with the reconstructed τ_{had} correctly matched to the truth is scaled to $(1+\alpha)p_{\mathrm{T}}^{\tau_{\mathrm{had}}}$.
2. In calculating $\chi^2(\alpha, f)$, the sum is performed over the region $38 \le m_{vis} \le 92$ GeV. For each hypothesis α, $\chi^2(\alpha, f)$ is minimized with respect to f. The optimal f is denoted by f^* and its uncertainty is determined by $\chi^2(\alpha, f^*) + 1$.
3. Let α_0 denote the α value minimizing the $\chi^2(\alpha, f^*)$ among all the hypotheses. Taking into account the statistical fluctuations of the MC samples, however, the optimal value and the statistical uncertainty, α^* and $\Delta\alpha$, are determined by the α vaules, $\alpha_{L,R}$, at the 2σ interval, which corresponds to $\chi^2(\alpha_0, f^*) + 4$, as shown in Eq. 14.

$$\alpha^* \equiv \frac{\alpha_L + \alpha_R}{2}\,, \quad \Delta\alpha \equiv \frac{\alpha_R - \alpha_L}{2 \times 2}$$
$$\chi^2(\alpha_{L,R}, f^*) \equiv \chi^2(\alpha_0, f^*) + 4\,, \quad \alpha_L < \alpha_R \tag{14}$$

The obtained TES in-situ α's are listed in the bottom of Table 14. The TES values in the forward-η region ($1.52 < |\eta| < 2.47$) and center-η region ($|\eta| < 1.37$) are also shown. Figure 70- 72 and Fig. 73- 75 show the related results for one-track and three-track τ_{had}, respectively. In both figures, (a) shows the m_{vis} distributions in the data (dots with error bar) and in the predictions with $\alpha = 0$ (black histogram) and $\alpha = \alpha_0$ (blue histogram); (b) shows the $\chi^2(\alpha, f^*)$ as a function of α; (c) shows the χ^2 value in each m_{vis} bin in the predictions with $\alpha = 0$ (black curve) and $\alpha = \alpha_0$ (blue curve).

D.5. systematic uncertainties

In this section, various systematic uncertainties are estimated below one by one.

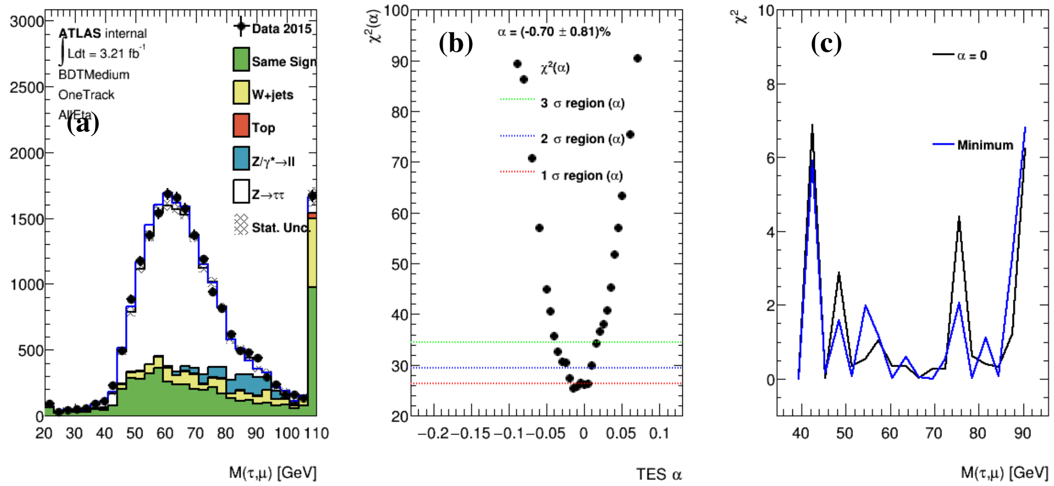

Figure 70: (a) shows the m_{vis} distributions. (b) shows the $\chi^2(\alpha)$ as a function of the TES in-situ α. (c) shows the χ^2 value in each m_{vis} bin. In (a) and (c), the black (blue) blank histogram or curve represents the result with the hypothesis $\alpha = 0$ (the optimal hypothesis α_0). All results are for the one-track τ_{had}.

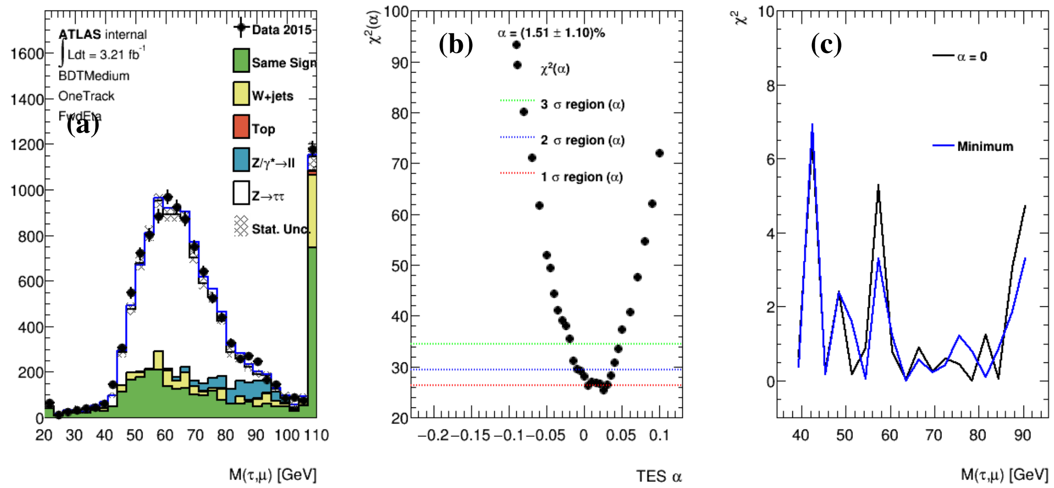

Figure 71: (a) shows the m_{vis} distributions. (b) shows the $\chi^2(\alpha)$ as a function of the TES in-situ α. (c) shows the χ^2 value in each m_{vis} bin. In (a) and (c), the black (blue) blank histogram or curve represents the result with the hypothesis $\alpha = 0$ (the optimal hypothesis α_0). All results are for the one-track τ_{had} in the forward-η region.

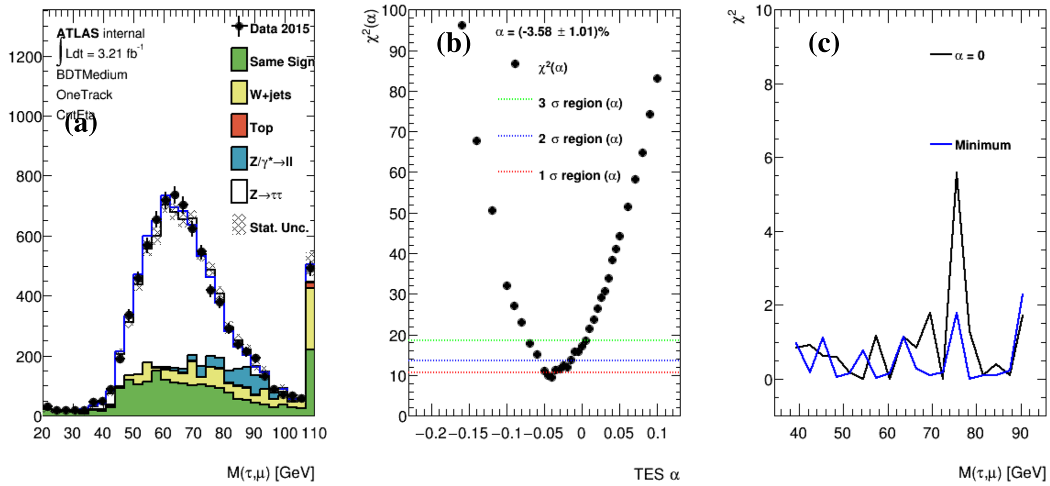

Figure 72: (a) shows the m_{vis} distributions. (b) shows the $\chi^2(\alpha)$ as a function of the TES in-situ α. (c) shows the χ^2 value in each m_{vis} bin. In (a) and (c), the black (blue) blank histogram or curve represents the result with the hypothesis $\alpha = 0$ (the optimal hypothesis α_0). All results are for the one-track τ_{had} in the center-η region.

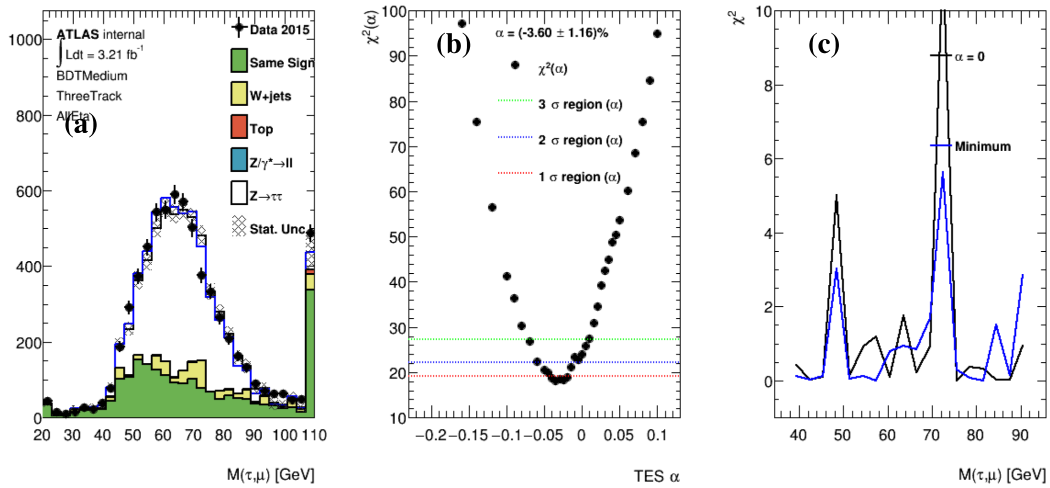

Figure 73: (a) shows the m_{vis} distributions. (b) shows the $\chi^2(\alpha)$ as a function of the TES in-situ α. (c) shows the χ^2 value in each m_{vis} bin. In (a) and (c), the black (blue) blank histogram or curve represents the result with the hypothesis $\alpha = 0$ (the optimal hypothesis α_0). All results are for the three-track τ_{had}.

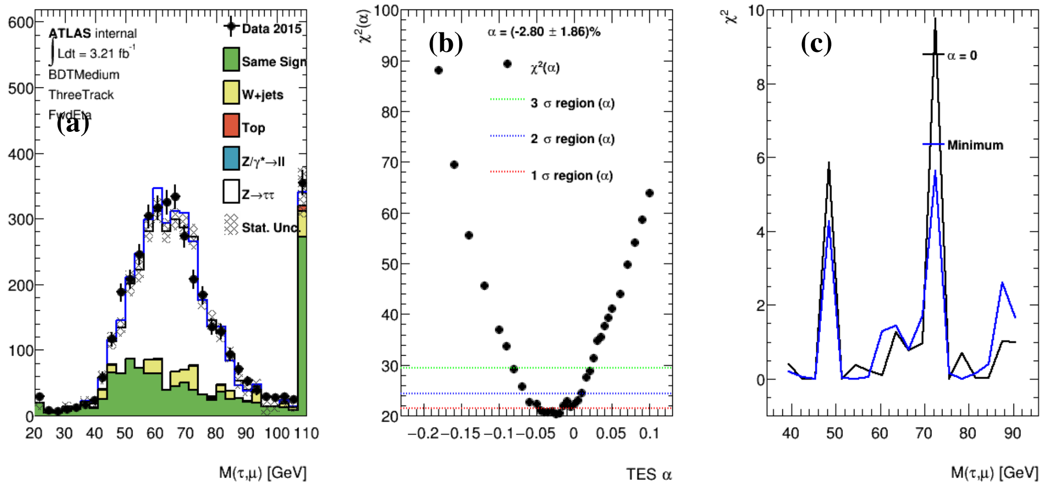

Figure 74: (a) shows the m_{vis} distributions. (b) shows the $\chi^2(\alpha)$ as a function of the TES in-situ α. (c) shows the χ^2 value in each m_{vis} bin. In (a) and (c), the black (blue) blank histogram or curve represents the result with the hypothesis $\alpha = 0$ (the optimal hypothesis α_0). All results are for the three-track τ_{had} in the forward-η region.

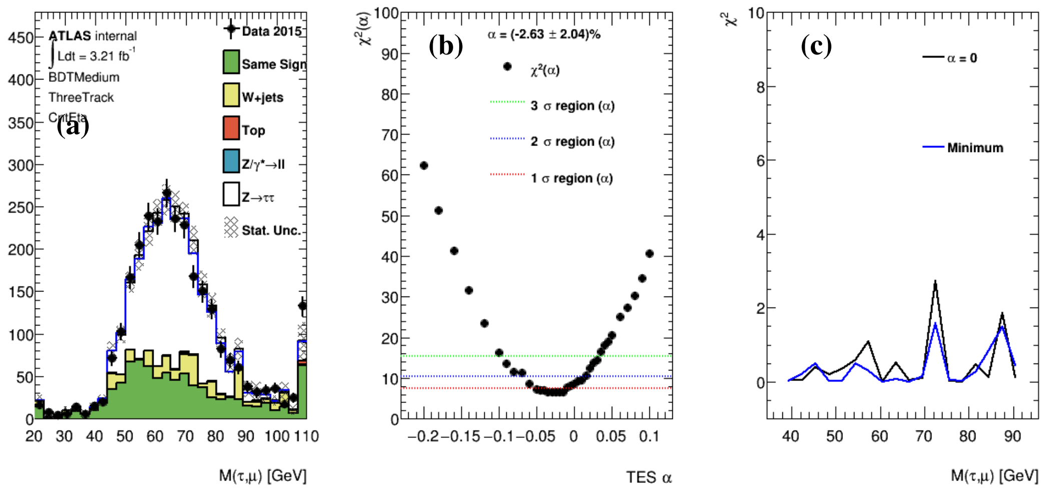

Figure 75: (a) shows the m_{vis} distributions. (b) shows the $\chi^2(\alpha)$ as a function of the TES in-situ α. (c) shows the χ^2 value in each m_{vis} bin. In (a) and (c), the black (blue) blank histogram or curve represents the result with the hypothesis $\alpha = 0$ (the optimal hypothesis α_0). All results are for the three-track τ_{had} in the center-η region.

1. Uncertainty of the factors R_{QCD}, k_W^{OS} and k_W^{SS}: The systematic uncertainty of R_{QCD} is investigated by varying the anti-isolation conditions of the muon candidate while the other factors are investigated by changing the requirements on m_T and $E_{\text{T}}^{\text{miss}}$. The uncertainties are found to be within ±20% of their nominal values. The contribution to the TES systematic uncertainty is thus estimated by varying the factors within ±20%.

2. Trigger, energy scale, reconstruction and identification of a muon track: Various systematics about the efficiency of selecting a muon candidate, including the trigger condition, energy scale, reconstruction and identification, are considered. The contribution to the TES systematic uncertainty is small.

3. Reconstruction of the missing transverse energy: Various systematics about the missing transverse energy, including the resolution and the energy scale of the soft tracks, are considered. The contribution to the TES systematic uncertainty is small.

4. Resolution of $p_{\text{T}}^{\tau_{\text{had}}}$: The effect of the resolution of $p_{\text{T}}^{\tau_{\text{had}}}$ is estimated by changing $p_{\text{T}}^{\tau_{\text{had}}}$ by $\pm 5\% \times (p_{\text{T}}^{\tau_{\text{had}}} - p_{\text{T}}^{\tau_{\text{had}}}(\text{truth}))$ in the signal MC sample, where $p_{\text{T}}^{\tau_{\text{had}}}(\text{truth})$ is the transverse momentum in the truth level.

5. m_{vis} range: In calculating $\chi^{\alpha,f}$, the sum is performed in the range $38 \leq m_{vis} < 92$ GeV. The lower and upper limits are changed within ±6 GeV individually to check the variation of the TES. The TES difference compared to the nominal values are taken as the systematic uncertainty.

6. τ_{had} identification: For each tau candidate, the medium identification condition is required. The effect is estimated by using a loose or tight identification condition (see Fig. 76- 77 taking three-track τ_{had} as example). It is the dominant systematic uncertainty for the TES of three-track τ_{had}.

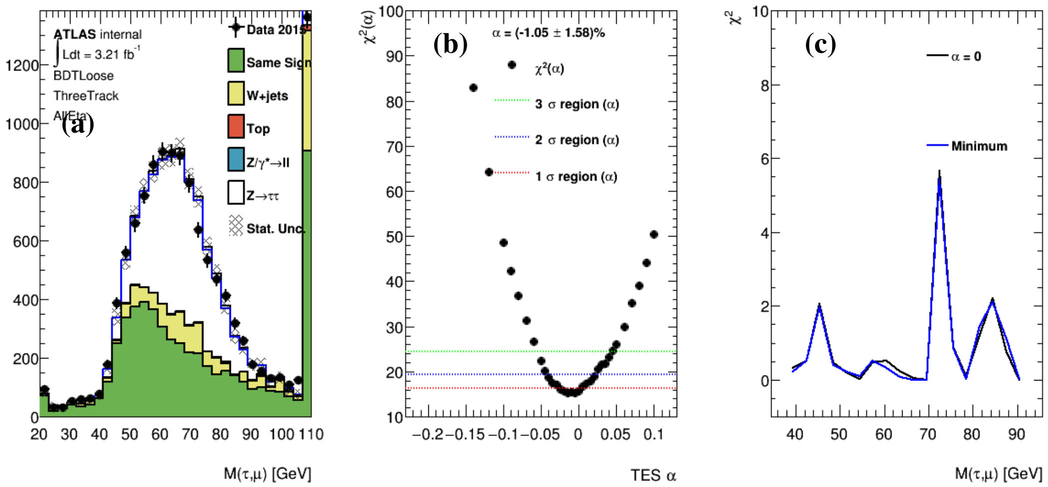

Figure 76: (a) shows the m_{vis} distributions. (b) shows the $\chi^2(\alpha)$ as a function of the TES in-situ α. (c) shows the χ^2 value in each m_{vis} bin. In (a) and (c), the black (blue) blank histogram or curve represents the result with the hypothesis $\alpha = 0$ (the optimal hypothesis α_0). All results are for the three-track τ_{had} passing the loose identification criteria.

7. Bin width of the m_{vis} distribution: The largest TES difference is taken as the systematic uncertainty by changing the nominal bin width 3 GeV to 2.25 GeV or 4.5 GeV.

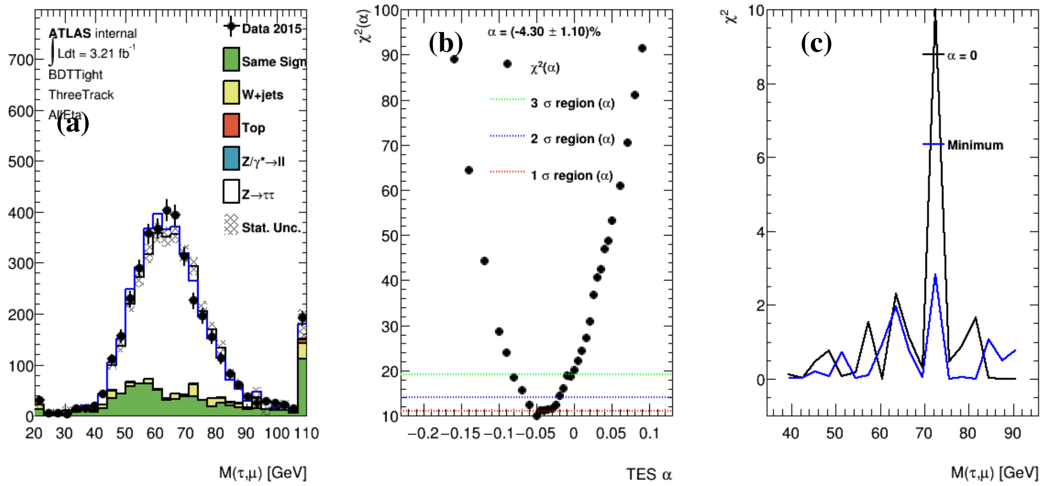

Figure 77: (a) shows the m_{vis} distributions. (b) shows the $\chi^2(\alpha)$ as a function of the TES in-situ α. (c) shows the χ^2 value in each m_{vis} bin. In (a) and (c), the black (blue) blank histogram or curve represents the result with the hypothesis $\alpha = 0$ (the optimal hypothesis α_0). All results are for the three-track τ_{had} passing the tight identification criteria.

Table 15 summarize the systematical uncertainties considered above. In the last line, the total systematic uncertainty is the squre root of the quadratic sum of the individuals assuming they are independent. For the TES of one-track τ_{had}, k_W^{OS} and the m_{vis} calculating range are the dominant contributions. For the TES of three-track τ_{had}, the systematic uncertainty due to the τ_{had} identification is dominant. Eq. 15 gives the final result of the TES in-situ.

$$\begin{aligned} \alpha &= (-0.70 \pm 0.81 \pm 1.19)\% \quad (\text{one-track} \quad \tau_{\mathrm{had}})\,, \\ \alpha &= (-3.60 \pm 1.16 \pm 2.99)\% \quad (\text{three-track} \quad \tau_{\mathrm{had}})\,, \end{aligned} \tag{15}$$

where the first uncertainty is statistical and the second uncertainty is systematical.

Table 15: Summary of the systematical uncertainties (unit: %).

Source	One-track τ_{had}	Three-track τ_{had}
R_{QCD}	0.08	0.80
k_W^{SS}	0.05	0.48
k_W^{OS}	0.64	0.77
Muon	0.18	0.62
$E_{\mathrm{T}}^{\mathrm{miss}}$	0.05	0.06
Resolution of $p_{\mathrm{T}}^{\tau_{\mathrm{had}}}$	0.33	0.56
m_{vis} Range	0.68	0.31
τ_{had} identification	0.47	2.55
Bin width	0.41	0.47
Total	1.19	2.99

E. Offline $t\bar{t}$ tau identification efficiency measurement

E.1. Brief Review Of This Study

E.1.1. Object Definition

Object definition is described in the table 16.

Table 16: Object Definition

muon
p_T > 10 GeV
$\|\eta\|$ < 2.7
Loose ID
Loose Isolation (applied only for $\|\eta\|$ < 2.5)
electron
p_T > 10 GeV
$\|\eta\|$ < 2.5 (Note: no crack veto)
LLH Loose ID
Loose Isolation
photon
p_T > 10 GeV
$\|\eta\|$ < 2.47
Tight ID
Tight Isolation
Jet
AntiKt4EMTopo
p_T > 30 GeV
$\|\eta\|$ < 2.5
JVT> 0.64 (applied only for $\|\eta\|$ < 2.4&&p_T < 50 GeV)
mv2c20, FixedCut
(60% efficiency, SF file: 13TeV/2015-PreRecomm-13TeV-MC12-CDI-October23_v2.root)
Jet/MET cleaning: LooseBad
MET
TST with el/mu soft term
Tau
p_T > 30 GeV
$\|\eta\|$ < 2.5 (excluding 1.37 < $\|\eta\|$ < 1.52)
Absolute Charge = 1
Number of Core Tracks = 1 or 3
Electron Overlap Removal through TauAnalysisTools
Muon Overlap Removal (muon p_T > 2.0, $\|\eta\|$ < 2.5, Loose ID, passHighPTCut)

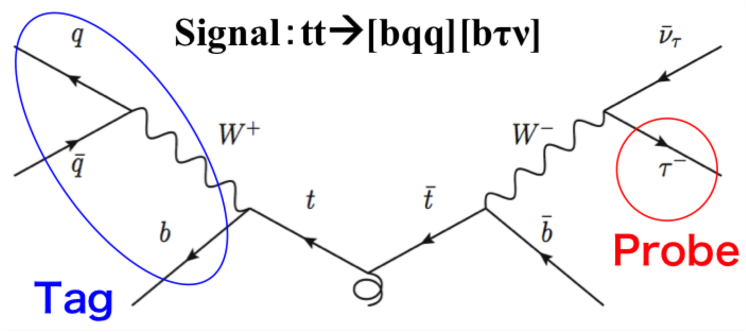

Figure 78: Feynman diagram of the signal event in this analysis

E.1.2. Pre-Selection For The Signal Region

The pre-selection for the signal region is defined as follows. I used HLT_xe70 (at that time, it was the lowest unprescaled trigger of MET). To avoid bad MET, I did Jet/MET Cleaning (bad jet veto). I did lepton veto to suppress leptonic backgrounds. Number of anti-b-jets are required at least 3, and number of b-jets at least 2. MET significance, defined by $E_{\mathrm{T}}^{\mathrm{miss}}[\ \mathrm{GeV}]/\sqrt{0.5\ \mathrm{GeV}\cdot\sum E_T}$, is required at least 9 to reduce w+jets, multi-jet events.

E.1.3. Tag And Probe Selection

A tag and probe selection explained in this section is applied to events remaining after the pre-selection.

Figure ?? is a feynman diagram of the signal event in this analysis. To select the signal events without offline tau identification and with suppressing bias in the selected samples as possible, 'tag' part is defined as finding hadronic top decay products and 'probe' is defined as a anti-b-jet not belong to hadronic top decay products. Hadronic top decay products are defined as a combination of 3 jets passing the following requirements.

1. $\chi^2 = (M_{jj} - M_w)^2/\sigma^2_{M_{jj}} + (M_{jjb} - M_t)^2/\sigma^2_{M_{jjb}}$
   - j: anti-bjet, b: b-jet, M_w: mass of w-boson, M_t: mass of top-quark, $\sigma_{M_{jj}}$ and $\sigma_{M_{jjb}}$: mass uncertainty propagated from jet energy uncertainty
   - find a combination of jjb with minimum χ^2
2. $\chi^2 < 4.0$
3. $M_{jjb} < 200$ GeV
4. $\Delta\phi_{jjb,\ E_{\mathrm{T}}^{\mathrm{miss}}} > 2.3$

If there is no combination satisfying these 4 requirements, those events are discarded. If a combination passing the all items is found out, then 'probe', hadronic tau, is defined in the following way.

1. Find a highest p_T anti-b-jet not belong to the 'tagged' particles
2. If there is a reconstructed tau object inside the jet, it is defined as 'probe'

Furthermore, the following additional cuts are applied for improving purity of the signal events.

1. $M_{T\,(\mathrm{probe},\ E_{\mathrm{T}}^{\mathrm{miss}})} < 120$ GeV
2. $\Delta R_{(\mathrm{probe,\ jet\ nearest\ to\ probe})} = [0.8,\ 2.0]$

E.1.4. Plots At The Signal Region ('No Tau ID' vs 'Tight ID')

This section shows important plots at the signal region without offline tau identification and with the "Tight" identification as a reference. Some variables used for selection of the signal region are shown in N-1 format.

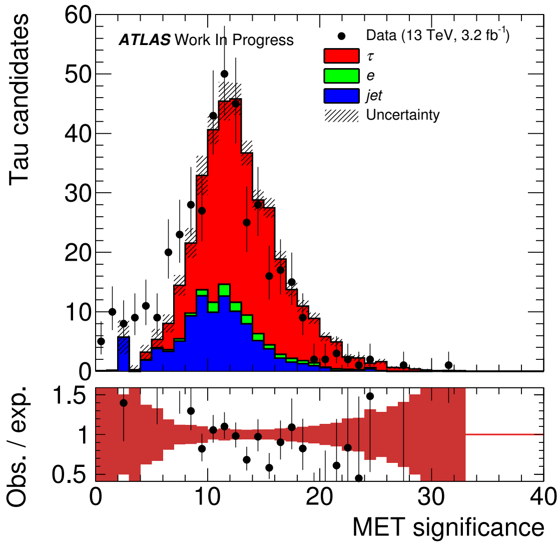

Figure 79: met significance without met significance >= 9 cut(no ID)

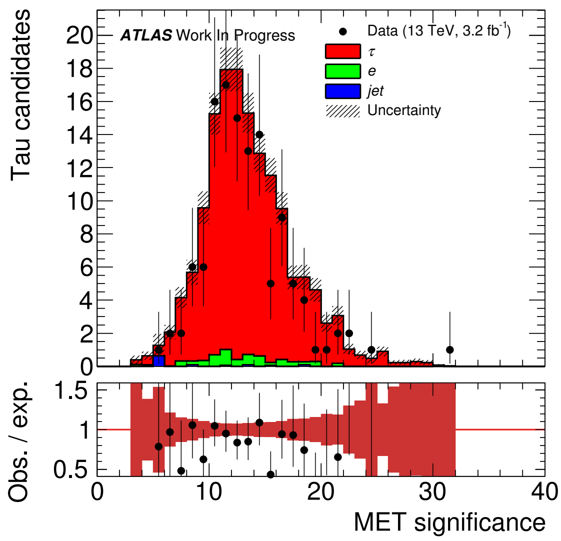

Figure 80: met significance without met significance >= 9 cut(Tight ID)

E.2. Background Estimation

E.2.1. Track Multiplicity For Template Fit

In the sample obtained after the selection, some probes are fake jets or fake electrons and events containing those probes are defined as backgrounds in this analysis. The primary background is $tt \rightarrow \tau$+jets, all jets, or other decay mode, where the probe is a fake jet. The second dominant one is the same events but the probe is a fake electron. To estimate the yeilds of these backgrounds in the signal region, track multiplicity, defined by 'number of core + wide tracks', where a core (wide) track is defined by a track associated to a tau vertex and being within $\Delta R = 0.2$ ([0.2, 0.4]) to the axis of momentum of the reconstructed tau object. Distribution of the track multiplicity at the signal region is shown in Figure ?? and one can see that there are 2 peaks at 1 and 3 tracks for the signal events (the probe is tau) because products of hadronic tau decay are basically 1 or 3 charged meson. The track multiplicity of the fake-jet backgrounds tend to

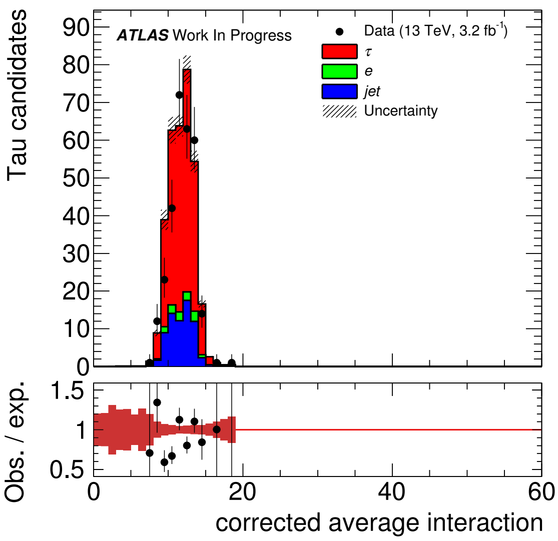

Figure 81: number of averaged interaction with pileup-reweight (no ID)

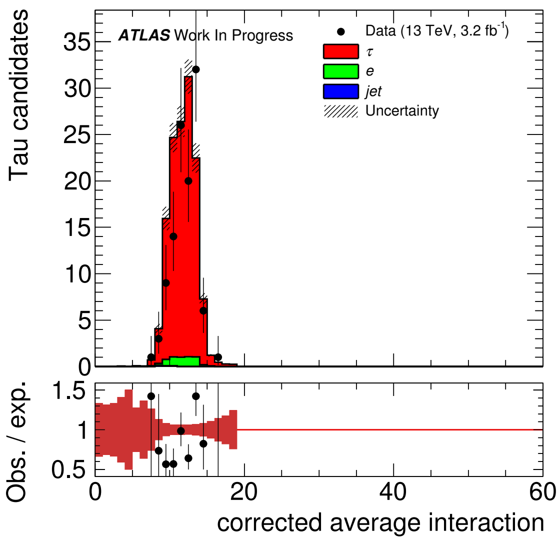

Figure 82: number of averaged interaction with pileup-reweight (Tight ID)

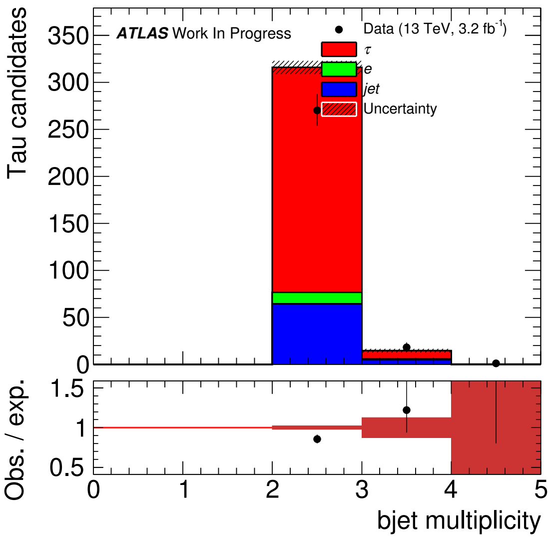

Figure 83: b-tagged jet multiplicity (no ID)

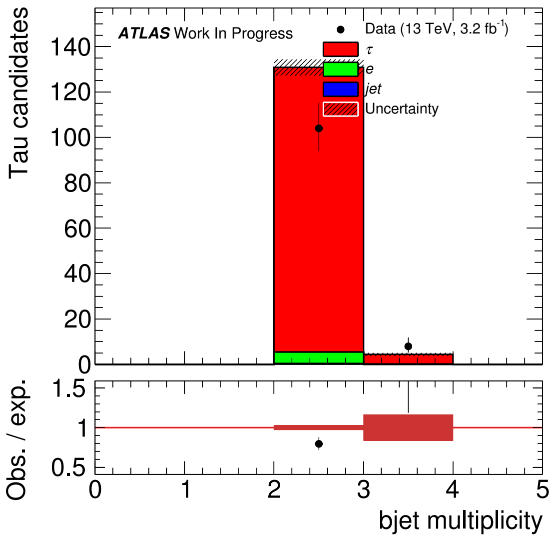

Figure 84: b-tagged jet multiplicity (Tight ID)

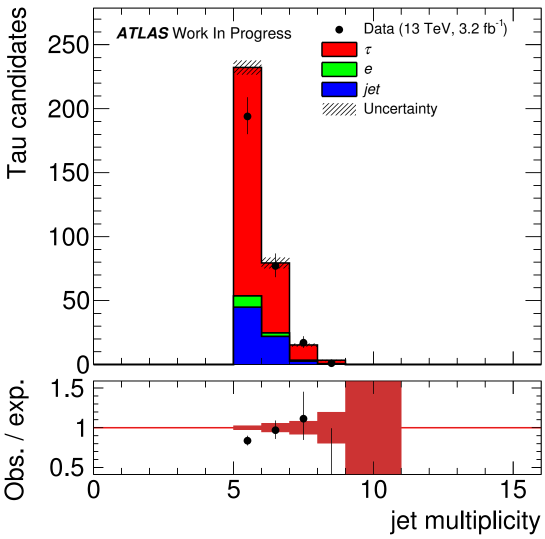

Figure 85: jet multiplicity (no ID)

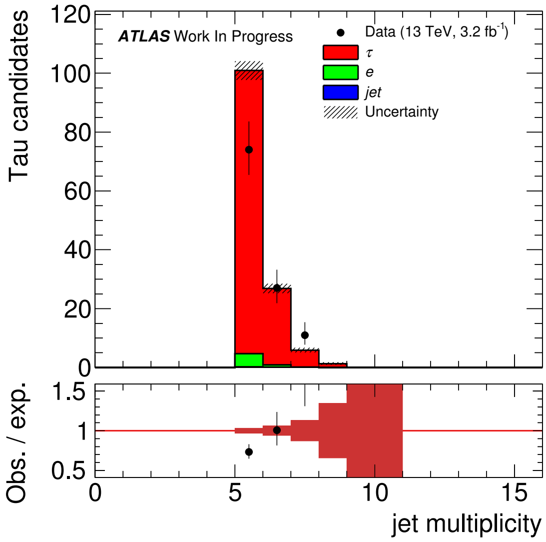

Figure 86: jet multiplicity (Tight ID)

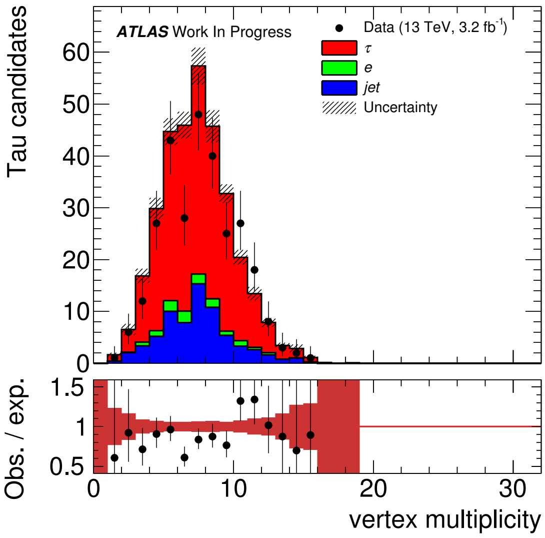

Figure 87: number of vertices(no ID)

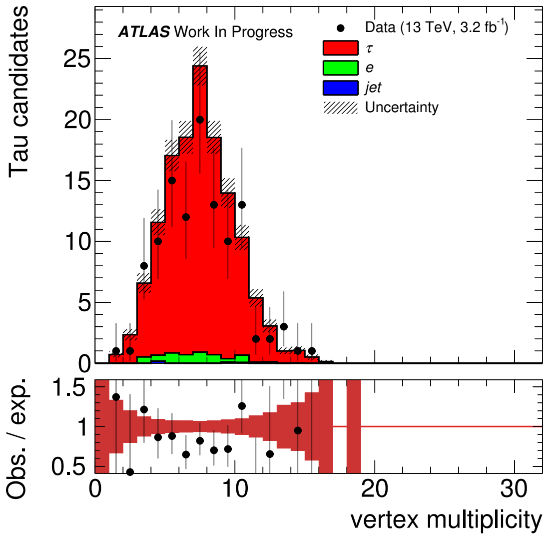

Figure 88: number of vertices(Tight ID)

Not reviewed, for internal circulation only

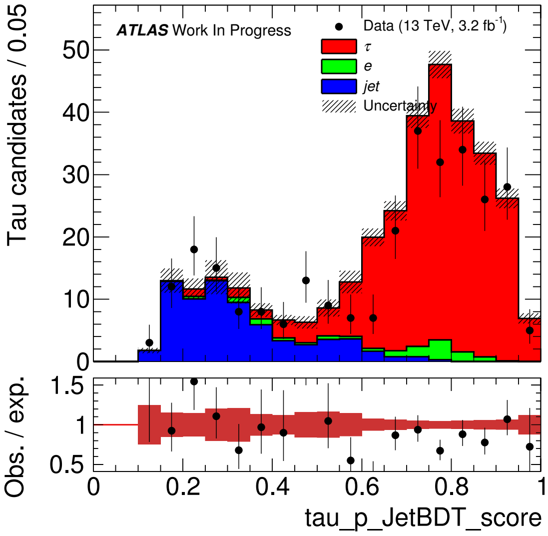

Figure 89: BDT score of offline tau ID (no ID)

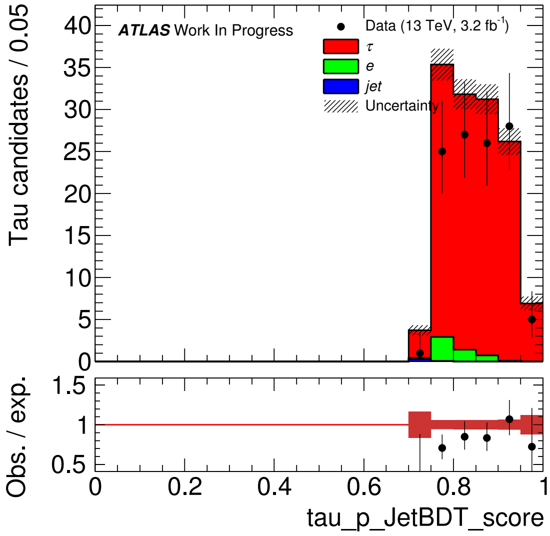

Figure 90: BDT score of offline tau ID (Tight ID)

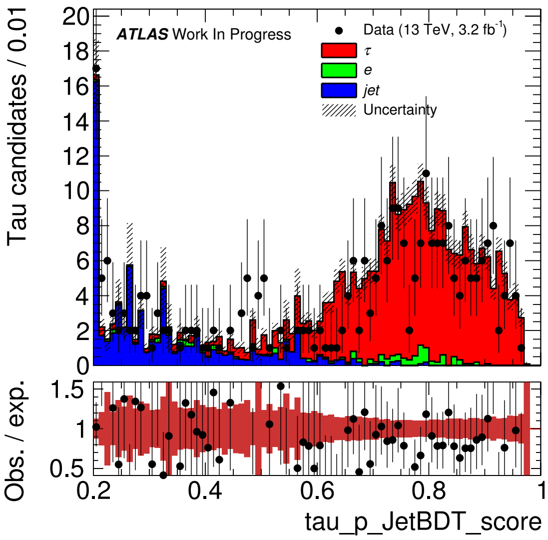

Figure 91: BDT score of offline tau ID with finer binning (no ID)

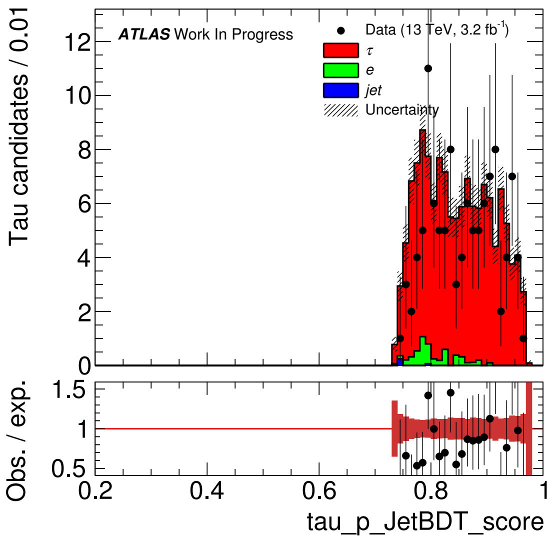

Figure 92: BDT score of offline tau ID with finer binning (Tight ID)

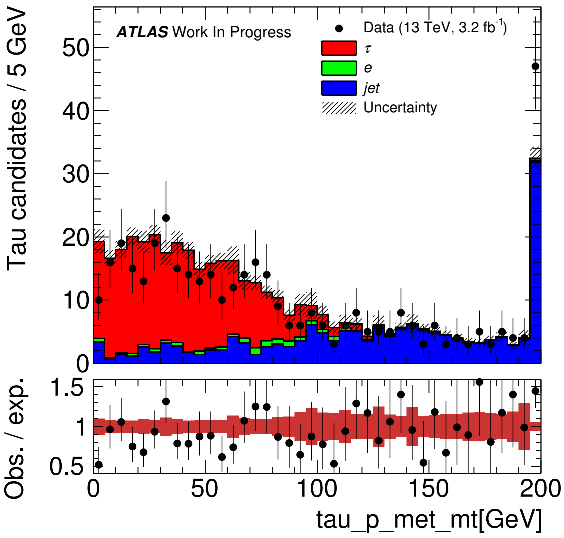

Figure 93: $M_T(\text{lep}, E_{\text{T}}^{\text{miss}})$ without $M_T(\text{lep}, E_{\text{T}}^{\text{miss}}) < 120$ GeV cut (no ID)

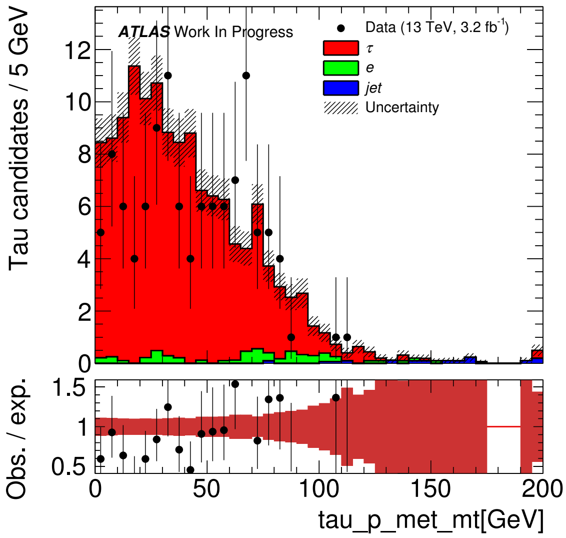

Figure 94: $M_T(\text{lep}, E_{\text{T}}^{\text{miss}})$ without $M_T(\text{lep}, E_{\text{T}}^{\text{miss}}) < 120$ GeV cut (Tight ID)

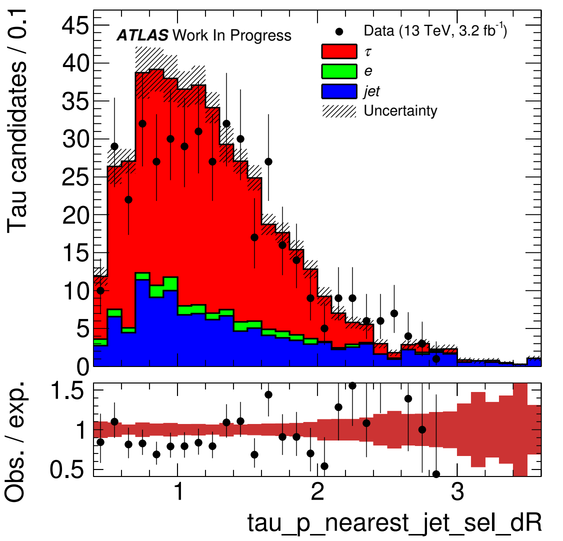

Figure 95: ΔR(probe, jet nearest to probe) without ΔR(probe, jet nearest to probe) = [0.8, 2.0] cut (no ID)

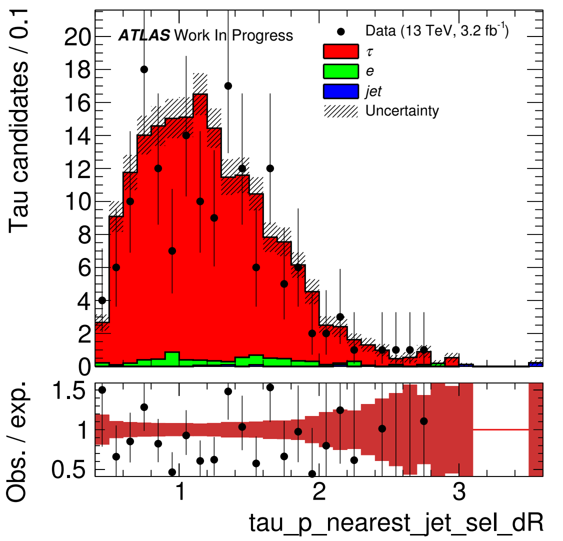

Figure 96: ΔR(probe, jet nearest to probe) without ΔR(probe, jet nearest to probe) = [0.8, 2.0] cut (Tight ID)

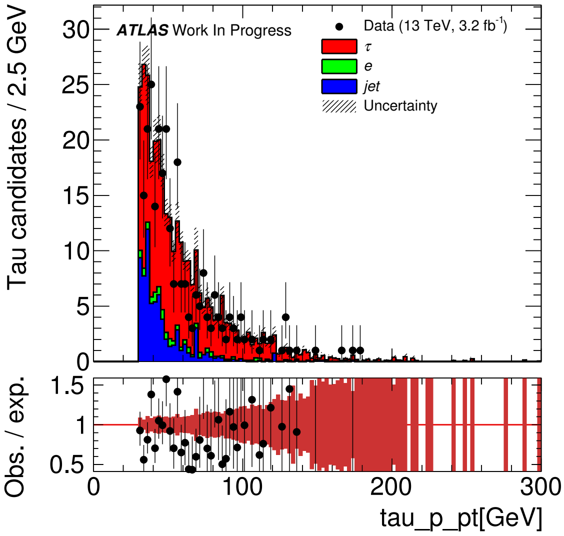

Figure 97: probe p_T (no ID)

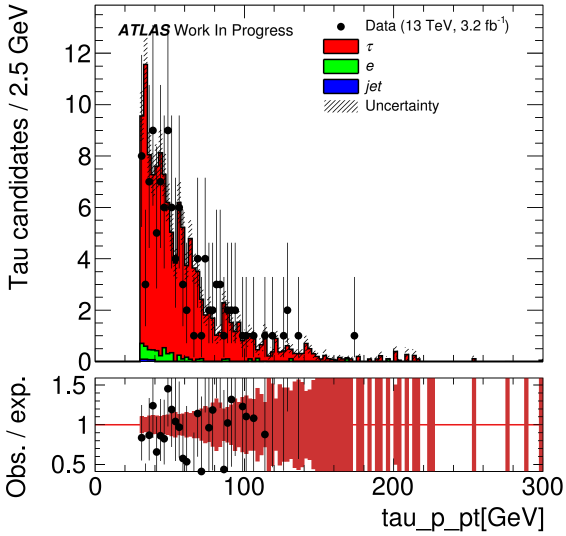

Figure 98: probe p_T (Tight ID)

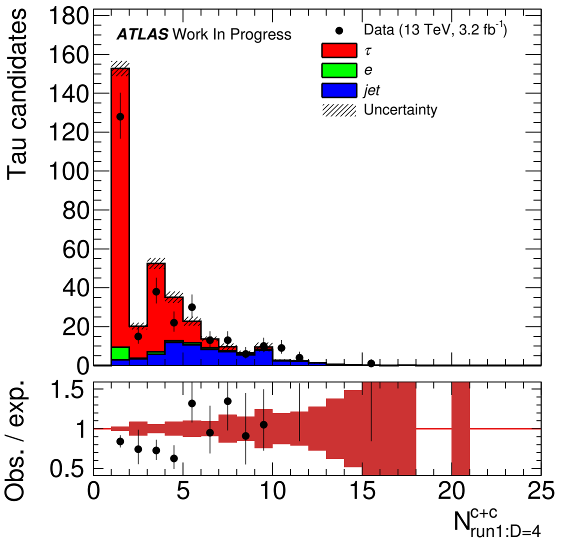

Figure 99: kt4-like track multiplicity within $\Delta R = 0.6$ (no ID)

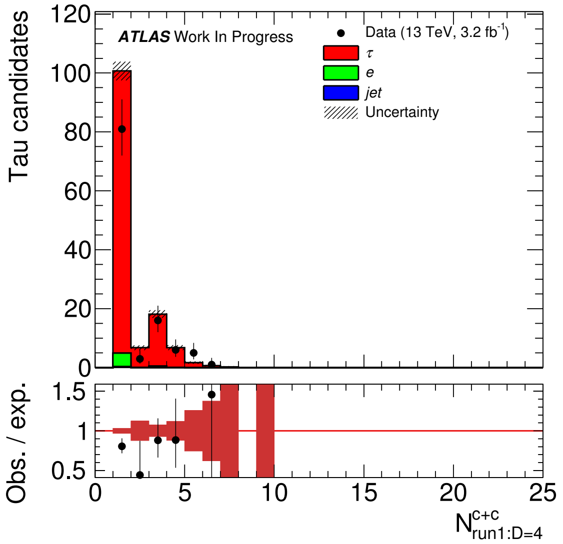

Figure 100: kt4-like track multiplicity within $\Delta R = 0.6$ (Tight ID)

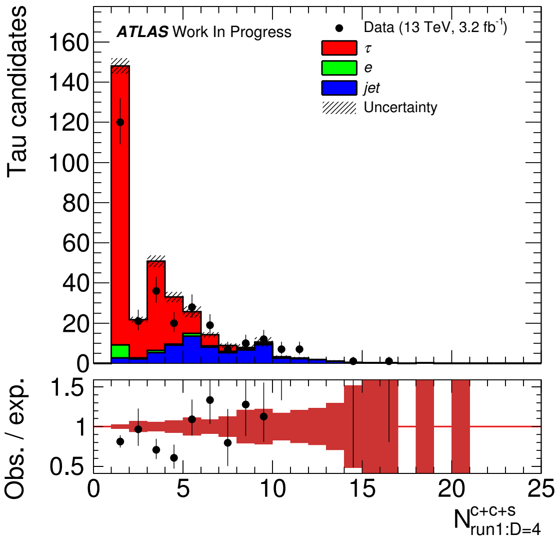

Figure 101: kt4-like track multiplicity within $\Delta R = 0.6$ with soft track term (no ID)

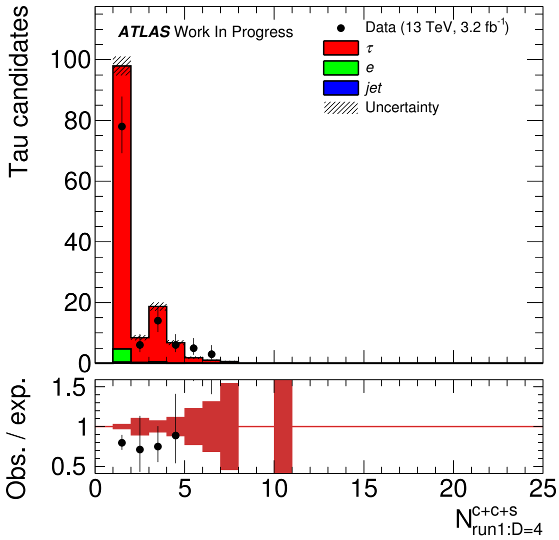

Figure 102: kt4-like track multiplicity within $\Delta R = 0.6$ with soft track term (Tight ID)

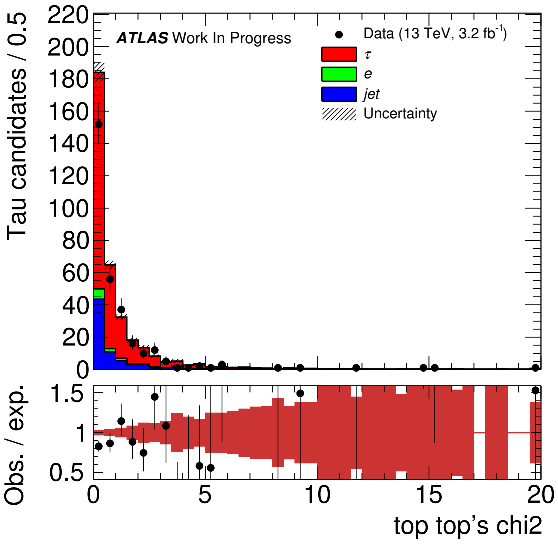

Figure 103: minimum χ^2 of jjb without $\chi^2 < 4.0$ cut (no ID)

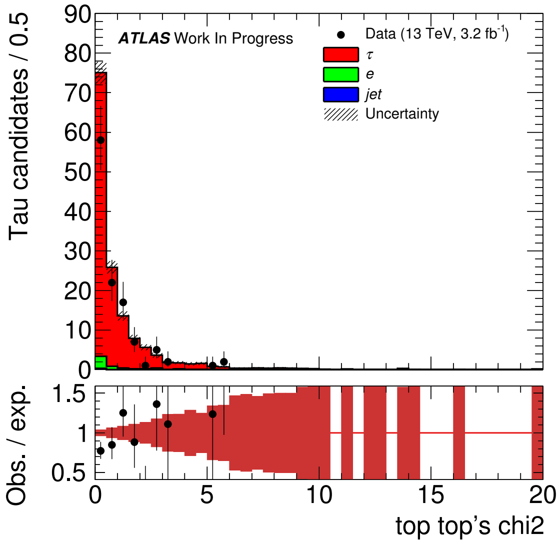

Figure 104: minimum χ^2 of jjb without $\chi^2 < 4.0$ cut (Tight ID)

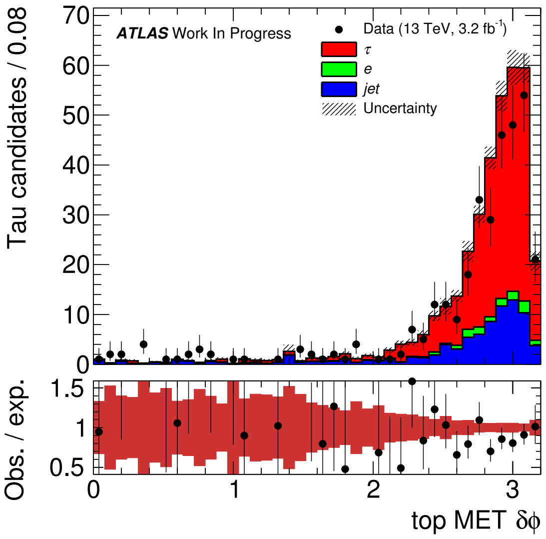

Figure 105: $\Delta\phi$(jjb, $E_{\mathrm{T}}^{\mathrm{miss}}$) without $\Delta\phi$(jjb, $E_{\mathrm{T}}^{\mathrm{miss}}$) (no ID)

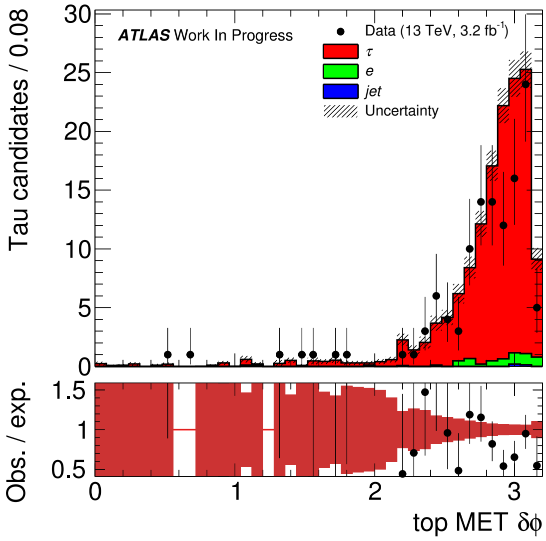

Figure 106: $\Delta\phi$(jjb, $E_{\mathrm{T}}^{\mathrm{miss}}$) without $\Delta\phi$(jjb, $E_{\mathrm{T}}^{\mathrm{miss}}$) (Tight ID)

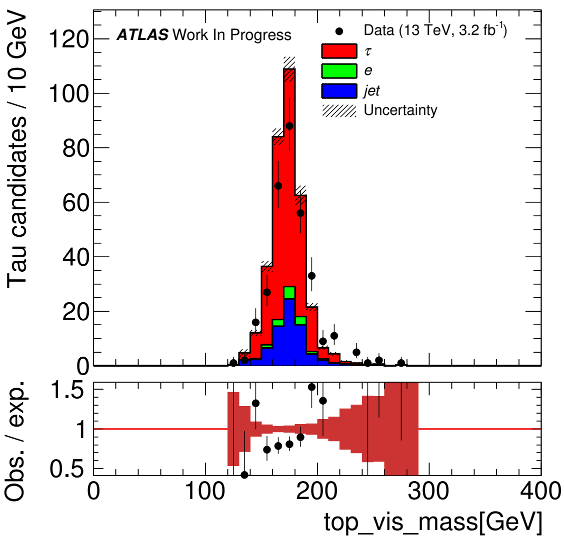

Figure 107: χ^2-base jjb mass without $M_{jjb} < 200$ GeV cut (no ID)

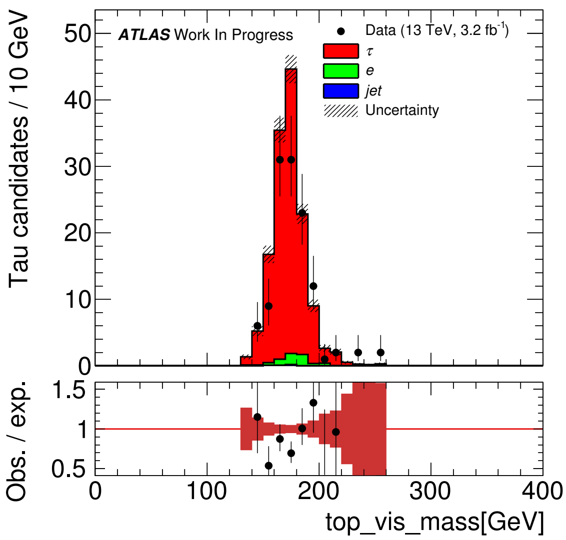

Figure 108: χ^2-base jjb mass without $M_{jjb} < 200$ GeV cut (Tight ID)

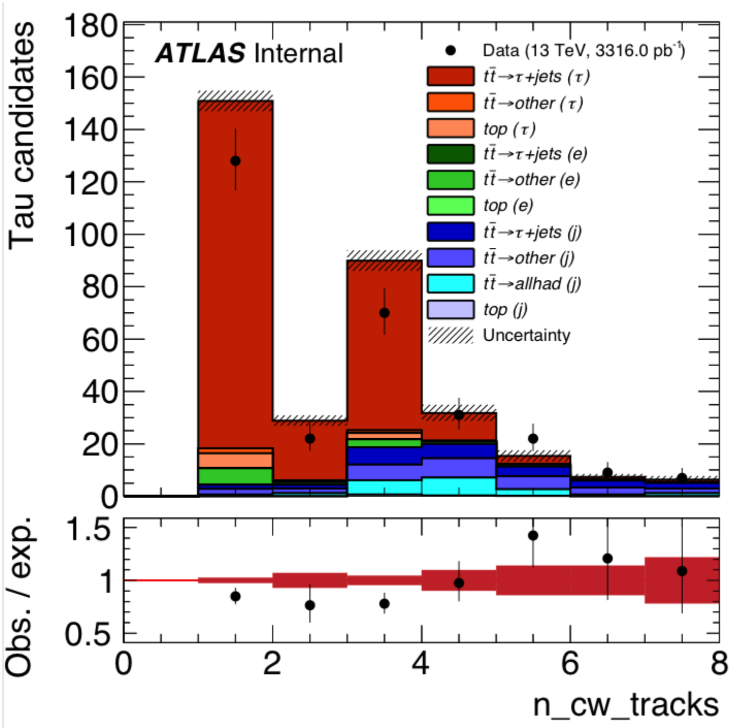

Figure 109: Track Multiplicity at the Signal Region: embraced characters, τ, e, j, mean indicate what the probe actually is.

be higher than the signal events, and that of the fake-electron backgrounds have one peak at 1 track. For background estimation, I did a simutaneous template fit with track multiplicty PDFs.

By the way, I didn't use a kt4-like track multiplicity, used in Run 1, because fit results are almost same between the simple track multiplicity used in this analysis and kt4-like one. Since the latter one needs more bins, statistics are not enough to obtain benefits of the shape differences.

E.2.2. Configuration Of Template Fit

In this analysis, 2 regions are used for simultaneous template fitting. The one region is same as the region after the selection explained in the section E.1.3 and is named 'total channel' from here. The other region is a part of the one, probes of which pass offline tau identification, and is named 'pass channel' from here. In each region, templates are prepared for tau, fake-jet, fake-electron. MC statistical uncertainty is also considered in the fit. The fitting software used in this analysis is 'HistFactory' (ref?). So the technical terms of HistFactory related to systematic uncertainty, OverallSys, HistoSys, are used to explain the fit configuration (OverallSys is uncertainty on normalization, and HistoSys is uncertainty on PDF shape).

E.2.3. Total Channel

Fit function in total channel is defined by equation 16:

$$\begin{aligned} &N^{\text{total}}_{\tau_{1,3}} \cdot \text{PDF}^{\text{total}}_{\tau_{1,3}} \cdot \text{HistoSys}^{\text{total}}_{\tau_{1,3},\ \text{radiation}} \cdot \text{HistoSys}^{\text{total}}_{\tau_{1,3},\ \text{geo}} \times \\ &N^{\text{total}}_{\tau_{1,3}} \cdot R^{\text{total}}_{e_{1,3}/\tau_{1,3}} \cdot \text{OverallSys}^{\text{total}}_{e_{1,3},\ \text{e-veto eff}} \cdot \text{PDF}^{\text{total}}_{e_{1,3}} \times \\ &N^{\text{total}}_{j_{1,3}} \cdot \text{PDF}^{\text{total}}_{j_{1,3}} \cdot \text{HistoSys}^{\text{total}}_{j_{1,3},\ \text{closure}} \end{aligned} \tag{16}$$

where fit parameters (also shared in pass channel) are:

- $N^{\text{total}}_{\tau_{1,3}}$: number of events where the probe with 1 or 3 core tracks is a tau
- $N^{\text{total}}_{j_{1,3}}$: number of events where the probe with 1 or 3 core tracks is a fake-jet

constant parameters are:

- $R^{\text{total}}_{e_{1,3}/\tau_{1,3}}$: defined by $\frac{\text{the expected yeild of events where the probe with 1 or 3 core tracks is a fake-electron}}{\text{the expected yeild of events where the probe with 1 or 3 core tracks is a tau}}$

the ways to construct each PDF are:

- $\text{PDF}^{\text{total}}_{\tau_{1,3}}$, $\text{PDF}^{\text{total}}_{e_{1,3}}$: MC modeling
- $\text{PDF}^{\text{total}}_{j_{1,3}}$: a data-driven modeling (will be explained in section E.2.5)

and considered systematic uncertainties are:

- $\text{HistoSys}^{\text{total}}_{\tau_{1,3},\ \text{radiation}}$: Shape uncertainty on the PDF coming from radiation tuning in MC modeling
- $\text{HistoSys}^{\text{total}}_{\tau_{1,3},\ \text{geo}}$: Shape uncertainty on the PDF coming from uncertainty on MC detector modeling (explained in appendix E.6)
- $\text{OverallSys}^{\text{total}}_{e_{1,3},\ \text{e-veto eff}}$: Overall uncertainty on the yeild coming from uncertainty on electron veto efficiency (50%). This parameter is also shared in pass channel.
- $\text{HistoSys}^{\text{total}}_{j_{1,3},\ \text{closure}}$: Shape uncertainty on the PDF (will be explained in section E.2.5)

The uncertainty on $R^{\text{total}}_{e_{1,3}/\tau_{1,3}}$ were checked and found negligible. The reason that the 50% relative uncertainty coming from electron veto efficiency is same as the analysis of offline tau identification efficiency throuth $Z \to \tau\tau$ events and is discribed at TauConf2015.

E.2.4. Pass Channel

Fit function in pass channel is defined by equation 17:

$$\begin{aligned} &N^{\text{total}}_{\tau_{1,3}} \cdot R_{\tau_1/\tau_{1,3}} \cdot \epsilon_{\tau_1} \cdot \text{PDF}^{\text{pass}}_{\tau_1} \cdot \text{HistoSys}^{\text{pass}}_{\tau_1,\ \text{radiation}} \cdot \text{HistoSys}^{\text{pass}}_{\tau_1,\ \text{geo}} \times \\ &N^{\text{total}}_{\tau_{1,3}} \cdot R_{\tau_3/\tau_{1,3}} \cdot \epsilon_{\tau_3} \cdot \text{PDF}^{\text{pass}}_{\tau_3} \cdot \text{HistoSys}^{\text{pass}}_{\tau_3,\ \text{radiation}} \cdot \text{HistoSys}^{\text{pass}}_{\tau_3,\ \text{geo}} \times \\ &N^{\text{total}}_{\tau_{1,3}} \cdot \text{OverallSys}^{\text{total}}_{e_{1,3},\ \text{e-veto eff}} \cdot R_{e_1/\tau_{1,3}} \cdot \epsilon_{e_1} \cdot \text{PDF}^{\text{pass}}_{e_1} \times \\ &N^{\text{total}}_{j_{1,3}} \cdot R_{j_1/j_{1,3}} \cdot \epsilon_{j_1} \cdot \text{OverallSys}^{\text{pass}}_{j_1,\ \text{stat fake eff}} \cdot \text{OverallSys}^{\text{pass}}_{j_1,\ \text{meas fake eff}} \cdot \text{PDF}^{\text{pass}}_{j_1} \times \\ &N^{\text{total}}_{j_{1,3}} \cdot R_{j_3/j_{1,3}} \cdot \epsilon_{j_3} \cdot \text{OverallSys}^{\text{pass}}_{j_3,\ \text{stat fake eff}} \cdot \text{OverallSys}^{\text{pass}}_{j_3,\ \text{meas fake eff}} \cdot \text{PDF}^{\text{pass}}_{j_3} \end{aligned} \tag{17}$$

where fit parameters appearing only in pass channel are:

- ϵ_{τ_1}: offline tau identification efficiency for tau with 1 core track
- ϵ_{τ_3}: offline tau identification efficiency for tau with 3 core tracks

constant parameters are:

- $R_{\tau_1/\tau_{1,3}}$: defined by $\frac{\text{the expected yeild of events where the probe with 1 core track is a tau}}{\text{the expected yeild of events where the probe with 1 or 3 core tracks is a tau}}$
- $R_{\tau_3/\tau_{1,3}}$: defined by $\frac{\text{the expected yeild of events where the probe with 3 core track is a tau}}{\text{the expected yeild of events where the probe with 1 or 3 core tracks is a tau}}$
- $R_{e_1/\tau_{1,3}}$: defined by $\frac{\text{the expected yeild of events where the probe with 3 core track is a fake-electron}}{\text{the expected yeild of events where the probe with 1 or 3 core tracks is a tau}}$
- $R_{j_1/j_{1,3}}$: defined by $\frac{\text{the expected yeild of events where the probe with 1 core track is a fake-jet}}{\text{the expected yeild of events where the probe with 1 or 3 core tracks is a fake-jet}}$
- $R_{j_3/j_{1,3}}$: defined by $\frac{\text{the expected yeild of events where the probe with 3 core track is a fake-jet}}{\text{the expected yeild of events where the probe with 1 or 3 core tracks is a fake-jet}}$
- ϵ_{e_1}: offline tau identification efficiency for fake-electron with 1 core track, which is estimated with MC.
- ϵ_{j_1}: offline tau identification efficiency for fake-jet with 1 core track, which is measured with a γ+jet sample (explained in section E.2.6)
- ϵ_{j_3}: offline tau identification efficiency for fake-jet with 3 core tracks, which is measured with a γ+jet sample (explained in section E.2.6)

the ways to construct each PDF are:

- $\text{PDF}^{\text{pass}}_{\tau_1}$, $\text{PDF}^{\text{pass}}_{e_1}$: MC modeling
- $\text{PDF}^{\text{pass}}_{\tau_3}$, $\text{PDF}^{\text{pass}}_{e_3}$: MC modeling
- $\text{PDF}^{\text{pass}}_{j_1}$: a data-driven modeling explained in section E.2.5
- $\text{PDF}^{\text{pass}}_{j_3}$: a data-driven modeling explained in section E.2.5

and considered systematic uncertainties are:

- $\text{HistoSys}^{\text{pass}}_{\tau_1,\text{ radiation}}$: Shape uncertainty on the PDF for tau with 1 core track coming from radiation tuning in MC modeling (explained in appendix E.6)
- $\text{HistoSys}^{\text{pass}}_{\tau_3,\text{ radiation}}$: Shape uncertainty on the PDF for tau with 3 core tracks coming from radiation tuning in MC modeling (explained in appendix E.6)
- $\text{HistoSys}^{\text{total}}_{\tau_1,\text{ geo}}$: Shape uncertainty on the PDF for tau with 1 core track coming from uncertainty on MC detector modeling (explained in appendix E.6)
- $\text{HistoSys}^{\text{total}}_{\tau_3,\text{ geo}}$: Shape uncertainty on the PDF for tau with 3 core tracks coming from uncertainty on MC detector modeling
- $\text{OverallSys}^{\text{total}}_{e_{1,3},\text{ e-veto eff}}$: Overall uncertainty on the yeild coming from uncertainty on electron veto efficiency (50%). This parameter is also shared in total channel.
- $\text{OverallSys}^{\text{pass}}_{j_1,\text{ stat fake eff}}$: Statistical uncertainty of measurement of offline tau identification efficiency for fake-jet with 1 core track
- $\text{OverallSys}^{\text{pass}}_{j_3,\text{ stat fake eff}}$: Statistical uncertainty of measurement of offline tau identification efficiency for fake-jet with 3 core tracks

- $\mathrm{OverallSys}^{\mathrm{pass}}_{j_1,\ \mathrm{meas\ fake\ eff}}$: Systematic Uncertainty of measurement of offline tau identification efficiency for fake-jet with 1 core track (explained in section E.7)
- $\mathrm{OverallSys}^{\mathrm{pass}}_{j_3,\ \mathrm{meas\ fake\ eff}}$: Systematic Uncertainty of measurement of offline tau identification efficiency for fake-jet with 3 core tracks (explained in section E.7)

The uncertainty on the constant parameters for pass channel were checked and found negligible.

E.2.5. Building Templates For Fake-Jets In A Data-Driven Way

Fake-jet templates in total and pass channel are built with data in a control region, where $tt \to \mu + jets$ events are enriched. The selection for the control region is:

1. HLT_xe70
2. No bad jets (Jet/MET cleaning)
3. Exact one muon passing tight ID and tight isolation
4. Electron veto
5. at least 2 b-jets
6. at least 2 anti-b-jets

And then leading 2 anti-b-jets are used as (fake-jet-enriched) probe. p_T distributions of the two are different, but track multiplicity of the two were found highly independent of p_{T}, so I didn't do pt-weight correction. Figure 110 shows the track multiplicity of the probe at the control region and shape of the distribution is used as the fake-jet templates at total and pass channel. Since there is a small contamination where the probe is tau, I corrected the shape with MC prediction, which is negligibly affected by systematic uncertainty on MC modeling. I also did closure test between the track multiplicity of fake-jet at the signal region and the one at the control region, which is shown in Figure 111. The shape difference in Figure 111 is considered as $\mathrm{HistoSys}^{\mathrm{total}}_{j_{1,3},\ \mathrm{closure}}$. This uncertainty is relatively negligible in pass channel and then is considered only in total channel.

E.2.6. Measurement Of Fake-Jet Efficiency

In pass channel, the track multiplicity of fake-jet becomes similar to that of tau, as you can see in Figure **??**. It was found difficult to determine normalization of the fake-jet template in pass channel by the fit, so I decided to measure fake-jet efficiency and to use the measured efficiency as a constant parameter with some types of systematic uncertaintes in the fit. Since it is difficult to prepare fake-jets in tt events with high statistics, I used fake-jets in a $\gamma + jet$ sample. The selection for this sample is:

1. A lot of triggers (listed in appendix E.8)
2. Exact 1 photon
    - $p_T > 30$ GeV, $|\eta| < 2.47$ (excluding crack region)
    - Tight ID, Tight Isolation

And then (fake-jet) probe is defined in the following way:

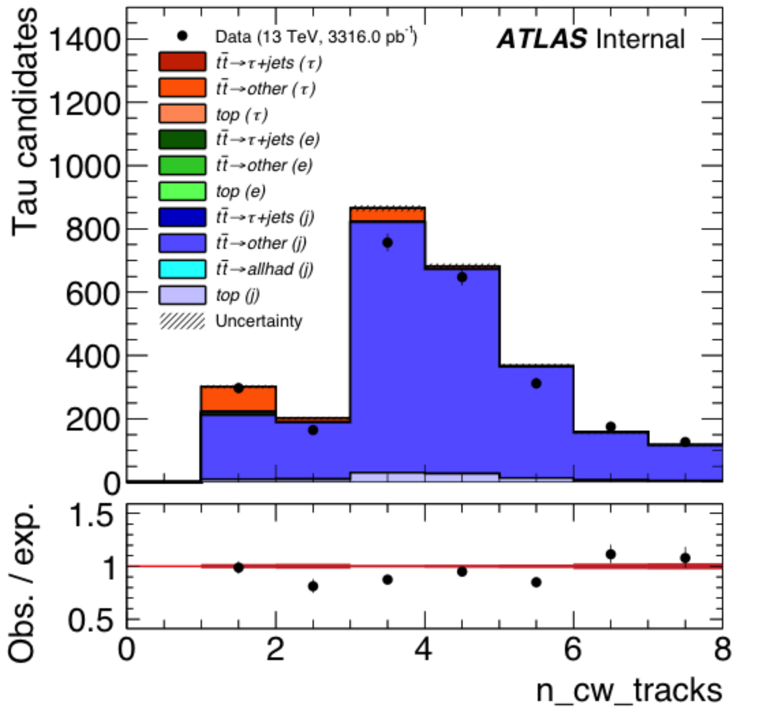

Figure 110: The track multiplicity of the probe at the control region in total channel

- Find a jet satisfying the below requirements
    1. $|\Delta\phi_{\gamma,\mathrm{jet}}| > 2.8$
    2. $|\Delta {p_T}_{\gamma,\mathrm{jet}}| < 50$ GeV
    3. There is a reconstructed tau object inside the jet

Figure **??** shows the fake-jet efficiency measured using the γ+jet control sample. In the fit, the 2 constant parameters ϵ_{j_1}, ϵ_{j_3}, correspond to the values corrected from the measured efficiency through a p_T reweighting process. The uncertainty on the constant parameters which I considered in the fit consists of statistical uncertainty of the measuement, systematic uncertainty from fake-photon contribution, and systematic uncertainty from the validity of the measurement. How I estimated the latter 2 systematic uncertainties is explained in appendix E.7.

E.3. Result

Summary of the fit results is shown in Table 17. In this analysis, I prepared 3 p_T bins, inclusive, [0,70] GeV, and [70,200] GeV. Figure 114 shows the distributions of the track multiplicity after the simultaneous fit in total and pass channel, where probe p_T binning is inclusive and 'Loose' tau ID is used for pass channel. Table 18 shows the effects of uncertainty sources for Medium ID and indicates statisical uncertainty is the most dominant.

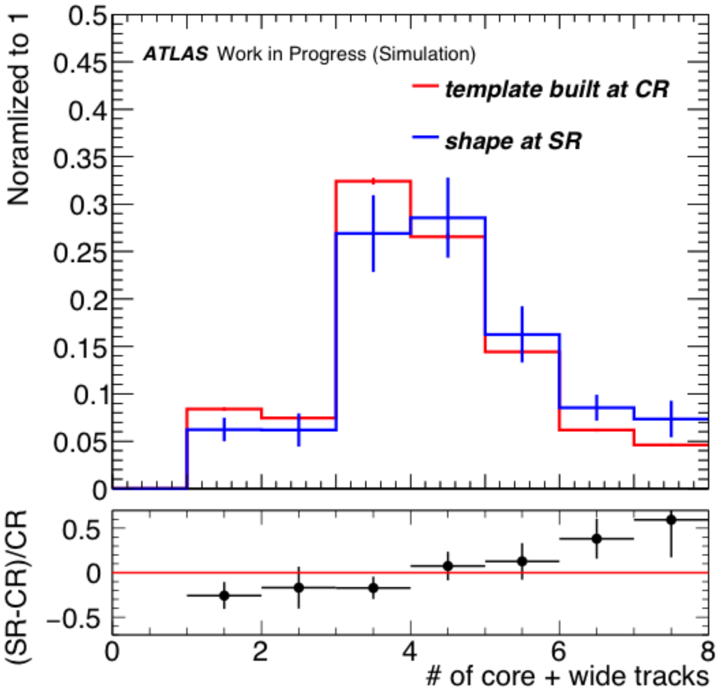

Figure 111: The closure test between the track multiplicity of fake-jet at the signal region and the one at the control region. The 2 distributions are modelled using ttbar MC.

E.4. Events Where Probe Is B-Jet

b-jets as probe could be one of sources making bias because the efficiency of b is higher than that of gluon and light quarks. For assuring that the effect is very small in this analysis, I checked 'truth flavor label' of probe and then number of b-jets selected as probe was assured to be negligible. Figure ?? shows 'truth flavor label' of probe at the signal region and indicates that not only b-jets but also c-jets don't affect the shape of track multiplicity so much.

E.5. Contribution Of Multi-Jet Events

Since statistics of MC sample of multi-jet events was not enough, it was difficult to estimate how many multi-jet events there are in the signal region in a rigorous, mathematical, or quantitative way. However, I prepared some plots showing variables sensitive to multi-jet events and supporting that the contribution of multi-jet events is negligible.

Figure 116 and 117 show met and met significance distribution at the signal region without met significance >= 9 cut. As we expect that Multi-jet events tend to have low met, some excess at low met (significance) can be seen and it indicates that met significance >= 9 cut can reduce multi-jet events up to a negligible level. Furthermore, Figure 118 and 119 show met significance distribution at the signal region without $M_{T,(\mathrm{probe,MET})} < 120$ GeV cut and without $M_{jjb} < 200$ GeV cut. These two cuts also strongly reduce multi-jet events, but the two figures show multi-jet-like excess does not appear and indicate that multi-jet

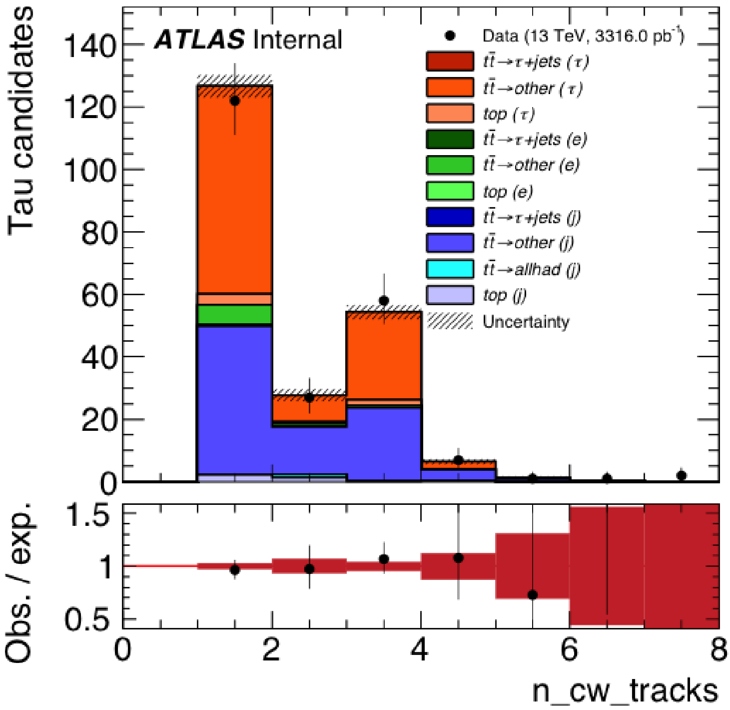

Figure 112: The track multiplicity of the probe at the control region in pass channel. The level of the offline tau identification level is 'Loose'.

events are already negligible before applying the cuts. From these studies, I decided to ignore multi-jet events in this analysis.

E.6. Geometrical Uncertainty On Tau Template

I estimated geometric uncertainties with samples same as ones used in the Ztautau tag and probe analysis. Figure 120 shows distributions of the track multiplicity of tau with some systematic variations. Those are considered as HistoSys (shpae uncertainty on the tau templates) in the template fit.

E.7. Systematic Uncertainty On Fake-Jet Efficiency

Since it was difficult to estimate fake-jet efficiency using $t\bar{t}$ events due to its statistics, instead I measured fake-jet efficiency with the $\gamma + jet$ sample. Measured fake-jet efficiency could vary with composition of parton flavor in fake-jet sample used to measure, and the measurement with $\gamma + jet$ could be the case.

E.7.1. Variation of Photon Isolation

In the $\gamma + jet$ sample, fake-photons could also be the fake-jet probes. Figure 121 and 122 shows the measured fake-jet efficiency using the sample of fake-jet probes and shows that the difference between

Not reviewed, for internal circulation only

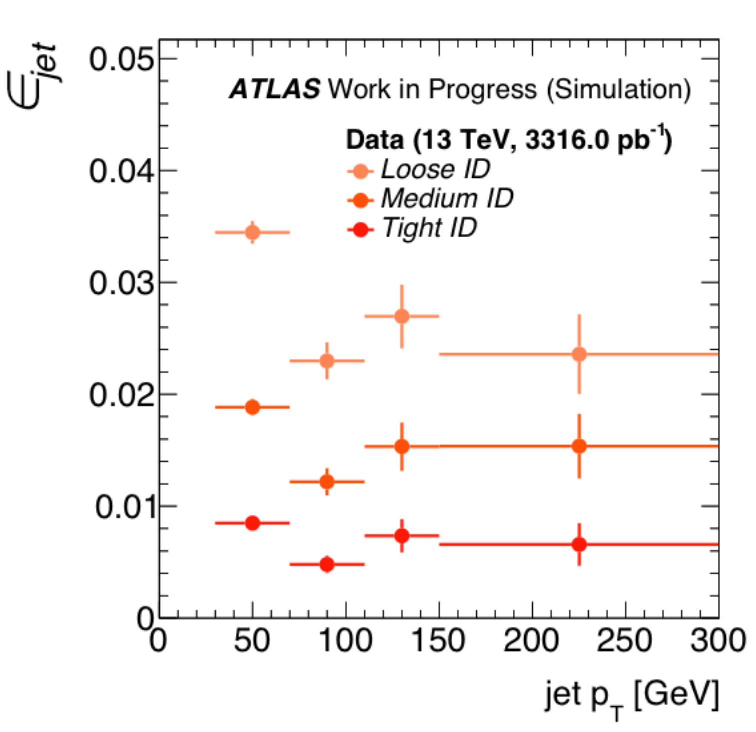

Figure 113: The fake-jet efficiency measured using the γ+jet control sample. 'Loose', 'Medium', and 'Tight' identification levels were checked respectively. In this plot, fake jets with 1 or 3 core tracks are used.

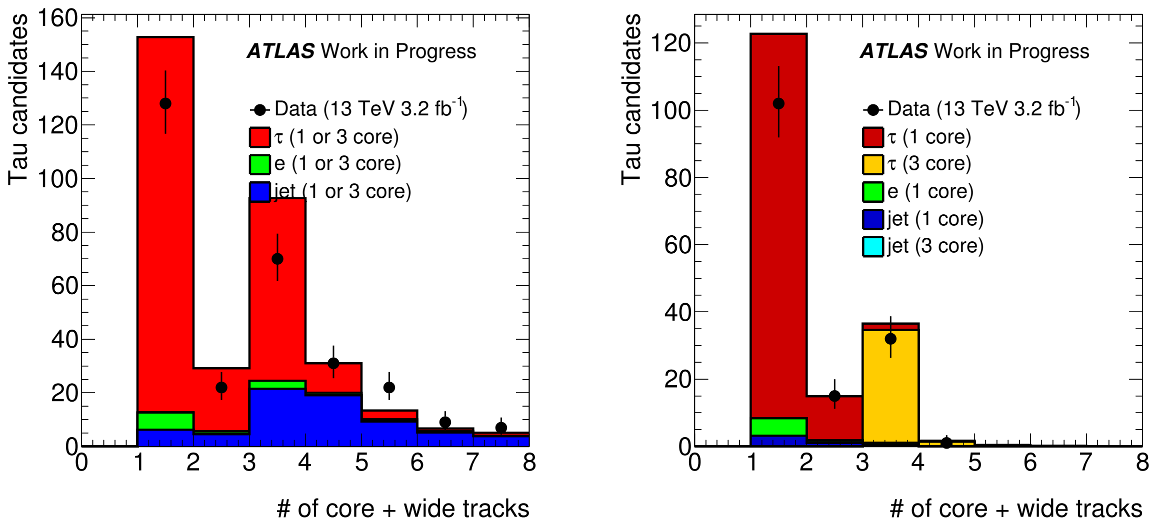

Figure 114: The distributions of the track multiplicity after the simultaneous fit in total (left) and pass (right) channel, where probe p_T binning is inclusive and 'Medium' tau ID is used for pass channel.

ID Level	p_T[GeV]	nCoreTracks	ϵ_{Data}	$\frac{\epsilon_{\mathrm{Data}}}{\epsilon_{\mathrm{MC}}}$
Loose	[30, 200]	1	$0.93^{+0.05}_{-0.11}(stat.)^{+0.05}_{-0.05}(syst.)$	$1.11^{+0.06}_{-0.13}(stat.)^{+0.06}_{-0.06}(syst.)$
Loose	[30, 200]	3	$0.65^{+0.14}_{-0.12}(stat.)^{+0.04}_{-0.02}(syst.)$	$1.04^{+0.22}_{-0.19}(stat.)^{+0.06}_{-0.04}(syst.)$
Loose	[30, 70]	1	$0.87^{+0.12}_{-0.10}(stat.)^{+0.05}_{-0.04}(syst.)$	$1.03^{+0.16}_{-0.14}(stat.)^{+0.06}_{-0.05}(syst.)$
Loose	[30, 70]	3	$0.67^{+0.12}_{-0.10}(stat.)^{+0.03}_{-0.02}(syst.)$	$1.10^{+0.26}_{-0.22}(stat.)^{+0.07}_{-0.04}(syst.)$
Loose	[70, 200]	1	$1.00^{+0.10}_{-0.08}(stat.)^{+0.05}_{-0.04}(syst.)$	$1.21^{+0.15}_{-0.13}(stat.)^{+0.08}_{-0.06}(syst.)$
Loose	[70, 200]	3	$0.60^{+0.10}_{-0.09}(stat.)^{+0.04}_{-0.03}(syst.)$	$0.94^{+0.33}_{-0.28}(stat.)^{+0.13}_{-0.09}(syst.)$
Medium	[30, 200]	1	$0.84^{+0.09}_{-0.13}(stat.)^{+0.09}_{-0.05}(syst.)$	$1.10^{+0.11}_{-0.15}(stat.)^{+0.11}_{-0.06}(syst.)$
Medium	[30, 200]	3	$0.50^{+0.18}_{-0.15}(stat.)^{+0.02}_{-0.00}(syst.)$	$1.11^{+0.29}_{-0.24}(stat.)^{+0.04}_{-0.00}(syst.)$
Medium	[30, 70]	1	$0.58^{+0.14}_{-0.12}(stat.)^{+0.07}_{-0.05}(syst.)$	$0.90^{+0.18}_{-0.15}(stat.)^{+0.08}_{-0.06}(syst.)$
Medium	[30, 70]	3	$0.42^{+0.16}_{-0.13}(stat.)^{+0.04}_{-0.00}(syst.)$	$1.26^{+0.35}_{-0.29}(stat.)^{+0.08}_{-0.00}(syst.)$
Medium	[70, 200]	1	$0.95^{+0.11}_{-0.09}(stat.)^{+0.05}_{-0.03}(syst.)$	$1.29^{+0.17}_{-0.15}(stat.)^{+0.07}_{-0.05}(syst.)$
Medium	[70, 200]	3	$0.46^{+0.14}_{-0.11}(stat.)^{+0.04}_{-0.00}(syst.)$	$1.02^{+0.41}_{-0.34}(stat.)^{+0.12}_{-0.00}(syst.)$
Tight	[30, 200]	1	$0.61^{+0.00}_{-0.16}(stat.)^{+0.00}_{-0.07}(syst.)$	$0.99^{+0.00}_{-0.19}(stat.)^{+0.00}_{-0.09}(syst.)$
Tight	[30, 200]	3	$0.41^{+0.21}_{-0.17}(stat.)^{+0.09}_{-0.05}(syst.)$	$1.31^{+0.33}_{-0.27}(stat.)^{+0.14}_{-0.08}(syst.)$
Tight	[30, 70]	1	$0.80^{+0.06}_{-0.20}(stat.)^{+0.00}_{-0.11}(syst.)$	$1.04^{+0.08}_{-0.27}(stat.)^{+0.00}_{-0.15}(syst.)$
Tight	[30, 70]	3	$0.53^{+0.20}_{-0.15}(stat.)^{+0.09}_{-0.06}(syst.)$	$1.18^{+0.44}_{-0.33}(stat.)^{+0.19}_{-0.13}(syst.)$
Tight	[70, 200]	1	$0.70^{+0.20}_{-0.16}(stat.)^{+0.23}_{-0.09}(syst.)$	$1.27^{+0.37}_{-0.29}(stat.)^{+0.41}_{-0.16}(syst.)$
Tight	[70, 200]	3	$0.39^{+0.18}_{-0.13}(stat.)^{+0.10}_{-0.06}(syst.)$	$1.44^{+0.65}_{-0.48}(stat.)^{+0.38}_{-0.21}(syst.)$

Table 17: The fit result for each pt bin, for each number of core tracks, and for each identification level.

Source	Uncertainty [%]	
	1-track	3-track
Jet template	2.0	4.1
Tau template	0.9	1.2
Ele template	1.5	4.4
Statistics	14.6	24.1
Total	16.0	24.5

Table 18: Dominant uncertainties on the tau identification efficiency correction factors estimated with the tt tag-and-probe method, and the total uncertainty, which combines systematic and statistical uncertainties. These uncertainties apply to $\tau_{\mathrm{had-vis}}$ candidates passing the *medium* tau identification algorithm with 30 GeV < p_{T} < 200 GeV

Loose and Tight isolation is at most 3 %. These differences are considered as OverallSys (normalization uncertainty) in the template fit.

E.7.2. Comparison of $\gamma + jet$ and $W + jet$

To estimate the impact of composition of parton flavor in fake-jet sample, I also measured fake-jet efficiency with $W(\mu\nu) + jet$ sample same as the W control retion of the Ztautau tag and probe analysis. Figure 123 shows comparison of fake-jet efficiency measured with the $\gamma + jet$ sample and with the $W + jet$ sample

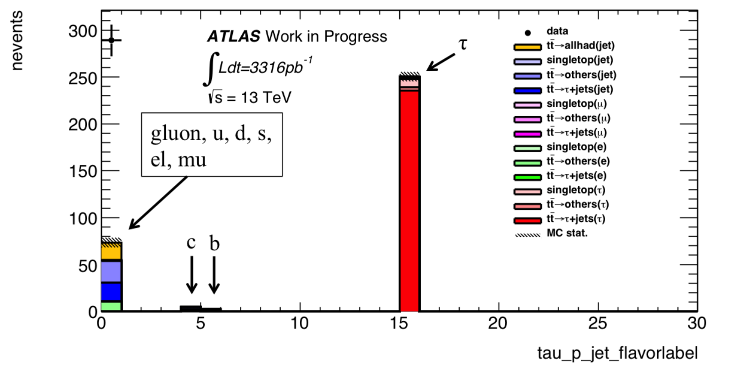

Figure 115: Truth flavor label of probe at the signal region.

for probe with 1 or 3 core tracks, 1 core track, and 3 core tracks respectively. It indicates the differences are at most 100 %, which are considered as OverallSys (normalization uncertainty) in the template fit.

E.8. All Triggers For The $\gamma + jet$ Sample

The following list shows all the triggers actually used for obtaining the $\gamma + jet$ sample. Since low-p_T single-photon triggers are highly prescaled, I sed single-jet and multi-jet triggers to obtain more statistics.

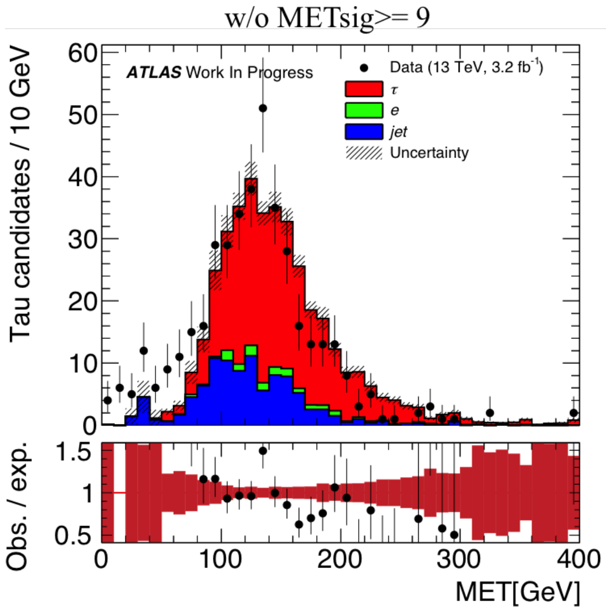

Figure 116: met distribution at the signal region without met significance >= 9 cut

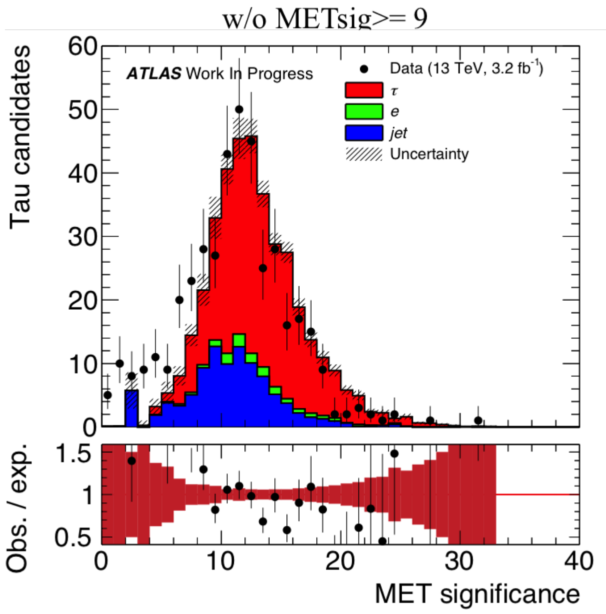

Figure 117: met significance distribution at the signal region without met significance >= 9 cut

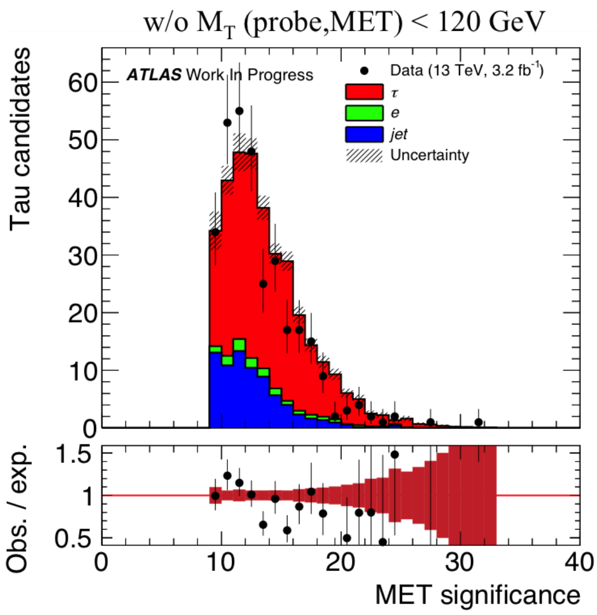

Figure 118: met significance distribution at the signal region without $M_{T,(\text{probe,MET})} < 120$ GeV cut

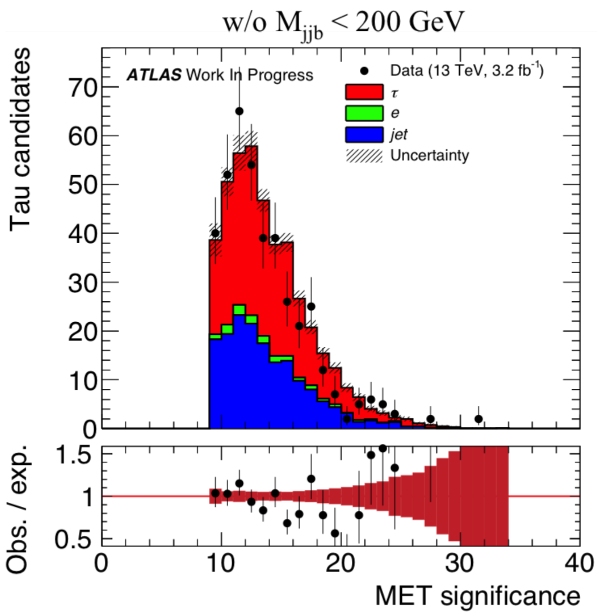

Figure 119: met significance distribution at the signal region without $M_{jjb} < 200$ GeV cut

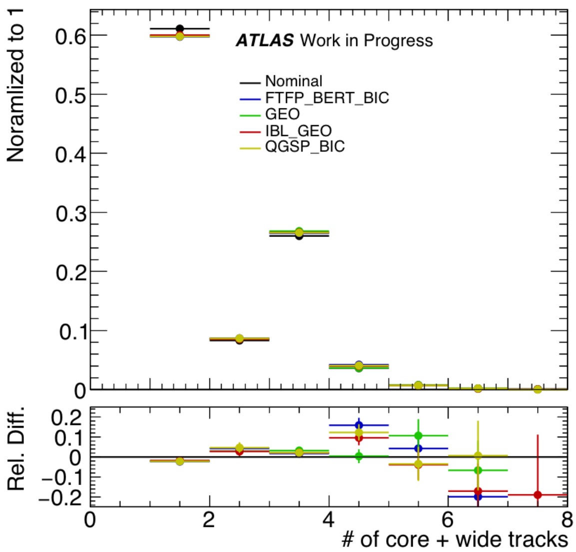

Figure 120: Distributions of the track multiplicity of tau with some systematic variations

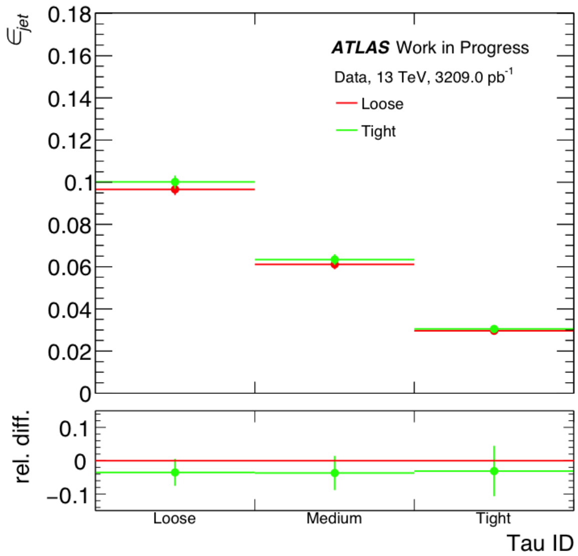

Figure 121: The measured fake-jet efficiency using the sample of fake-jet probes with 1 core track

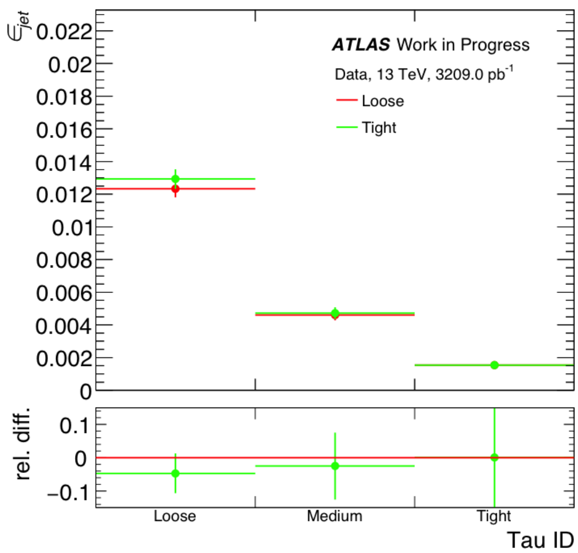

Figure 122: The measured fake-jet efficiency using the sample of fake-jet probes with 3 core tracks

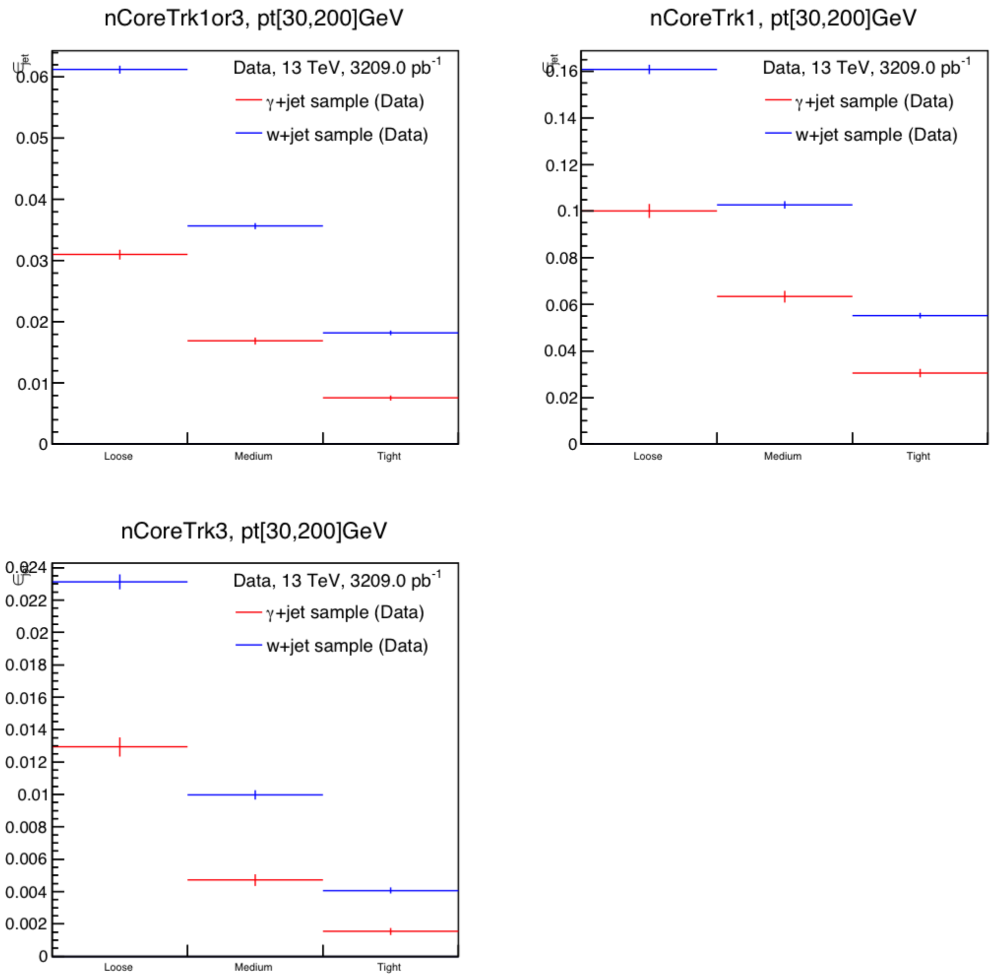

Figure 123: Measured fake-jet efficiency with $\gamma + jet$ sample and with the $W + jet$ sample for probe with 1 or 3 core tracks, 1 core track, and 3 core tracks respectively.

Table 19: All triggers for $\gamma + jet$ sample

single-jet trigger	multi-jet trigger	single-photon trigger
HLT_j15	HLT_3j175	HLT_g10_loose
HLT_j25	HLT_4j25	HLT_g15_loose
HLT_j35	HLT_4j45	HLT_g20_loose
HLT_j45	HLT_4j85	HLT_g50_loose
HLT_j55	HLT_4j100	HLT_g40_loose
HLT_j60	HLT_5j25	HLT_g60_loose
HLT_j85	HLT_5j45	HLT_g70_loose
HLT_j100	HLT_5j55	HLT_g80_loose
HLT_j110	HLT_5j60	HLT_g100_loose
HLT_j150	HLT_5j70	HLT_g120_loose
HLT_j175	HLT_5j85	HLT_g140_loose
HLT_j200	HLT_6j25	HLT_g15_loose_L1EM3
HLT_j260	HLT_6j45	HLT_g15_loose_L1EM7
HLT_j300	HLT_6j45_0eta240	HLT_g20_loose_L1EM12
HLT_j320	HLT_6j45_0eta240_L14J20	HLT_g20_loose_L1EM15
HLT_j360	HLT_6j45_0eta240_L15J150ETA25	HLT_g25_loose_L1EM15
HLT_j380	HLT_6j50_0eta240_L14J20	HLT_g35_loose_L1EM15
HLT_j400	HLT_6j50_0eta240_L15J150ETA25	HLT_g40_loose_L1EM15
HLT_j420	HLT_6j55_0eta240_L14J20	HLT_g45_loose_L1EM15
HLT_j440	HLT_6j55_0eta240_L15J150ETA25	HLT_g50_loose_L1EM15
HLT_j460	HLT_7j25	HLT_g60_loose_L1EM15VH
	HLT_7j45	HLT_g40_tight_xe40noL1
	HLT_7j45_0eta240_L14J20	
	HLT_7j45_0eta240_L15J150ETA25	
	HLT_7j45_L14J20	

F. Online $t\bar{t}$ tau identification efficiency measurement

In pp collisions at $\sqrt{s} = 13$ TeV the production cross section for $t\bar{t}$ pairs is predicted to be 832^{+40}_{-46}pb [29, 30]. With an integrated luminosity of 3.2fb^{-1}, the 2015 ATLAS dataset contains a few million such pairs. The combined branching ratio for the decays of $t\bar{t}$ pairs into a $[b\mu\nu_\mu][b\tau\nu_\tau]$ final state is about 1%.

Similarly to the $Z \to \tau\tau$ process, these events can be used to measure the efficiency of the τ trigger in a tag-and-probe analysis, where the μ acts as the tag and the τ as the probe. The p_{T} spectrum of hadronically decaying τ leptons from top quarks is somewhat harder than those originating from $Z \to \tau\tau$ decays, courtesy of the top quark mass being higher than the Z mass. These can thus be used to measure the trigger efficiency in a region of p_{T} which is otherwise difficult to access.

F.1. Event Selection

In this analysis, τ decays from $t\bar{t} \to [b\mu\nu_\mu][b\tau\nu_\tau]$ events are considered. A tag-and-probe selection is employed, where the μ acts as the tag and the hadronically decaying τ as the probe. In order to suppress non-$t\bar{t}$ processes and obtain a high purity, at least two jets are required in the event, of which at least one is identified as coming from a b-quark (b-tagged). The working point used for b-tagging is chosen to have an efficiency of 77%.

Trigger efficiencies are measured for all three offline τ identification working points (*loose*, *medium*, and *tight*), and the offline identification criterion on the probe τ is selected accordingly. The full list of selection requirements can be found in Table 20.

F.2. Backgrounds and Templates

Simulated events originating from $t\bar{t}$, single top quark, and electroweak processes are generated using the Powheg-Box generator, with the CT10 PDF set for the matrix element calculations. The parton shower, the fragmentation, and the underlying event are simulated using Pythia.

F.2.1. Signal events

All simulated events originating from $t\bar{t}$, single top quark, and electroweak processes where the probe τ is matched to a true hadronically decaying τ are considered as signal events.

F.2.2. Jet fakes modeled with data

The main backgrounds are events where a quark- or gluon-initiated jet is reconstructed and selected (misidentified) as the probe τ. These backgrounds come both from strong interactions (multi-jet events) and from $t\bar{t}$, single top quark, and electroweak processes. The backgrounds are to a large degree modeled using events in the signal region where the opposite-sign charge requirement on the μ and the τ has been inverted (same-sign (SS) data).

Table 20: Event selection requirements for $t\bar{t} \to [b\mu\nu_\mu][b\tau\nu_\tau]$ events.

	Requirement
Trigger	`HLT_mu20_iloose_L1MU15`
μ	Medium quality Trigger matched Inner detector hit $p_T > 22$ GeV $\|\eta\| < 2.5$
e	Loose likelihood ID Inner detector hit $p_T > 15$ GeV $\|\eta\| < 1.37$ or $1.52 < \|\eta\| < 2.47$
τ	Loose, medium, or tight offline ID $\|q\| = 1$ $N_{track} = 1$ or $N_{track} = 3$ $p_T > 20$ GeV $\|\eta\| < 1.37$ or $1.52 < \|\eta\| < 2.47$ No overlapping electron
jet	$p_T > 20$ GeV $\|\eta\| < 4.5$ JVT > 0.64 ($\|\eta\| < 2.4$ and $p_T < 50$ GeV) 77% tagging efficiency for b-jets
preselection	One primary vertex with at least 4 tracks One reconstructed μ No other reconstructed leptons One or more reconstructed τ The μ and the τ have opposite-sign charges Two reconstructed jets
signal region	Gradient isolation on the μ At least one b-tagged jet
QCD control region	Inverted gradient isolation on the μ No b-tagged jet

The normalization (r_{QCD}) factors for the SS data background are derived in control regions rich in multi-jet events, while being poor in signal events and events from other backgrounds. For more information on how the r_{QCD} factors are derived, see Section F.2.5.

F.2.3. Jet fakes modeled with simulated events

In $t\bar{t}$ events where a quark-initiated jet is misidentified as the probe, the fraction of events where the tag μ and the probe τ have opposite-sign charges is greater than the fraction with same-sign charges. When the quark comes from the hadronic decay of a W boson, its charge is partly anti-correlated with the charge of the μ, and the misidentified probe τ can inherit the anti-correlation. Because of this anti-correlation, such events are not completely covered by the SS data background. Some anti-correlation can also be expected in other processes, most notably $Z \to \tau\tau$, where an extra jet is misidentified as coming from a b-quark. Events from $t\bar{t}$, single top quark, and electroweak processes, where a quark-initiated jet is misidentified as the probe, are modeled using simulation with the opposite-sign charge requirement, from which events with the same-sign charge have been subtracted.

F.2.4. Lepton fakes

A very small background ($\sim$ 2.5% of the events with a medium offline identification requirement on the probe τ) comes from events where a lepton is misidentified as the probe. These events from $t\bar{t}$, single top quark, and electroweak processes are also modeled using simulation with the opposite-sign charge requirement, from which events with the same-sign charge have been subtracted.

The signal and background composition for events in the signal region, with a medium offline identification requirement on the probe τ, can be found in Table 21.

Table 21: Signal and background composition for events in the signal region, with a medium offline identification requirement on the probe τ.

	Events	Fraction
Signal	2781.2	52.9%
SS data	1820.4	34.6%
jet $\to \tau$ (MC)	525.9	10.0%
$\{e, \mu\} \to \tau$ (MC)	133.5	2.5%
Total	5261.0	–
Data	5482	–

F.2.5. SS data normalization factors

The normalization factors (r_{QCD}) for the SS data background are parametrized as a function of

- offline τ identification requirement: loose, medium, tight;
- τ N_{track} requirement: 1 or 3;
- 1-track τ: $p_{\text{T}} \leq 40$ GeV or $p_{\text{T}} > 40$ GeV;

- 3-track τ: $p_T \leq 35$ GeV, 35 GeV $< p_T \leq 50$ GeV, or $p_T > 40$ GeV;

The selection criteria applied on the hadronically decaying τ candidates by the identification algorithm at the trigger level changes the SS data normalization factors. Therefore, these are computed separately for selections without applying a τ trigger, and for selections where the τ trigger with a medium online identification criterion, the *track-two* tracking algorithm, and a p_T threshold of 25 GeV is applied (`HLT_tau25_medium1_tracktwo`). It is assumed that only the online identification criterion and the tracking algorithm, and not the p_T threshold, have a large impact on the normalization factors. Therefore, the normalization factors computed for the trigger with a p_T threshold of 25 GeV are used for all triggers with the same online identification criterion and tracking algorithm, even with higher p_T thresholds.

The normalization factors are computed as the ratio of opposite-sign and same-sign events in the QCD control region (see Table 20) with the selected parametrization and with or without τ trigger

$$r_{\mathrm{QCD}}(N_{\mathrm{track}}, \mathrm{ID}, p_T, \mathrm{trigger}) = \frac{N_{\mathrm{OS}}^{\mathrm{QCD\ CR}}(N_{\mathrm{track}}, \mathrm{ID}, p_T, \mathrm{trigger})}{N_{\mathrm{SS}}^{\mathrm{QCD\ CR}}(N_{\mathrm{track}}, \mathrm{ID}, p_T, \mathrm{trigger})}.$$

They are subsequently applied to same-sign events in the signal region to form the (normalized) SS data background

$$\mathrm{SS\ data}(\ldots) = \sum_{p_T} r_{\mathrm{QCD}}(p_T, \ldots) \times \mathrm{SS}^{\mathrm{SR}}(p_T, \ldots)$$

where the contributions from the different p_T ranges have been merged to cover the whole τ p_T range.

The systematic uncertainties related to the SS data normalization factors are split into a statistical and a systematic component. The statistical components is computed assuming that the number of OS and SS events in the QCD control region are distributed according to the normal distribution. To derive the systematic component cuts on two isolation variables are used: the distribution of momentum of tracks inside a cone of $\Delta R < 0.3$ (`ptvarcone30`), and the distribution of energy of calorimeter deposits inside a cone of $\Delta R < 0.2$ (`topoetcone20`) of the μ direction, relative to the offline μ p_T. The cuts are placed and varied individually (between 0.1 and 0.4), and the envelope of the change of the SS data normalization factor under each variation makes one component of the systematic uncertainty. The total systematic uncertainty on the SS data normalization factor is computed by adding the two components in quadrature.

The normalization factors for 1-track, 3-track, and 1- or 3-track τ candidates are shown in Table 22, Table 23, and Table 24 respectively. The τ p_T distributions of opposite-sign and same-sign events in the QCD control region with a *medium* offline τ identification requirement are shown in Figure 124.

F.3. Systematic Uncertainties

The systematic uncertainties that are considered for the analysis are related to

- μ: trigger; reconstruction, and offline identification efficiency; energy scale
- τ: reconstruction and offline identification efficiency; energy scale
- b-jets: (mis-)tagging efficiency of jets originating from b-quarks, c-quarks, and light (uds) quarks
- calculation of the SS data normalization factors (r_{QCD})

	1-track τ candidate		
	loose	**medium**	**tight**
Without τ trigger			
$p_T \leq 40$ GeV	1.13 ± 0.02 ± 0.04	1.19 ± 0.02 ± 0.06	1.20 ± 0.03 ± 0.08
$p_T > 40$ GeV	1.24 ± 0.03 ± 0.05	1.28 ± 0.04 ± 0.08	1.28 ± 0.06 ± 0.10
With τ trigger			
$p_T \leq 40$ GeV	1.18 ± 0.03 ± 0.07	1.21 ± 0.03 ± 0.10	1.25 ± 0.04 ± 0.11
$p_T > 40$ GeV	1.28 ± 0.04 ± 0.07	1.35 ± 0.05 ± 0.09	1.33 ± 0.07 ± 0.11

Table 22: SS data normalization factors (r_{QCD}) with statistical and systematic uncertainties for events with 1-track τ candidates, for selections without and with requiring a τ trigger with a p_T threshold of 25 GeV, and for different ranges in τ p_T.

	3-track τ candidate		
	loose	**medium**	**tight**
Without τ trigger			
$p_T \leq 35$ GeV	1.17 ± 0.02 ± 0.05	1.22 ± 0.04 ± 0.09	1.39 ± 0.08 ± 0.20
35 GeV $< p_T \leq 50$ GeV	1.32 ± 0.05 ± 0.10	1.49 ± 0.09 ± 0.11	1.70 ± 0.17 ± 0.19
$p_T > 50$ GeV	1.58 ± 0.10 ± 0.08	1.95 ± 0.22 ± 0.22	1.83 ± 0.37 ± 0.42
With τ trigger			
$p_T \leq 35$ GeV	1.21 ± 0.08 ± 0.13	1.22 ± 0.11 ± 0.19	1.35 ± 0.19 ± 0.42
35 GeV $< p_T \leq 50$ GeV	1.38 ± 0.07 ± 0.13	1.58 ± 0.12 ± 0.17	1.66 ± 0.21 ± 0.22
$p_T > 50$ GeV	1.80 ± 0.15 ± 0.13	2.06 ± 0.29 ± 0.33	2.03 ± 0.48 ± 0.68

Table 23: SS data normalization factors (r_{QCD}) with statistical and systematic uncertainties for events with 3-track τ candidates, for selections without and with requiring a τ trigger with a p_T threshold of 25 GeV, and for different ranges in τ p_T.

	1- or 3-track τ candidate		
	loose	**medium**	**tight**
Without τ trigger			
$p_T \leq 40$ GeV	1.15 ± 0.01 ± 0.03	1.20 ± 0.02 ± 0.05	1.24 ± 0.03 ± 0.08
$p_T > 40$ GeV	1.30 ± 0.03 ± 0.05	1.38 ± 0.04 ± 0.08	1.36 ± 0.06 ± 0.07
With τ trigger			
$p_T \leq 40$ GeV	1.19 ± 0.02 ± 0.07	1.22 ± 0.03 ± 0.10	1.26 ± 0.04 ± 0.12
$p_T > 40$ GeV	1.34 ± 0.04 ± 0.07	1.43 ± 0.05 ± 0.10	1.39 ± 0.07 ± 0.11

Table 24: SS data normalization factors (r_{QCD}) with statistical and systematic uncertainties for events with 1- or 3-track τ candidates, for selections without and with requiring a τ trigger with a p_T threshold of 25 GeV, and for different ranges in τ p_T.

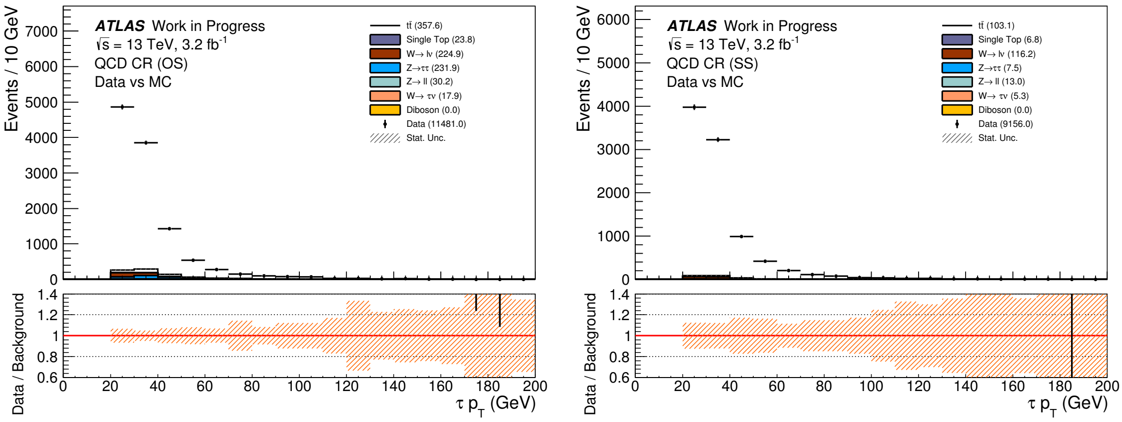

(a) (b)

Figure 124: Distributions of τ p_{T} in data and simulated events (MC) in the QCD control region, with opposite-sign and same-sign events in the left and right plots respectively.

The systematic uncertainties related to trigger, reconstruction, and offline identification efficiencies, as well as those related to the calculation of SS data normalization factors have both statistical and systematic components that are treated individually. The systematic uncertainties related to b-jets are based on an *eigenvector variation method* where the covariance matrices of each source of uncertainty are summed and its eigenvectors calculated. These eigenvectors are then used as a basis for systematic variations, rather than varying the source of each uncertainty.

The overall effect of a specific systematic uncertainty is measured by comparing the yields of background events from SS data and simulated events with and without applying the systematic variation. These effects are less than 1% for all systematic uncertainties considered, except for the statistical and systematic components of the SS data normalization factors (`RQCD_STAT`, `RQCD_SYST`). Systematic uncertainties (including both statistical and systematic components) whose overall effect is 0.05% or less are not used in (*pruned* from) the analysis. The remaining systematic uncertainties are listed in Table 25.

	1-track		**3-track**	
	Without trigger	**With trigger**	**Without trigger**	**With trigger**
RQCD_STAT	1.83%	2.39%	3.59%	6.72%
RQCD_SYST	4.09%	5.84%	6.53%	9.30%
BJET_EIGEN_B0	0.19%	0.22%	0.05%	0.08%
BJET_EIGEN_B1	0.06%	0.07%	0.04%	0.05%
BJET_EIGEN_C0	0.08%	0.11%	0.08%	0.13%
BJET_EIGEN_LIGHT0	0.09%	0.07%	0.06%	0.15%
MUON_TRIG_STAT	0.12%	0.14%	0.05%	0.07%
MUON_TRIG_SYST	0.06%	0.07%	0.02%	0.03%

Table 25: Overall effect of individual systematic uncertainty on all backgrounds measured in selections without and with requiring a τ trigger with a p_{T} threshold of 25 GeV, and for 1-track and 3-track τ candidates separately. If the systematic uncertainty consists of both upward and downward variations, the variation resulting in the highest effect is shown. Systematic uncertainties (or pairs thereof) whose overall effect is 0.05% or less are not shown.

F.4. Method

The efficiency of the τ trigger is measured in signal events (signal), and in data where all backgrounds have been subtracted (data-background). The ratio of the efficiency in data-background and signal (scale factor) can be used as a weight for simulated events where a hadronically decaying τ candidate is matched to the τ trigger object being considered, and to a true hadronically decaying τ lepton. The efficiency is defined as

$$\varepsilon = \frac{C(\text{passed})}{C(\text{total})}$$

where $C(\text{total})$ is the number of events that fulfill the event selection, and $C(\text{passed})$ the number of events that also pass the τ trigger. The efficiency is calculated for bins in reconstructed τ p_{T}. The statistical uncertainty on the efficiency is computed using a Bayesian prior condition in the division, where the efficiency is restricted to the range [0, 1]. Statistical uncertainties are computed for both the signal and the data-background efficiency.

The systematic uncertainties only affect the subtraction of the background, and thus only the data-background efficiency. The total systematic uncertainty is computed bin-by-bin by considering the change in efficiency when applying the systematic variation to all backgrounds compared to the nominal case. All systematic uncertainties are considered correlated with regard to requiring a τ trigger except for `RQCD_STAT` and `RQCD_SYST`, since different SS data normalization factors are used for selections with and without a τ trigger requirement. For correlated systematic uncertainties, the individual deviations from the nominal case are computed as

$$E^{i}_{\text{up|down}} = \frac{C(\text{passed}, \text{syst}^{i}_{\text{up|down}})}{C(\text{total}, \text{syst}^{i}_{\text{up|down}})} - \frac{C(\text{passed})}{C(\text{total})}$$

where $C(\text{total}, \text{syst}^{i}_{\text{up|down}})$ is the total number of events that fulfill the event selection for the given (upwards or downwards) systematic variation, and similarly for the number of events that also pass the τ trigger. For uncorrelated uncertainties, the variations in the total and passed number of events are instead treated as individual systematic uncertainties, each with a corresponding deviation from the nominal case:

$$E^{i,\text{total}}_{\text{up|down}} = \frac{C(\text{passed})}{C\left(\text{total}, \text{syst}^{i}_{\text{up|down}}\right)} - \frac{C(\text{passed})}{C(\text{total})}$$

$$E^{i,\text{passed}}_{\text{up|down}} = \frac{C\left(\text{passed}, \text{syst}^{i}_{\text{up|down}}\right)}{C(\text{total})} - \frac{C(\text{passed})}{C(\text{total})}$$

All positive and negative contributions are summed in quadrature to form the total upward and downward systematic uncertainties on each bin:

$$E^{\text{total}}_{\text{up}} = \sqrt{\sum_i \max(E^{i}_{\text{up}}, E^{i}_{\text{down}})^2}$$

$$E^{\text{total}}_{\text{down}} = \sqrt{\sum_i \min(E^{i}_{\text{up}}, E^{i}_{\text{down}})^2}$$

The scale factor is defined as

$$\text{SF} = \frac{\varepsilon_{\text{data-background}}}{\varepsilon_{\text{signal}}}$$

and the total uncertainty on the scale factor becomes

$$E_{\text{up}}^{\text{SF,total}} = \sqrt{(E_{\text{up}}^{\text{data-background,stat}})^2 + (E_{\text{up}}^{\text{data-background,syst}})^2 + (E_{\text{down}}^{\text{signal,stat}})^2}$$

$$E_{\text{down}}^{\text{SF,total}} = \sqrt{(E_{\text{down}}^{\text{data-background,stat}})^2 + (E_{\text{down}}^{\text{data-background,syst}})^2 + (E_{\text{up}}^{\text{signal,stat}})^2}$$

F.5. Results

F.5.1. Control plots

A comparison between data and signal plus background is shown for distributions of kinematic variables and event variables in the signal region with a *medium* offline identification requirement on the hadronically decaying τ candidate, and with 1 or 3 tracks inclusively. Distributions of kinematic variables of the μ can be found in Figure 125, while those related to the hadronically decaying τ candidate can be found in Figure 126. Figure 127 shows distributions of the τ N_{track} and the output score of the offline τ identification boosted decision tree (BDT) algorithm. Distributions of N_{jets} and $N_{b-\text{jets}}$ can be found in Figure 128, and distributions of missing E_{T} ($E_{\text{T}}^{\text{miss}}$) and the transverse mass (m_{T}) between the τ and the $E_{\text{T}}^{\text{miss}}$ in Figure 129.

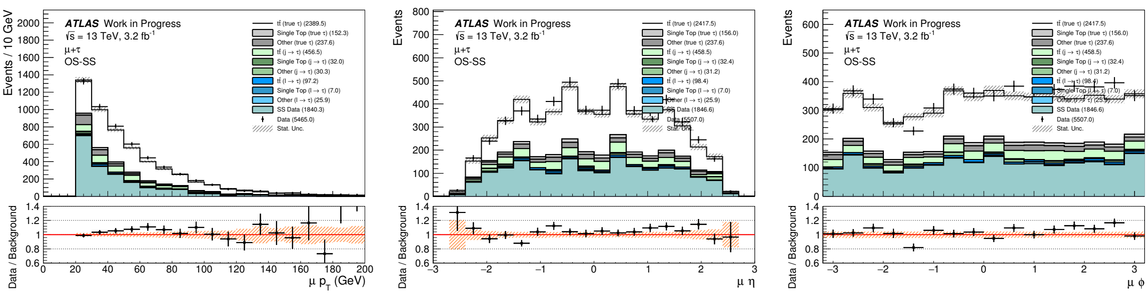

(a) (b) (c)

Figure 125: Kinematic distributions of the tag μ in the signal region with a *medium* offline identification requirement on the hadronically decaying τ candidate, and with 1 or 3 tracks inclusively.

F.5.2. Control plots with τ trigger

The comparison between data and signal plus background is made for events in the signal region with a *medium* offline identification requirement on the hadronically decaying τ candidate, and also for events fulfilling the same selection with the additional requirement that the τ trigger with a p_{T} threshold of 25 GeV is fired. The τ p_{T} distributions with and without applying the τ trigger with a p_{T} threshold of 25 GeV are shown in Figure 130.

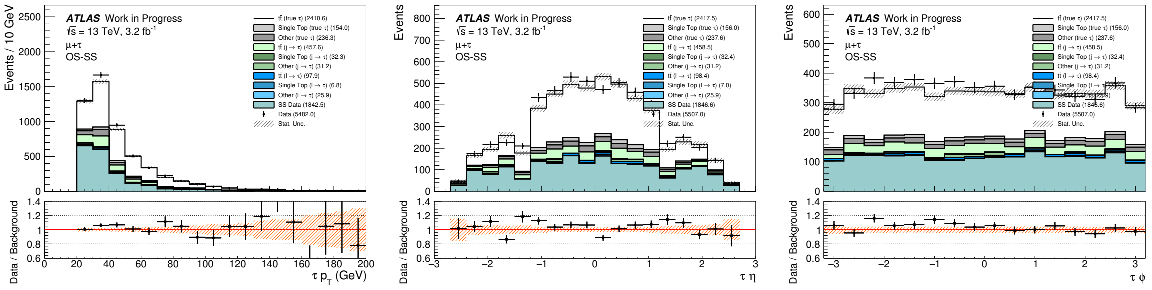

(a) (b) (c)

Figure 126: Kinematic distributions of the probe τ in the signal region with a *medium* offline identification requirement on the hadronically decaying τ candidate, and with 1 or 3 tracks inclusively.

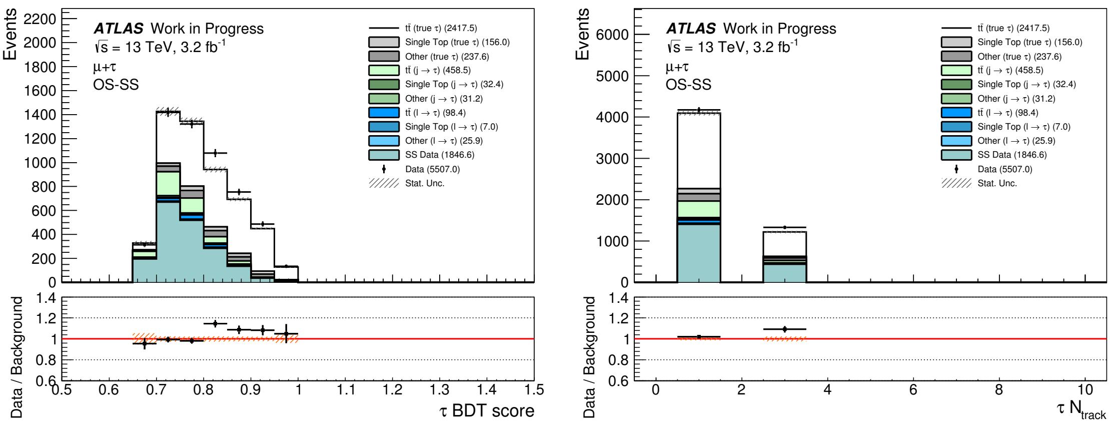

(a) (b)

Figure 127: Distributions of the offline τ BDT score and N_{track} in the signal region with a *medium* offline identification requirement on the hadronically decaying τ candidate, and with 1 or 3 tracks inclusively.

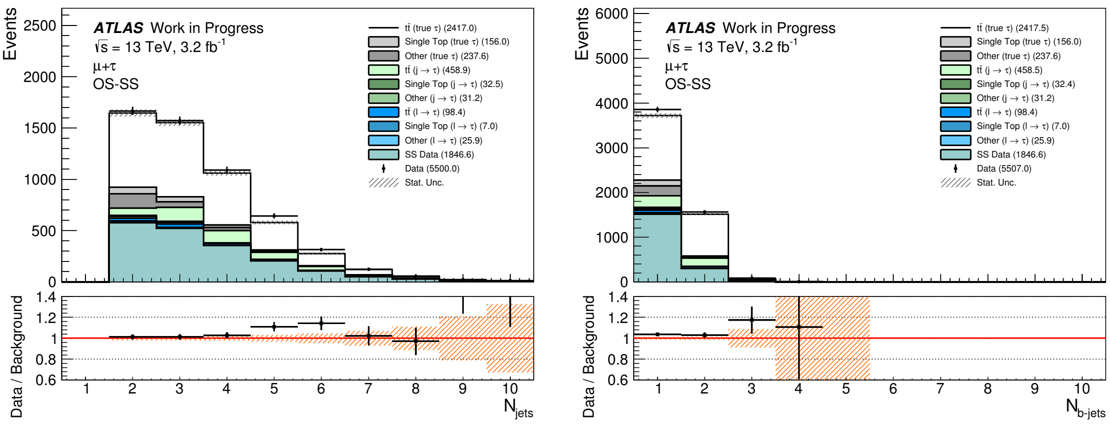

(a) (b)

Figure 128: Distributions of the number of jets and number of *b*-tagged jets in the signal region with a *medium* offline identification requirement on the hadronically decaying τ candidate, and with 1 or 3 tracks inclusively.

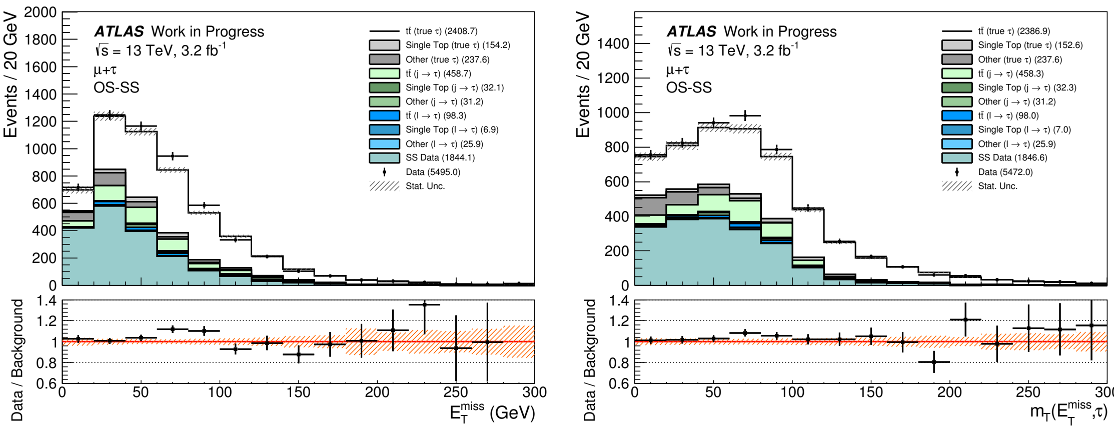

(a) (b)

Figure 129: Distributions of $E_{\mathrm{T}}^{\mathrm{miss}}$ and m_{T} in the signal region with a *medium* offline identification requirement on the hadronically decaying τ candidate, and with 1 or 3 tracks inclusively.

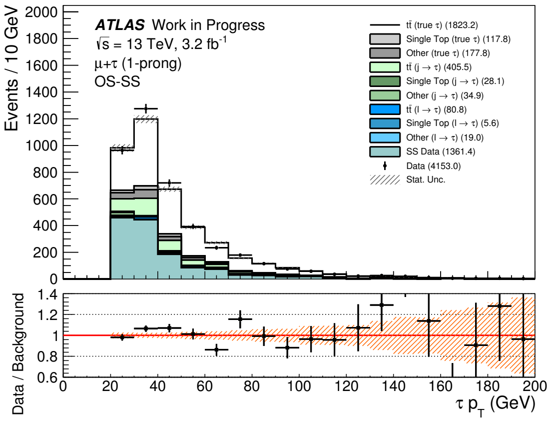

(a)

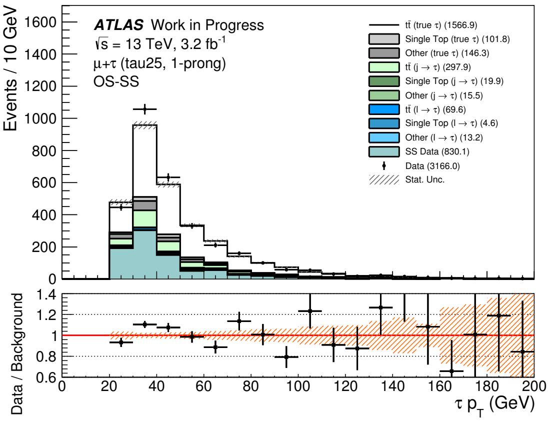

(b)

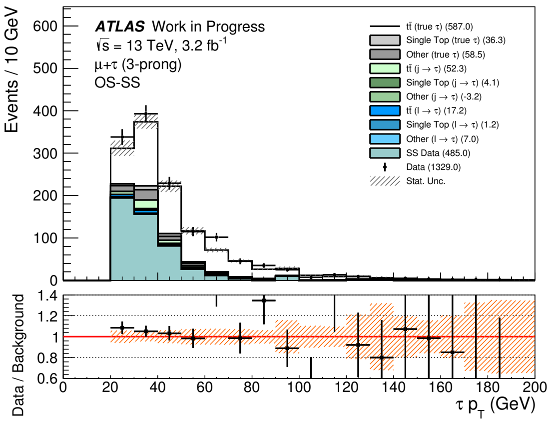

(c)

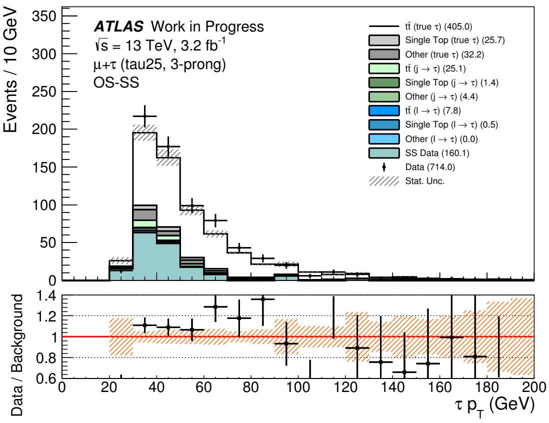

(d)

Figure 130: Distributions of τ p_{T} in the signal region with a *medium* offline identification requirement on the hadronically decaying τ candidate. The distributions on the top and bottom rows are for 1-track and 3-track τ candidates, while the left and right columns are with and without applying the τ trigger with a p_{T} threshold of 25 GeV, respectively.

F.5.3. Efficiencies and scale factors

The efficiencies for signal and data-background, as well as the corresponding scale factors for the τ trigger with a p_{T} threshold of 25 GeV are shown in Figure 131, Figure 132, and Figure 133 for a *loose*, *medium*, and *tight* offline identification requirement on the hadronically decaying τ candidate, respectively.

For *medium* offline ID, the scale factors are consistent with 1 above 39 GeV for 1-track, and above 43 GeV for 3-track τ candidates. Above 100 GeV, the 3-track τ candidates do not have sufficient statistics for a precise measurement of the trigger efficiency. Up to about 40 GeV, the $Z \to \tau\tau$ tag-and-probe analysis provides results with lower statistical and systematic uncertainty.

Both the scale factors for *loose* and *tight* offline ID for 1-track τ candidates show less consistency with 1. In the case of *loose* offline ID, this might be attributed to a slightly lower purity, or that *loose* offline ID τ candidates actually have a lower identification efficiency at the trigger level for data than for simulated events, but it could as well be attributed to a statistical fluctuation. For the *tight* offline ID it could be an effect of lower statistics than for *medium* offline ID, or it might be that the trigger efficiency in simulated events is overestimated in the range 50 – 100 GeV. For the 3-track τ candidates the statistical uncertainties dominate.

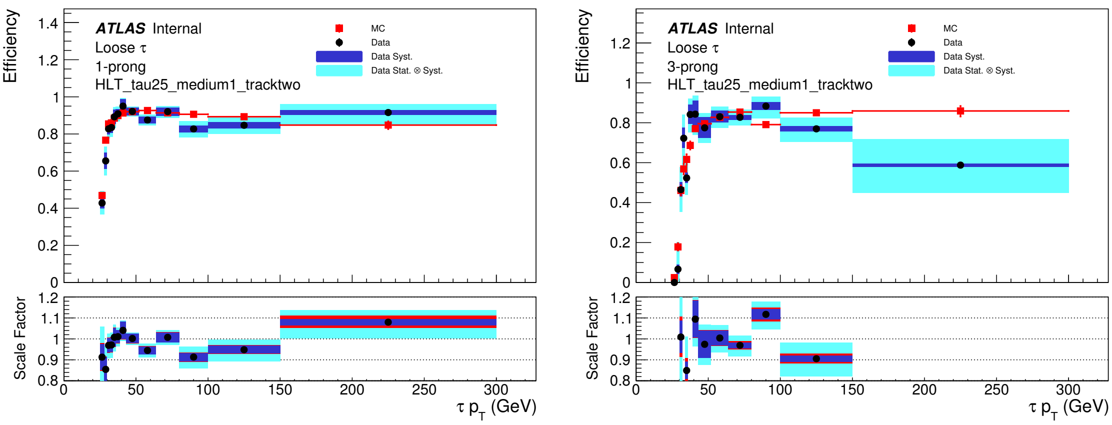

(a) (b)

Figure 131: Efficiencies for signal and data-background and corresponding scale factors for the τ trigger with $p_{\mathrm{T}} > 25$ GeV, and for hadronically decaying τ candidates with a *loose* offline identification requirement.

F.6. Combination of results from $Z \to \tau\tau$ and $t\bar{t}$ trigger tag-and-probe analyses

The scale factors from the tag-and-probe measurements with both $Z \to \tau\tau$ and $t\bar{t}$ are combined in a best linear unbiased estimate (BLUE) [31, 32] fit. An overview of the method and its application to efficiencies and scale factors can be found in [33]. The fit assumes uncorrelated statistical uncertainties, and correlated systematic uncertainties.

The fit is performed with the BLUE ROOT code [34, 35]. The BLUE ROOT code doesn't handle asymmetric uncertainties, and the down uncertainty on the scale factors has been used. The up uncertainties

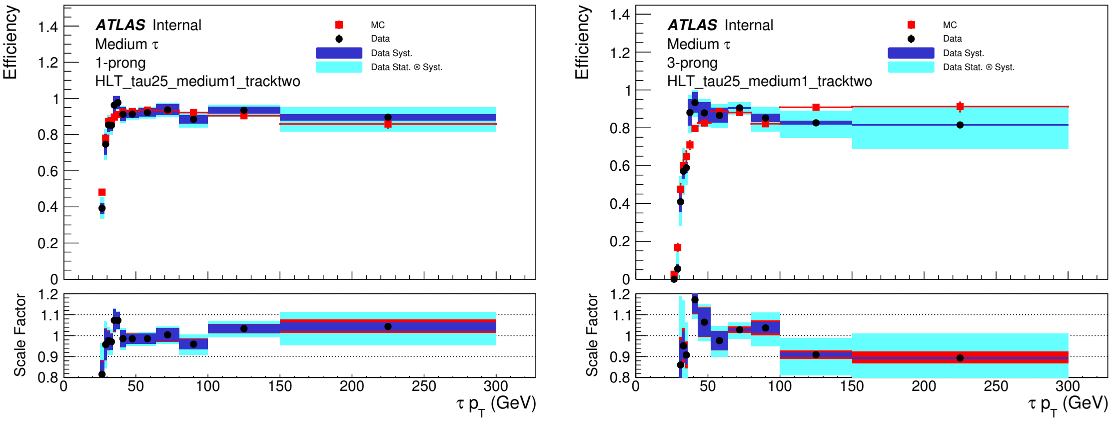

(a) (b)

Figure 132: Efficiencies for signal and data-background and corresponding scale factors for the τ trigger with $p_{\mathrm{T}} > 25$ GeV, and for hadronically decaying τ candidates with a *medium* offline identification requirement.

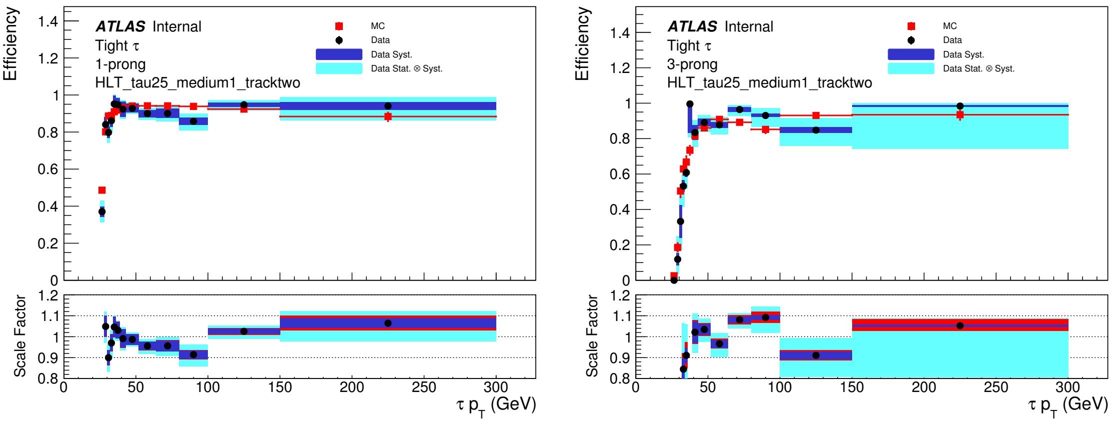

(a) (b)

Figure 133: Efficiencies for signal and data-background and corresponding scale factors for the τ trigger with $p_{\mathrm{T}} > 25$ GeV, and for hadronically decaying τ candidates with a *tight* offline identification requirement.

are generally smaller, and lead to a more constrained uncertainty on the combination, but at the cost of larger pulls in the fit. The fit is done separately for 1- and 3-track τ candidates, and the results are discussed in the following.

The importances of the two contributions are shown in Figure 134. At $p_{\mathrm{T}} < 50$ GeV, the $Z \to \tau\tau$ measurement is completely dominant with weights close to unity. The $t\bar{t}$ measurement starts to become important around $p_{\mathrm{T}} = 50$ GeV, and is dominant, with weights ranging from 0.6¯0.85, at $p_{\mathrm{T}} > 65$ GeV. The importance of the $t\bar{t}$ measurement is overall larger for 1-track τ candidates.

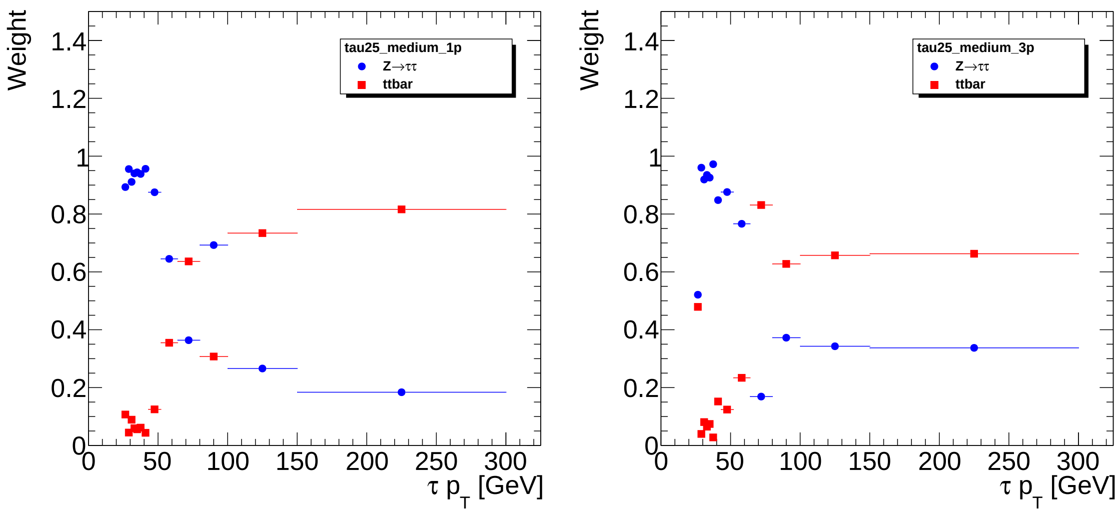

(a) (b)

Figure 134: Weights for the scale factors from the $Z \to \tau\tau$ and $t\bar{t}$ trigger tag-and-probe measurements, as used in the combined result of the BLUE fit.

The pulls of the two contributions are shown in Figure 135. The pulls show some tension in the majority of the bins, but they are mostly constrained to $\sim 1\sigma$ and $\sim 0.5\sigma$ for 1- and 3-track τ candidates respectively. Two bins show particularly large pulls for both 1- and 3-track τ candidates, and these pulls are explained by the statistical variations in the OS and SS data causing anomalous efficiencies in the $t\bar{t}$ measurement.

The scale factors from the combined result of the BLUE fit are shown in Figure 136, along with statistical and systematic uncertainties. Comparisons of the combined result and the scale factors from the individual $Z \to \tau\tau$ and $t\bar{t}$ measurements are shown in Figure 137. The comparisons show that the combined result in general has a better compatibility with unity after the trigger has reached the efficiency plateau. The total uncertainties on the scale factors are also constrained by the fit, and results in a more robust result in the range 50 GeV $< p_{\mathrm{T}} <$ 100 GeV, while above this region the combination is statistically limited.

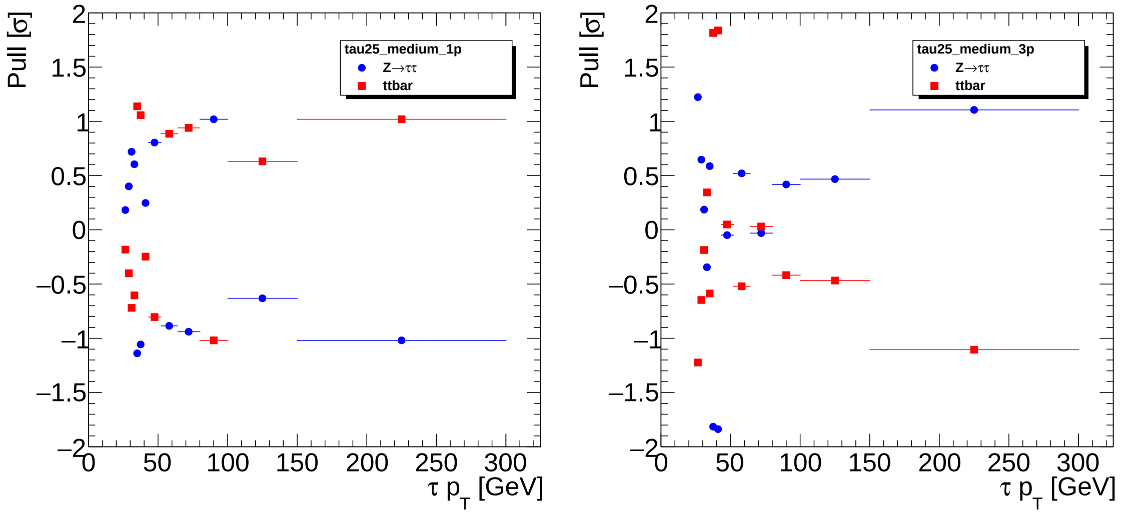

(a) (b)

Figure 135: Pulls describing the tension between the scale factors from the $Z \rightarrow \tau\tau$ and $t\bar{t}$ trigger tag-and-probe measurements, as a result of the BLUE fit.

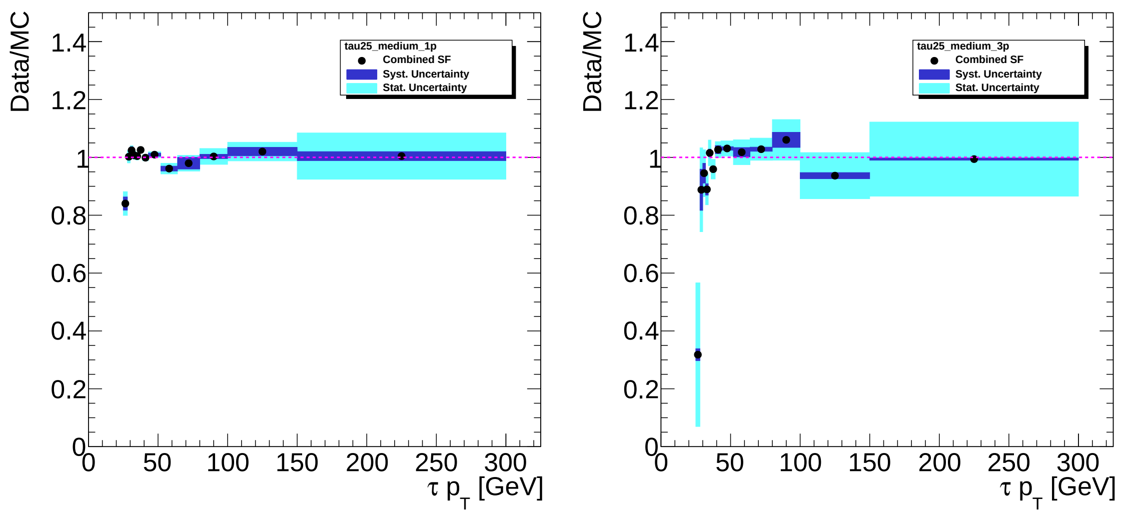

(a) (b)

Figure 136: Scale factors from the combined result of the BLUE fit of the individual $Z \rightarrow \tau\tau$ and $t\bar{t}$ measurements.

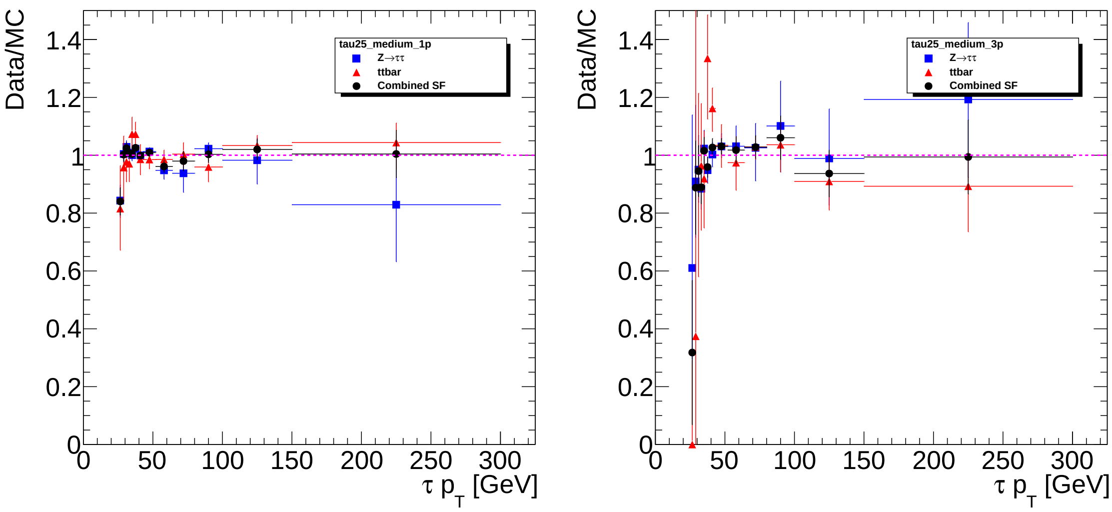

(a)

(b)

Figure 137: Comparisons of the scale factors from the combined result, and the individual $Z \rightarrow \tau\tau$ and $t\bar{t}$ measurements. The uncertainties in the error bars are the total systematic and statistical uncertainties.

G. High-p_{T} tau identification

The uncertainty on the identification of tau decays via the tag and probe method in section A applies only to the modelling of low-p_{T} tau decays, where $p_{\mathrm{T}}^{\tau} < 100$ GeV. A separate study is conducted to investigate the performance of tau identification at high-p_{T}. Due to the low number of $Z \rightarrow \tau\tau$ events in the high-p_{T} region, the performance of the tau identification algorithm is instead tested on jets, with the aim of investigating any discrepancies between the efficiencies measured in MC simulation and data.

G.1. Samples and event selection

The dijet events are simulated in Pythia 8.1 [10]. The samples are differentiated according the truth jet p_{T} as shown in table 26.

sample name	lead jet truth p_{T} range [GeV]
JZ2	60-160
JZ3	160-400
JZ4	400-800
JZ5	800-1300
JZ6	1300-1800
JZ7	1800-2500

Table 26: The various dijet simulation samples and lead jet truth p_{T} ranges used in the analysis.

A region of phase space enriched in dijet events is selected. The event must fire one of the single jet triggers with online p_{T} requirements listed in table 27 along with the corresponding luminosities. In order to scale the simulated dijet background to the combination of triggers, each trigger is used in a specific lead jet p_{T} range, also listed in the table. The p_{T} range is selected to be a region in which the trigger is at its maximum efficiency. The dijet selection cuts applied to data and simulation are:

- tag object $p_{\mathrm{T}} > 150$ GeV
- number of tracks in tag object > 1
- $\cos(\Delta\phi_{\;tag\,-\,probe}) < -0.90$
- the p_{T}-difference between tag and probe objects < 10 %
- tag and probe object $|\eta| < 1.37$ or $1.52 < |\eta| < 2.47$
- loose electron BDT veto applied to the probe object
- probe object has unit charge
- probe object has 1 or 3 charged tracks

where ‘tag’ refers to the highest p_{T} jet, and ‘probe’ refers to the candidate tau object. The selection ensures a high purity of dijet events with the tag and probe objects originating from the hard scatter, whilst the requirements on the probe object maintain similarity to the candidate tau particles used in analyses.

In figures 138 and 139 the tau identification BDT score distributions of the probe candidate tau are shown for, respectively, 1-prong and 3-prong taus firing the various single jet triggers. Given the large statistical

Online p_T requirement [GeV]	Luminosity [pb^{-1}]	Lead jet p_T range [GeV]
110	1.39	150-200
150	5.18	200-250
200	19.03	250-300
260	66.06	300-350
320	184.79	350-400
360	3209.05	> 400

Table 27: Online p_T requirement of single jet triggers and corresponding luminosities in the 2015 dataset, along with the corresponding lead jet p_T range each trigger is used in.

uncertainty on the simulation of dijet events, reasonable agreement between data and MC simulation is seen in the case of 1-prong candidate taus. In the case of 3-prong candidate tau particles, the simulation is overestimated. The data and expected simulation from all the single jet triggers is combined and the overall p_T, η and ϕ distributions of the tag jet and probe tau objects seen in figures 140 and 141, for cases where the probe tau has 1-prong and 3-prong. Finally, figure 142 shows number of vertices for the 1-prong and 3-prong cases, whilst figure 143 shows the number of tracks in the tag and probe objects before the cut on the probe charge and number of tracks is applied.

These checks confirm that the kinematic distributions are comparable between data and simulation in shape. The difference between data and simulation in the 3-prong case is likely due to the difficulty in modelling dijet events, particularly in a new energy regime. Fortunately the issue appears to be one of normalisation, with similarity in the data and simulation shapes, and so should not bias the final result which compares efficiencies.

G.2. Mis-identification rate of tau particles

The mis-identification rate of tau particles is checked by measuring the efficiency of the tau identification algorithm in accepting probe candidate tau objects in the dijet region described in section G.1. The loose, medium and tight working points used in the identification of tau particles require a p_T dependent cut on this BDT score. The efficiency is defined as:

$$\varepsilon = \frac{C(\text{pass cut})}{C(\text{total})}$$

where $C(\text{total})$ is the total number of events passing the dijet selection criteria, and $C(\text{pass cut})$ is the number that additionally pass a cut on the BDT score, and is calculated in bins of reconstructed tau p_T. Figures 144 to 147 show the efficiencies for various BDT score cuts on the probe object as a function its p_T.

A linear function is fit to the ratio of the data and simulation efficiencies and the fit parameters displayed. Across almost all the efficiency plots the uncertainty on the slope parameter is greater than the value of the slope parameter itself. This is consistent with the assumption that the modelling of candidate tau particles does not significantly deteriorate as a function of p_T.

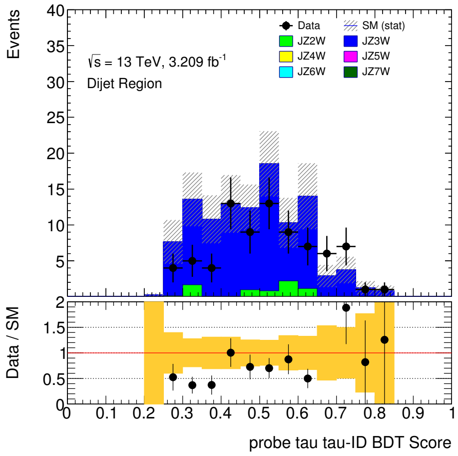

(a) Online p_T requirement 110 GeV

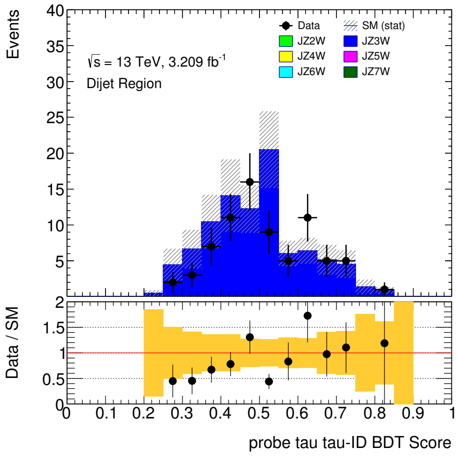

(b) Online p_T requirement 150 GeV

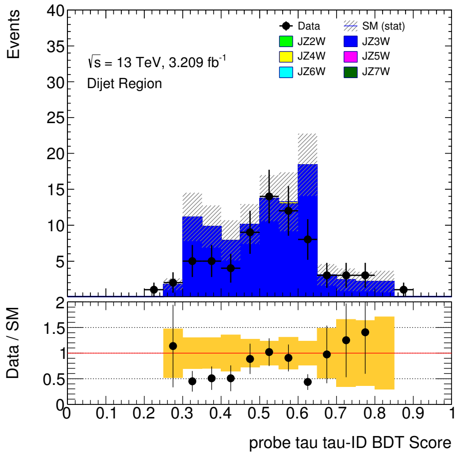

(c) Online p_T requirement 200 GeV

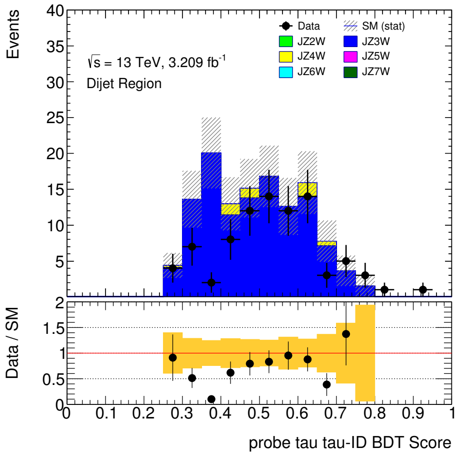

(d) Online p_T requirement 260 GeV

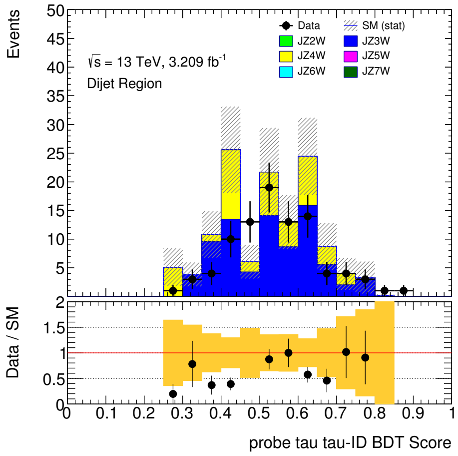

(e) Online p_T requirement 320 GeV

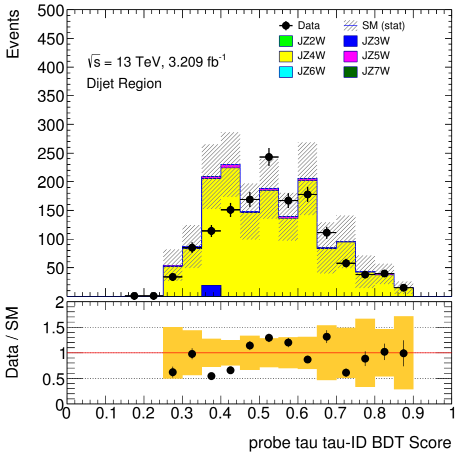

(f) Online p_T requirement 360 GeV

Figure 138: Tau identification BDT scores of the 1-prong probe tau candidate particles for various single jet triggers used in the dijet tag and probe analysis.

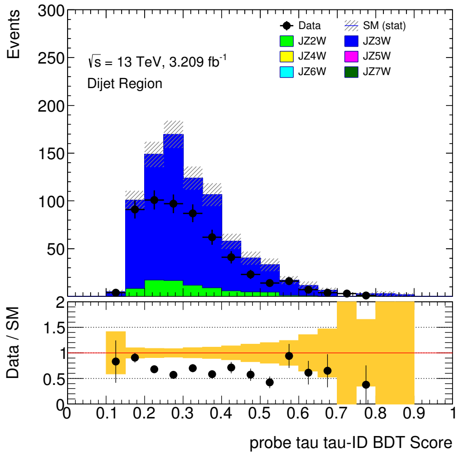

(a) Online p_{T} requirement 110 GeV

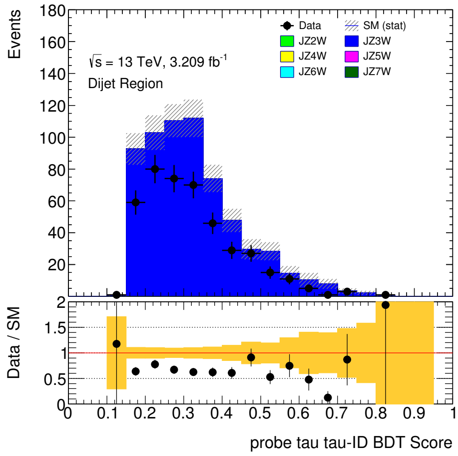

(b) Online p_{T} requirement 150 GeV

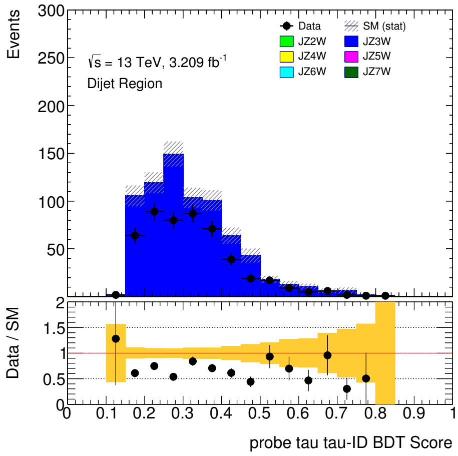

(c) Online p_{T} requirement 200 GeV

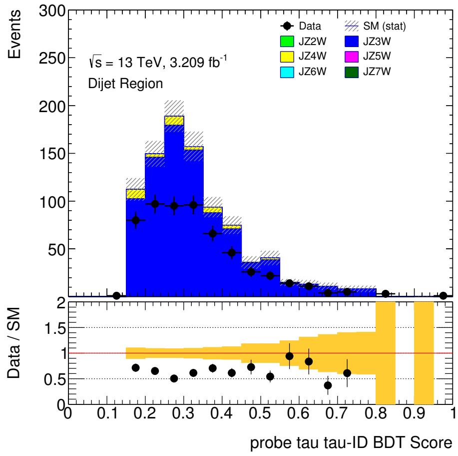

(d) Online p_{T} requirement 260 GeV

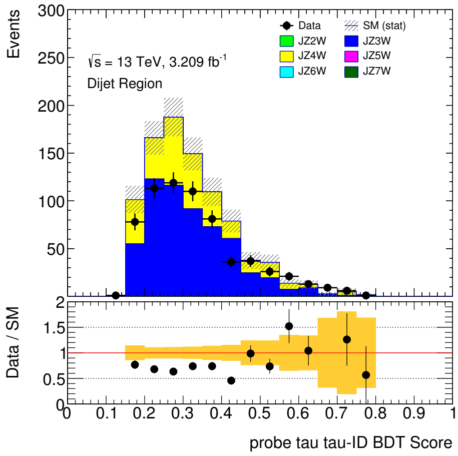

(e) Online p_{T} requirement 320 GeV

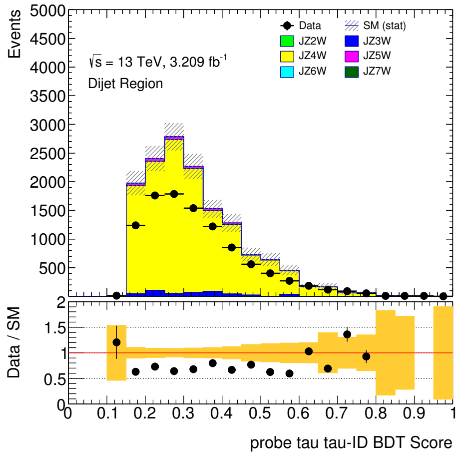

(f) Online p_{T} requirement 360 GeV

Figure 139: Tau identification BDT scores of the 3-prong probe tau candidate particles for various single jet triggers used in the dijet tag and probe analysis.

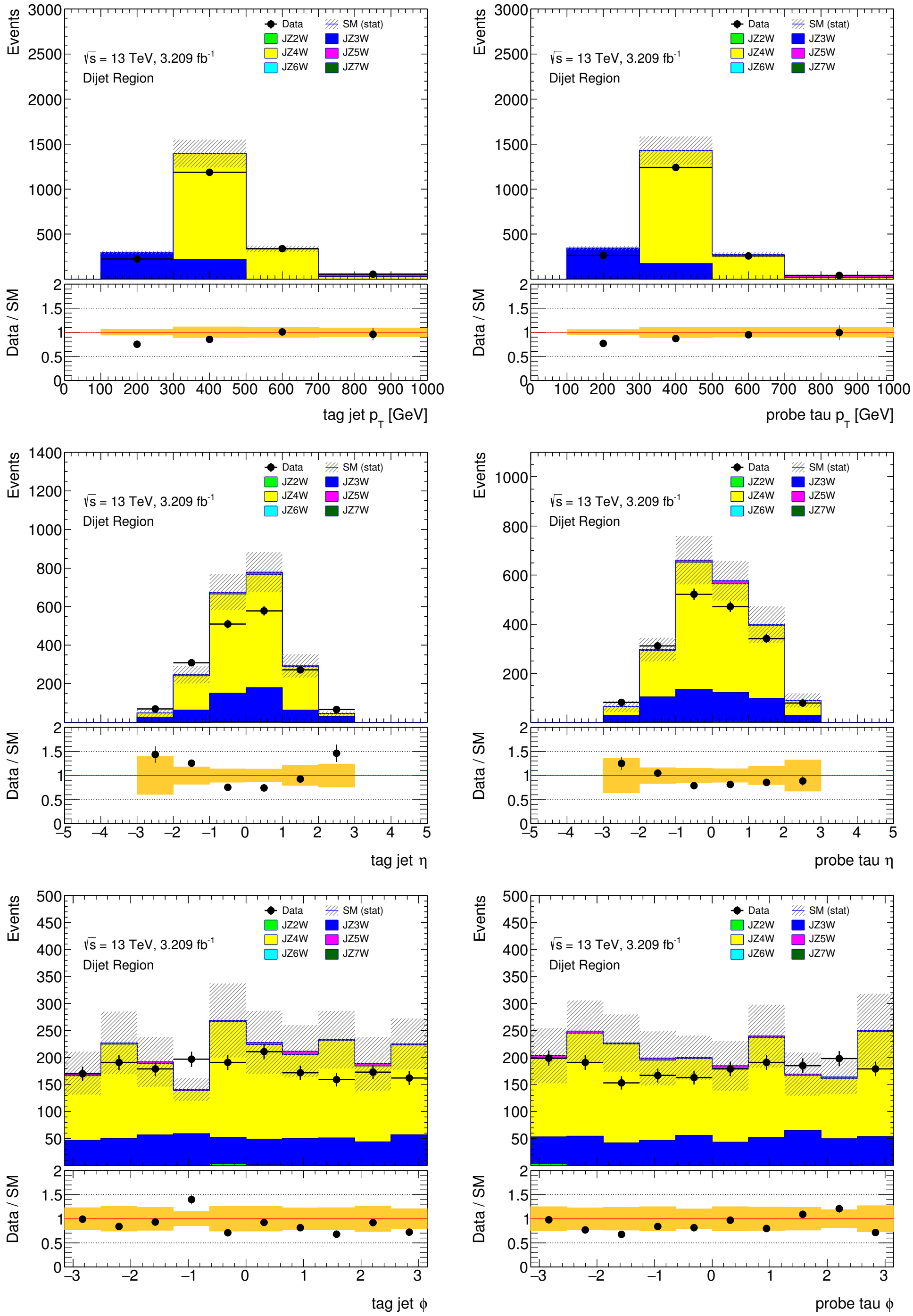

Figure 140: p_{T}, η and ϕ distributions of the (left) tag, and (right) probe objects, for the case of a 1-prong probe tau

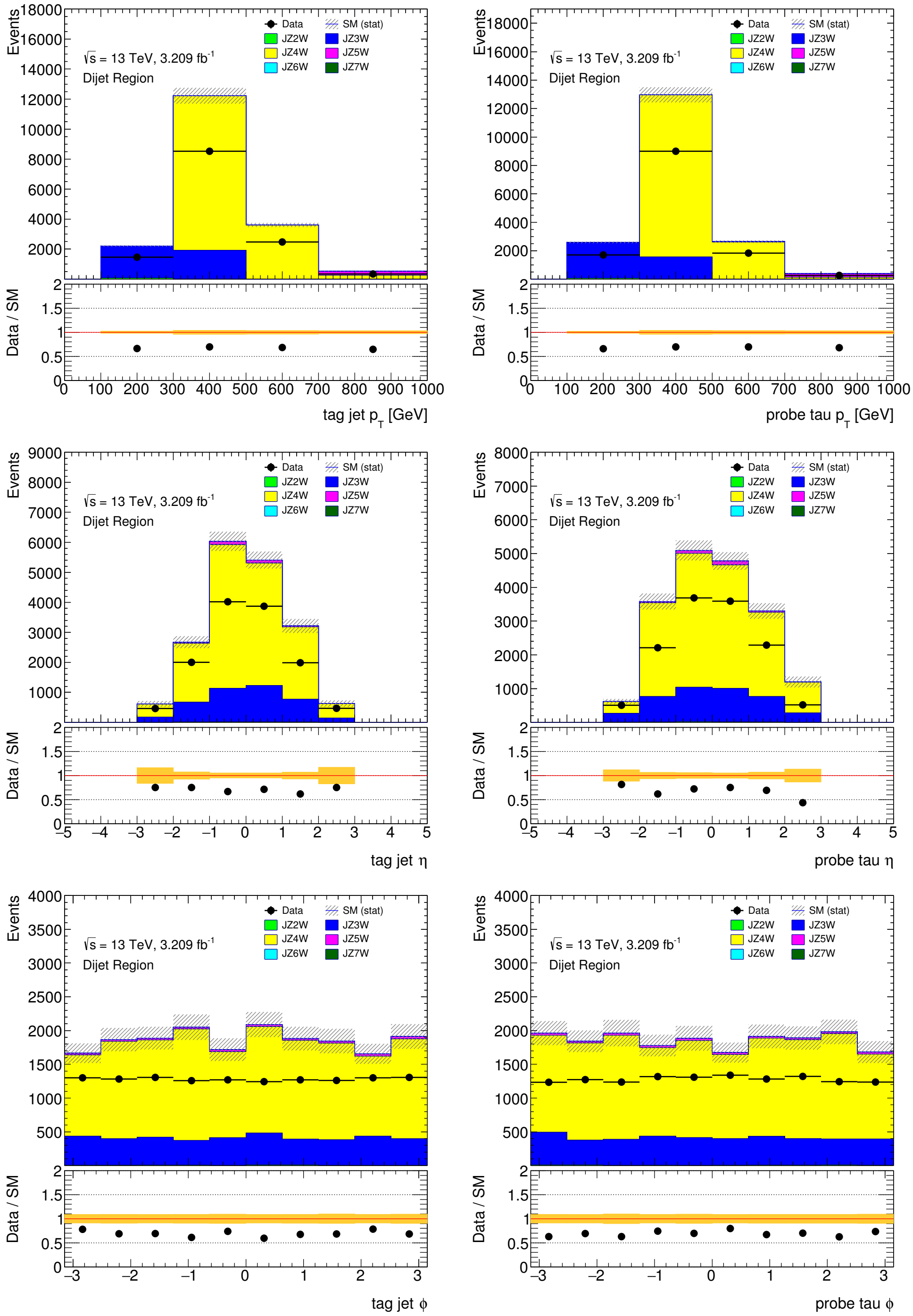

Figure 141: p_{T}, η and ϕ distributions of the (left) tag, and (right) probe objects, for the case of a 3-prong probe tau

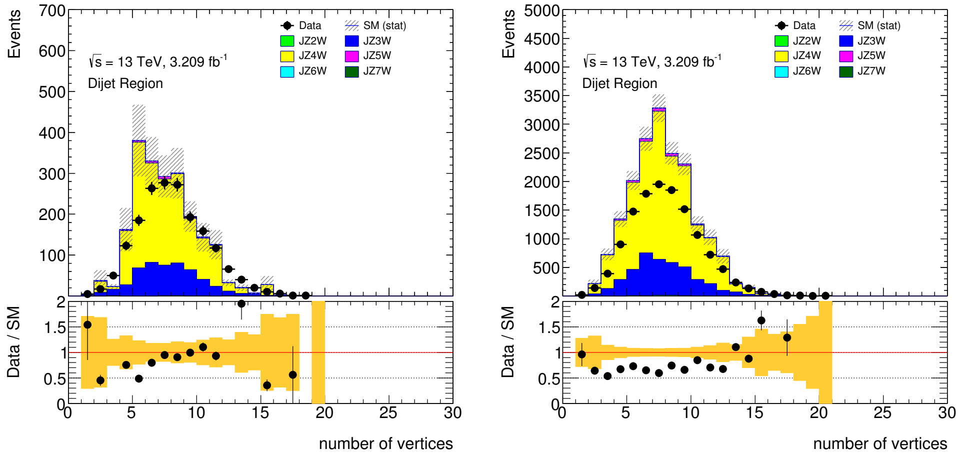

Figure 142: Distributions of number of vertices in (left) 1-prong and (right) 3-prong case.

G.3. High-p_T tau uncertainty inflation

The uncertainty on these slope parameters can be used to propagate the uncertainty on the identification of tau particles in high-p_T regimes. In the $H/A \to \tau\tau$ analysis, which has a significant number of high-p_T tau particles in the signal region, the tau identification efficiency region is approximately 85% for 1-prong taus, and 65% for 3-prong taus. A comparable mis-identification probability occurs in the dijet selection region when cuts are applied to BDT scores of 0.40 in the case of 1-prong probe objects and 0.25 in the case of 3-prong probe objects. The tau identification uncertainty is therefore inflated by 0.019%/ GeV for 1-prong taus and 0.010%/ GeV for 3-prong taus, and summed in quadrature with the low-p_T uncertainty:

$$(\Delta\varepsilon^{1-prong})^2 = (\Delta\varepsilon^{1-prong}_{low-p_\mathrm{T}})^2 + (0.00019/\ \mathrm{GeV} \times (p_\mathrm{T} - 100\ \mathrm{GeV}))^2$$

$$(\Delta\varepsilon^{1-prong})^2 = (\Delta\varepsilon^{1-prong}_{low-p_\mathrm{T}})^2 + (0.00010/\ \mathrm{GeV} \times (p_\mathrm{T} - 100\ \mathrm{GeV}))^2$$

This inflation on the uncertainty accounts for the possibility of a deterioration in tau identification for high-p_T tau candidate particles. Figure 148 shows how the uncertainty on the tau identification increases as a function of the tau p_T.

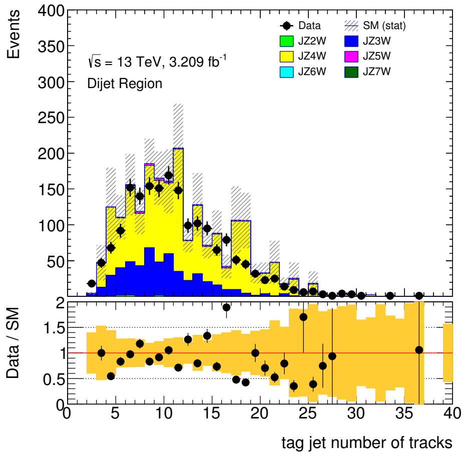

(a) Tag jet (1-prong probe tau)

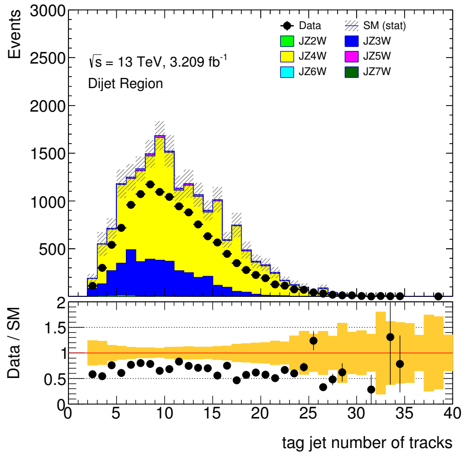

(b) Tag jet (3-prong probe tau)

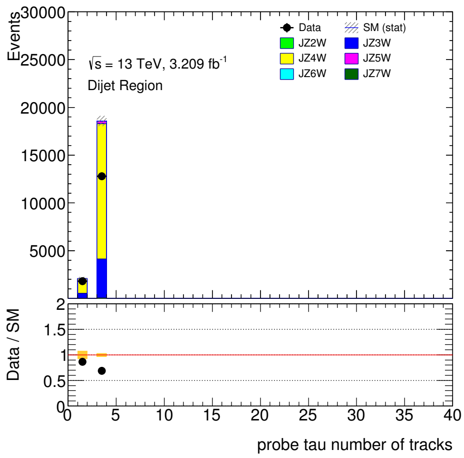

(c) Probe tau (1-prong or 3-prong)

Figure 143: Distributions of number of tracks in a) the tag jet in the case of a 1-prong probe tau, b) the tag jet in the case of a 3-prong probe tau, and c) the probe tau in 1-prong and 3-prong cases combined.

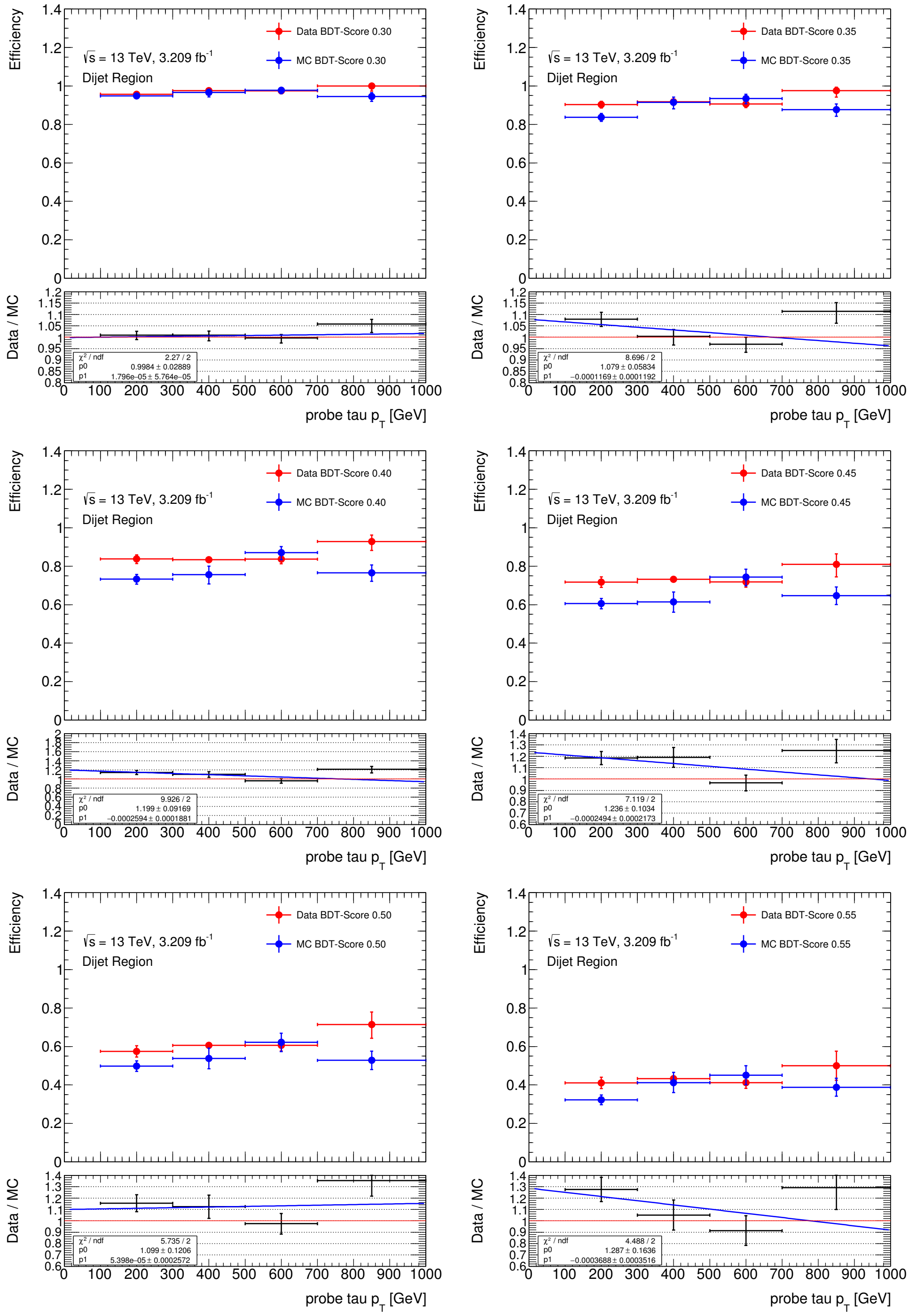

Figure 144: Mis-identification efficiencies of probe 1-prong tau candidates for cuts on various different tau identification BDT scores, as a function of the probe object p_T. Both data and MC simulation are shown as well as the ratio between the two. A linear fit is placed on the data-simulation ratio, and the relevant fit parameters displayed.

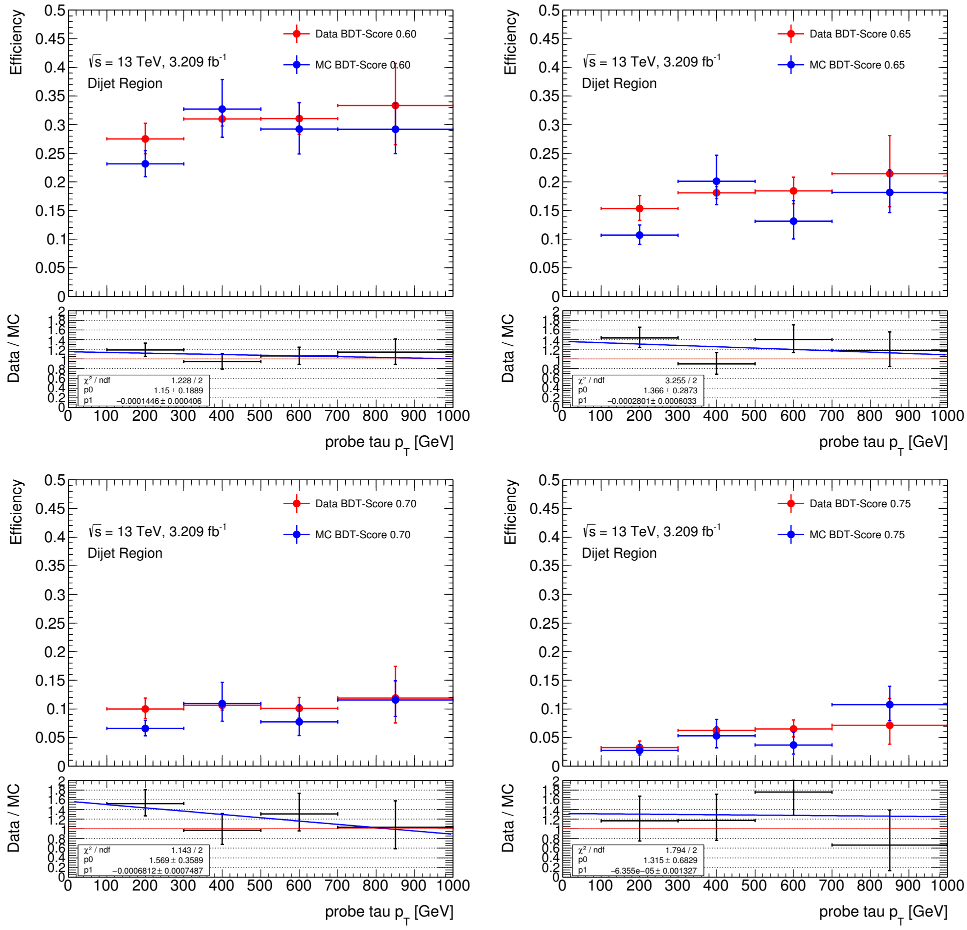

Figure 145: Mis-identification efficiencies of probe 1-prong tau candidates for cuts on various different tau identification BDT scores, as a function of the probe object p_{T}. Both data and MC simulation are shown as well as the ratio between the two. A linear fit is placed on the data-simulation ratio, and the relevant fit parameters displayed.

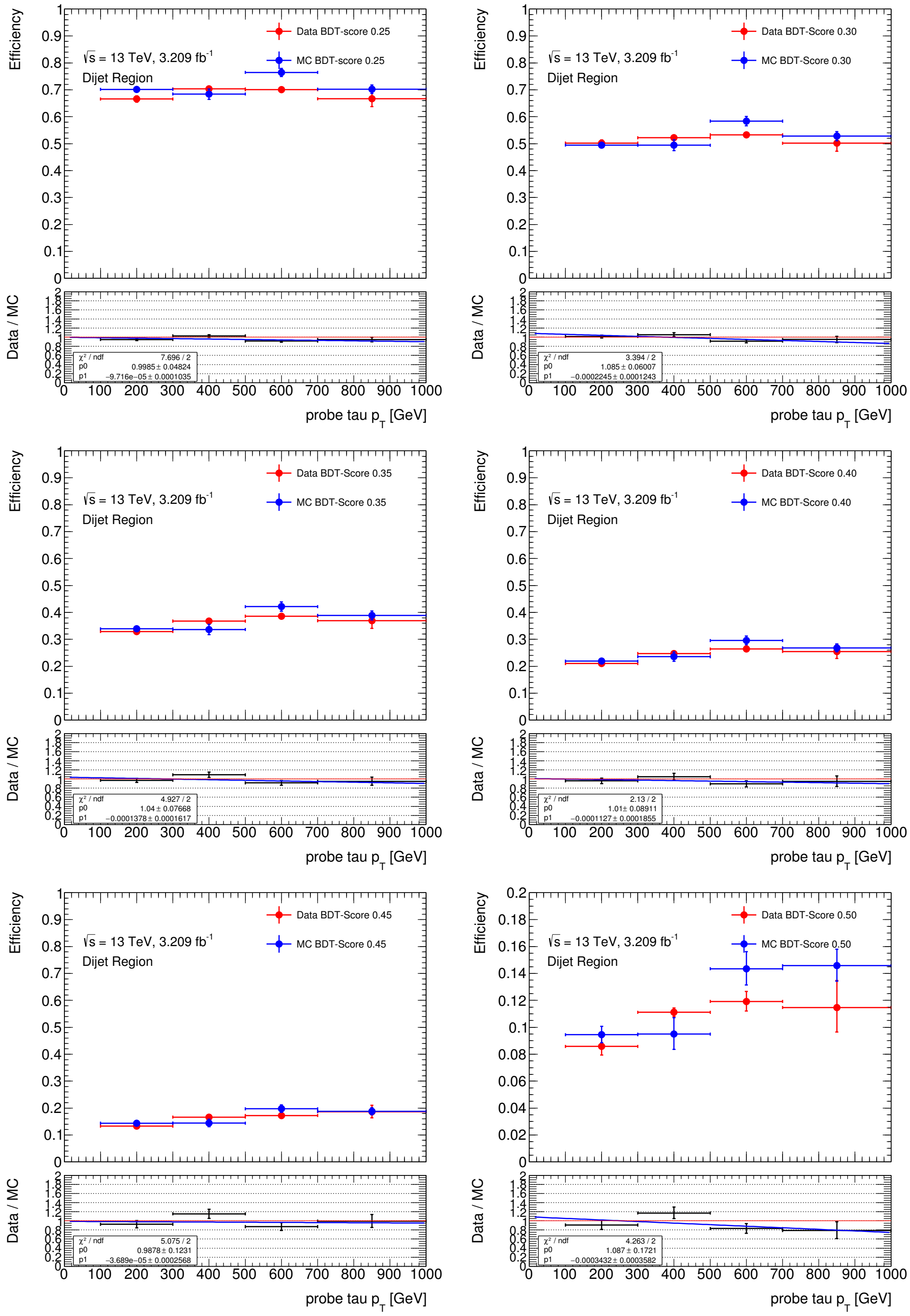

Figure 146: Mis-identification efficiencies of probe 3-prong tau candidates for cuts on various different tau identification BDT scores, as a function of the probe object p_T. Both data and MC simulation are shown as well as the ratio between the two. A linear fit is placed on the data-simulation ratio, and the relevant fit parameters displayed.

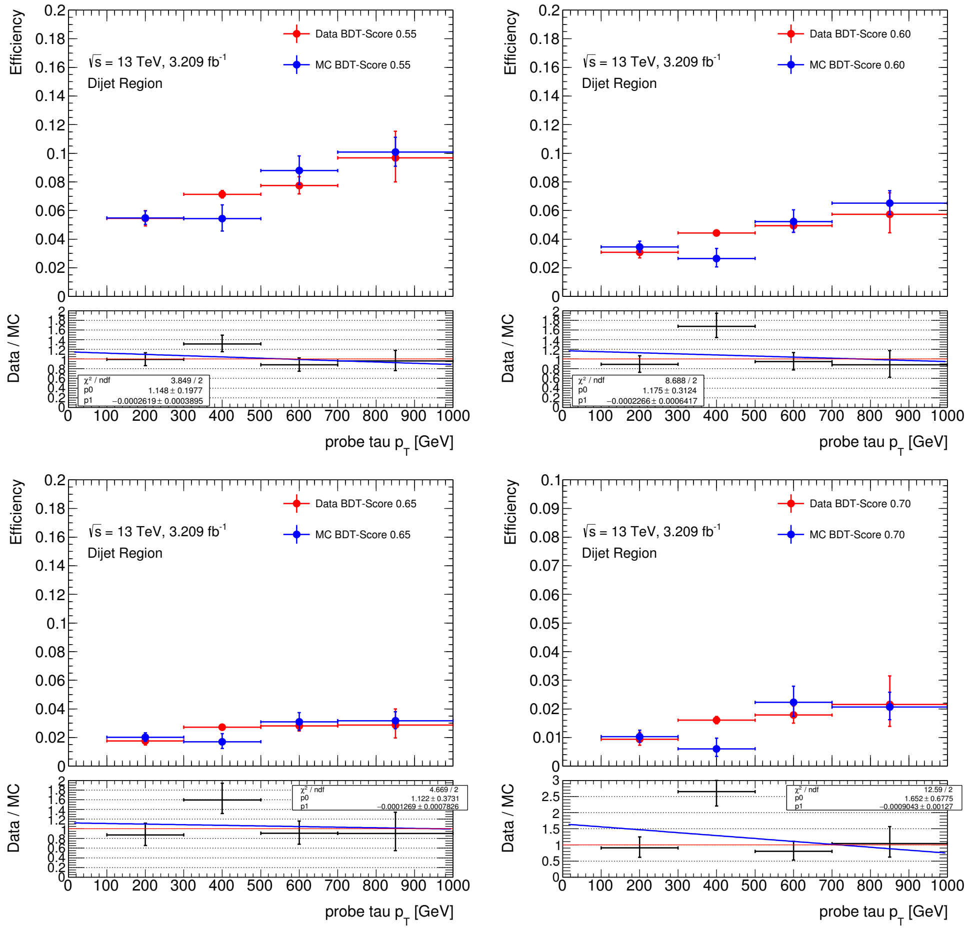

Figure 147: Mis-identification efficiencies of probe 3-prong tau candidates for cuts on various different tau identification BDT scores, as a function of the probe object p_T. Both data and MC simulation are shown as well as the ratio between the two. A linear fit is placed on the data-simulation ratio, and the relevant fit parameters displayed.

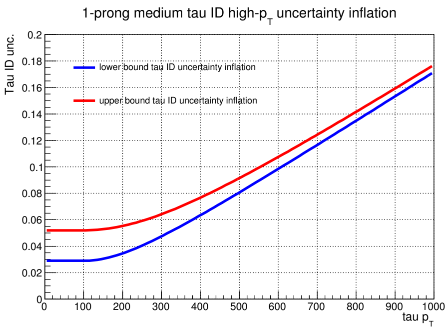

(a) 1-prong Medium tau

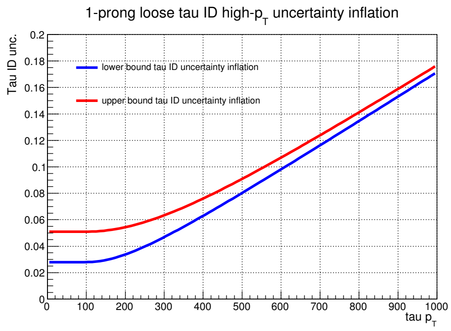

(b) 1-prong Loose tau

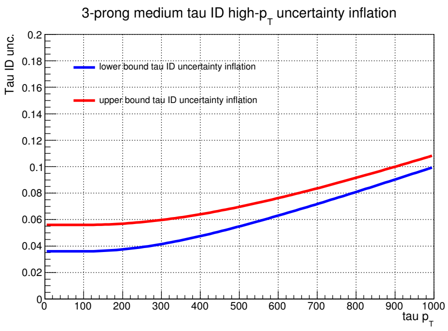

(c) 3-prong Medium tau

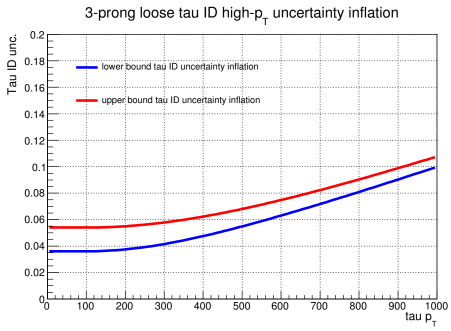

(d) 3-prong Loose tau

Figure 148: Inflation in the uncertainty on the tau identification algorithm as a function of tau candidate p_{T} for various BDT identification working points

H. MVA-based $\tau_{\text{had-vis}}$ energy calibration

The multivariate-analysis-based (MVA-based) $\tau_{\text{had-vis}}$ energy calibration is a new way of calculating visible tau four-momentum using a combination of calorimeter and substructure information. The direction (η-ϕ) is taken directly from the substructure reconstruction, which uses reconstructed charged and neutral pions, providing 5 times better resolution than the calo-based (Baseline) reconstruction from 2015. The energy calibration uses boosted decision trees (BDT) regression to combine calorimeter and substructure information, providing 2 times better resolution than the baseline at low p_{T} ($\sim$ 20 GeV). At high p_{T} the MVA and baseline energy resolutions converge. The overall performance is shown in figure 149.

The final choices of regression algorithm, input variables and regression target are supported by studies that were done using MC15a inclusive $Z \rightarrow \tau\tau$ and mass-binned Drell-Yan $\tau\tau$ samples with medium tau ID requirement. The results of these studies are discussed in the following subsections.

H.1. MVA regression algorithms

MVA regression were performed by using Toolkit for Multivariate Data Analysis with ROOT (TMVA) [24]. TMVA provides a ROOT-integrated environment for processing and evaluating MVA algorithms. A number of MVA algorithms are available in TMVA for single-target regression. They include, for example, linear discriminant analysis (LD), k-nearest neighbour (k-NN), multilayer perceptron (MLP) and boosted decision trees (BDT). These algorithms make use of training events, for which a desired output is known, to approximate the underlying functional behaviour defining the target value.

In order to determine which regression algorithm is more suitable for calculating $\tau_{\text{had-vis}}$ energy, different algorithms were processed on a same set of $Z \rightarrow \tau\tau$ and Drell-Yan $\tau\tau$ training samples. Their performance were then evaluated on another independent set of testing samples. Figure 150 compares the resolutions of the MVA responses ($p_{\text{T}}^{\text{cali}}$) calculated by LD, k-NN, MLP and BDT. Different settings of the algorithms may lead to different performance. In general, settings that require a longer training time give better performance. The comparison was performed using settings such that the training time of each algorithm is limited to $\sim$ 1 day for $\sim 3 \times 10^{6}$ events. The result shows that the resolution of the BDT response is generally better than that of the other algorithms. It is also known that, compared to k-NN and MLP, BDT is more robust against weak variables and suffers less from the curse of dimensionality. For these reasons, subsequent studies and the final calibration were also done using BDT regression.

H.2. Input variables and regression target

A list of input variables that were used for the MVA-based $\tau_{\text{had-vis}}$ energy calibration and their definitions is shown in Table 28. The transverse momenta p_{T}^{LC} and $p_{\text{T}}^{\text{TPF}}$ are the basic input variables that provide basic knowledge about the $\tau_{\text{had-vis}}$ energy. Other input variables are proven to be useful in improving the resolution or closure of the calibration. The regression target is the ratio of the true $\tau_{\text{had-vis}}$ transverse momentum ($p_{\text{T}}^{\text{true,vis}}$) to $p_{\text{T}}^{\text{interp}}$.

The variables μ and n_{PV} are included to provide information about multiple interactions occurring in the same and neighbouring bunch crossings (pile-up). Figure 151 shows a comparison of the non-closure of the BDT response trained with or without μ and n_{PV} as input variables. The non-closure is the offset of

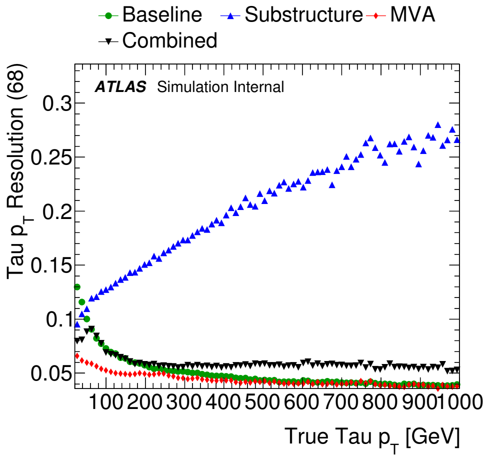

(a) Resolution against true p_T

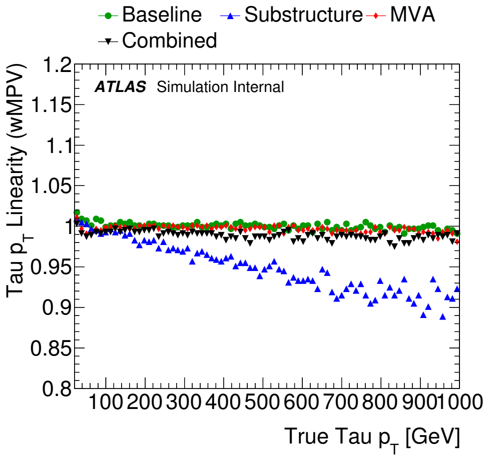

(b) Linearity against true p_T

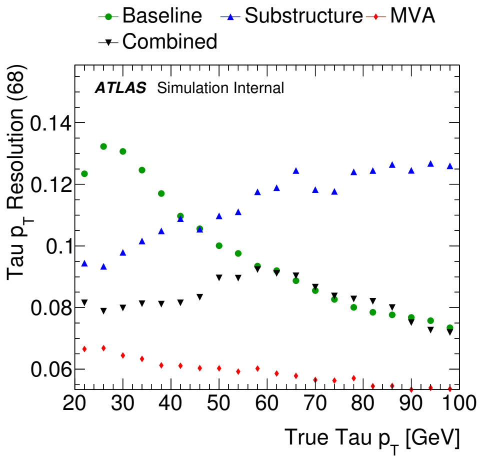

(c) Resolution against true p_T at $p_T < 100$ GeV

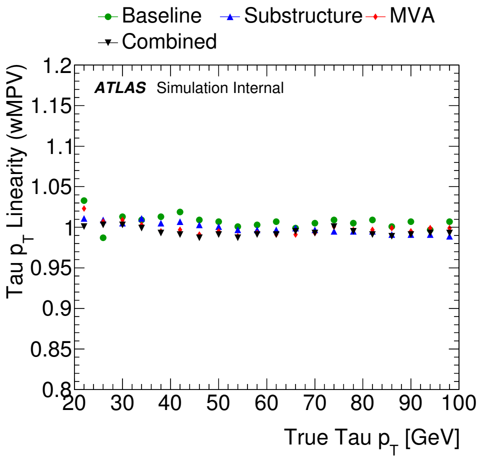

(d) Linearity against true p_T at $p_T < 100$ GeV

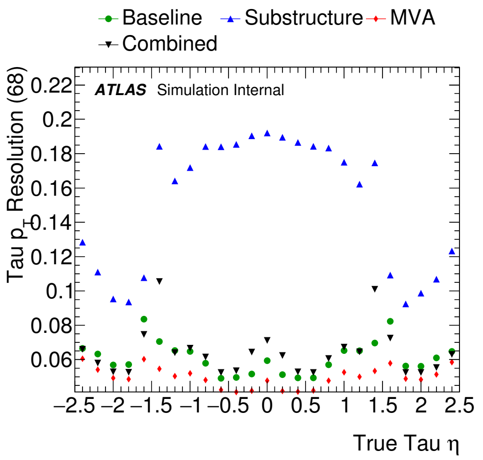

(e) Resolution against true η

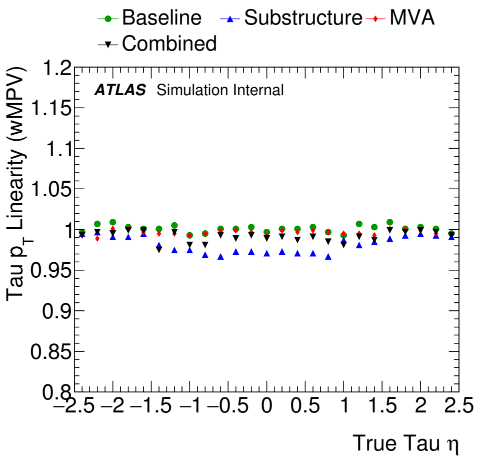

(f) Resolution against true η

Figure 149: The resolutions and linearities of the MVA-based $\tau_{\mathrm{had-vis}}$ energy calibration, compared to the Baseline and substructure reconstructions, and the resolution-weighted average of both (Combined). The resolution is defined as the half-width of the symmetric 68% confidence interval of the ratio of the calibrated p_T (p_T^{cali}) to the true p_T ($p_T^{\mathrm{true,vis}}$). The linearity is defined as the most probable value of the ratio $p_T^{\mathrm{cali}}/p_T^{\mathrm{true,vis}}$.

Number of primary vertices, n_{PV}	
Number of primary vertices in the event	
Average interactions per crossing, μ	
Average number of interactions per bunch crossing	
Cluster shower depth, $\lambda_{\mathrm{centre}}$	
Distance of the cluster shower centre from the calorimeter front face measured along the shower axis	
Cluster second moment in λ, $\left\langle\lambda^2\right\rangle$	
Cluster second moment in λ, the distance of cell from the shower center along the shower axis	
Cluster first moment in energy density, $\langle\rho\rangle$	
Cluster first moment in energy density $\rho = E/V$	
Cluster presampler fraction, $f_{\mathrm{presampler}}$	
Fraction of cluster energy deposited in the barrel and endcap presamplers	
Cluster EM-like probability, P_{EM}	
Classification probability of the cluster to be EM-like	
Number of associated tracks, n_{track}	
Number of tracks associated with the $\tau_{\mathrm{had-vis}}$	
Number of reconstructed neutral pions, n_{π^0}	
Number of reconstructed neutral pions associated with the $\tau_{\mathrm{had-vis}}$	
Relative difference of pion energies, γ_π	
Relative difference of the total charged pion energy E_{charged} and the total neutral pion energy E_{neutral}: $\gamma_\pi = (E_{\mathrm{charged}} - E_{\mathrm{neutral}})/(E_{\mathrm{charged}} + E_{\mathrm{neutral}})$	
Calo-based pseudorapidity, η_{calo}	
Calorimeter-based (Baseline) pseudorapidity	
Interpolated transverse momentum, $p_{\mathrm{T}}^{\mathrm{interp}}$	
Transverse momentum interpolated from LC and substructure reconstruction. Detailed definition is given in section H.4.	
Ratio of $p_{\mathrm{T}}^{\mathrm{LC}}$ to $p_{\mathrm{T}}^{\mathrm{interp}}$, $p_{\mathrm{T}}^{\mathrm{LC}}/p_{\mathrm{T}}^{\mathrm{interp}}$	
Ratio of the local hadron calibration transverse momentum to $p_{\mathrm{T}}^{\mathrm{interp}}$	
Ratio of $p_{\mathrm{T}}^{\mathrm{TPF}}$ to $p_{\mathrm{T}}^{\mathrm{interp}}$, $p_{\mathrm{T}}^{\mathrm{TPF}}/p_{\mathrm{T}}^{\mathrm{interp}}$	
Ratio of the substructure reconstruction transverse momentum to $p_{\mathrm{T}}^{\mathrm{interp}}$	

Table 28: List of input variables used for $\tau_{\mathrm{had-vis}}$ energy MVA regression. The cluster variables are the energy weighted averages over the jet seed constituents. Detailed definitions of the cluster variables can be found in [18].

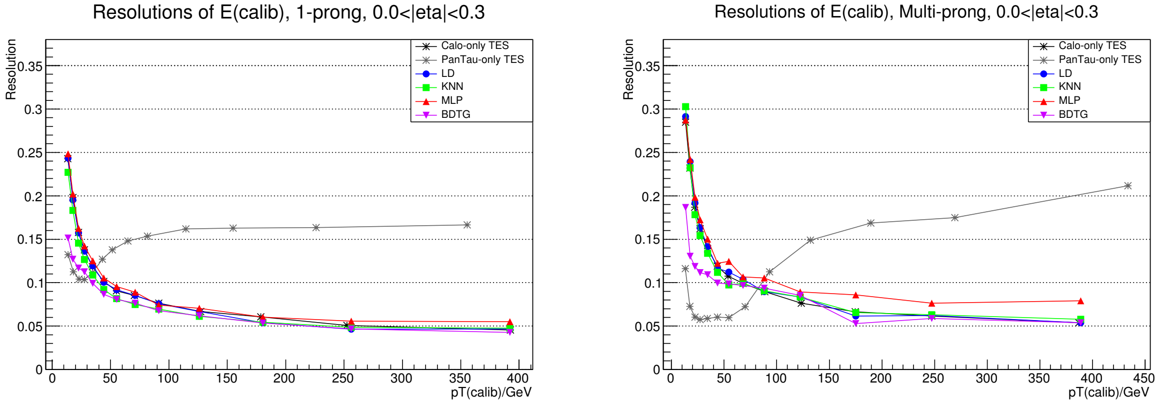

(a) 1-prong $\tau_{\text{had-vis}}$ (b) multi-prong $\tau_{\text{had-vis}}$'s

Figure 150: The resolutions of $p_{\text{T}}^{\text{cali}}$ for (a) 1-prong and (b) multi-prong $\tau_{\text{had-vis}}$'s obtained by LD (blue), k-NN (green), MLP (red) and BDT (violet) regression algorithms. The resolutions of calo-based (black) and substructure (grey) calibrations are plotted in the same figures for comparison. Results for $|\eta| > 0.3$ were not shown here, but their features are similar.

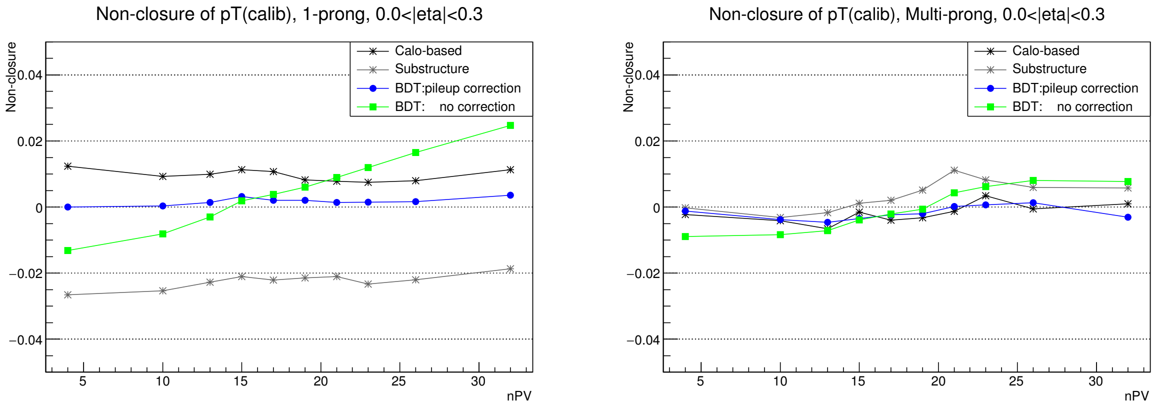

(a) 1-prong $\tau_{\text{had-vis}}$ (b) multi-prong $\tau_{\text{had-vis}}$'s

Figure 151: The non-closure of $p_{\text{T}}^{\text{cali}}$ against n_{PV} for (a) 1-prong and (b) multi-prong $\tau_{\text{had-vis}}$'s obtained by BDT regressions with (blue) or without (green) the variables μ and n_{PV}. Results for $|\eta| > 0.3$ were not shown here, but their features are similar.

the most probable value of the ratio $p_{\text{T}}^{\text{cali}}/p_{\text{T}}^{\text{true,vis}}$ away from one. It can be seen from the result that by including μ and n_{PV} as inputs, the non-closure has been significantly improved against pile-up.

The Baseline $\tau_{\text{had-vis}}$ reconstruction used p_{T}^{LC} and cluster variables to calibrate the $\tau_{\text{had-vis}}$ energy. Following the same idea, cluster variables are also included as input to the MVA training. It is shown that the cluster variables listed in Table 28 can be used by the BDT algorithm to significantly improve $\tau_{\text{had-vis}}$ energy resolution at low p_{T}. Figure 152 shows the resulted resolution for BDT trainings with or without cluster variables.

γ_{π} and n_{π^0} are variables that provide information about the τ decay modes. It has also been shown that the inclusion of these variables improves the resolution of the BDT response at low p_{T}. The result of the

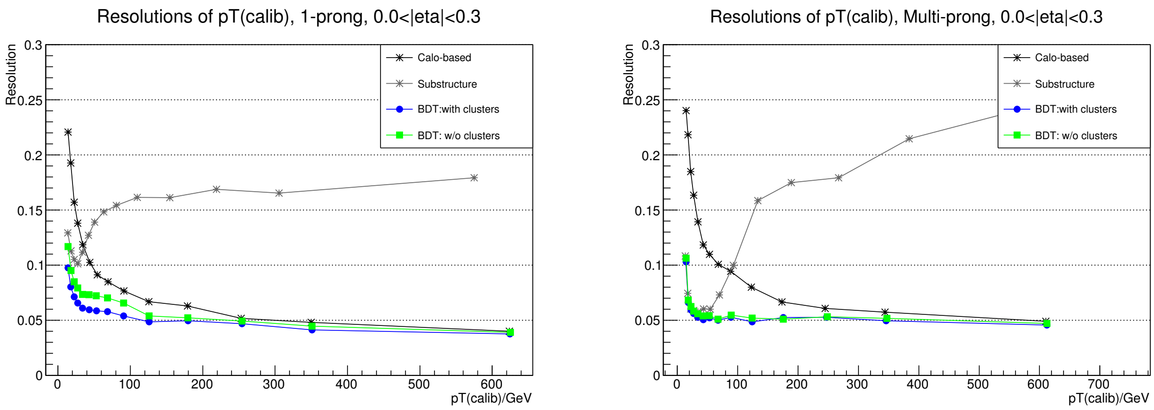

(a) 1-prong $\tau_{\mathrm{had-vis}}$ (b) multi-prong $\tau_{\mathrm{had-vis}}$'s

Figure 152: The resolutions of $p_{\mathrm{T}}^{\mathrm{cali}}$ for (a) 1-prong and (b) multi-prong $\tau_{\mathrm{had-vis}}$'s obtained by BDT regressions with (blue) or without (green) the cluster variables. Results for $|\eta| > 0.3$ were not shown here, but their features are similar.

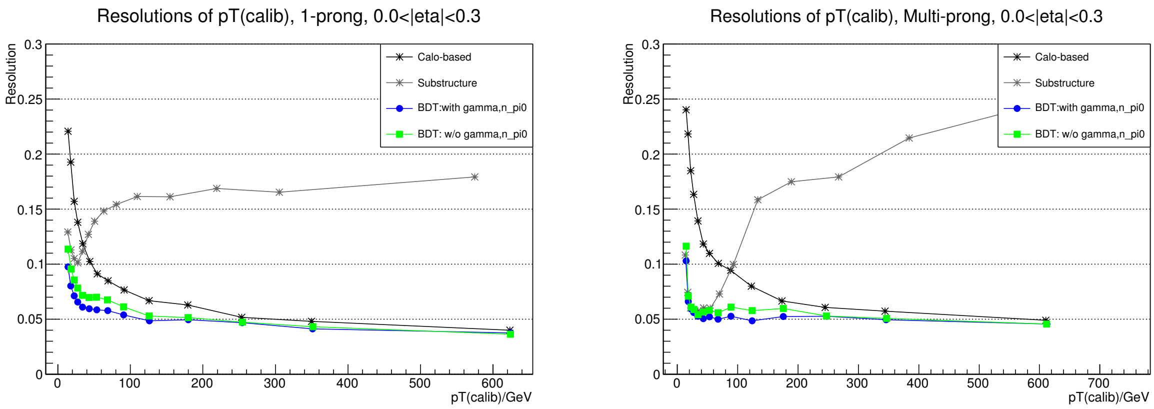

(a) 1-prong $\tau_{\mathrm{had-vis}}$ (b) multi-prong $\tau_{\mathrm{had-vis}}$'s

Figure 153: The resolutions of $p_{\mathrm{T}}^{\mathrm{cali}}$ for (a) 1-prong and (b) multi-prong $\tau_{\mathrm{had-vis}}$'s obtained by BDT regressions with (blue) or without (green) the the variables γ_{π} and n_{π^0}. Results for $|\eta| > 0.3$ were not shown here, but their features are similar.

study is shown in figure 153.

H.3. Raw values and ratios of variables

MVA training algorithms are sensitive to correlations between variables. In general, having two or more highly correlated input variables are not desirable. The algorithms are likely to treat some of the input variables as redundant information. For $\tau_{\mathrm{had-vis}}$ energy calibration, the different energy scales $p_{\mathrm{T}}^{\mathrm{LC}}$ and $p_{\mathrm{T}}^{\mathrm{TPF}}$ are highly correlated variables. If the raw values of the energy scales are used as input, there are chances that the MVA regression cannot make full use of the available information. Therefore, ratios of these variables are used instead of the raw values to reduce their correlation. Figure 154 compares the

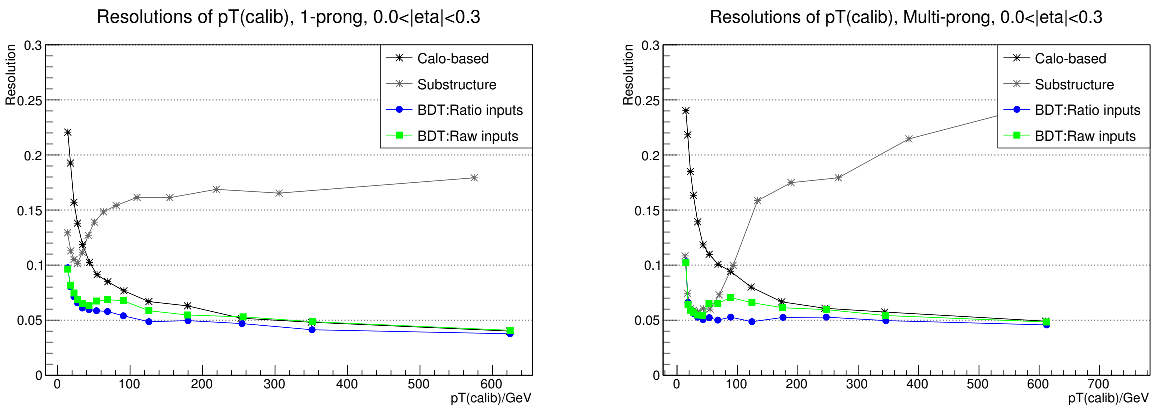

(a) 1-prong $\tau_{\mathrm{had-vis}}$ (b) multi-prong $\tau_{\mathrm{had-vis}}$'s

Figure 154: The resolutions of $p_{\mathrm{T}}^{\mathrm{cali}}$ for (a) 1-prong and (b) multi-prong $\tau_{\mathrm{had-vis}}$'s obtained by BDT regressions using the raw values (green) of $p_{\mathrm{T}}^{\mathrm{LC}}$ and $p_{\mathrm{T}}^{\mathrm{TPF}}$ as inputs and their ratios to $p_{\mathrm{T}}^{\mathrm{interp}}$ (blue) as inputs. Results for $|\eta| > 0.3$ were not shown here, but their features are similar.

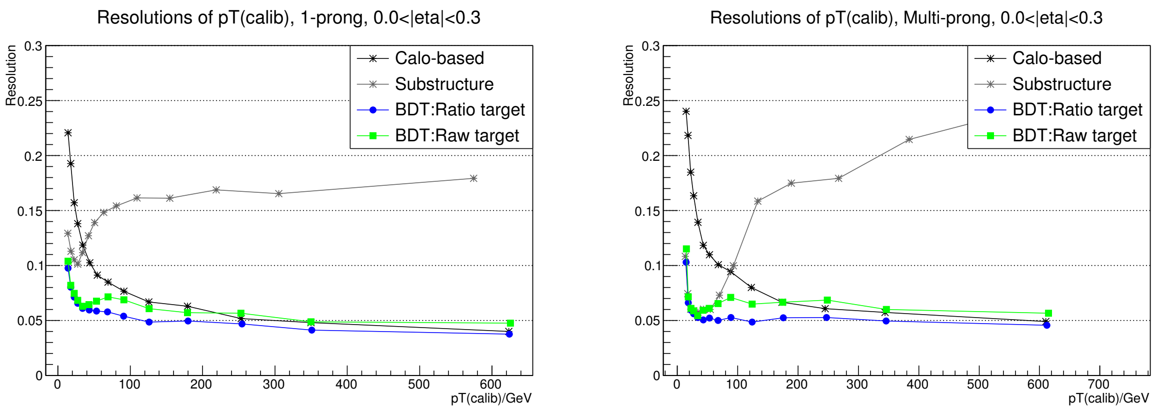

(a) 1-prong $\tau_{\mathrm{had-vis}}$ (b) multi-prong $\tau_{\mathrm{had-vis}}$'s

Figure 155: The resolutions of $p_{\mathrm{T}}^{\mathrm{cali}}$ for (a) 1-prong and (b) multi-prong $\tau_{\mathrm{had-vis}}$'s obtained by BDT regressions using the raw values (green) of $p_{\mathrm{T}}^{\mathrm{true,vis}}$ as target and its ratio to $p_{\mathrm{T}}^{\mathrm{interp}}$ (blue) as target. Results for $|\eta| > 0.3$ were not shown here, but their features are similar.

resolution of the BDT regression trained using the raw values of $p_{\mathrm{T}}^{\mathrm{LC}}$ and $p_{\mathrm{T}}^{\mathrm{TPF}}$ as inputs to that using the ratios $p_{\mathrm{T}}^{\mathrm{LC}}/p_{\mathrm{T}}^{\mathrm{interp}}$ and $p_{\mathrm{T}}^{\mathrm{TPF}}/p_{\mathrm{T}}^{\mathrm{interp}}$ as inputs. The reason of introducing the variable $p_{\mathrm{T}}^{\mathrm{interp}}$ will be discussed later in section H.4.

For the regression target, the ratio of $p_{\mathrm{T}}^{\mathrm{true,vis}}$ to $p_{\mathrm{T}}^{\mathrm{interp}}$ is used instead of the raw values of $p_{\mathrm{T}}^{\mathrm{true,vis}}$. The rationale is that the ratio $p_{\mathrm{T}}^{\mathrm{true,vis}}/p_{\mathrm{T}}^{\mathrm{interp}}$ only spans a narrow range around unity while $p_{\mathrm{T}}^{\mathrm{true,vis}}$ spans a wide range from zero to over a thousand GeV. The regression towards the ratio can give a precise "correction factor" to $p_{\mathrm{T}}^{\mathrm{interp}}$ without having to predict the precise value of $p_{\mathrm{T}}^{\mathrm{true,vis}}$ over a wide range. The difference in resolution of using raw values or ratios as the regression target can be seen in figure 155.

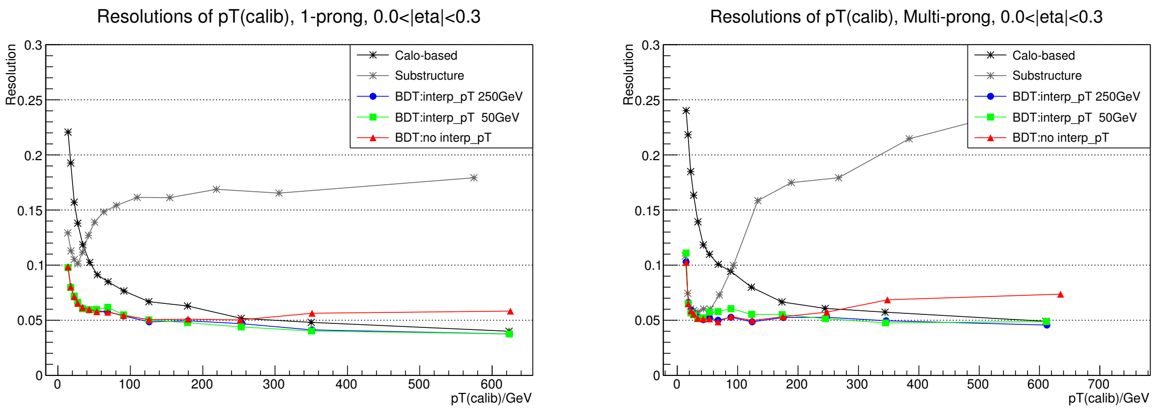

(a) 1-prong $\tau_{\mathrm{had-vis}}$ (b) multi-prong $\tau_{\mathrm{had-vis}}$'s

Figure 156: The resolutions of $p_{\mathrm{T}}^{\mathrm{cali}}$ for (a) 1-prong and (b) multi-prong $\tau_{\mathrm{had-vis}}$'s obtained by BDT regressions with or without (red) introducing the variable $p_{\mathrm{T}}^{\mathrm{interp}}$, with $x = 250$ (blue) or $x = 50$ (green). Results for $|\eta| > 0.3$ were not shown here, but their features are similar.

H.4. Interpolated transverse momentum

Before the interpolated transverse momentum $p_{\mathrm{T}}^{\mathrm{interp}}$ was introduced to the MVA calibration, $p_{\mathrm{T}}^{\mathrm{true,vis}}/p_{\mathrm{T}}^{\mathrm{TPF}}$ had been used as the regression target. This, however, created an issue since the native resolution of $p_{\mathrm{T}}^{\mathrm{TPF}}$ can introduce error to the target and affect the precision of the BDT regression. Since the resolution of $p_{\mathrm{T}}^{\mathrm{TPF}}$ is worse at higher p_{T}, the effect is especially seen at $p_{\mathrm{T}} \gtrsim 250$ GeV. Using $p_{\mathrm{T}}^{\mathrm{true,vis}}/p_{\mathrm{T}}^{\mathrm{LC}}$ as target, on the other hand, worsen the resolution at low p_{T}. Therefore, a new variable $p_{\mathrm{T}}^{\mathrm{interp}}$ is introduced and is defined as

$$p_{\mathrm{T}}^{\mathrm{interp}} = f_x \times p_{\mathrm{T}}^{\mathrm{LC}} + (1 - f_x) \times p_{\mathrm{T}}^{\mathrm{TPF}}, \tag{18}$$

where f_x is a weight between zero and one and is a function of $p_{\mathrm{T}}^{\mathrm{LC}}$:

$$f_x(p_{\mathrm{T}}^{\mathrm{LC}}) = \frac{1}{2}\left(1 + \tanh \frac{p_{\mathrm{T}}^{\mathrm{LC}} - x \text{ GeV}}{20 \text{ GeV}}\right). \tag{19}$$

In other words, $p_{\mathrm{T}}^{\mathrm{interp}}$ is the weighted average of $p_{\mathrm{T}}^{\mathrm{TPF}}$ and $p_{\mathrm{T}}^{\mathrm{LC}}$ with $p_{\mathrm{T}}^{\mathrm{TPF}}$ weighted more at low p_{T} and $p_{\mathrm{T}}^{\mathrm{LC}}$ weighted more at high p_{T}. x defines the point where the transition from low p_{T} to high p_{T} occurs.

In figure 156, it can be seen that the resolution for multi-prong taus at high p_{T} is improved by introducing $p_{\mathrm{T}}^{\mathrm{interp}}$. It has also been observed that a transition at low p_{T} ($x = 50$) creates an unwanted effect that worsen the resolution around the transition. A transition at higher p_{T} ($x = 250$) is therefore more preferable. The final MVA-based calibration uses $p_{\mathrm{T}}^{\mathrm{interp}}$ with $x = 250$.

H.5. Settings of BDT training

As mentioned previously, settings of the training algorithm might affect the performance of the calibration significantly. Table 29 lists out the configurable options of the BDT training algorithm and their values used for the MVA-based $\tau_{\mathrm{had-vis}}$ energy calibration.

Options of BDT training	Values
Boosting type	Gradient boosting
Number of trees	2000
Shrinkage	0.1
Fraction of bagged samples	0.5
Number of grid points used in node splitting	200
Maximum depth of each tree	5

Table 29: List of configurable options of the BDT training algorithm and their values used for the MVA-based $\tau_{\mathrm{had-vis}}$ energy calibration.

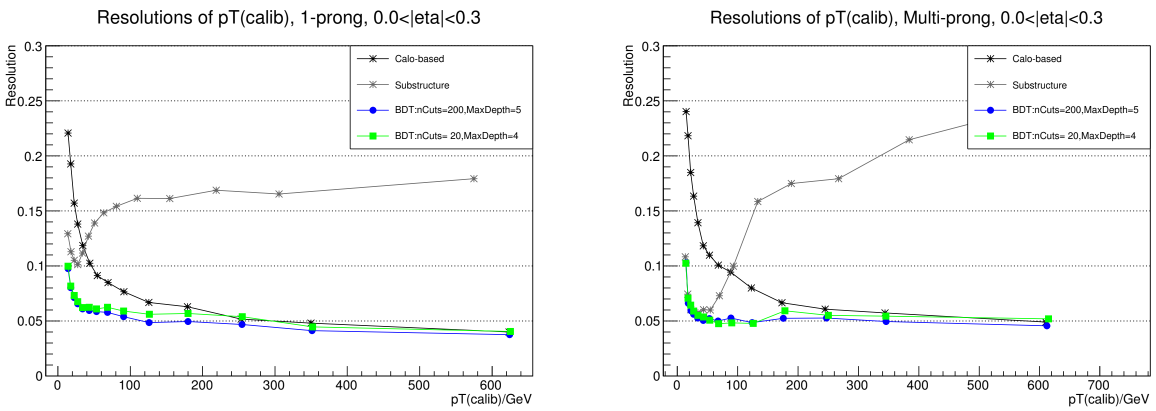

(a) 1-prong $\tau_{\mathrm{had-vis}}$

(b) multi-prong $\tau_{\mathrm{had-vis}}$'s

Figure 157: The resolutions of $p_{\mathrm{T}}^{\mathrm{cali}}$ for (a) 1-prong and (b) multi-prong $\tau_{\mathrm{had-vis}}$'s obtained by BDT regressions with nCuts=200, MaxDepth=5 (blue) and nCuts=20, MaxDepth=4 (green). Results for $|\eta| > 0.3$ were not shown here, but their features are similar.

The impact of changing the number of grid points used in node splitting (nCuts) and the maximum depth of trees (MaxDepth) on the resulted resolution has been investigated. Figure 157 shows the difference of using nCuts = 20 and MaxDepth = 4 compared to nCuts = 200 and MaxDepth = 5. The resolution is slightly improved by increasing nCuts and MaxDepth while the training time stills remain reasonable ($\sim$ 1.5 days).